

Functional Assessment of the Thoracic Aorta in Patients with Aortic Valve Pathology using Patient-Specific Computational Fluid Dynamics

Thesis submitted to
University of London

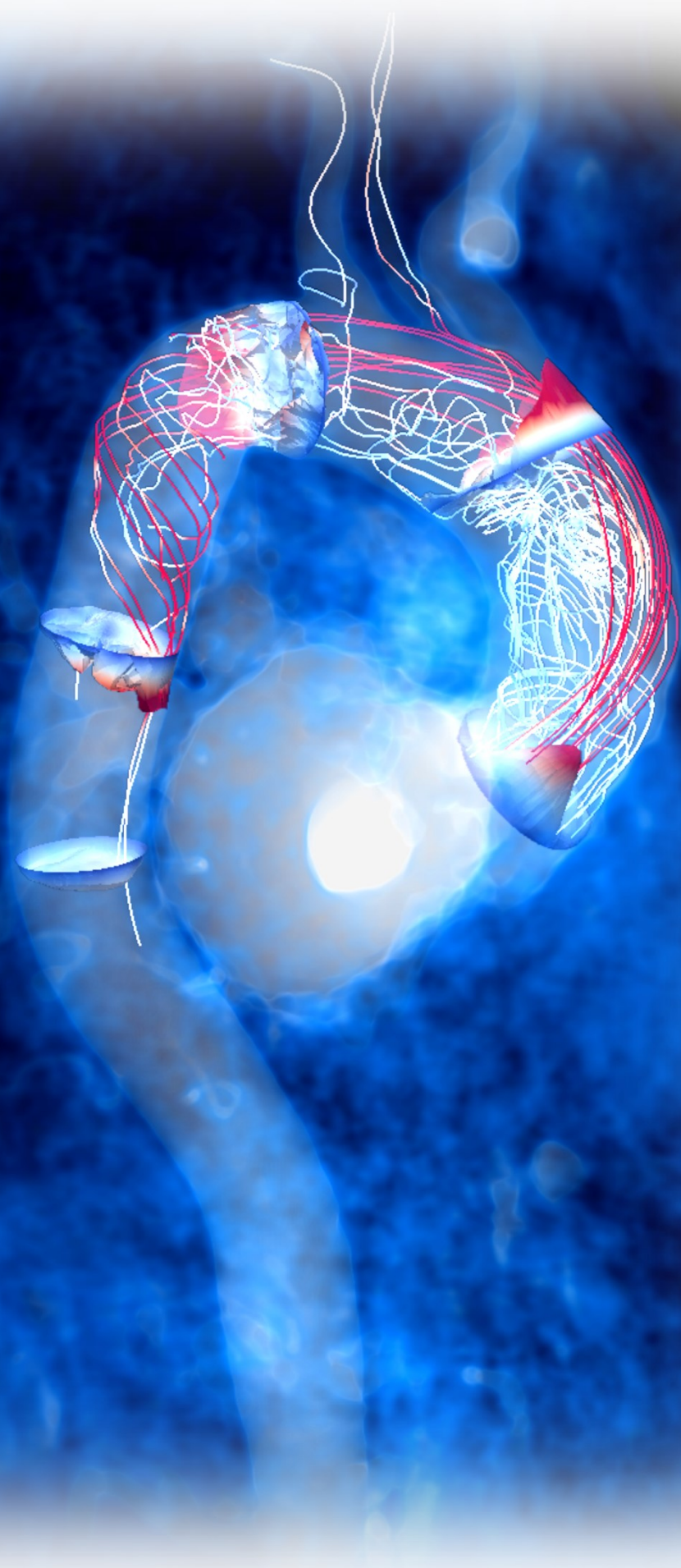
For the degree of
Doctor of Philosophy

By
Pouya Youssefi

Department of Cardiac and Vascular Sciences

St. George's University of London

2017



“Let the beauty of what you love be what you do.”

Rumi, 1207 - 1273

ABSTRACT

This thesis contributes to knowledge by assessing the link between the aortic valve and pathology of the thoracic aorta from both a biomechanical and computational fluid dynamics viewpoint. For many years, international guidelines for intervention on the aorta have concentrated on size alone. However, aortic size alone does not distinguish between different pathological processes which vary in their risk of acute complications. Large registries indicate acute aortic dissection or rupture can occur when the aortic size is below intervention criteria. There is strong evidence for a link between aortic valve morphology and aortopathy. What is missing is a functional assessment of the aorta in order to fully investigate the haemodynamic causes of aortopathy.

We have carried out computational fluid dynamics (CFD) of the thoracic aorta in a patient-specific manner in order to measure flow indices and wall biomechanics of the thoracic aorta. To achieve this, we have devised a novel method of acquiring patient-specific velocity profiles above the aortic valve from MRI image data. This has allowed us to run patient-specific CFD simulations. We have compared this novel method with simple “idealised” velocity profiles traditionally used in CFD simulations of the cardiovascular system. We have shown that the traditional “idealised” inflow conditions oversimplify flow in the thoracic aorta, and do not exhibit the complex fluid dynamics encountered (Study 1).

Using this methodology, we have performed an “in-vitro” comparison of aortic haemodynamics between tricuspid and bicuspid aortic valves (BAV) using a phantom heart and aorta model (Study 2). This has shown bicuspid valves to create eccentric and asymmetrical flow patterns, with higher levels of wall shear stress in the greater curvature of the ascending

aorta. This leads on to the “in-vivo” study comparing aortic haemodynamics in 45 subjects separated into 5 groups (Study 3): healthy tricuspid aortic valve, tricuspid aortic valve with stenosis, tricuspid aortic valve with regurgitation, right-left fusion bicuspid aortic valve with stenosis, and right-non fusion bicuspid aortic valve with stenosis. Results show increased velocity jets at the periphery of the aorta in BAV patients. Velocity streamlines show that these narrow jets impact on the greater curvature of the ascending aorta, and subsequently spiral around the ascending aorta and arch. They cause increased wall shear stress and reduced oscillatory shear index at the greater curvature, corresponding to larger mid-ascending aorta diameters.

We further investigated the effects of aortic root intervention on haemodynamics of the aorta (Study 4). Our results showed that valve-sparing aortic root replacement, using the remodelling technique, leads to a reduction of wall shear stress in the native preserved aortic root (interleaflet triangles and commissures) and greater curvature of the ascending aorta. There is increased axial velocity, and reduced radial velocity, indicating enhanced forward flow. However, this was observed alongside a small increase in wall shear stress in the arch and descending aorta.

The outcomes in aortic haemodynamics from this work may relate to a potential explanation for the increased incidence of aortopathy in BAV patients. This has highlighted the need to develop a functional assessment of the thoracic aorta in order to understand the haemodynamic causes for aortopathy, as well as a means of better predicting complications. CFD, if carried out in a patient-specific manner, provides a potential method of acquiring this functional assessment. It may help in assessment of the adequacy of current management and imaging guidelines of the aortic valve and aorta.

ACKNOWLEDGEMENTS

This body of work represents the translation of what started out as an idea, and an area of cardiac surgery which I am greatly interested in. But what developed was a fascination, and a rejuvenation of my love for mathematics and physics, from which I now realise arises physiology. To get to this stage where I can put words to paper has taken not only perseverance and sacrifice, but kind support from a number of talented individuals. It is now that the end of this journey draws closer that I can admit how much I have enjoyed it.

Marjan Jahangiri - Firstly, I would like to thank Professor Marjan Jahangiri for giving me the platform and confidence to embark on this project. Your dedication to work, your support and mentorship, and your strength and tenacity know no boundaries. The longer I have known you, the more I learn the reasons why you do what you do, are who you are, and achieve what you strive for. That, I realise now, is what teaching is.

Alberto Figueroa - To Professor Alberto Figueroa, I will be forever grateful for making the decision on the day I met you and presented my ideas, that I was worth taking on. You took me under your wings and gave me the foundations of fluid dynamics on which to continue. Your attention to detail has kept my feet on the ground, but your training has allowed me to sprout new wings and fly. I am indebted to you and your trust that I, as a surgeon, could pull this off.

Rajan Sharma - A big thank you to Dr. Rajan Sharma for your support and wise words. Your expertise and guidance has kept me focused and helped me put together my ideas.

Aberto Gomez - No words can describe how grateful I am to Alberto Gomez, who has contributed to this work by writing the *Matlab* code for velocity profile acquisition. I am still in amazement at your coding genius, and I thank you for all the hours you spent working on this. None of this would have been possible without your help.

Des Dillon-Murphy & Chris Arthurs - A special thank you to Des Dillon-Murphy and Chris Arthurs, for your unremitting patience and friendship. I feel proud to have worked in a team of such accomplished yet selfless engineers who were always willing to help explain, guide, and solve endless problems. From the many things I have learned from you, one that stands out is the patience to unravel every challenge with the fundamentals of science and mathematics.

Nicole Radford - I am indebted also to Nicole Radford, my constant friend and accomplice who sits beside me and has kept me going to reach this stage. Your help, care and companionship has given me the energy and support I needed on even the most sleep-deprived days.

Most of all, I need to thank my amazing family. I would never have had the opportunity of meeting the talented people above had it not been for my wonderful Mum and Dad. Thank you for instilling in me the self-belief to always search for my dreams, and for the never-ending sacrifices you have made throughout your lives which have allowed me to be standing here today.

And finally, to my beautiful wife and best friend Izzi, who walks every step by my side. You have endured this difficult time with me, and for each night that I have not been by your side, you have been in my heart, pushing me on. To my endearing and delightful son Caspian, the light of my life. You are the reminder of why I must work hard every day and be proud of what I do, so that hopefully you can one day be proud of me too.

ACHIEVEMENTS

AWARDS

- 2015 **Walton Lillehei Young Investigator Award** – European Association
for Cardiothoracic Surgery (EACTS) 2015: Effect of Aortic Valve
Morphology on Fluid Dynamics of the Thoracic Aorta
- 2016 **Ronald Edwards Medal for Best Scientific Presentation** – Society for
Cardiothoracic Surgery (SCTS) 2016: Effect of Aortic Valve
Morphology on Fluid Dynamics of the Thoracic Aorta
- 2017 **Bob Bonser Medal For Aortic Surgery** – Society for Cardiothoracic
Surgery (SCTS) 2017: Effect of Valve-Sparing Aortic Root
Replacement on Haemodynamics of the Thoracic Aorta Using Patient-
Specific Computational Fluid Dynamics
- 2015 **AATS Resident Competition Bronze Medal Prize:** Fluid Dynamics
of the Thoracic Aorta – an Insight into Aneurysm Formation
- 2015 **Royal College of Surgeons of England Research Fellowship**
- 2016 **Dunhill Medical Trust Research Fellowship**
- 2015 **Marfan Association Grant**

PUBLICATIONS

Youssefi P, Gomez A, He T, Anderson L, Bunce N, Sharma R, Figueroa A, Jahangiri M. Patient-Specific Computational Fluid Dynamics – Assessment of Aortic Hemodynamics in a Spectrum of Aortic Valve Pathologies.

J Thorac Cardiovasc Surg. 2017; 153(1): 8-20

Youssefi P, Sharma R, Figueroa A, Jahangiri M. Functional Assessment of Thoracic Aortic Aneurysms – The Future of Risk Prediction?

Br Med Bull. 2017; 121(1): 61-71

Youssefi P, Jahangiri M. Removing the Bicuspid Source of Aortopathy Prevents Further Dilatation.

Eur J Cardiothorac Surg. 2017; 51(1): 193

Youssefi P, Gomez A, Sharma R, Jahangiri M, Figueroa A. Effect of Patient-Specific Inflow Velocity Profile on Haemodynamics of the Thoracic Aorta.

Accepted by Journal of Biomechanical Engineering – in press

Youssefi P, Jahangiri M. ‘Thoracic Aortic Surgery in Marfan Syndrome’.

‘Diagnosis and Management of Marfan Syndrome’ edited by A H Child, 2015

Springer Publishers – ISBN 978-1-4471-5442-6

INTERNATIONAL PRESENTATIONS

- Oct 2017 **European Association for Cardiothoracic Surgery (EACTS).**
Vienna, Austria
- Effect of Valve-Sparing Aortic Root Replacement on Haemodynamics of the Thoracic Aorta using Patient-Specific Computational Fluid Dynamics*
- Youssefi P**, Gomez A, He T, Anderson L, Tome M, Bunce N, Sharma R, Figueroa A, Jahangiri M.
- Oral Presentation
-
- Oct 2016 **European Association for Cardiothoracic Surgery (EACTS).**
Barcelona, Spain
- In Vitro Comparison of Aortic Haemodynamics in Bicuspid and Tricuspid Aortic Valves using Patient-Specific Computational Fluid Dynamics*
- Youssefi P**, Gomez A, He T, Anderson L, Bunce N, Sharma R, Figueroa A, Jahangiri M.
- Oral Presentation
-
- May 2016 **American Association for Thoracic Surgery (AATS) Aortic Symposium.**
New York, USA
- Remodelling of the Aortic Root: Short and Mid Term Outcomes*
- Bilkhu R, Viviano A, Soppa G, **Youssefi P**, Edsell M, van Besouw JP, Jahangiri M.

Oral Presentation

Oct 2015 **American Association for Thoracic Surgery (AATS) Aortic Symposium Workshop.**

Kobe, Japan

Patient-Specific Fluid Dynamics – A New Diagnostic Tool for Assessment of the Thoracic Aorta?

Youssefi P, Gomez A, Sharma R, Figueroa A, Jahangiri M.

Oral Presentation

Oct 2015 **European Association for Cardiothoracic Surgery (EACTS)**

Amsterdam, NL

Effect of Aortic Valve Morphology on Fluid Dynamics of the Thoracic Aorta

Youssefi P, Gomez A, He T, Bunce N, Sharma R, Figueroa A, Jahangiri M.

Oral Presentation

Sept 2015 **World Society of Cardiothoracic Surgeons (WSCTS)**

Edinburgh, UK

Haemodynamic Markers of Aortopathy – Moving Away from Size

Youssefi P, Gomez A, He T, Bunce N, Sharma R, Figueroa A, Jahangiri M.

Accepted for Oral Presentation

April 2015 **American Association for Thoracic Surgery (AATS)**

Seattle, USA

Fluid Dynamics of the Thoracic Aorta – An Insight into Aneurysm Formation?

Youssefi P, Gomez A, Sharma R, Figueroa A, Jahangiri M.

Poster Presentation

NATIONAL PRESENTATIONS

March 2017 **Society of Cardiothoracic Surgeons Annual Meeting**

Belfast

Effect of Valve-Sparing Aortic Root Replacement on Haemodynamics of the Thoracic Aorta using Patient-Specific Computational Fluid Dynamics

Youssefi P, Gomez A, He T, Anderson L, Tome M, Bunce N, Sharma R, Figueroa A, Jahangiri M.

Oral Presentation

March 2017 **Society of Cardiothoracic Surgeons Annual Meeting**

Belfast

In Vitro Comparison of Aortic Haemodynamics in Bicuspid and Tricuspid Aortic Valves using Patient-Specific Computational Fluid Dynamics

Youssefi P, Gomez A, He T, Anderson L, Bunce N, Sharma R, Figueroa A, Jahangiri M.

Oral Presentation

March 2017 **Society of Cardiothoracic Surgeons Annual Meeting**

Belfast

Aortic Arch Intervention in Patients Who Have Undergone Aortic Root Replacement: A 6 Year Follow Up

Bilkhu R, Diab M, **Youssefi P**, Sharma R, Child A, Tome M, Edsell M, Jahangiri M.

Oral Presentation

March 2016 **Society of Cardiothoracic Surgeons Annual Meeting,**

Birmingham

Effect of Aortic Valve Morphology on Fluid Dynamics of the Thoracic Aorta

Youssefi P, Gomez A, He T, Anderson L, Bunce N, Sharma R, Figueroa A, Jahangiri M.

Oral Presentation

“Have patience. All things are difficult before they become
easy.”

Saadi, 1208 - 1291

CONTENTS

Abstract	4
Acknowledgements	6
Achievements	8
Abbreviations	23
List of Figures	26
List of Tables	34
Statement of Originality	35
Chapter 1: Aims & Hypothesis	36
1.1 Aims	37
1.2 Hypothesis	38
Chapter 2: Introduction	39
2.1 Overview	40
2.2 Anatomy of the Aortic Valve and Thoracic Aorta	40
2.2.1 History	41
2.2.2 Aortic Valve and Root	43
2.2.3 Valve Leaflets	45
2.2.4 Annulus	45

2.2.5	Sinuses of Valsalva and Sinotubular Junction	48
2.2.6	Interleaflet Triangles	48
2.2.7	Ascending Aorta	49
2.2.8	Aortic Arch	50
2.2.9	Descending Thoracic Aorta	52
2.2.10	Embryology	52
2.3	Bicuspid Aortic Valve	56
2.3.1	BAV Related Aortopathy	57
2.3.1.1	Medial Degeneration	59
2.3.1.2	Fibrillin	59
2.3.1.3	Matrix Metalloproteinases	60
2.4	Clinical Need for Functional Assessment	62
2.5	Modalities of Haemodynamic Assessment	67
2.5.1	Computational Fluid Dynamics	67
2.5.1.1	Imaging and Modelling	67
2.5.1.2	Boundary Conditions	68
2.5.2	4D Flow MRI	70
2.5.3	Comparison of CFD and 4D Flow MRI	70
2.6	Haemodynamic Parameters and Clinical Implications	71
2.6.1	Wall Shear Stress	72

2.6.2	Flow Patterns	80
2.6.3	Helical Flow	82
2.6.4	Oscillatory Shear Index	82
Chapter 3:	Methods	84
3.1	Overview	85
3.1.1	Workflow of Methodology: Imaging and CFD	87
3.2	Imaging	89
3.2.1	Imaging the Aorta	89
3.2.2	Flow Imaging	90
3.2.3	Aortic Valve Morphology	91
3.3	Computational Fluid Dynamics	92
3.3.1	Geometric Modelling and Segmentation of the Aorta	92
3.3.2	Mesh Generation	95
3.3.3	Finite Element Analysis	98
3.3.4	Constitutive Material Models	98
3.3.5	Time Integration Strategy	98
3.4	Inflow Boundary Conditions	99
3.4.1	Overview	99
3.4.2	Flow MRI	100
3.4.3	Velocity and Flow Extraction	101

3.4.4	Lumen Segmentation	101
3.4.5	Mapping of Velocity Profile onto Inlet Mesh of Aorta Model	103
3.4.6	Validation of Mapping Process	108
3.5	Outflow Boundary Conditions	108
3.5.1	Validation of Outflow Boundary Conditions	111
3.6	Quantification of Haemodynamic Indices	112
3.6.1	Flow Patterns	112
3.6.2	Flow Asymmetry	113
3.6.3	Flow Dispersion	114
3.6.4	Helicity	115
3.6.5	Wall Indices	117
Chapter 4:	Study 1: Impact of Patient-Specific Inflow Velocity Profile on Haemodynamics of the Thoracic Aorta	120
4.1	Overview	121
4.2	Background	121
4.2.1	Idealised Velocity Profiles	122
4.3	Methods	127
4.3.1	Study Population	130
4.3.2	Inflow Velocity Profile	131

4.3.3	Quantification of Flow Characteristics	131
4.3.4	Quantification of Wall Mechanics	132
4.4	Study 1A Results: Flow Characteristics	132
4.4.1	Velocity Patterns	132
4.4.2	Velocity Magnitude Waveforms	142
4.4.3	Helicity	144
4.4.4	Velocity Streamlines	144
4.4.5	Velocity Pathlines	146
4.4.6	Flow Asymmetry and Dispersion	148
4.5	Study 1B Results: Wall Mechanics	151
4.5.1	Patient Demographics	151
4.5.2	Velocity Profiles	151
4.5.3	Wall Shear Stress	152
4.5.4	Mean WSS	155
4.5.5	Oscillatory Shear Index	162
4.6	Summary	164
Chapter 5:	Study 2: “In Vitro” Comparison of Aortic Haemodynamics in Bicuspid and Tricuspid Aortic Valves Using a Phantom Heart and Aorta Model	166
5.1	Overview	167
5.2	Background	167

5.3	Methods	168
5.3.1	Phantom Heart and Aorta Model	168
5.3.2	Aortic Valve	171
5.3.3	Imaging and CFD	172
5.3.4	Haemodynamic Parameters	173
5.4	Results	174
5.4.1	Velocity Profiles	174
5.4.2	Flow Patterns	175
5.4.3	Wall Shear Stress	178
5.4.4	Oscillatory Shear Index	181
5.5	Summary	184
Chapter 6:	Study 3: Assessment of Aortic Hemodynamics in a Spectrum of Aortic Valve Pathologies	186
6.1	Overview	187
6.2	Background	187
6.3	Methods	188
6.3.1	Study Population	188
6.3.2	Statistical Analysis	190
6.4	Results	191
6.4.1	Velocity Profiles	191

6.4.2	Flow Patterns	194
6.4.3	Wall Shear Stress	196
6.4.4	Oscillatory Shear Index	200
6.5	Summary	202
Chapter 7:	Study 4: Effect of Valve-Sparing Aortic Root Replacement on	
	Haemodynamics of the Thoracic Aorta	204
7.1	Overview	205
7.2	Background	205
7.3	Methods	207
7.3.1	Study Population	207
7.3.2	Haemodynamic Parameters	208
7.3.3	Statistical Analysis	211
7.4	Results	211
7.4.1	Patient Demographics	211
7.4.2	Root Geometry	213
7.4.3	Velocity Streamlines and Flow Patterns	215
7.4.4	Axial and Radial Velocity	217
7.4.5	Wall shear stress – Aortic root	220
7.4.6	Wall shear stress – Remaining aorta	223
7.5	Summary	226

Chapter 8: Discussion	227
8.1 Overview	228
8.2 Study 1: Impact of Patient-Specific Inflow Profile	228
8.3 Study 2: “In Vitro” Comparison Using Phantom	233
8.4 Study 3: Aortic Valve Pathologies	235
8.5 Study 4: Valve-Sparing Aortic Root Replacement	237
8.6 Limitations	240
Chapter 9: Conclusions	243
9.1 Study 1: Impact of Patient-Specific Inflow Profile	244
9.2 Study 2: “In Vitro” Comparison Using Phantom	245
9.3 Study 3: Aortic Valve Pathologies	245
9.4 Study 4: Valve-Sparing Aortic Root Replacement	246
Chapter 9: Future Work	247
10.1 Addressing limitations	248
10.2 Future projects	249
10.2.1 Longitudinal studies	249
10.2.2 Histopathological / Proteomic comparison studies	250
10.2.3 Post intervention studies	251
10.3 Final words	252
Bibliography	253

ABBREVIATIONS

AAo	ascending aorta
ACEi	angiotensin converting enzyme inhibitor
ANOVA	analysis of variance
AR	aortic regurgitation
ARB	angiotensin receptor blocker
AS	aortic stenosis
BAV	bicuspid aortic valve
Bpm	beats per minute
CAD	computer aided design
CFD	computational fluid dynamics
CMR	cardiovascular magnetic resonance imaging
CoA	coarctation of the aorta
CT	computed tomography
ECM	extracellular matrix
FoV	field of view
HFI	helical flow index
HPC	high performance supercomputer

IRAD	International Registry for Acute Aortic Dissections
LCS	left coronary sinus
LVOT	left ventricular outflow tract
MAA	mid-ascending aorta
MIP	maximum intensity projection
MMP	matrix metalloproteinase
MRA	magnetic resonance angiography
MWSS	mean wall shear stress
NCS	non-coronary sinus
NURBS	non-uniform rotational basis spline
OSI	oscillatory shear index
PHA	phantom heart and aorta
PC-MRI	phase-contrast magnetic resonance imaging
PS	patient-specific
RCR	resistance capacitance resistance
RCS	right coronary sinus
RL	right-left
RN	right-non
SI	Svensson index
SOV	sinuses of Valsalva

SSFP	steady-state in free precession
STJ	sino-tubular junction
TAV	tricuspid aortic valve
TE	echo time
TEVAR	thoracic endovascular aortic repair
TGFb	transforming growth factor b
TIMP	tissue inhibitor of MMP
TR	repetition time
Venc	encoding velocity constant
Vmax	maximal velocity
VSMC	vascular smooth muscle cell
VSRR	valve-sparing root replacement
WSR	wall shear rate
WSS	wall shear stress

LIST OF FIGURES

- Figure 2.1 Anatomy of thoracic aorta.
- Figure 2.2 Leonardo da Vinci - The aortic valve and root.
- Figure 2.3 One of the first illustrations of the anatomy of the heart.
- Figure 2.4 Aortic valve position in relation to the other heart valves and structures.
- Figure 2.5 The aortic root.
- Figure 2.6 Diagrammatic representation of the aortic root.
- Figure 2.7 The opened aortic root seen from within the lumen.
- Figure 2.8 The most common aortic arch branching pattern.
- Figure 2.9 Map showing the different anatomical zones of the aortic arch.
- Figure 2.10 Electron micrograph of a mouse embryo showing the outflow tract with division between proximal and distal portions.
- Figure 2.11 Embryo at Carnegie stage 15.
- Figure 2.12 Embryo at Carnegie stage 22.
- Figure 2.13 The classification and incidence of bicuspid aortic valves according to site of cusp fusion.

-
- Figure 2.14** Ascending aortic diameter (cm) as a function of height (cm) among children with BAV vs controls with TAV.
- Figure 2.15** Histopathological features of bicuspid aortopathy.
- Figure 2.16** Yearly rates of rupture, dissection or death according to aortic size.
- Figure 2.17** Distribution of aortic size at the time of presentation with acute type A aortic dissection.
- Figure 2.18** The relationship between wall tension (T), pressure (P) and radius (R) for a cylindrical and spherical vessel according to the Law of Laplace.
- Figure 2.19** Two patients with identical diameters of ascending aorta but very different quality aortic wall.
- Figure 2.20** Flow through a vessel showing wall shear stress is parallel to the vessel wall, whereas blood pressure and tensile stress are perpendicular to the vessel wall.
- Figure 2.21** Wall shear stress measurements in cerebral artery aneurysms.
- Figure 2.22** Wall shear stress measurements in the thoracic aorta from CFD studies.
- Figure 2.23** Velocity jets from a right-left fusion BAV patient directed towards the right-anterior aortic wall.
- Figure 2.24** Elevated aortic WSS generated by aberrant flow from cusp fusion corresponded to more severe extracellular matrix (ECM) dysregulation.
- Figure 2.25** 3D streamline visualization of peak systolic blood flow in patients with BAV in comparison with an aorta size-matched control subject and a healthy volunteer.
- Figure 3.1** Patient-specific components of CFD undertaken in this thesis.

-
- Figure 3.2** Steps involved in the workflow of running CFD simulations for this thesis.
- Figure 3.3** The 3 reconstructed planes from MRA image data (axial, coronal and sagittal planes).
- Figure 3.4** Flow MRI (phase-contrast MRI) at the level of the sinotubular junction.
- Figure 3.5** Cine sequences through the aortic valve showing a bicuspid aortic valve.
- Figure 3.6** Non-Uniform Rotational B-Splines (NURBS) provide a 3D modelling framework based on geometric primitives and drawn curves.
- Figure 3.7** The segmentation and lofting process.
- Figure 3.8** Outline of the lofted aorta model (blue outlines) superimposed on the MRA data.
- Figure 3.9** Tetrahedral mesh of the thoracic aorta.
- Figure 3.10** Segmentation of the lumen boundaries from Flow MRI to create the velocity profile.
- Figure 3.11** Velocity profile obtained from Flow MRI, before mapping to the aorta model geometry.
- Figure 3.12** Rotation contour alignment.
- Figure 3.13** Non-rigid alignment between the Flow MRI derived contour and the aorta model contour at the inlet.
- Figure 3.14** Dense deformation mapping from the aorta model to the Flow MRI imaging contour interpolated from vectors using bicubic B-splines.

-
- Figure 3.15** Inflow velocity profile mapped onto the inlet of the aorta mesh.
- Figure 3.16** Four Windkessel outflow boundary conditions representing the distal vascular bed (arteries, arterioles, capillaries, venules and veins) of each of the outlets (innominate artery, left common carotid artery, left subclavian artery, descending aorta).
- Figure 3.17** Five example planes along the thoracic aorta where in-depth analysis of velocity maps, velocity profiles, axial and radial velocity vectors were analysed.
- Figure 3.18** Velocity maps during peak systole.
- Figure 3.19** Division of the ascending aorta into 8 longitudinal sectors.
- Figure 4.1** Poiseuille flow geometry in a pipe.
- Figure 4.2** Parabolic velocity profile.
- Figure 4.3** Parabolic velocity profile in a fully developed pipe flow.
- Figure 4.4** Velocity vectors showing the parabolic and plug velocity profile shapes in 3-dimensions.
- Figure 4.5** Inflow boundary conditions for subject *TAV* and subject *AS-BAV*.
- Figure 4.6** 2D and 3D representations of velocity magnitude, and radial (e.g. in-plane) velocity components at mid-ascending aorta plane for subject *TAV*.
- Figure 4.7** 2D and 3D representations of velocity magnitude, and radial (e.g. in-plane) velocity components at mid-arch plane subject *TAV*.
- Figure 4.8** 2D and 3D representations of velocity magnitude, and radial (e.g. in-plane) velocity components at mid-descending aorta plane for subject *TAV*.

-
- Figure 4.9** 2D and 3D representations of velocity magnitude, and radial (e.g. in-plane) velocity components at mid-ascending aorta plane for subject *AS-BAV*.
- Figure 4.10** 2D and 3D representations of velocity magnitude, and radial (e.g. in-plane) velocity components at mid-arch plane subject *AS-BAV*.
- Figure 4.11** 2D and 3D representations of velocity magnitude, and radial (e.g. in-plane) velocity components at mid-descending aorta plane for subject *AS-BAV*.
- Figure 4.12** Maximal through-plane velocity (V_{max}), radial velocity and flow rate along the cardiac cycle at 3 planes for subjects *TAV* and *AS-BAV*.
- Figure 4.13** Velocity streamlines and 2D visualisation of velocity magnitude at 5 planes along the thoracic aorta during late systole.
- Figure 4.14** Pathlines and mean absolute HFI calculated using the subject-specific inflow velocity profile for subject *TAV* and subject *AS-BAV* at $t=100, 200, 400,$ and 900 ms.
- Figure 4.15** Flowasymmetry along 3 planes of the thoracic aorta for subjects *TAV* and *AS-BAV*.
- Figure 4.16** Flowdispersion along 3 planes of the thoracic aorta for subjects *TAV* and *AS-BAV*.
- Figure 4.17** Patient-specific and parabolic velocity profiles for the 4 subjects, with corresponding flow rate waveforms.
- Figure 4.18** Wall shear stress (WSS) plots throughout the cardiac cycle. Each line represents one of the 8 anatomical sectors of the ascending aorta.
- Figure 4.19** Plots of mean wall shear stress (MWSS) for each of the 8 sectors of the ascending aorta.

-
- Figure 4.20 MWSS comparison for *TAV*.
- Figure 4.21 MWSS comparison for *AS-BAV*.
- Figure 4.22 MWSS comparison for *AR-BAV*.
- Figure 4.23 MWSS comparison for *N-BAV*.
- Figure 4.24 Radial graphs of oscillatory shear index (OSI) for each of the 8 sectors of the ascending aorta.
- Figure 5.1 Schematic diagram showing the components of the PHA model.
- Figure 5.2 Trileaflet bioprosthetic valve and “bicuspidised” bioprosthetic valve with 2 leaflets sutured together to create a raphe.
- Figure 5.3 Velocity profiles above the aortic valve for the 3 simulations. Arrows show velocity vectors with velocity magnitude represented by arrow length and colour.
- Figure 5.4 Velocity streamlines and velocity maps at the 7 aortic planes at peak systole for the 3 simulations. Wall shear stress maps at peak systole.
- Figure 5.5 Velocity streamlines and velocity maps at the 7 aortic planes at peak systole for the 3 simulations. Wall shear stress maps at peak systole.
- Figure 5.6 MWSS maps at the 7 planes along the thoracic aorta. Yellow colour represents higher MWSS levels.
- Figure 5.7 Graph showing averaged MWSS at each of the 7 aortic planes.
- Figure 5.8 Three-dimensional radar plots of MWSS for each of the 8 sectors of the ascending aorta.

-
- Figure 5.9** Radar plots of OSI for each of the 8 sectors of the ascending aorta.
- Figure 6.1** Velocity profiles above the aortic valve in the 5 study groups.
- Figure 6.2** Graph showing Flow_{asymmetry} for the 5 study groups.
- Figure 6.3** 3D velocity streamlines showing trajectory of velocity during peak systole for example patients from the 5 study groups.
- Figure 6.4** Mean wall shear stress (MWSS) maps for example patients from the 5 study groups.
- Figure 6.5** Wall shear stress (WSS) plots throughout the cardiac cycle for example patients from each of the 5 groups.
- Figure 6.6** Plots of mean wall shear stress (MWSS) for each of the 8 sectors of the ascending aorta.
- Figure 6.7** Radial graphs of oscillatory shear index (OSI) for each of the 8 sectors of the ascending aorta.
- Figure 7.1** The sinuses of Valsalva have been excised from the aortic root, leaving the native valve leaflets and hinges, interleaflet triangles and commissures. A tube graft is tailored to create 3 neo-sinuses of Valsalva.
- Figure 7.2** MRA and 3D model of the thoracic aorta with separation of the different anatomical sectors of the aorta.
- Figure 7.3** Pre and post-op 3-dimensional shape of the aortic root for 3 subjects.
- Figure 7.4** Velocity Streamlines for a subject pre and post-op during early systole and late systole.

-
- Figure 7.5** Velocity vectors during systole at mid-sinus, sinotubular junction, mid-ascending aorta, mid-arch, and mid-descending aorta before and after surgery for a patient.
- Figure 7.6** Averaged velocity throughout the cardiac cycle before and after surgery at the mid-sinus, mid-ascending aorta, and mid-arch planes for an example patient.
- Figure 7.7** WSS maps during peak systole in each of the individual sinuses of Valsalva before and after surgery.
- Figure 7.8** Radar plot showing pre-op (red) and post-op (blue) peak WSS in each interleaflet triangle and commissure.
- Figure 7.9** WSS maps during systole for two patients before and after VSRR.
- Figure 7.10** Peak WSS before and after surgery for each sector of the remaining thoracic aorta.

LIST OF TABLES

- Table 3.1** Example values of the lumped parameter Windkessel boundary conditions for a subject.
- Table 4.1** Demographics, aortic dimensions and Windkessel outlet boundary condition parameters.
- Table 4.2** Helical Flow Index during systole, diastole, and the whole cardiac cycle for the thoracic aorta for particles which traversed the aorta and left the simulation domain through the descending aortic boundary.
- Table 5.1** Values of the lumped parameter Windkessel boundary conditions for each outlet.
- Table 6.1** Demographics, aortic dimensions and hemodynamic indices in the 5 study groups.
- Table 6.2** Hemodynamic indices in the 5 study groups.
- Table 7.1** Demographics and aortic dimensions.

STATEMENT OF ORIGINALITY

I certify that this thesis and the research to which it refers are the product of my own work. Any ideas, quotations or data from the work of others are fully acknowledged with standard referencing practice.

Signature:

1

AIMS & HYPOTHESIS:

“If you have built castles in the air, your work need not be lost; that is where they should be. Now put the foundations under them.”

Henry Thoreau, 1817 - 1862

Contents

1.1	Aims	37
1.2	Hypothesis	38

1.1 AIMS

- (i) To develop a new method of acquiring patient-specific blood velocity profiles above the aortic valve in order to run patient-specific computational fluid dynamics (CFD) of the thoracic aorta.
- (ii) To compare flow and wall mechanics in CFD simulations using patient-specific velocity profiles versus traditionally used “idealised” velocity profiles.
- (iii) To use a phantom heart and aorta model with different aortic valve morphologies to achieve an “in-vitro” comparison of aortic haemodynamics in tricuspid and bicuspid aortic valves.
- (iv) To carry out an “in-vivo” comparison of aortic haemodynamics in subjects with different tricuspid and bicuspid aortic valve morphologies.
- (v) To compare pre-op and post-op aortic haemodynamics following surgical intervention on the aortic root.

1.2 HYPOTHESIS

Aortic valve and root morphology has significant effects on flow patterns and wall mechanics of the thoracic aorta. Haemodynamic indices such as wall shear stress are altered by pathology of the aortic valve and may be related to disease processes of the thoracic aorta.

2

INTRODUCTION

“Anatomy is to physiology as geography is to history;
it describes the theatre of events.”

Jean Fernel, 1542

Contents

2.1	Overview	40
2.2	Anatomy of the Aortic Valve and Thoracic Aorta	40
2.3	Bicuspid Aortic Valve	56
2.4	Clinical Need for Functional Assessment	62
2.5	Modalities of Haemodynamic Assessment	67
2.6	Haemodynamic Parameters and Clinical Implications	71

2.1 OVERVIEW

The aortic valve acts as the gatekeeper to the systemic circulation, an important structure to facilitate (or hamper) the role of the heart in perfusing the body with oxygenated blood. Its highly complex structure and relationship with the aortic root has been the subject of intense research and debate over the last 30 years.

The thoracic aorta, with its curvilinear candy-cane shape, has the arduous task of handling the forces and pressures of blood ejected through the aortic valve, and distributing them to organs directly above and below the heart.

The importance of the relationship between anatomy to physiology, anatomy to function, and thus anatomy to pathology is shown with clarity in this part of the human body, and is the underlying setting of the subject of this thesis.

2.2 ANATOMY OF THE AORTIC VALVE AND THORACIC AORTA

The thoracic aorta can be divided into 4 anatomical sections: the root (containing the aortic valve), ascending aorta, aortic arch, and descending thoracic aorta.

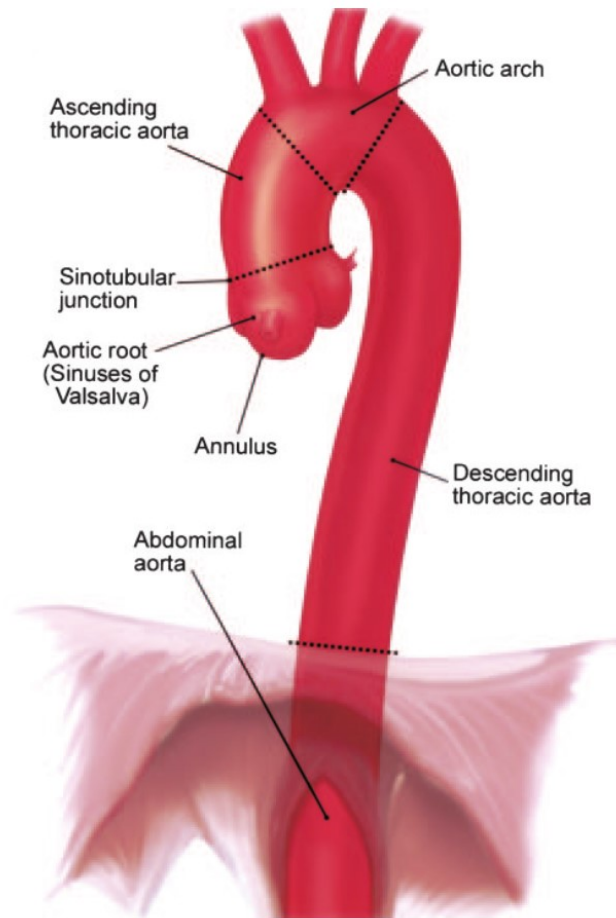


Figure 2.1. Anatomy of thoracic aorta. (Isselbacher 2005)

2.2.1 History

The earliest records of the anatomy of the aortic valve and root come from the Renaissance, with descriptions and drawings by Leonardo da Vinci. Among the 30,000 pages of his notebooks are anatomical studies that, had they been published at the time, might have changed the course of medicine (Clayton 2012). His findings were well ahead of his times, even contrary to the belief at the time that the heart churned blood and generated heat and ‘vital spirit’.



Figure 2.2. Leonardo da Vinci - The aortic valve and root, showing his appreciation of the trileaflet valve with sinuses of Valsalva and vortical flow characteristics. (Vinci)

Following Leonardo da Vinci, the next anatomist to study the heart and its valves was Andreas Vesalius, in one of the most influential books on human anatomy, *De Humani Corporis Fabrica* (Vesalius 1544). However, for the next 400 years, any further study of the human heart was limited.

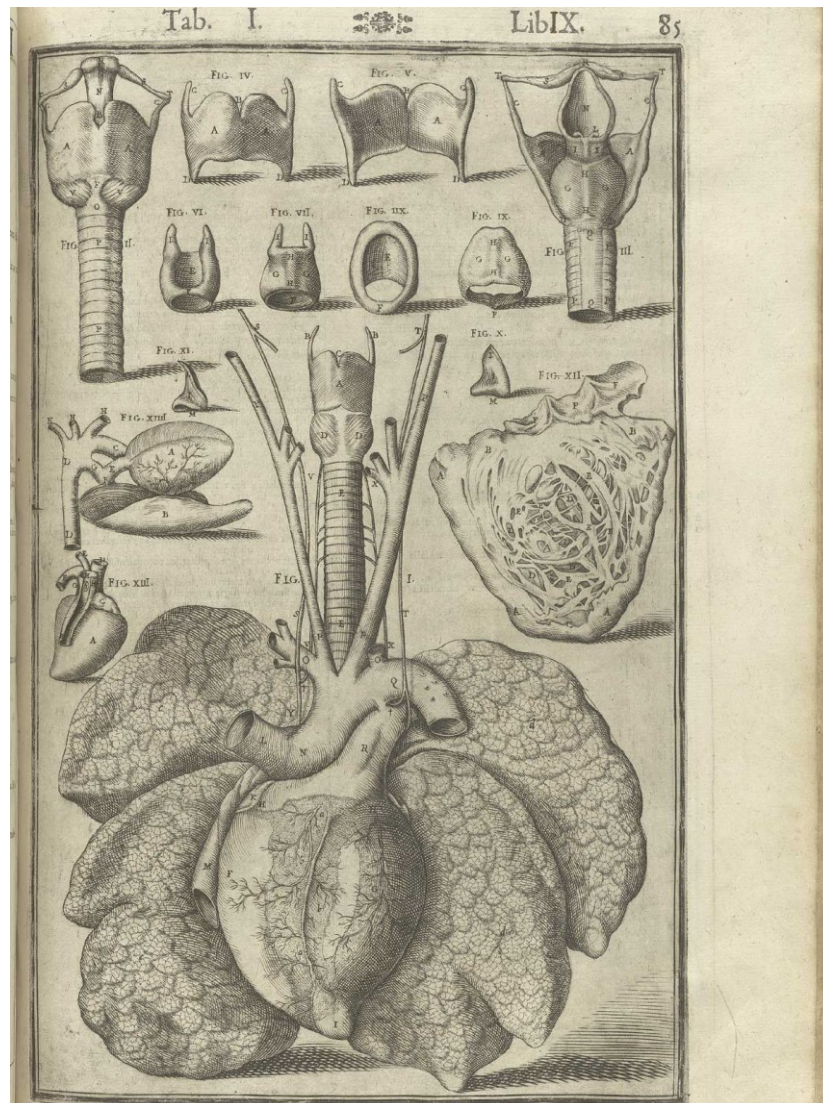


Figure 2.3. One of the first illustrations of the anatomy of the heart, with clear drawings of the ascending aorta and arch, as well as finer details such as the vagus nerves and coronary arteries. (Vesalius 1544)

2.2.2 Aortic Valve and Root

The aortic valve forms the centre-piece of the heart. All 4 chambers of the heart are directly related to this structure. The leaflets of the aortic valve and their supporting structures are incorporated directly into the cardiac skeleton (Anderson 2000).

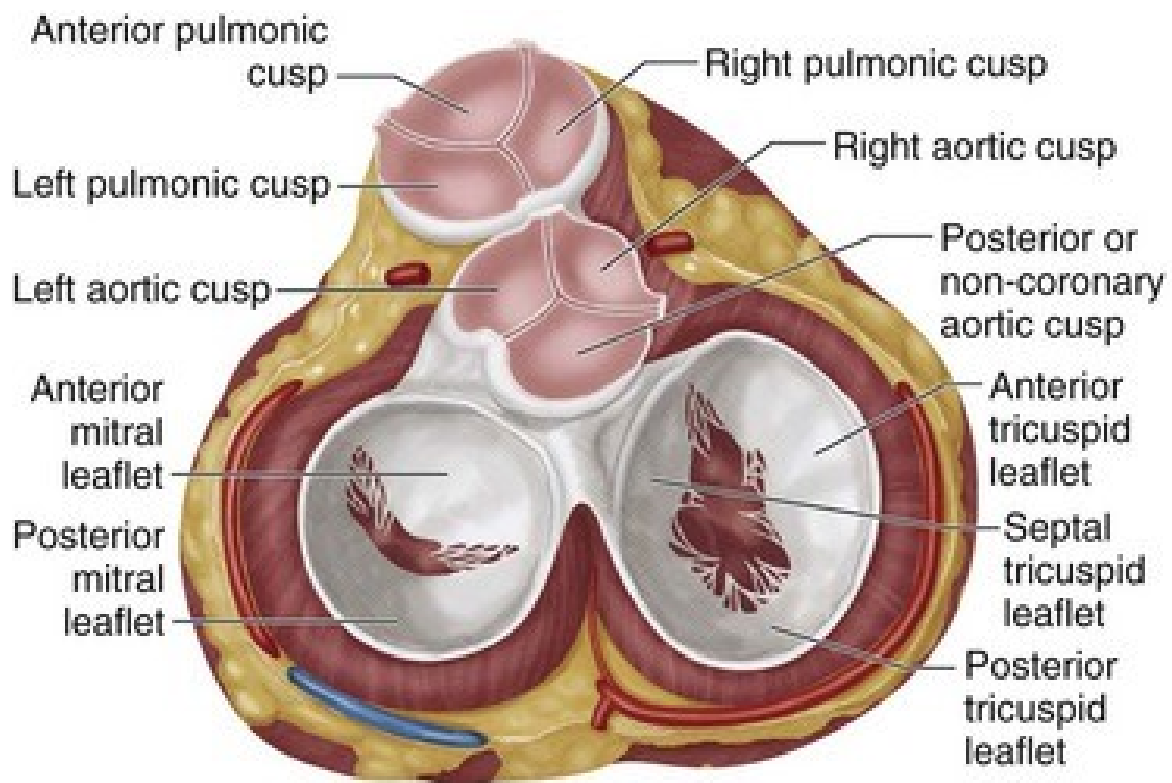


Figure 1.4. Aortic valve position in relation to the other heart valves and structures. (Cohn 2008)

The aortic root consists of the functional aortic annulus, the aortic valve leaflets with their attachments, and the 3 bulges in the aortic wall named the sinuses of Valsalva. It is from the sinuses that the 2 coronary arteries supplying blood to the myocardium arise. The left coronary artery arises from the left coronary sinus, and the right coronary artery arises from the right coronary sinus. The remaining sinus is named the non-coronary sinus. In the same respect, the 3 aortic valve leaflets are named the left, right and non-coronary leaflets.

2.2.3 Valve Leaflets

The aortic valve leaflets provide the sealing mechanism to prevent blood regurgitating back into the left ventricle. The aortic and mitral valvar orifices are fitted alongside each other within the circular short axis of the left ventricle. The leaflets are attached in part to the muscular walls of the left ventricle. The leaflets can be divided into 3 parts:

- The basal part or leaflet attachment
- The belly of the leaflet
- The free margin, with a thickened central nodule (nodule of Arantius) – this provides the area of coaptation with the other leaflets

The tri-leaflet design allows an optimal solution for low resistance valve opening (Thubrikar 1989). All structures distal to the leaflets are subject to arterial haemodynamics, whereas all structures proximal are subjected to ventricular haemodynamics.

2.2.4 Annulus

The aortic annulus, otherwise named the ventriculo-aortic junction or basal ring, describes the transition zone between the left ventricle and the aortic root. This zone is often described by different specialists in different ways. For the cardiologist and echocardiographer, the annulus relates to the plane passing through the nadir of the semilunar leaflet hinges. For the cardiac surgeon, it corresponds to the leaflet hinge-lines onto which a prosthetic valve is sewn. For an anatomist, the annulus is where the myocardium of the left ventricle ends and the aortic wall begins (de Kerchove et al. 2013b).

If the annulus is thought of as a ring, one half of its circumference is a fibrous portion, and the other half is a muscular portion. The fibrous portion lies beneath the non-coronary sinus and

half of the left coronary sinus. It consists of the aorto-mitral continuity, where the base of the anterior leaflet of the mitral valve becomes continuous with the annulus. The muscular portion lies beneath the right coronary sinus and the other half of the left coronary sinus. This consists of the muscular interventricular septum.

Within the lumen of the aortic root, the majority of the leaflet hinge-lines lie above the level of the annulus. The lowest points of the leaflet hinge-lines cross the level of the annulus. The highest points reach to within 1-2mm of the sino-tubular junction. On the outside of the aortic root, the annulus corresponds to the transition zone between myocardial tissue and the aorta. Around the left and non-coronary sinus, this zone corresponds to the roof of the left atrium. Around the right coronary sinus, it corresponds to right ventricular outflow tract and myocardium overlying the interventricular septum (Anderson 2000).

The aorta is a dynamic structure, and changes size and shape during the cardiac cycle. There is a 10% change in diameter of the annulus between systole and diastole, with a relatively greater deformation within the muscular portion compared to the fibrous portion of the annulus (Tilea et al. 2013).

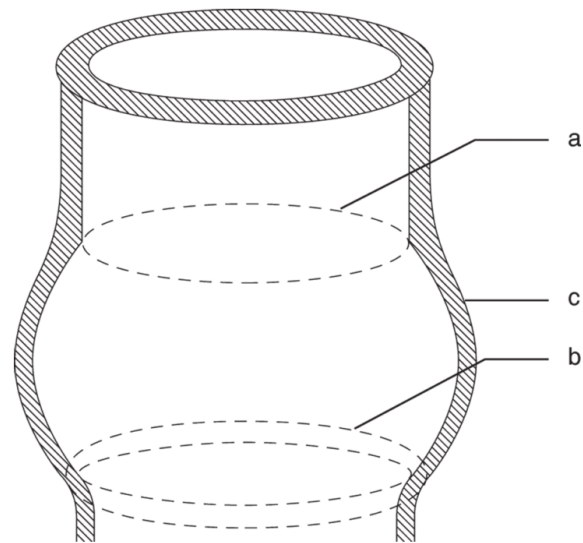


Figure 2.5. The aortic root: a = Sinotubular junction; b = ventriculo-aortic junction; c = sinuses of Valsalva (de Kerchove et al. 2013a)

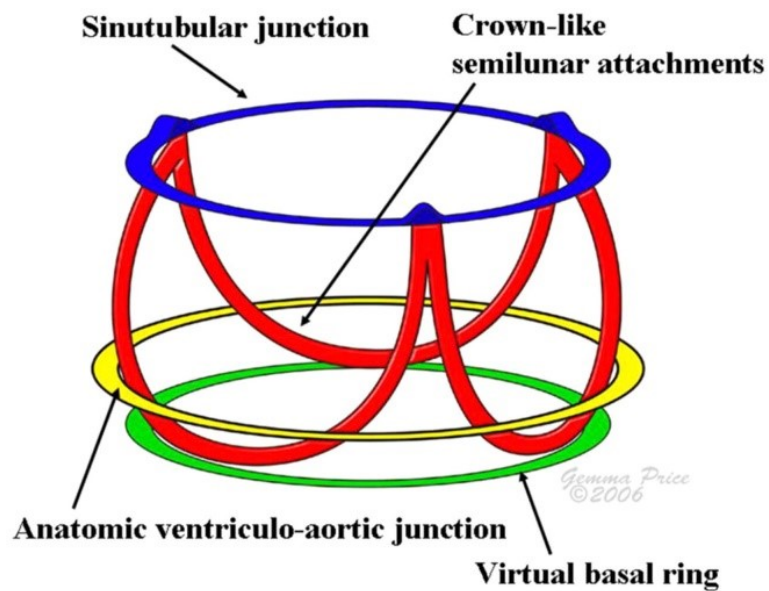


Figure 2.6. Diagrammatic representation of the aortic root. (Piazza et al. 2008)

2.2.5 Sinuses of Valsalva and Sinotubular Junction

At the point where the bulging sinuses of Valsalva end, and the tube-like ascending aorta starts, is named the sino-tubular junction. The circumference of the sino-tubular junction is similar to that of the annulus, and often slightly smaller. This gives the aortic root a structure which allows the aortic valve leaflets to co-apt and close during diastole in a way which prevent regurgitation of blood back into the ventricle.

2.2.6 Interleaflet Triangles

The interleaflet triangles are the areas bound by the commissures superiorly (the apex of the triangle), two adjacent valve hinges laterally (the sides of the triangle) and the annulus inferiorly (base of the triangle). They are extensions of the ventricular outflow tract, however histologically they consist of thinned aortic wall (Charitos et al. 2013). The interleaflet triangle between the right and non-coronary sinuses is in direct continuity with membranous septum which contains the bundle of His. This is of particular importance in aortic valve procedures where sutures placed low down and deep into the base of this triangle can disrupt conduction pathways and lead to heart block, potentially necessitating permanent pacemaker implantation. The interleaflet triangle underneath the left and non-coronary sinuses is related to the anterior mitral valve leaflet.

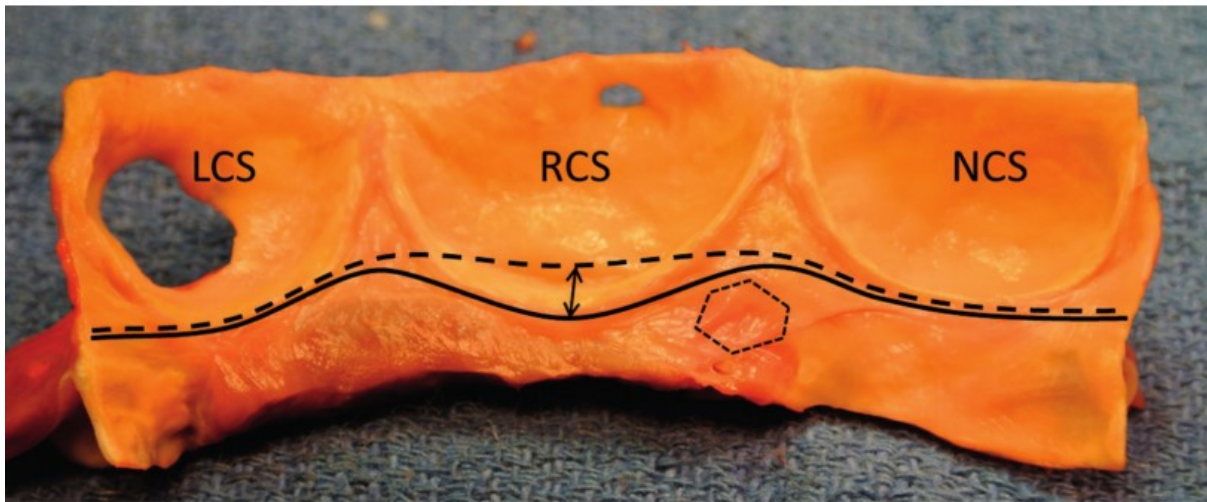


Figure 2.7. The opened aortic root seen from within the lumen. Continuous black line shows the ventriculo-aortic junction; interrupted black line shows the limit of proximal aortic root dissection in valve-sparing aortic root surgery; double black arrow shows the segment of myocardium included into the base of the right coronary sinus; dotted line encircles the membranous septum; LCS = left coronary sinus; RCS = right coronary sinus; NCS = non-coronary sinus. (de Kerchove et al. 2013a)

2.2.7 Ascending Aorta

The ascending aorta commences at the junction between the sinuses of Valsalva, and the tubular ascending aorta, named the sino-tubular junction. Here, it is around 3cm in diameter in a healthy adult. It ascends for a short distance before curving posteriorly and to the left before it becomes the aortic arch. The ascending aorta is contained within the pericardial sac, and is enclosed in a tube of serous pericardium, which it shares with the pulmonary artery. To the right of the ascending aorta lies the superior vena cava, anteriorly in the lower part lies the appendage of the right atrium (which also lies in front of the aortic root), and to the left lies the pulmonary trunk. The right main pulmonary artery travels behind the ascending aorta.

2.2.8 Aortic Arch

The aortic arch can be divided into 3 hypothetical areas: right, central and left. The right part consists of the short length between the pericardial fold and the origin of the brachiocephalic artery (the first of 3 major head and neck vessels which branch from the aortic arch). The central part, which is convex in shape, gives rise to the brachiocephalic artery, left common carotid artery, and left subclavian artery.

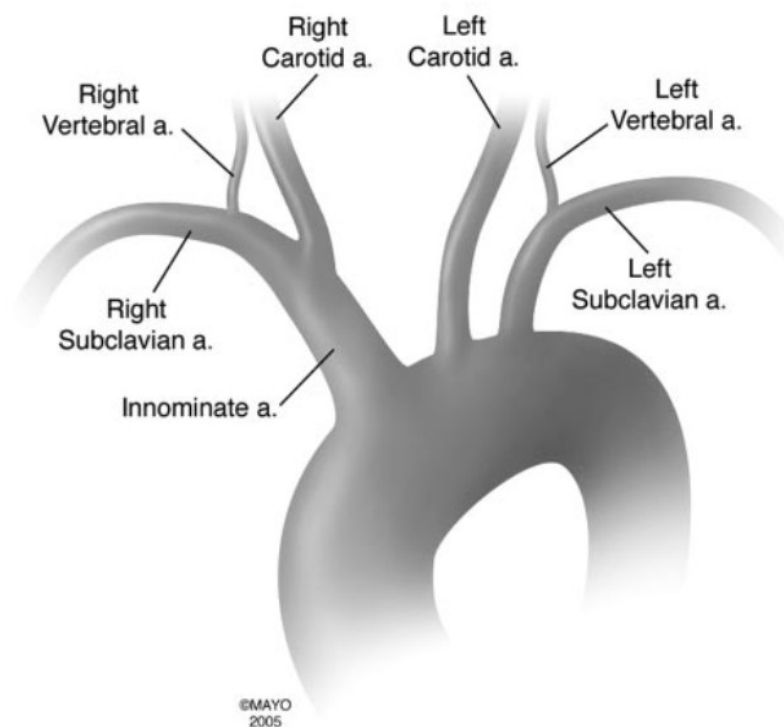


Figure 2.8. The most common aortic arch branching pattern. (Layton et al. 2006)

The aortic arch has been anatomically classified into different “zones” following the technical challenges of thoracic endovascular aortic repair (TEVAR). Zone 0 is the ascending aorta and reaches to just beyond the brachiocephalic artery; zone 1 covers the portion of the arch between

the brachiocephalic artery and (including) the left common carotid artery; zone 2 is between the left common carotid artery and (including) the left subclavian artery; zone 3 covers the proximal descending thoracic aorta distal to the left subclavian artery; and zone 4 covers the mid-descending thoracic aorta (Criado et al. 2005).

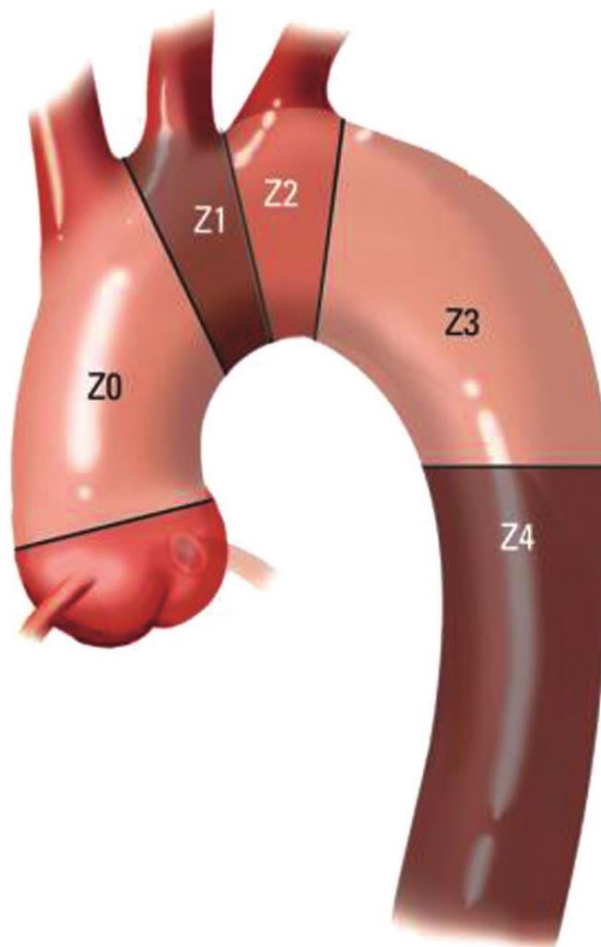


Figure 2.9. Map showing the different anatomical zones of the aortic arch. (Vallabhajosyula et al. 2012)

2.2.9 Descending Thoracic Aorta

The aortic arch continues as the descending thoracic aorta just below the aortic isthmus. This is the section of the distal arch that is positioned between the origin of the left subclavian artery and the attachment of the ligamentum arteriosum. During foetal development, this area is significantly narrowed. Just distal to attachment of the ductus arteriosus, the aorta has a fusiform dilatation, called the aortic spindle. The narrowing of the isthmus and the dilatation of the spindle even themselves out, but still persist to a minor degree in the adult. On average, the diameter of the spindle is 3mm larger than the isthmus in adults.

2.2.10 Embryology

The primary cardiac crescent is formed bilaterally within the embryonic disc, and its cells migrate into the cervical region of the embryo to form the primary heart tube. This single tube eventually divides into two tubes with subsequent twisting right-ward onto itself, called “d” looping. A second cardiogenic area is located posterior to the dorsal wall of the developing pericardial cavity, and its cells migrate into the cardiac region to populate the outflow tract and aortic arches (Anderson et al. 2003b).

The heart tube is organised as an inner layer of endocardium and an outer layer of myocardium. These layers are separate by an extracellular matrix called the cardiac jelly. Once the heart tube “d” loops, the jelly overlying the future atrioventricular canal and outflow tract develops into swellings called the cardiac cushions (Anderson et al. 2003a).

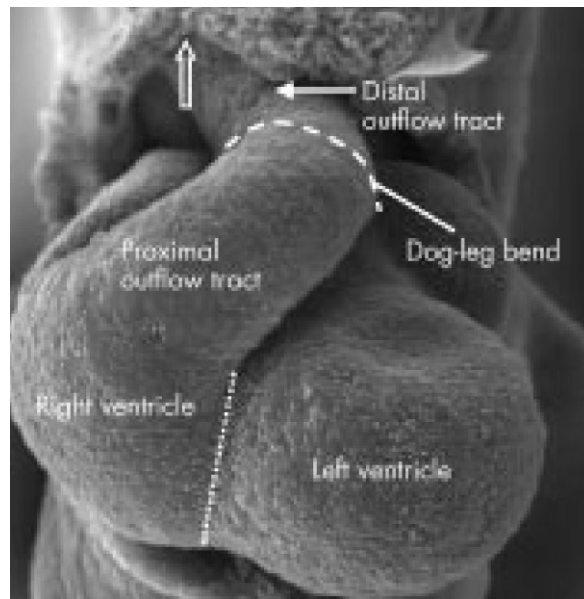


Figure 2.10. Electron micrograph of a mouse embryo showing the outflow tract with division between proximal and distal portions (dotted line). The distal portion extends to the margins of the pericardial cavity (arrow). (Anderson et al. 2003b)

The outflow tract divides into proximal and distal sections. The proximal section separates into future aortic and pulmonary components. Two additional intercalated cushions grow in the opposite quadrants of the common outflow tract. Cavitation occurs in the fused distal parts of the proximal cushions as well as the intercalated cushions to form the primordiums of the arterial valvular leaflets and sinuses (Tilea et al. 2013). These structures are formed upstream of the sinotubular junction. As these cushions cavitate, the central luminal part of each cushion forms the valvular leaflets, and the peripheral part arterialises to form the wall of the sinuses (Anderson et al. 2003b).

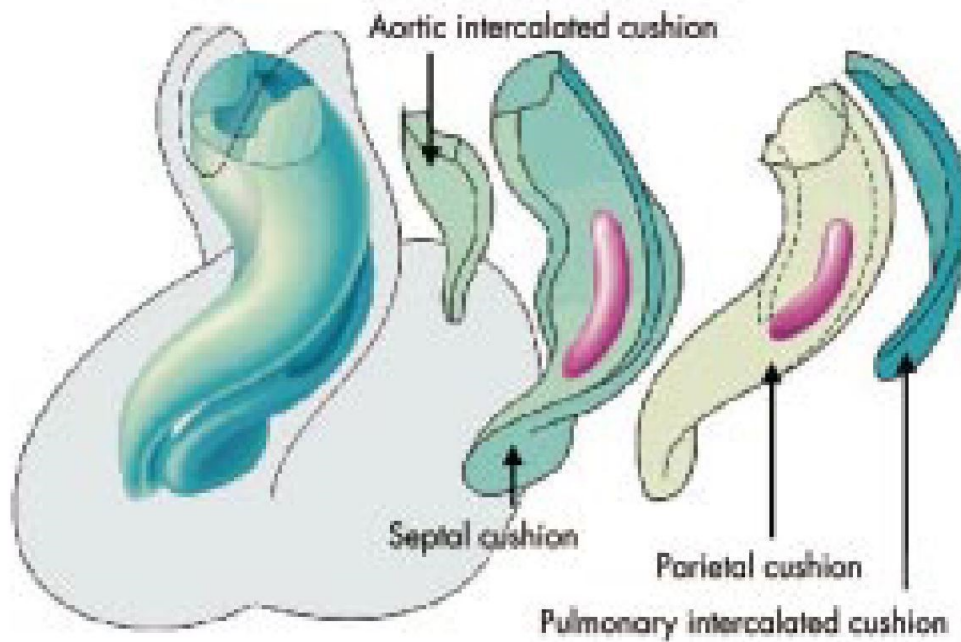


Figure 2.11. Embryo at Carnegie stage 15. To the left is shown the spiralling nature of the opposing endocardial cushions which extend throughout the length of the outflow tract. To the right are shown the individual cushions. The intercalated cushions are located anteriorly (within the future aortic primordium) and posteriorly (within the future pulmonary outflow tract). The purple zones mark the sites of condensed mesenchyme that have populated the cushions, migrating in from the neural crest. (Anderson et al. 2003b)

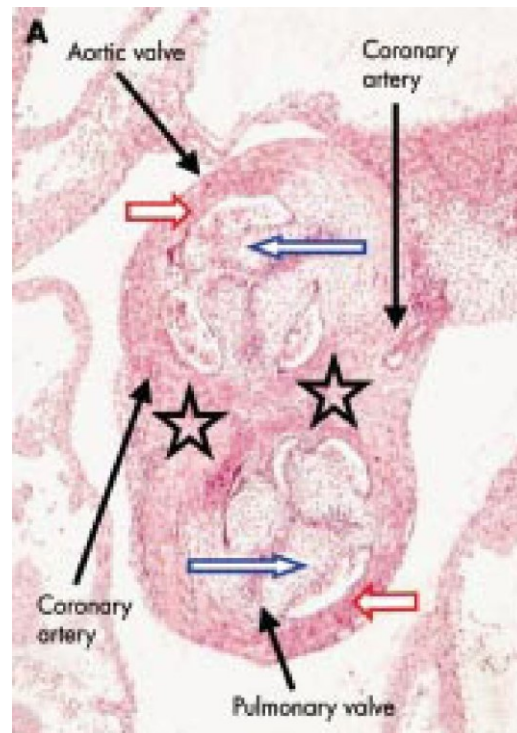


Figure 2.12. Embryo at Carnegie stage 22, cut transversely across the developing arterial valves. Cavities have now developed in the cushions occupying the distal part of the proximal outflow tract, forming two layers that give rise to the valvar leaflets luminally (blue arrows) and the walls of the supporting sinuses on the mural aspect (red arrows). The mural components are beginning to arterialise. The sinuses and their accompanying leaflets derived from the intercalated cushions, shown by the arrows, form one sinus each for the aorta and pulmonary trunk. The walls of both these sinuses have arterialised, the myocardial covering having disappeared. The myocardium still forms a cuff, however, around the sinuses and leaflets excavated from the fused proximal cushions (stars). Each of the two cushions will contribute one sinus and leaflet to the aorta, and a facing sinus and leaflet to the pulmonary trunk. (Anderson et al. 2003b)

2.3 BICUSPID AORTIC VALVE

The bicuspid aortic valve (BAV) is the most common congenital cardiac abnormality with an estimated prevalence of 1-2% (Ward 2000). It is 3 times more common in men than in women (Tutar et al. 2005). The high prevalence of this condition makes its correlation with aortic aneurysms (and their propensity for dissection and rupture) even more significant.

The exact pathogenesis of BAV is not yet fully understood, although there is strong indication of a genetic component both from its association with coarctation of the aorta (CoA), and through reports of the heritable nature of this condition. Reports indicate a link between BAV and CoA of between 20% and 85% (Presbitero et al. 1987, Stewart et al. 1993). There is a 10% chance of a first degree relative having a BAV in patients with the disease (Huntington et al. 1997). The strongest genetic link discovered is a mutation in the *NOTCH1* gene codes for a transmembrane receptor which has a role in determining cell outcome in organogenesis (Garg et al. 2005).

The BAV is composed of 2 leaflets, with one often being larger than the other. The commonest configuration is fusion of the left and right cusps, leading to a valve with 2 cusps with the commissures in the anteroposterior direction. The second most common is fusion of the right and non-coronary cusps, and the least common is fusion of the left and non-coronary cusps (Roberts 1970). A classification by Schaefer et al. has recognised these as type 1, 2 and 3 BAV (Schaefer et al. 2008).

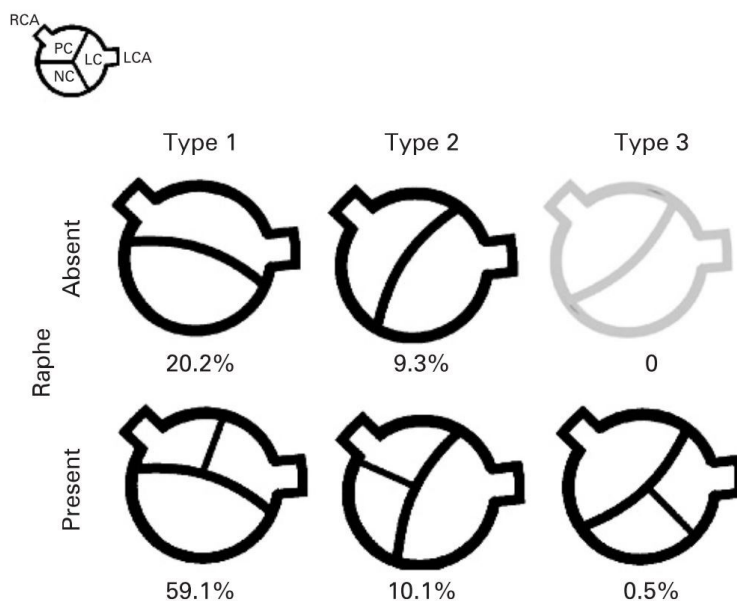


Figure 2.13. The classification and incidence of bicuspid aortic valves according to site of cusp fusion. (Schaefer et al. 2008)

2.3.1 BAV Related Aortopathy

BAV is often associated with aneurysm of the ascending aorta or aortic root (Nistri et al. 1999). This dilatation can lead to eventual dissection or rupture (Della Corte et al. 2007). Patients who have BAV tend to have larger aortas than those with tricuspid aortic valves (Morgan-Hughes et al. 2004). The prevalence of ascending aorta dilatation in patients with BAV ranges from 7.5% to 59% at the annulus, 16% to 78% at the sinus of Valsalva, 15% to 79% at the STJ, 35% to 68% in the ascending aorta (Hahn et al. 1992, Nistri et al. 1999). A study of prevalence by age quintile showed dilatation in 56% of those ages <30 years old, and up to 88% of those aged >80 years old (Della Corte et al. 2007).

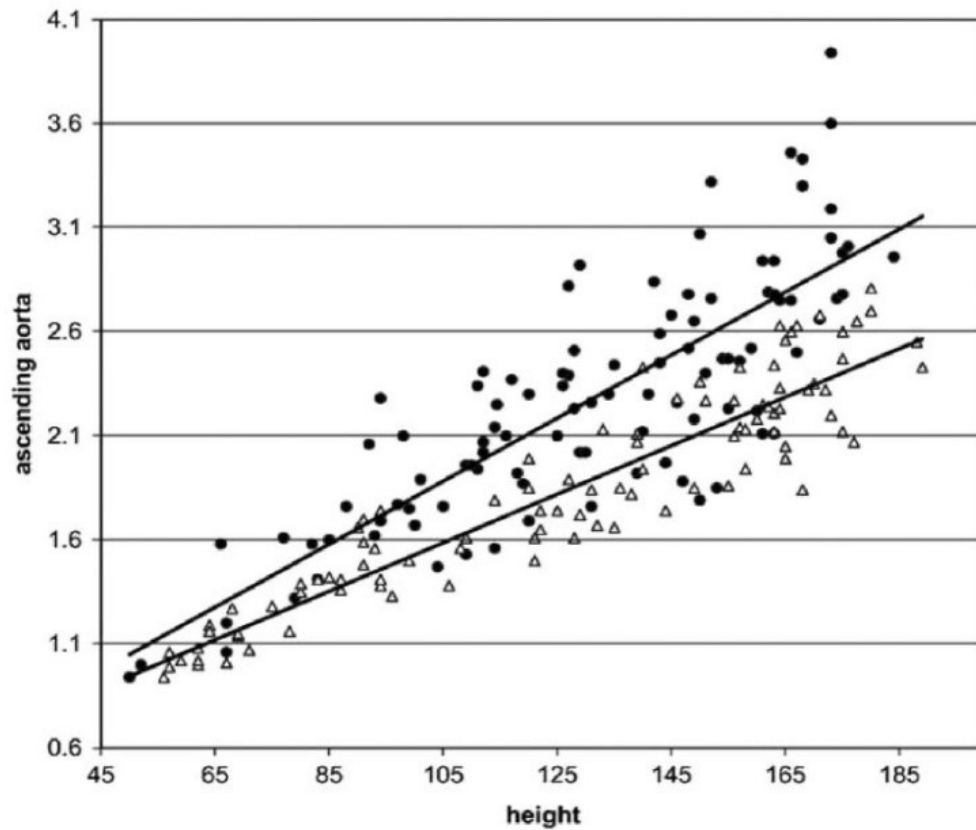


Figure 2.14. Ascending aortic diameter (cm) as a function of height (cm) among children with BAV (n=101) vs controls with TAV (n=97). The upper slope (circles) represents the BAV group ($y=0.0151x+0.2926$), and the lower slope (triangles) represents the TAV group ($y=0.0117x+0.362$). (Beroukhim et al. 2006)

Enlargement of the ascending aorta in BAV has a typical asymmetrical configuration at the convexity of the aorta (Bauer et al. 2006). In keeping with this phenotypic appearance, an asymmetric spatial pattern of extracellular matrix (ECM) protein expression has been shown in the convexity of the dilated BAV aorta as compared to the concavity (Cotrufo et al. 2009, Cotrufo et al. 2005, Della Corte et al. 2006, Della Corte et al. 2008). Furthermore, the non-dilated BAV aorta has shown similar patterns (Della Corte et al. 2008). BAV related aortic disease has histopathological similarities to Marfan Syndrome, namely medial degeneration,

increased matrix metalloproteinase (MMP) activity, and decreased fibrillin-1 in the aortic wall (Nataatmadja et al. 2003).

2.3.1.1 Medial Degeneration

The relationship between BAV and degeneration of the aortic media was documented as early as 1972 (McKusick 1972). Cystic medial necrosis is present in the aortas of BAV patients, and is the underlying histological abnormality in ascending aorta dilatation and dissection (Isselbacher 2005). It is characterised by vascular smooth muscle cell (VSMC) loss in the absence of inflammation, elastic fibre fragmentation, and an increase in basophilic ground substance within the ascending aorta (de Sa et al. 1999). It is in the convexity (greater curvature) of the ascending aorta where higher rates of VSMC apoptosis and medial degeneration are seen (Cotrufo et al. 2005, Nataatmadja et al. 2003).

2.3.1.2 Fibrillin

VSMC produce extracellular matrix (ECM) proteins such as collagen, elastin and fibrillin, thus playing an important role in remodelling of the aortic media. There is defective protein transport of fibrillin, fibronectin and tenascin from VSMC to the ECM, leading to reduce fibrillin deposition in the ECM (Nataatmadja et al. 2003). Fibrillin-1 is a very important component of the ECM, and forms microfibrils with elastin. It plays a crucial role in elasticity of the aortic wall, and its deficiency leads to a fragile aorta at risk of dilatation and dissection (Dingemans et al. 2000). Mutations of the FBN1 gene, which encodes fibrillin-1, are associated with the development of Marfan Syndrome. The histological changes seen in BAV aortas

appear to lie in the middle of a continuum between TAV aneurysms and Marfan Syndrome aneurysms.

2.3.1.3 Matrix Metalloproteinases

Matrix metalloproteinases (MMPs) are endopeptidases which break down ECM, and their increased activity has been related to aneurysm formation. MMP-2 has been shown to be increased in aneurysmal aortas of BAV patients (LeMaire et al. 2005). Increased turbulence has been demonstrated to lead to MMP-2 activation (Gambillara et al. 2005). Tissue inhibitors of MMPs (TIMPs) regulate their activity in the aortic media. An increase in the MMP:TIMP ratio plays a role in aneurysm formation. This increase in the ratio has been shown in BAV aortas (Ikonomidis et al. 2012).

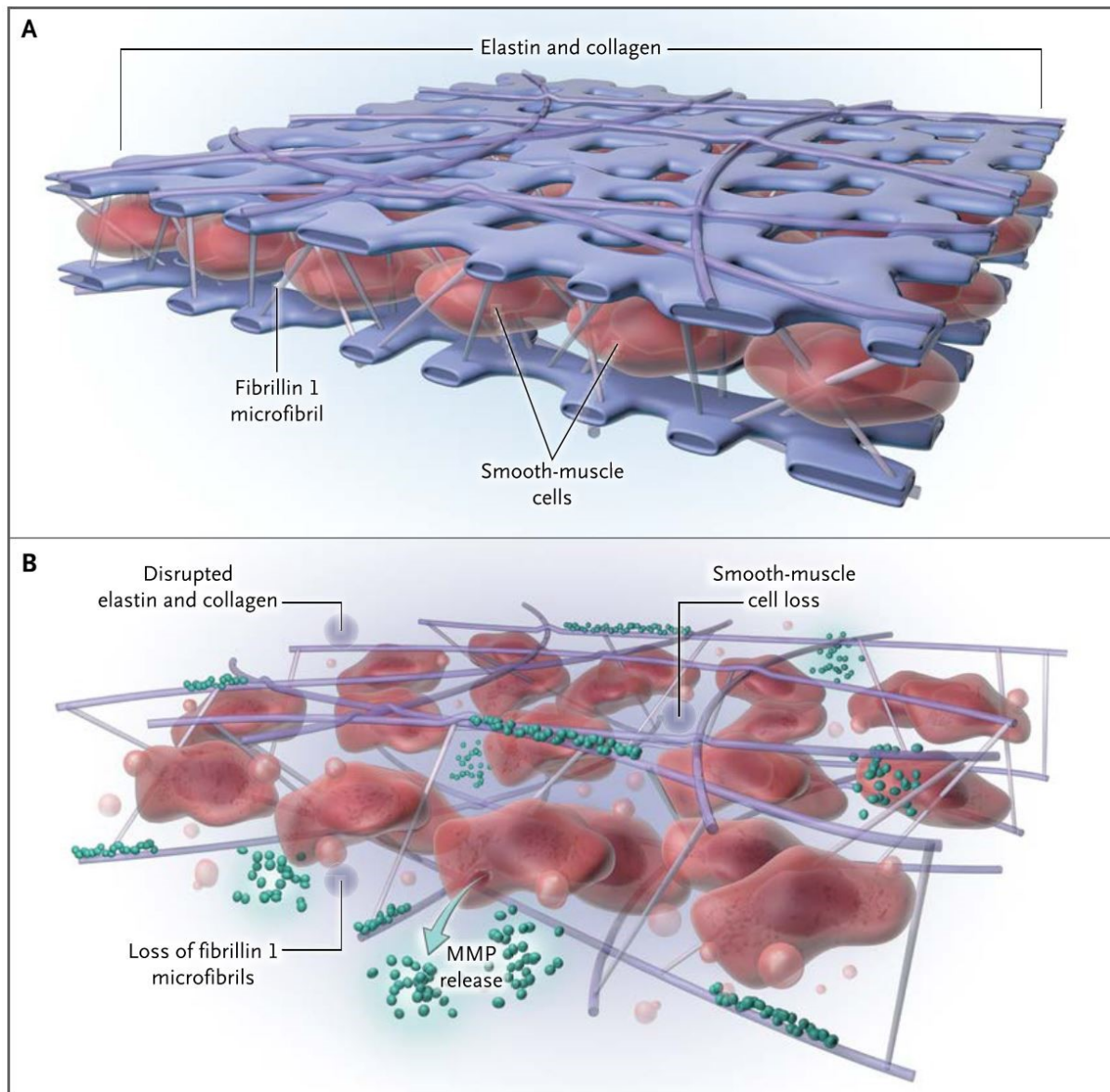


Figure 2.15. Histopathological features of bicuspid aortopathy. At the histologic level, the smooth-muscle cells in the aorta in persons with tricuspid valves are secured to the adjacent elastin and collagen matrix by fibrillin 1 microfibrils (Panel A). The aorta in persons with bicuspid valves may be deficient in fibrillin 1. This deficiency culminates in a disrupted architecture whereby smooth-muscle cells detach, accompanied by a surge in local levels of matrix metalloproteinases (MMPs), leading to loss of integrity in the extracellular matrix and the accumulation of apoptotic cells. These events may lead to an aorta with weakened structural integrity and reduced elasticity (Panel B). (Verma et al. 2014)

Despite all of the knowledge on the histopathological basis of BAV aortopathy, there is still controversy regarding the cause of dilatation of the aorta in BAV patients. Two main theories exist: (1) genetic theory, where aortic wall weakness is a result of the common genetic developmental defect affecting both the aortic valve and the aortic wall; (2) haemodynamic theory, where turbulent flow and eccentric jets caused by BAV leads to abnormal haemodynamic stress on the aortic wall and subsequently to aortopathy. The haemodynamic theory has gained strong support with recent advances in functional imaging.

2.4 CLINICAL NEED FOR FUNCTIONAL ASSESSMENT

For many years, size has been the principle decision-making criteria for intervention on the thoracic aorta (Erbel et al. 2014, Svensson et al. 2013). Guidelines for the treatment of aortic disease concentrate on maximal aortic diameter and risk factors for dissection. Surgical replacement of the aorta is recommended when the aortic size reaches 55mm, with earlier intervention recommended in the presence of connective tissue disorders (45mm) or bicuspid aortic valve (50mm) when risk factors are present (Erbel et al. 2014, Hiratzka et al. 2016). These risk factors include family history of acute aortic syndrome (aortic dissection, rupture, or intramural haematoma), rapidly increasing aortic size, and coarctation.

Yet despite these guidelines, there still remains a significant incidence of acute aortic events in patients whose aortas are smaller than these intervention thresholds. Elefteriades et al. found that in patients with aortic size below 50mm, there still remains an incremental yearly risk of rupture, dissection or death above 5% (Elefteriades et al. 2010). These results were supported by data from the International Registry for Acute Aortic Dissections (IRAD), which showed that the highest incidence of acute aortic dissections occur at aortic size 50-54mm, which falls below the standard size criteria of 55mm for surgical intervention (Pape et al. 2007).

Furthermore, they showed that more aortic dissections occur when the aorta is sized 40-49mm, as compared to 55-64mm.

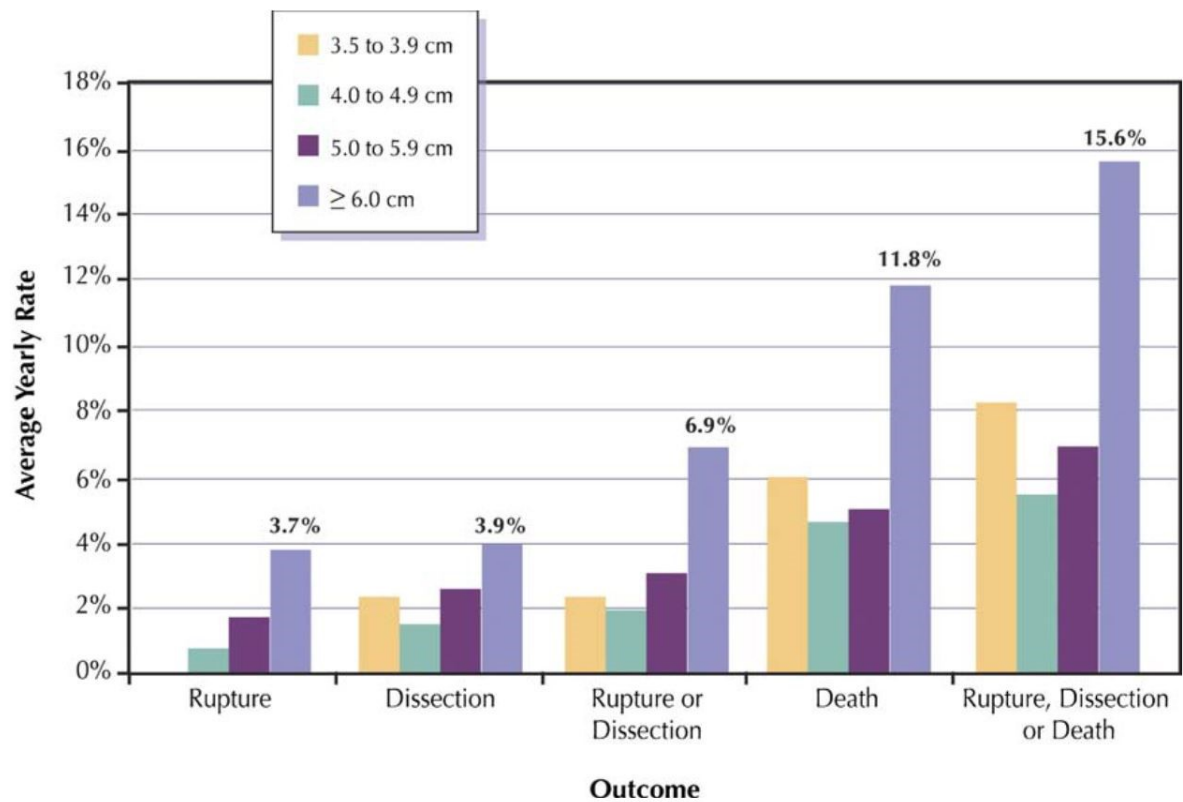


Figure 2.16. Yearly rates of rupture, dissection or death according to aortic size. (Elefteriades et al. 2010)

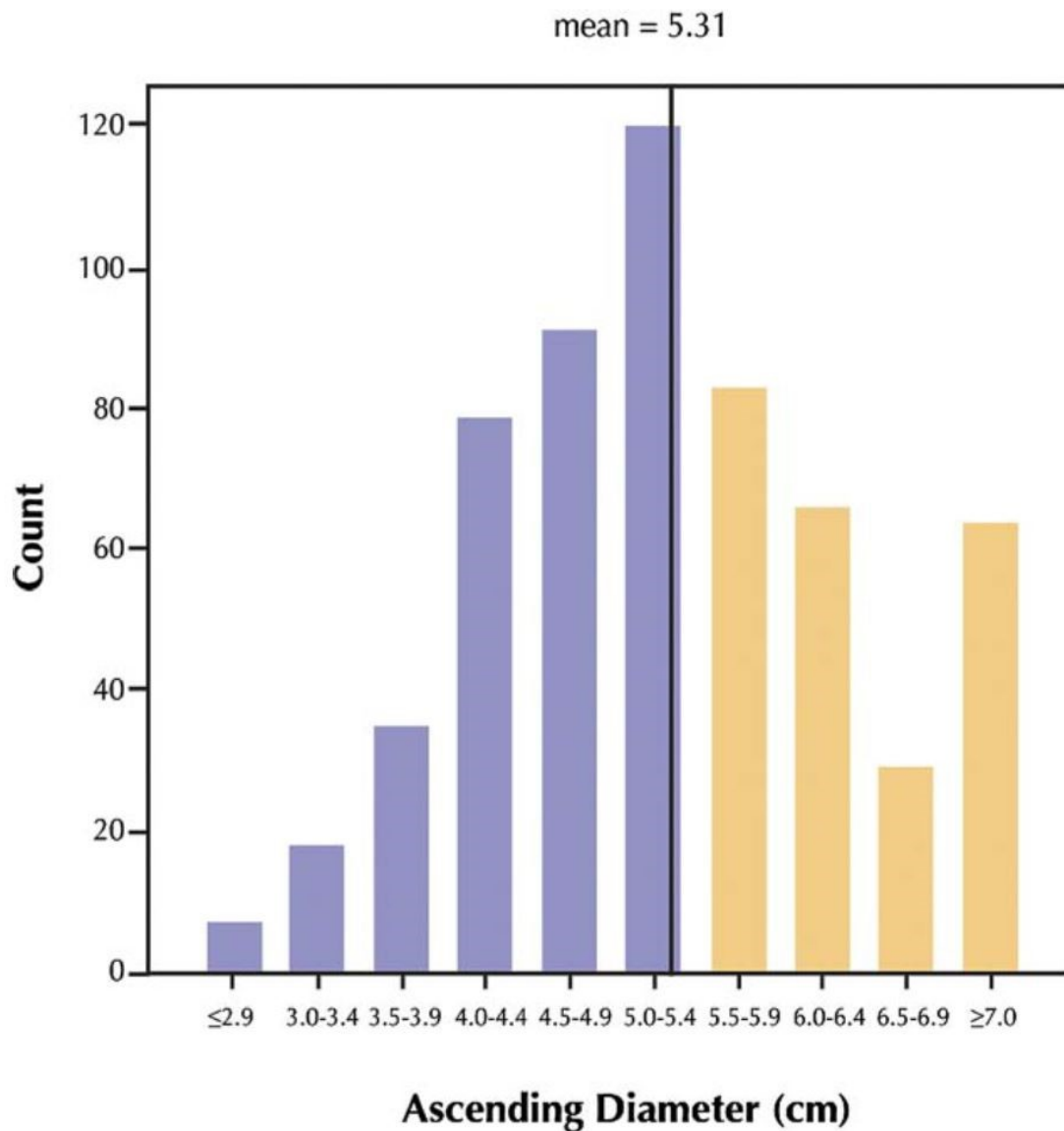


Figure 2.17. Distribution of aortic size at the time of presentation with acute type A aortic dissection. (Pape et al. 2007)

These datasets indicate that current intervention guidelines for management of the thoracic aorta may not be fully adequate in preventing acute complications. They suggest further information about the patient's individual aorta beyond size may be necessary to better predict

future aortic dilatation and aortic events, as well as plan timing of intervention. As yet, there is no functional assessment of the thoracic aorta.

Currently, a number of challenges face the cardiac surgeon and cardiologist in assessing and managing patients with thoracic aortic aneurysms. One challenge is deciphering which patients with aortic dilatation are likely to further dilate, rupture or dissect imminently. Two very different patients may both present with an aortic size of 50mm, with similar blood pressures. The Law of Laplace states that wall tension, a function of the pressure and the radius, will be the same in both patients' aortas (Laplace 1805). Yet one may have a stable aortic wall with low chance of dissection, and the other may have an area of aortic wall which is very thin with impending rupture or dissection. At this time, there is no formalised method of distinguishing between these two aortas (see [Figure 2.19](#)). Another grey area for decision-making is whether to replace a moderately dilated ascending aorta when surgically intervening on the aortic valve, to prevent future surgery if the aorta dilates above size criteria for surgery. Bicuspid aortic valves are associated with aortic aneurysms, however we have shown no significant dilatation of the remaining ascending aorta or arch after bicuspid aortic valve/root replacement at 5 year follow-up (Abdulkareem et al. 2013). The difficulties in decision-making and management of these patients would be made easier if more information is available about each individual's aortic haemodynamics and its effects on aortic pathology.

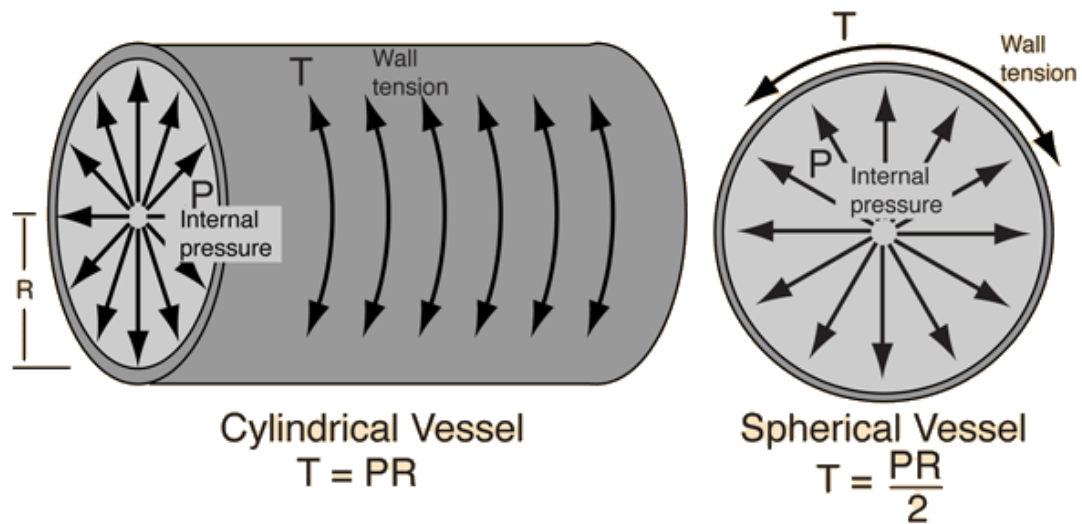
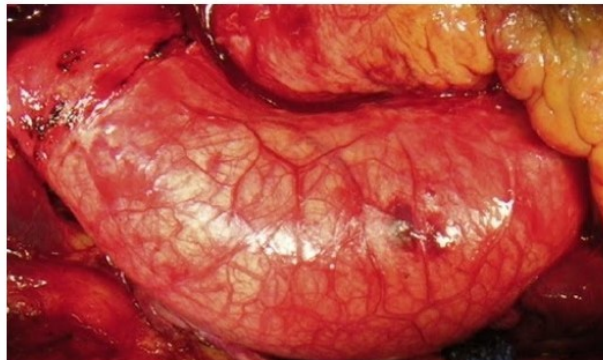


Figure 2.18. The relationship between wall tension (T), pressure (P) and radius (R) for a cylindrical and spherical vessel according to the Law of Laplace.

Patient A
5.0cm ascending aorta



Patient B
5.0cm ascending aorta



Figure 2.19. Two patients with identical diameters of ascending aorta, however patient A shows a very homogeneous and stable appearance, whereas patient B shows a very thinned out area in the convexity which is at high risk of rupture or dissection (yellow arrow).

2.5 MODALITIES OF HAEMODYNAMIC ASSESSMENT

To functionally assess the thoracic aorta, detailed haemodynamic measurements are required to investigate a variety of flow characteristics and biomechanical forces. However, measurement of in-vivo haemodynamics can be difficult and invasive (Xiong et al. 2011). Detailed anatomical imaging with assessment of flow and velocities enables calculation of physiological parameters without the need for invasive monitoring.

2.5.1 Computational Fluid Dynamics

Computational fluid dynamics (CFD) is an ever increasing approach to quantify haemodynamics in high spatial and temporal resolution (Cebal et al. 2002, Milner et al. 1998). Computational simulations of blood flow can be used in the study of aortic wall biomechanics, as well as blood flow characteristics which may be involved in aortic disease processes. CFD has been applied in assessment of aneurysms and rupture risk (Fillinger et al. 2003, Fillinger et al. 2002, Les et al. 2010), the design and assessment of vascular devices (Li et al. 2005, Stuhne et al. 2004), and the planning and outcome prediction of vascular surgeries (Migliavacca et al. 2006, Soerensen et al. 2007, Taylor et al. 1999).

2.5.1.1 Imaging and Modelling

In order to perform CFD simulations, detailed anatomical imaging is required to create accurate 3-dimensional geometric models of the thoracic aorta. Imaging modalities such as Cardiovascular Magnetic Resonance Imaging (CMR) or multi-slice computed tomography (CT) may be used to acquire the anatomical data. In the case of CMR, aortic anatomy can be visualised either using angiography (MR Angiography) where intravenous contrast is injected,

or through high-resolution cardiac and respiratory gated 3D steady-state in free precession (SSFP). In the case of MR Angiography, the contrast load is usually less nephrotoxic than that used in CT Angiography. CT Angiography may also be carried out with ECG-gating in order to reduce motion artefact.

Geometric models of the aorta are reconstructed by segmenting the imaging data. The vessel segmentation procedure is carried out by identifying the vessel boundary through thresholding, where differences in pixel intensity are used to automatically detect vessel boundaries, or by manual interaction. An automated lofting process then interpolates all segmented boundaries thus creating the 3-dimensional model of the aorta and its branches. The geometric model is then used to create a detailed mesh of the aorta. It is at the grid-points throughout this mesh where haemodynamic variables such as velocity, stress and pressure are calculated. Therefore the mesh may be made to be finer near the vessel wall, in order to provide more data points in regions of interest (Torii et al. 2011).

2.5.1.2 Boundary Conditions

The geometric mesh of the aorta provides the framework of data points (or nodes) at which haemodynamic calculations can be made. In order for blood flow CFD simulations to be carried out, conditions have to be imposed at the inlet of the aorta (i.e. the aortic root) as well as the outlet of each branch of the aorta (for e.g. the head and neck vessels and descending thoracic aorta). A key aspect in the endeavour of accurate CFD simulations is the specification of physiologically accurate boundary conditions (Lee et al. 2004, Lee et al. 2007, Milner et al. 1998, Moyle et al. 2006, Steinman 2002, Steinman et al. 2002, Vignon-Clementel et al. 2010, Wake et al. 2009).

CFD models can be constructed using relatively few measurements of blood velocity and flow, that is if significant haemodynamic assumptions are allowed. However, conformity of the modelled fluid dynamics with the patient's actual physiology depends greatly on how patient-specific these measurements are. Up until recently, many studies used idealised velocity profiles for the inflow boundary conditions. Such studies have modelled inflow boundary conditions using simple profiles (such as a parabolic or Womersley) (Campbell et al. 2012). This has been shown to have a significant effect on haemodynamic calculations further along the aorta (Nakamura et al. 2006). However, the aortic valve is a complex trileaflet structure, and in union with the sinuses of Valsalva and coronary arteries which make up the aortic root, leads to intricate flow patterns entering the ascending aorta (Sigovan et al. 2015). These flow patterns are much more complex than the simple idealised profiles. Furthermore, an array of pathologies may affect the aortic valve, including stenosis, regurgitation, and importantly the congenital malformation causing the valve to be bicuspid (Waller et al. 1994a, Waller et al. 1994b). Therefore, there is a need to apply accurate patient-specific inflow boundary conditions to CFD simulations of the thoracic aorta in order to achieve meaningful haemodynamic measurements.

CMR allows flow measurement using phase-contrast (PC-MRI) techniques by means of gradient echo sequences. This measures blood flow and velocity at a given plane along the aorta. If measured at or above the aortic valve, these flow measurements can be used to assign an inlet velocity profile into the aortic model, thereby forming the inlet boundary condition for CFD simulations.

The anatomical mesh and boundary conditions are then fed into a computational solver where blood flow simulations are carried out to solve a set of equations (e.g. Navier-Stokes equations for blood flow) enforcing conservation of mass (continuity). This calculates the relevant

haemodynamic variables throughout the aorta which can then be post-processed to analyse for different flow characteristics and biomechanical forces.

2.5.2 4D Flow MRI

In flow MRI, phase-contrast methods are used to encode blood flow velocities along all dimensions. This permits acquisition of spatially registered flow data along with morphological data (Markl et al. 2016). 4D flow MRI is the acquisition of 3D cine PC-MRI acquired in a time-resolved ECG-gated manner with three-directional velocity encoding. It allows post-hoc time-resolved 3D visualisation along with quantification of flow at any location within a volume (Markl et al. 2012). In addition to the acquisition of basic flow volumes and velocities, other haemodynamic measurements can also be calculated, as discussed later. Some of these haemodynamic measurements relating to flow and velocity are the same as those calculated using CFD.

2.5.3 Comparison of CFD and 4D Flow MRI

One of the challenges of 4D flow MRI is that the acquisition of velocity data in three dimensions can be time-consuming, meaning the patient has to undergo a longer scan time. Spatial resolution can be lower than CFD, and provides an ensemble-averaged haemodynamic assessment over several cardiac cycles. On the other hand, CFD has no limit in temporal and spatial resolution. Furthermore, it also provides spatially-varying description of pressure indices (not just velocity). In the most sophisticated settings, CFD can also account for wall motion via fluid-structure interaction formulations. (Xiong et al. 2011) The imaging time required to obtain aortic anatomical data for the geometric mesh, as well as the flow data (PC-

MRI) above the aortic valve for the inflow boundary conditions, is much shorter in duration compared to 4D flow MRI. Therefore, patients have to spend much less time in the MRI scanner. However, the subsequent blood flow simulations are computationally expensive and are of varying duration.

Whereas 4D flow MRI is limited to only acquiring live data from patients, CFD has the capacity to simulate proposed changes in anatomy and physiological parameters which may be the result of medical, surgical or pharmacological interventions, in order to see the effect that these may have on haemodynamics and biomechanics. (Figuroa et al. 2009, LaDisa et al. 2011, Prasad et al. 2013) This allows simulating interventions and procedures to see their effects, without putting patients at the risks of the intervention.

Nevertheless, CFD and 4D flow MRI can be used together to further improve understanding of hemodynamics in aortic disease. They are different experimental techniques, with different strengths and weaknesses.

2.6 HAEMODYNAMIC PARAMETERS & CLINICAL IMPLICATIONS

Disease processes such as aneurysm formation and atherosclerosis are largely dependent on haemodynamic factors in the vascular system (Friedman et al. 1981, Humphrey et al. 2008, Yeung et al. 2006, Zarins et al. 1983). Flow characteristics play an important role in this disease process, with effects on endothelial homeostasis (Chien et al. 1998, Davies 1995) and response of smooth muscle cells and fibroblasts (Chien et al. 1998, Gibbons et al. 1994, Humphrey 2008, Langille 1996).

2.6.1 Wall Shear Stress

Wall shear stress (WSS) refers to the force per unit area exerted by a moving fluid in the direction of that vessel (Efstathopoulos et al. 2008). According to the Newtonian incompressible fluid approximation, WSS depends on the dynamic viscosity μ of the fluid, and the velocity gradient near the vessel wall, namely the wall shear rate (WSR):

$$\text{WSS} = \mu \text{WSR} = \mu \frac{du}{dr}$$

where WSS is measured in pressure units (dyn/cm^2), μ is the dynamic viscosity of blood, measured in Poise, du/dr is the velocity gradient of the blood which is called Shear Rate (SR), measured in s^{-1} . When considering the vessel wall, this gradient is the WSR. WSR is a measure of the rate of velocity increase when moving away from the vessel wall (where according to the no slip condition the velocity is zero).

In a complex 3D geometry such as the aorta, wall shear stress $\overline{\text{WSS}}$ can be obtained as follows:

$$\overline{\text{WSS}} = \mu(\nabla\vec{u} + \nabla\vec{u}^T)\vec{n}$$

where μ is the blood viscosity, $\nabla\vec{u}$ is the gradient of the velocity field, $\nabla\vec{u}^T$ is the transpose of the gradient of the velocity field, and \vec{n} is the unit normal vector to the vessel wall.

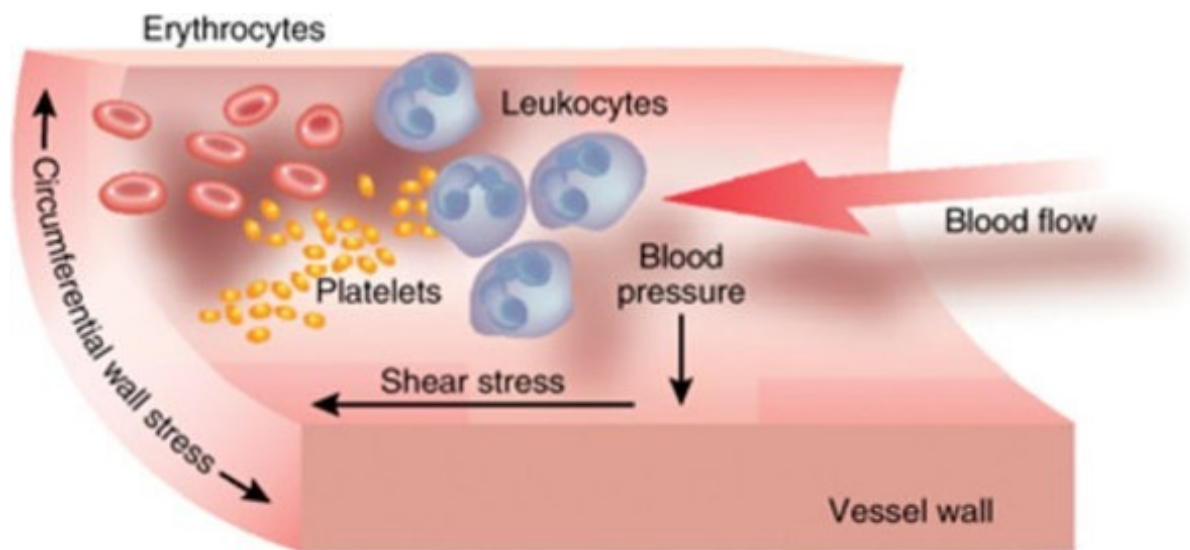


Figure 2.20. Flow through a vessel showing wall shear stress is parallel to the vessel wall, whereas blood pressure and tensile stress are perpendicular to the vessel wall. (Li et al. 2008)

WSS was first associated with vasculopathy in the context of plaque formation. Gnasso et al. observed that WSS was lower in those carotid arteries which had higher levels of plaque formation (Gnasso et al. 1997). Furthermore, a correlation was found between low WSS and an increase in the intima-media thickness of carotid arteries (Gnasso et al. 1996). Malek et al. described how $WSS < 4 \text{ dyn/cm}^2$ stimulates an atherogenic phenotype, whereas a level $> 15 \text{ dyn/cm}^2$ induces endothelial quiescence and an atheroprotective gene expression profile (Malek et al. 1999).

Subsequently, focus has turned to the link between high WSS and aneurysm formation. This was first reported in the cerebral circulation. Cebal et al. assessed rupture sites of cerebral aneurysms and found that they correlated with areas of high WSS (Cebal et al. 2015).

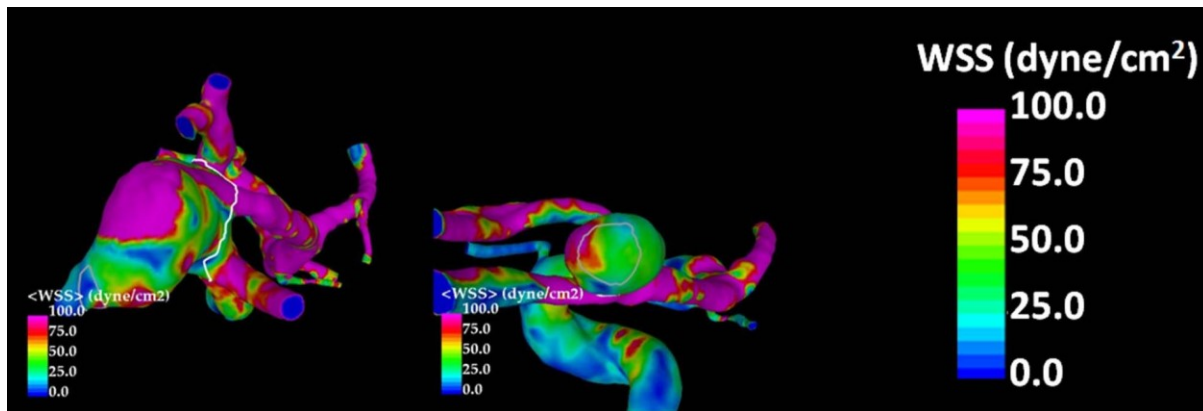


Figure 2.21. Wall shear stress measurements in cerebral artery aneurysms. (Cebal et al. 2015)

In turn, WSS in the thoracic aorta has been the recent subject of intense research, particularly in the context of aortic valve-related aortopathy. Nathan et al. used ECG-gated CT images of patients with BAV and TAV to create 3D meshes of the thoracic aorta (Nathan et al. 2011). They then applied a uniform pressure load of 120mmHg as the inflow to the aorta, and used CFD to calculate WSS. They showed an increase in WSS in the ascending aorta of BAV patients. The significant limitation of this study was that their inflow was non-pulsatile and non-patient-specific, let alone valve-specific. They did not input any real-life flow parameters into their CFD model.

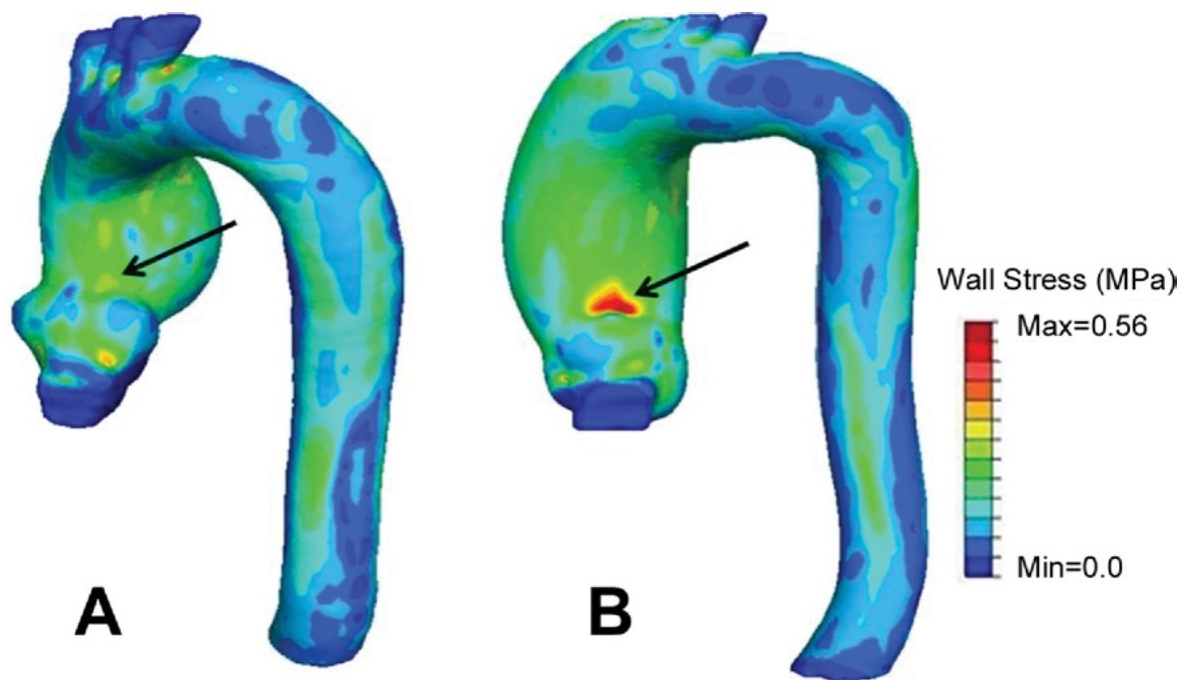


Figure 2.22. Wall shear stress measurements in the thoracic aorta from CFD studies. Wall stress in the ascending aorta of (A) a patient with a tricuspid aortic valve, and aortic root, sinotubular, and maximum ascending aortic diameter of 4.0, 3.4, and 5.4 cm, respectively, and (B) a patient with a bicuspid aortic valve, and aortic root, sinotubular junction, and maximum ascending aortic diameter of 3.8, 3.5, and 5.1 cm, respectively. (Nathan et al. 2011)

Barker et al. found that WSS in the ascending aorta of patients with BAV was significantly elevated compared to healthy volunteers (Barker et al. 2012). BAV with fusion of the right and non-coronary cusps was shown to have higher WSS and larger ascending aorta size (Bissell et al. 2013). The ascending aorta is the commonest site of aneurysm formation in BAV. Mahadevia et al. further sub-analysed regional WSS distribution in circumferential sub-sectors of the ascending aorta of patients with BAV compared to tricuspid aortic valve (TAV) (Mahadevia et al. 2014). They found elevated WSS in the right-anterior wall of the ascending aorta for right-left fusion BAV, and right-posterior wall for right-non fusion BAV. These regions correspond to the greater curvature of the ascending aorta, the typical site of dilatation

in BAV-related aortopathy. It must be noted that these are all 4D flow MRI studies, and one of the major limitations of 4D flow MRI is that spatial resolution can be lower than CFD, and provides an ensemble-averaged haemodynamic assessment over several cardiac cycles.

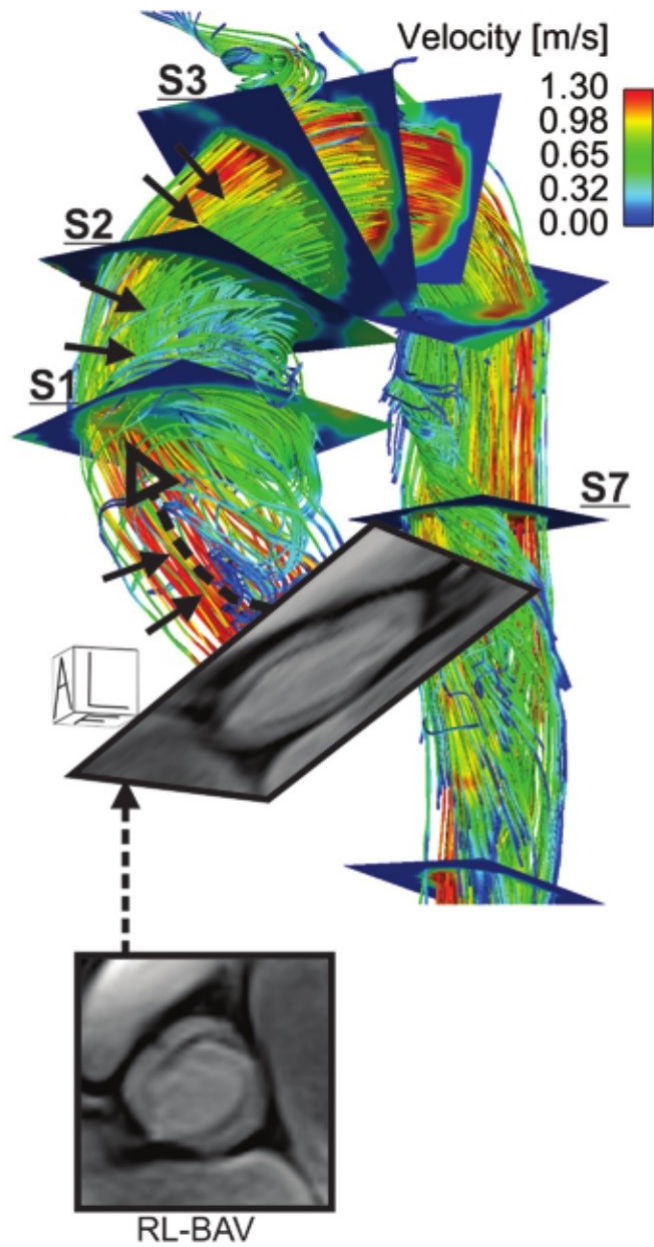


Figure 2.23. Velocity jets from a right-left fusion BAV patient directed towards the right-anterior aortic wall, as indicated by the open black arrows. The position of the velocity jets correspond to the position of elevated WSS (closed black arrows). (Barker et al. 2012)

The trend that WSS is elevated in the greater curvature of BAV aortas correlates well with the findings of Della Corte et al. who found that medial degeneration was more severe in this region (Della Corte et al. 2006). Type I and III collagen were reduced, and smooth muscle cell apoptosis was seen to be increased in the greater curvature even before significant dilatation had occurred (Della Corte et al. 2008). An important recent study by Guzzardi et al. has shown a direct link between WSS and changes in the wall of the ascending aorta (Guzzardi et al. 2015). BAV patients undergoing ascending aorta replacement had pre-operative WSS mapping. At the time of surgery, paired aortic wall samples were taken from regions of elevated WSS and normal WSS. They found increased transforming growth factor β -1, matrix metalloproteinase (MMP)-1, MMP-2 and MMP-3 in regions of high WSS, indicating extracellular matrix dysregulation. Furthermore, there was higher medial elastin degradation in regions of high WSS. To support this finding, High WSS has also been associated with internal elastic lamina loss in basilar arteries (Metaxa et al. 2010).

High WSS may thus promote a series of responses which produce thinning of the aortic wall, and in doing so contribute to aneurysm formation. This may help to explain why some patients with aortic size below current intervention criteria develop acute aortic complications.

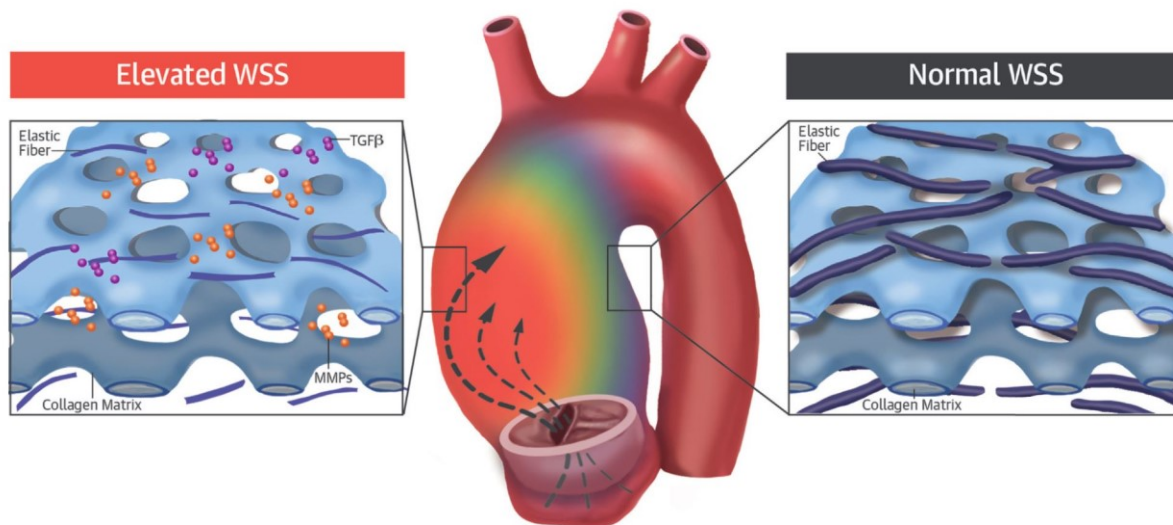


Figure 2.24. Elevated aortic WSS generated by aberrant flow from cusp fusion corresponded to more severe extracellular matrix (ECM) dysregulation than adjacent regions of normal WSS in the same patient's aorta. Characteristic medial degeneration was observed throughout the aorta, but elastic fiber degeneration was more severe in regions of elevated WSS (less elastin, thinner fibers, and greater distances between laminae), where higher concentrations of mediators of ECM dysregulation (matrix metalloproteinase [MMP] and transforming growth factor b [TGFb]) are also observed. (Guzzardi et al. 2015)

WSS also increases the actions of many kinases which phosphorylate signalling proteins such as adhesion site proteins and mitogen-activated protein kinase pathways in endothelial cells. Downstream of these signalling cascades, transcription factors such as AP-1, NK-kappa B, Sp-1 and Egr-1 are activated resulting in induction of genes encoding for vasoactivators, adhesion molecules, monocyte chemoattractants and growth factors. Thus vascular structure and function can be modulated (Chien et al. 1998, Davies 1995).

2.6.2 Flow Patterns

Flow patterns in the thoracic aorta differ significantly depending on aortic valve morphology. Flow profiles exiting the aortic root for healthy TAV show broad centrally distributed jets, whereas in BAV there is asymmetry with higher velocity jets at the periphery near the aortic wall. The flow angle of blood exiting the aortic valve is elevated in BAV, and flow displacement (a measure of flow eccentricity) is consistent with differences in regionally increased ascending aorta WSS (Mahadevia et al. 2014).

Velocity streamlines help to visualise the direction of flow at any given time in the cardiac cycle. Streamlines are tangent to the velocity vector, and show the direction in which a fluid element will travel at any point in time. Healthy TAV produce laminar flow patterns with parallel streamlines indicating flow in line with the aortic wall. In contrast, velocity streamlines in BAV show eccentric jets with disrupted patterns, loss of laminar flow, and impingement of flow at the greater curvature (Mahadevia et al. 2014).

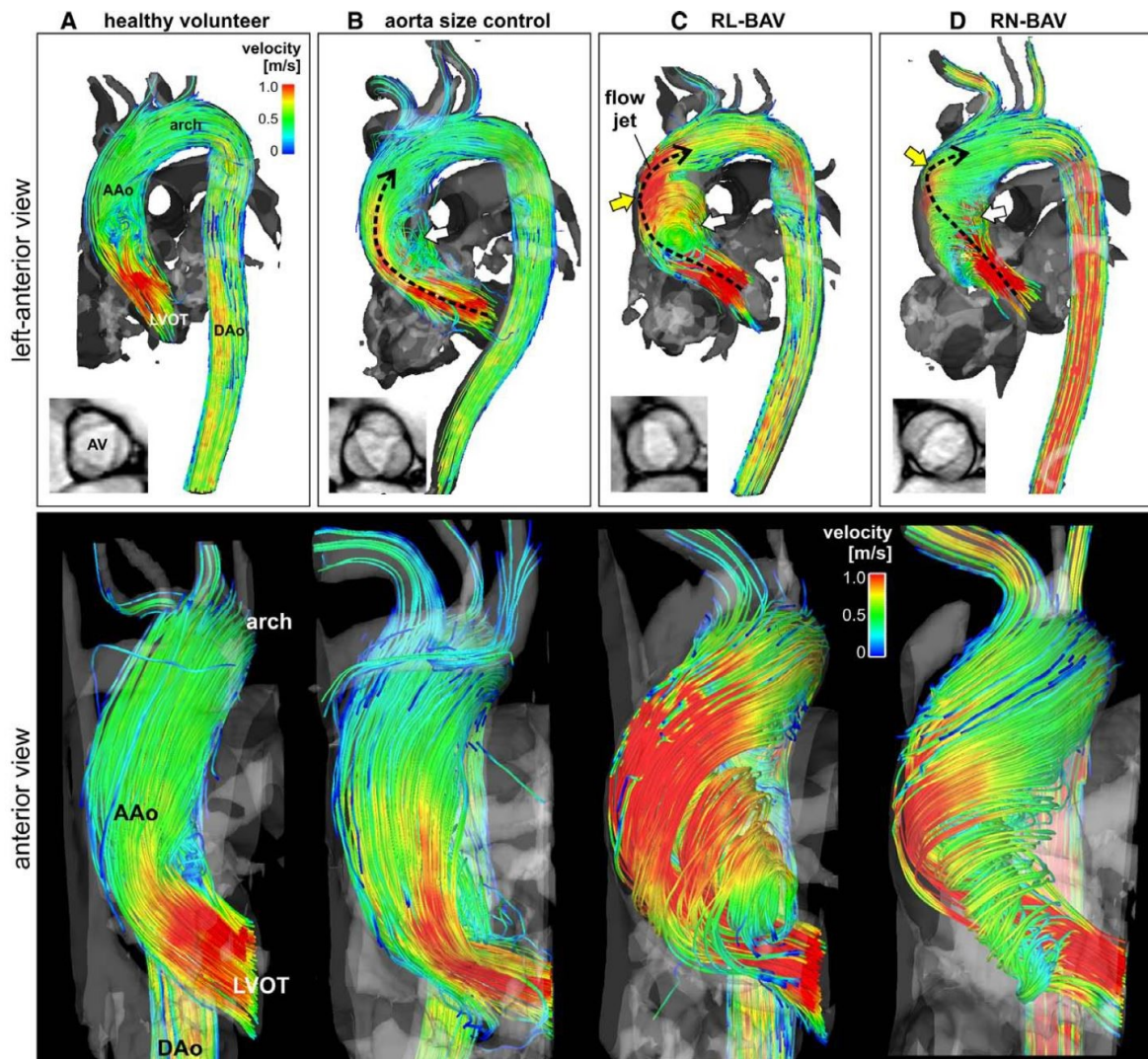


Figure 2.25. Top, 3D streamline visualization of peak systolic blood flow in patients with BAV (C and D) in comparison with an aorta size–matched control subject (B) and a healthy volunteer (A). Note the presence of distinctly different 3D outflow flow jet patterns (black dashed arrows) in the ascending aorta (AAo) for patients B and C. Bottom, 3D flow patterns in the left ventricular outflow tract (LVOT) and AAO distal to the aortic valve. Note the different systolic aortic valve outflow flow jet patterns (red indicating high velocities > 1 m/s) and wall impingement zones that correspond to variable exertion of high wall shear forces between different valve groups (C and D) and aorta size–matched controls (B) and healthy volunteers (A). BAV indicates bicuspid aortic valve; RL, right and left coronary leaflet; and RN, right and noncoronary leaflet. (Mahadevia et al. 2014)

2.6.3 Helical Flow

It is increasingly recognised that flow in the thoracic aorta contains significant radial (non-axial) components associated with helical flow (Markl et al. 2004). This is due to a combination of factors including ventricular twist and torsion during systole (Baciewicz et al. 1991, Farthing et al. 1979), the fluid mechanics of the aortic valve and aortic root (Bellhouse et al. 1969), and the curved morphology of the ascending, arch and descending aorta (Chandran 1993, Chandran et al. 1979, Yearwood et al. 1980, Yearwood et al. 1982). From a physiological viewpoint, helical flow may be beneficial and/or detrimental. It may comprise a degree of normal organ perfusion (Frazin et al. 1996). On the other hand, it has been shown to play an important role in plaque deposition, (Kilner et al. 1993) and vasculopathy (Frazin et al. 1990). Pritchard et al. demonstrated differences in monocyte adhesion to the vascular wall (important cells in the pathogenesis of atherosclerotic plaques) related to the radial component of velocity (Pritchard et al. 1995).

Bissell et al. compared helical flow patterns in BAV and TAV patients (Bissell et al. 2013). They found BAV was associated with abnormal right-handed helical flow, which correlated with higher rotational helical flow, higher WSS and larger ascending aortas. BAV with right-non cusp fusion and right-handed flow showed the most severe flow abnormalities. On the other hand, patients with BAV who had normal flow patterns elicited WSS and aortic dimensions comparable to healthy volunteers (Bissell et al. 2013).

2.6.4 Oscillatory Shear Index

In pulsatile flow, the temporal variation in WSS direction can be expressed in terms of the OSI:

$$\text{OSI} = \frac{1}{2} \left(1 - \frac{|\int_0^T WSS_z dt|}{\int_0^T |WSS_z| dt} \right)$$

where an OSI value of zero indicates unidirectional flow throughout the pulsatile cycle, and a value of 0.5 indicates that flow oscillates forward and backward for the same period of time during the cycle (i.e. disturbed flow). OSI essentially measures the degree of disturbed flow at the vessel wall, and has been shown to be associated with vasculopathy (Hardman et al. 2013).

The following chapters will describe the methodology involved, followed by results from 4 separate studies. Each study chapter will begin with its individual brief introduction.

3

METHODS

“The true method of knowledge is experiment.”

William Blake, 1757 - 1827

Contents

3.1	Overview	85
3.2	Imaging	89
3.3	Computational Fluid Dynamics	92
3.4	Inflow Boundary Conditions	99
3.5	Outflow Boundary Conditions	108
3.6	Quantification of Haemodynamic Indices	112

3.1 OVERVIEW

The methods chapter will discuss in detail the data acquisition and imaging, the segmentation approach for production of 3-dimensional models and meshes, and the inflow and outflow boundary conditions applied. Further attention will be given to the proposed novel method of obtaining patient-specific velocity profiles above the aortic valve from imaging data and mapping to geometric models of the patient's aorta, thus creating a patient-specific inflow boundary condition. The mapped velocity profiles, in conjunction with the patient's aortic model and outflow boundary conditions, enable a truly patient-specific approach to CFD (Figure 3.1).

The methods described in this chapter pertain to that used for the 4 following chapters. Further details related to each chapter's individual methodology will be described in further detail in each relevant chapter.

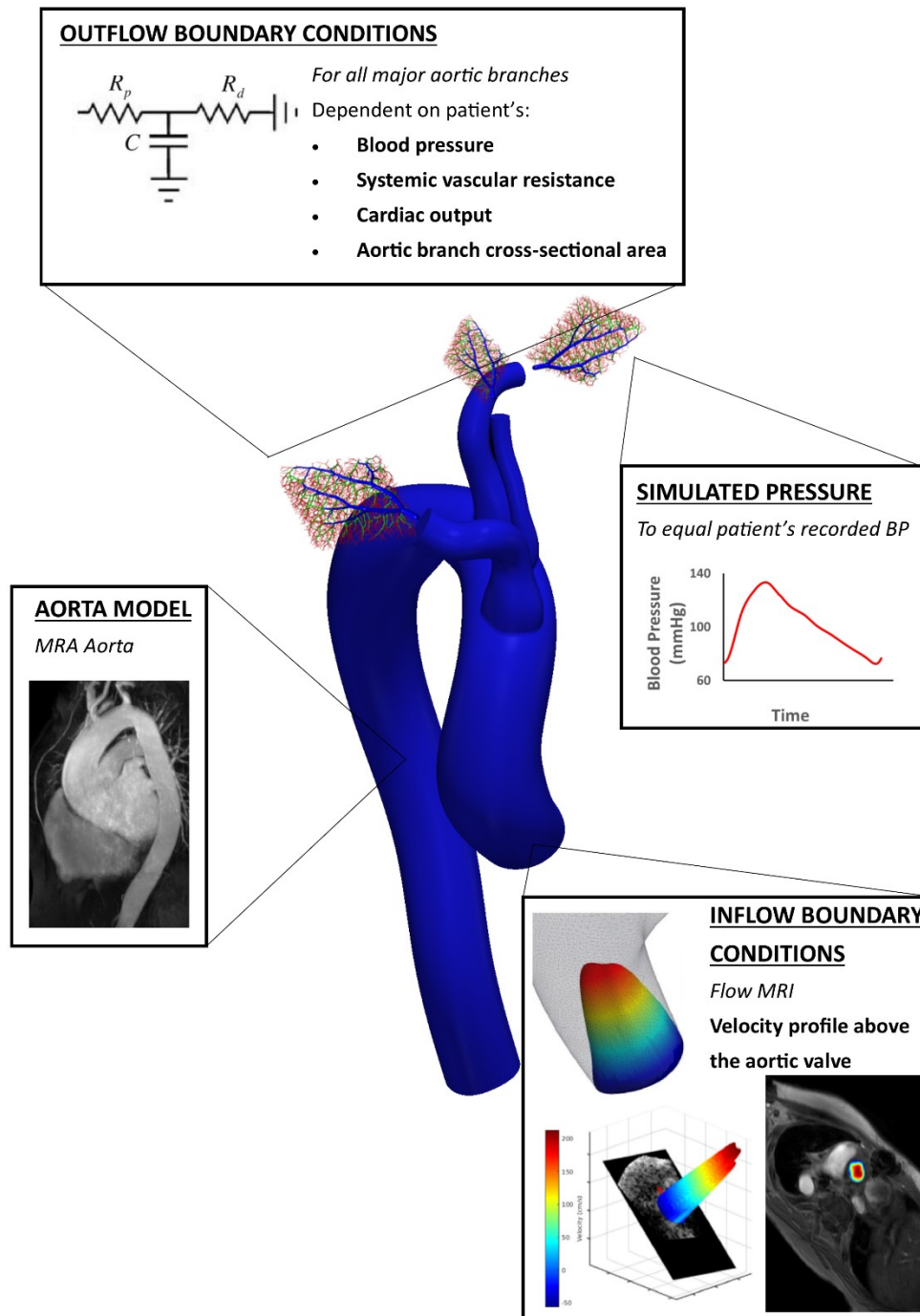


Figure 3.1. The patient-specific components of CFD undertaken in this thesis. The aorta model is based on MR angiography of the patient's aorta. The inflow boundary conditions are dependent on the flow data above the aortic valve, which is mapped to the inlet of the aorta model. The outflow boundary conditions are individually prescribed for each outlet branch of the aorta, and are dependent on the patient's recorded blood pressure, cardiac output, calculated systemic vascular resistance, and cross-sectional area of each branch. As a validation tool, the blood pressure generated by the CFD simulation is checked against the patient's recorded blood pressure and should be equal.

2.1.1 Workflow of Methodology: Imaging and CFD

Figure 3.2 below illustrates the steps involved in the methodology. Firstly, imaging of the aorta, aortic valve, and flow studies are carried out using magnetic resonance imaging (MRI). Then, geometric models of the aorta are segmented and meshed. The velocity profile above the aortic valve from flow studies is mapped to the inlet of the aorta model thus creating a patient-specific inflow boundary condition. The outflow boundary conditions are assigned in a patient-specific manner according to the patient measurements. The blood flow simulation is run for a number of cardiac cycles on a high performance supercomputer (HPC) with subsequent computational fluid dynamics analysis of both flow and aortic wall biomechanics.

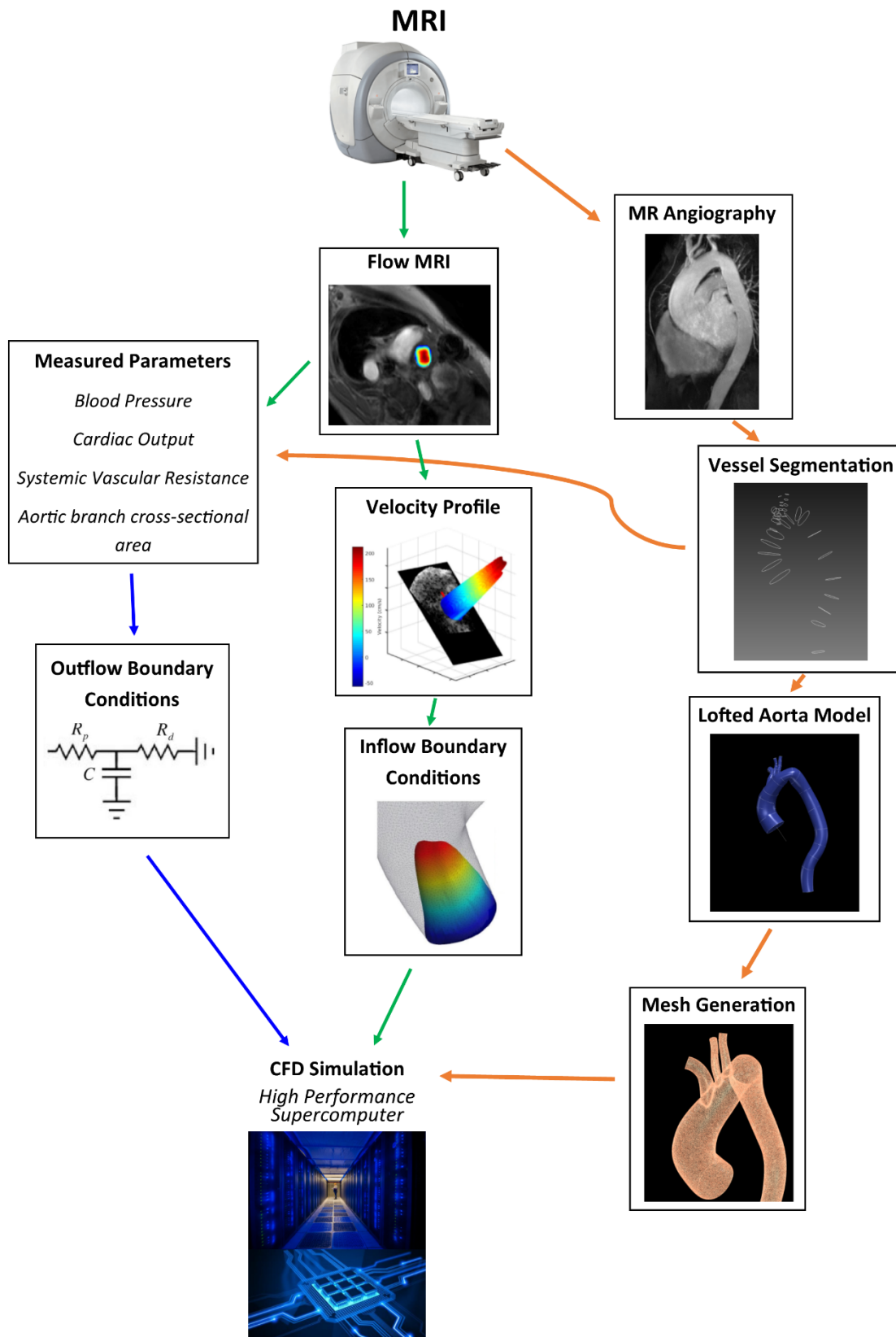


Figure 3.2. Steps involved in the workflow of running CFD simulations for this thesis.

3.2 IMAGING

3.2.1 Imaging the Aorta

Subjects underwent standard of care Cardiac Magnetic Resonance (CMR) imaging and Magnetic Resonance Angiography (MRA) to image the entire thoracic aorta, including the head and neck vessels. Gadolinium (0.3 ml/kg; gadodiamide, Omniscan®, GE Healthcare, Waukesha, WI) was infused with a breath-held 3D fast gradient echo sequence using a Philips Achieva 3T scanner (Philips Medical Systems, Eindhoven, Netherlands). Acquired slice thickness was 1.0-2.0 mm, with 56–80 sagittal slices per volume. A 344×344 acquisition matrix was used with a field of view (FoV) of $35 \text{ cm} \times 35 \text{ cm}$ (reconstructed to slices with a spatial resolution of $0.49 \text{ mm} \times 0.49 \text{ mm}$, and resampled to a slice thickness of 1.00 mm). Other parameters included a repetition time (TR) of 3.9 ms, echo time (TE) of 1.4 ms, and a flip angle of 27° .

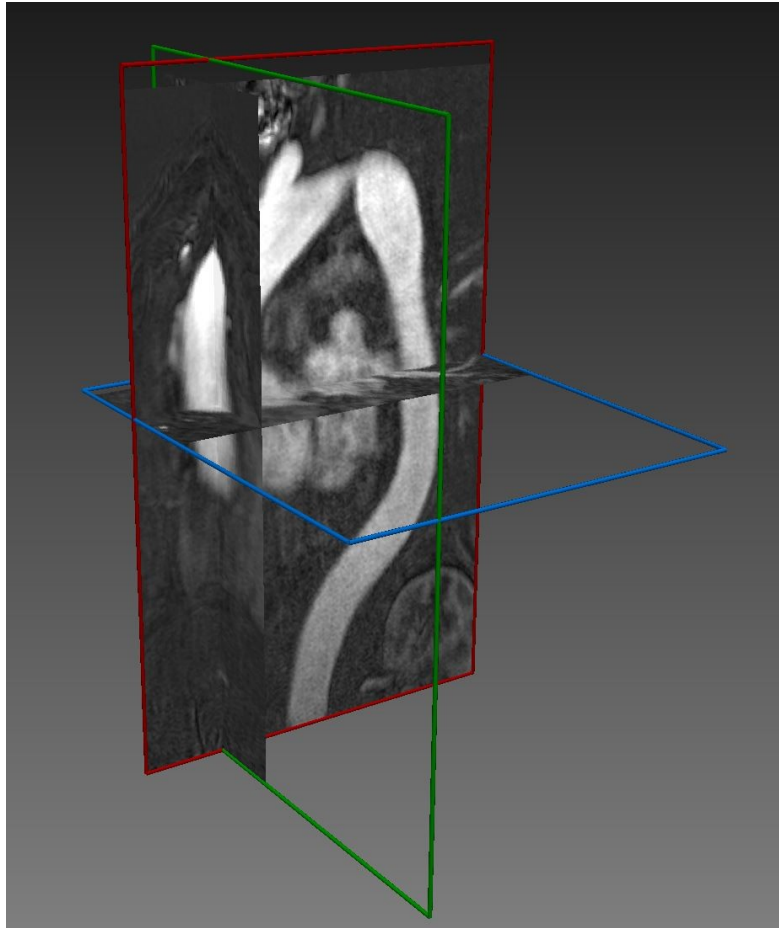


Figure 3.3. The 3 reconstructed planes from MRA image data (axial, coronal and sagittal planes).

3.2.2 Flow Imaging

Time-resolved, 2D through-plane flow-MRI (phase-contrast MRI) was acquired orthogonally in the ascending aorta above the aortic valve. The specific location of this plane was either at the sinotubular junction (in the studies which did not include modelling the aortic root), or just above the aortic valve in the proximal part of the aortic root (in the study which did include modelling the aortic root). These are described in more detail in each relevant chapter.

Heart rates ranged between 50-95 bpm during which 30 images were reconstructed. Imaging parameters included: TR 4.2 ms, TE 2.4 ms, flip angle 15° , Field of View (FoV) $35 \text{ cm} \times 30$

cm, acquisition matrix of 152 x 120, slice thickness 8 mm, voxel size 2.3 mm × 2.4 mm × 8 mm (reconstructed to 1.37 mm x 1.36 mm x 8 mm). Data acquisition was carried out with a breath-hold and gated to the cardiac cycle using ECG leads attached to the subject during the CMR scan. Average scan times were 20 minutes. Immediately after scanning, supine measurement of bilateral upper limb blood pressure was performed.

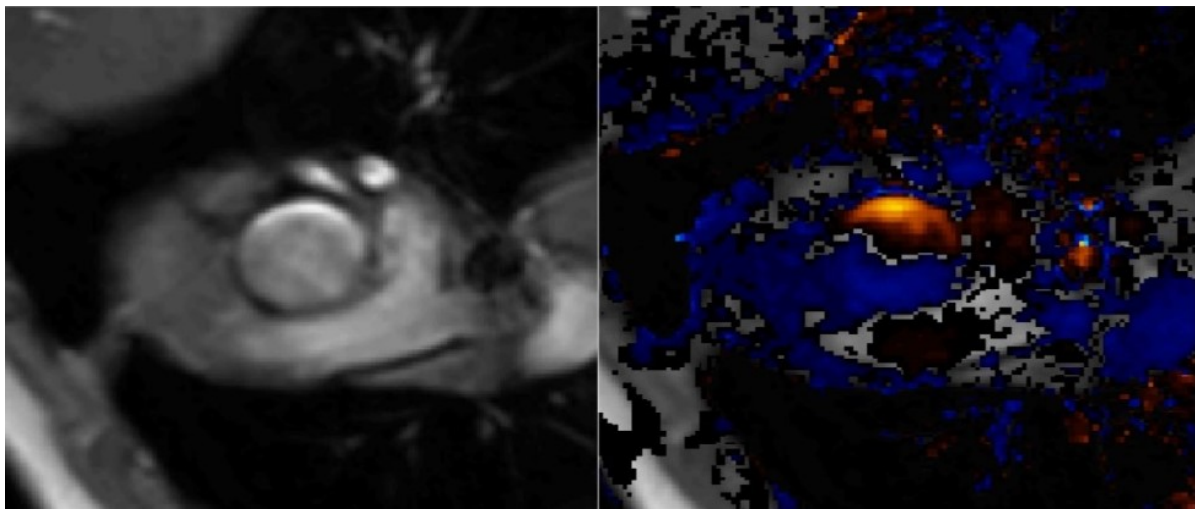


Figure 3.4. Flow MRI (phase-contrast MRI) at the level of the sinotubular junction. The image on the left shows the velocity data in black and white. The image on the right shows superimposed colour flow. The red and blue colours indicate flow in opposite directions.

3.2.3 Aortic Valve Morphology

Cine sequences at the level of the aortic valve (5-8 slices) were carried out for assessment of aortic valve morphology. This allowed visualisation of the valve leaflets in short axis, along with their motion during systole and diastole. The orientation of valve leaflets, along with the presence of absence of raphe (in the case of BAVs) was established. Thus valves were classified as tricuspid or bicuspid, and in the latter case, the fusion pattern was also recorded.

Furthermore, if patients underwent surgery on the aortic valve or aorta, confirmation of valve morphology was further ascertained.

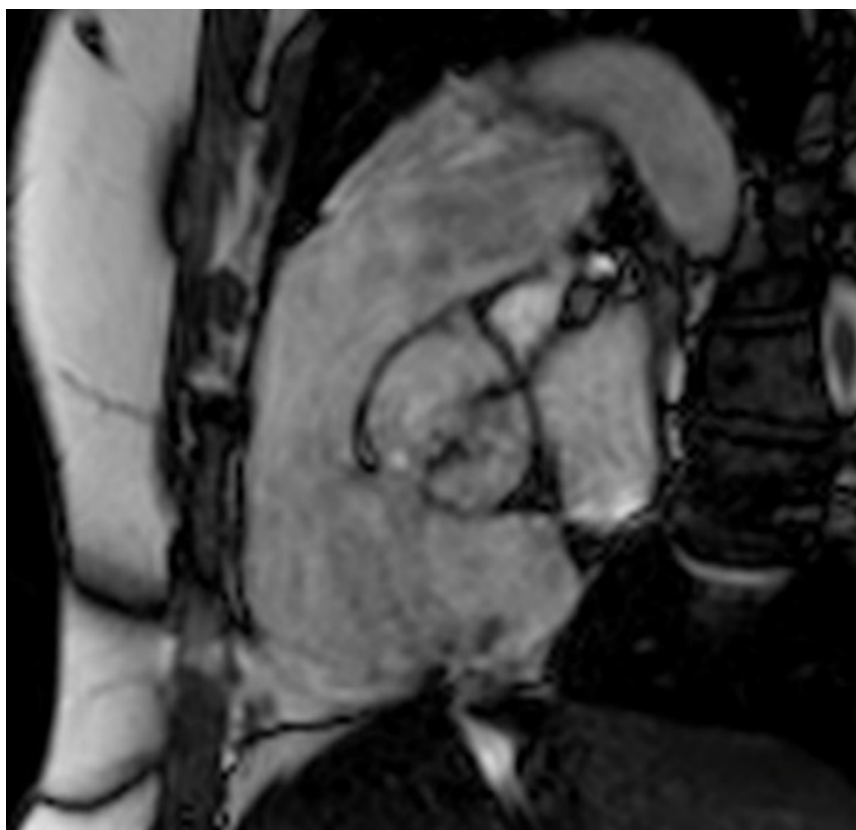


Figure 3.5. Cine sequences through the aortic valve showing a bicuspid aortic valve.

3.3 COMPUTATIONAL FLUID DYNAMICS

3.3.1 Geometric Modelling and Segmentation of the Aorta

Three-dimensional geometric CAD (computer aided design) models of the thoracic aorta were created for each subject based on the MRA data. A 2D segmentation paradigm originally introduced in Wang et al. was utilised (Wang et al. 1999). Centreline paths were defined along the thoracic aorta, innominate artery, left common carotid artery, and left subclavian artery. MRA data was re-sampled in planes perpendicular to these paths. The vessel segmentation

procedure was carried out by identifying the vessel boundary through thresholding, where differences in pixel intensity are used to automatically detect vessel boundaries, or by manual interaction. An automated lofting process then interpolated all segmented boundaries thus creating the three-dimensional model of the arteries. This utilised non-uniform rotational basis splines (NURBS) to produce an accurate and smooth solid model which could subsequently be meshed (Farin 1995). A careful visual comparison was made by superimposing this model onto the maximum intensity projections (MIPs) of the MRAs in order to ensure accuracy.

The first plane to be segmented was at the sinotubular junction in the studies which did not include the aortic root. This first segment would ultimately become the inlet into the aorta model and be the site of the inflow boundary condition. In the study which included the aortic root, the first plane to be segmented was in the proximal root, at around the level of the annulus. The last plane of the aorta to be segmented was in the descending aorta at the level of the diaphragm (where the thoracic aorta finishes and the abdominal aorta begins). This last segment would become the one of the outlets of the model and become the site of the outflow boundary condition of the aorta. As for the head and neck vessels, the final segmented planes would become the other 3 outlets and form the outflow boundary conditions of the innominate, left common carotid and left subclavian arteries.

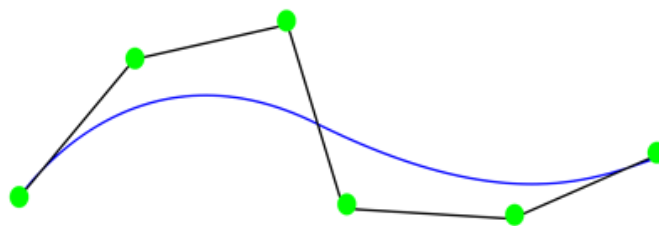


Figure 3.6. Non-Uniform Rotational B-Splines (NURBS) provide a 3D modelling framework based on geometric primitives and drawn curves.

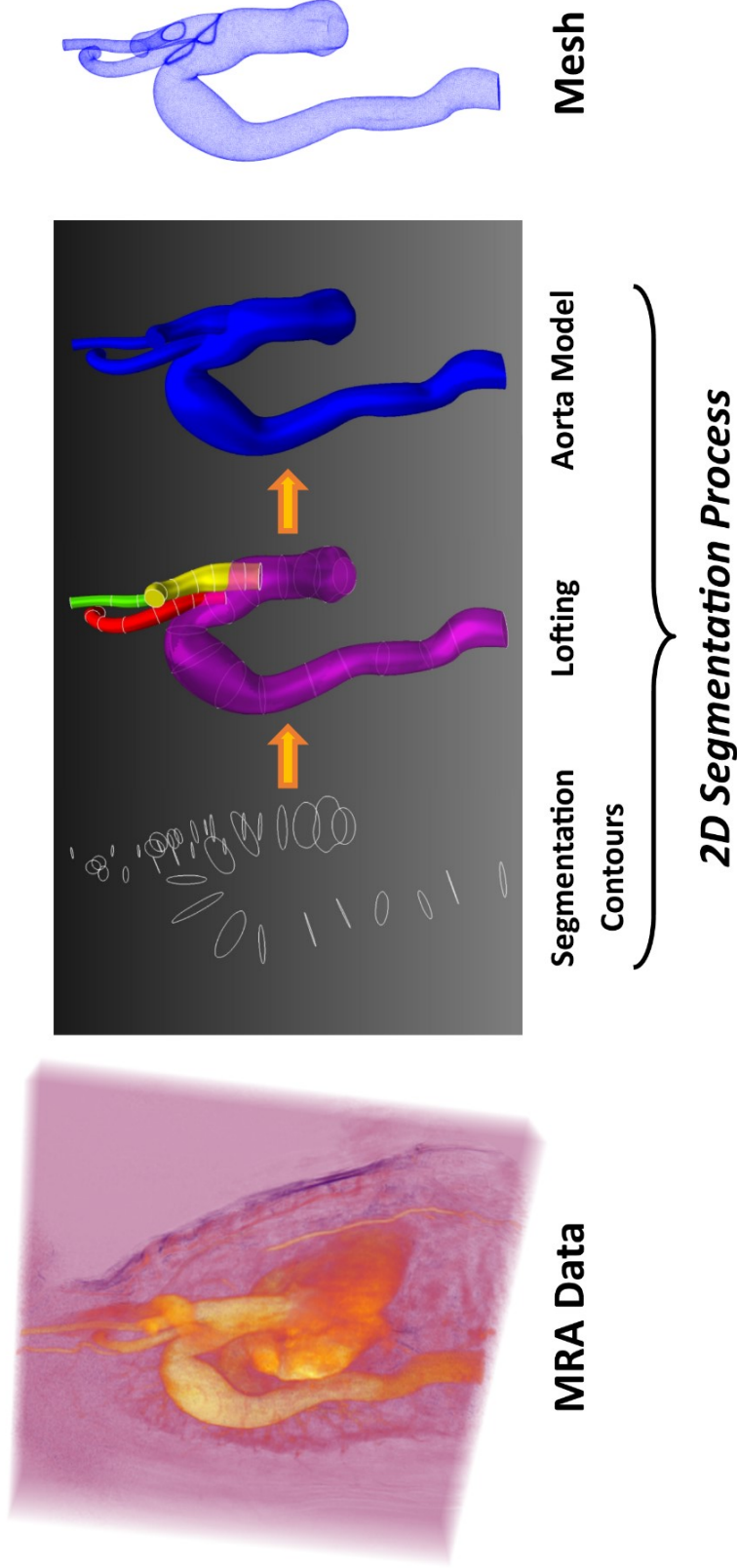


Figure 3.7. The segmentation and lofting process. On the left, the MRA data shows the anatomy of the thoracic aorta. To the right is shown the 2D segmentation process which involves creation of segmented contours of the aortic lumen; these contours are then lofted together to create a Non-Uniform Rational Basis Spline (NURBS) analytical representation of each vessel; finally the lofted surfaces are joined and blended to remove sharp edges between branching vessels.

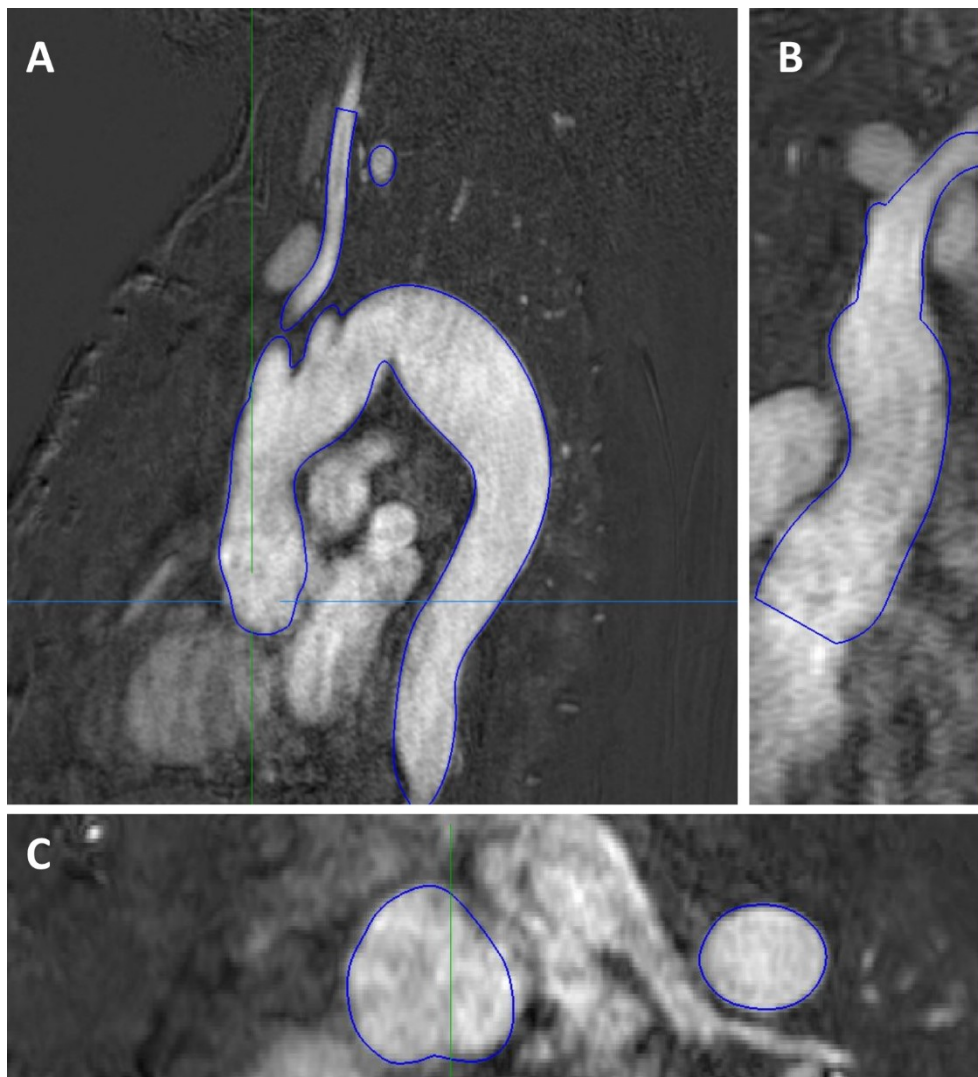


Figure 3.8. Outline of the lofted aorta model (blue outlines) superimposed on the MRA data. **A** shows this in the sagittal plane, **B** shows this in the coronal plane, and **C** shows the axial plane.

3.3.2 Mesh Generation

A mesh was created from this aorta model in order to assign data points in 3D space within the model for assessment of haemodynamic parameters. A tetrahedral mesh was created by discretising this model. It was important to create a mesh which was fine enough to produce

accurate results. In blood flow modelling, haemodynamic parameters such as WSS and velocity patterns can be significantly affected by meshes which are too coarse, as a degree of unphysiological numerical viscosity is introduced (Taylor et al. 2009). The mesh was created for each subject's aorta model using a combination of boundary layer and local curvature based refinement. The mesh was created using a global mesh size of 1mm with maximum curvature size 0.02mm. A boundary layer size of 0.5mm was applied with 5 layers of incremental expansion. This meant that at the boundary layer, i.e. at the vessel walls, the mesh was much finer in order to appreciate differences in wall mechanics such as WSS to a much higher degree of detail and resolution. A pulsatile flow simulation was run, followed by a field-based anisotropic mesh refinement (Muller et al. 2005). This resulted in a final mesh consisting of between 2 – 6 million tetrahedral elements amongst the different subjects.

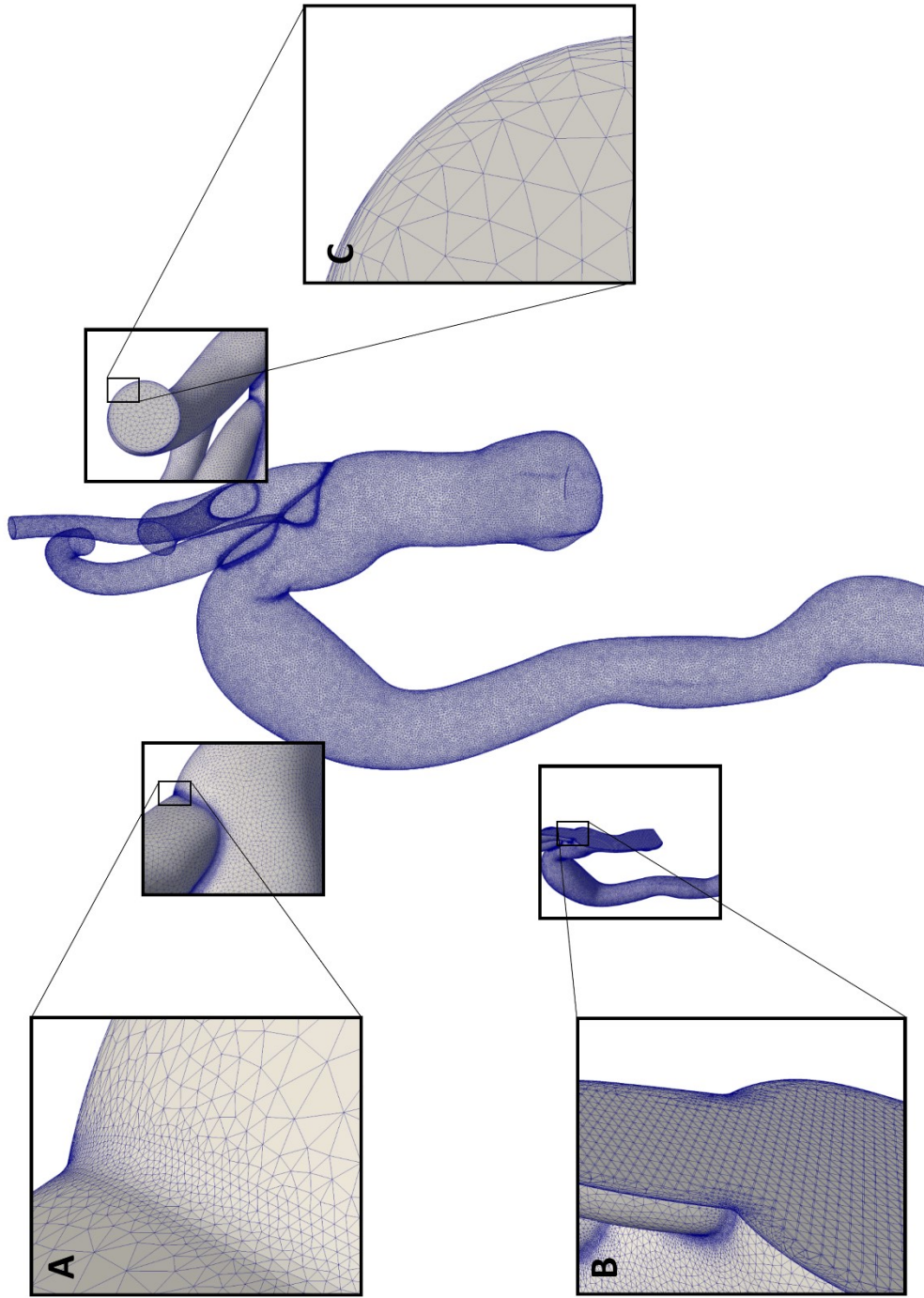


Figure 3.9. Tetrahedral mesh of the thoracic aorta. **A** shows the smooth blending which has been carried out at the interface between two vessels (in this case the innominate artery and the aorta). A maximum curvature size of 0.02mm was applied which makes the mesh much finer and smoother at these blended interfaces. **B** shows a slice through the ascending aorta and innominate artery, and reveals that the mesh is more refined and detailed closer to the vessel walls. This is seen again in **C** which shows a close-up of a cross-section through the left subclavian artery. Here, 5 layers of incremental expansion are seen (i.e. the mesh layers become thinner and closer together as you approach the vessel wall).

3.3.3 Finite Element Analysis

Blood flow simulations were carried out using stabilised finite element methods to solve equations enforcing conservation of mass (continuity) and balance of linear momentum (Navier-Stokes) for the flow of an incompressible Newtonian fluid. This was processed in a 3D rigid domain reconstructed from image data, coupled to patient-specific haemodynamic conditions at both the inlet and outlets of the computational domain. It therefore signifies a multi-scale approach to blood flow modelling, as haemodynamics are calculated over the entire circulation and not just the image-based portion of the thoracic aorta (Vignon-Clementel et al. 2006). The validated in-house open-source code CRIMSON was used for this process (<http://www.crimson.software/>) (Figueroa et al.).

3.3.4 Constitutive Material Models

Blood was modelled as a Newtonian fluid with density $\rho = 1.06 \text{ g/cm}^3$ (Xiao et al. 2013) and dynamic viscosity $\mu = 0.04 \text{ Poise}$ (Kim et al. 2009). Blood flow was assumed to be incompressible. A coupled multi-domain formulation was used to link lumped parameter models for the distal vessels (innominate artery, left common carotid artery, left subclavian artery, and descending aorta) to the three-dimensional vascular model mesh (see section 1.5 below). The model required the prescription of one inlet/inflow boundary condition, and 4 outlet/outflow boundary conditions.

3.3.5 Time Integration Strategy

An initial pressure equal to that of the patient's recorded diastolic blood pressure was applied at the inlet nodes to create the initial stress load and start the simulations, which then continued

in a pulsatile manner according to the inflow boundary conditions generated from the PC-MRI data. Residual controls were set, which limit the sum total of all the individual nodal residuals for the entire mesh. These were set at 1×10^{-3} . All simulations achieved 100% of residuals $< 1 \times 10^{-3}$. A time-step size of 0.00025 sec was utilised, which for example equated to 4000 time steps per cardiac cycle for a patient with a heart rate of 60bpm and a cardiac cycle of 1.0 seconds. Simulations were run for 3-8 cardiac cycles until achieving periodicity in the flow and pressure fields. Fifty time points were processed per cardiac cycle, and the last cardiac cycle was used for the purpose of data analysis. Simulations were run on 256 cores of a 640 core SGI Altix-UV High Performance Supercomputer (HPC) with Nehalem-EX architecture.

3.4 INFLOW BOUNDARY CONDITIONS

3.4.1 Overview

In this thesis, we propose a novel method of obtaining patient-specific blood velocity profiles above the aortic valve from imaging data (flow MRI), and mapping them to geometric models of the patient's aorta. The proposed method establishes a pointwise connection between the imaging flow data, and the contours of the aorta model geometry, from which a smooth deformation field is calculated. This deformation field is used to map the velocity data from the imaging flow data to the aorta model.

Flow MRI can be used to obtain a velocity profile over the cross-section of the vessel of interest. However, a difficulty encountered when using a velocity profile obtained from imaging data is the spatial mapping between the imaging data and the model inlet. Flow MRI and MRA (used to create the aorta model) generate different forms of data, and thus mapping one to the other is not straightforward. Furthermore, the flow MRI data for the velocity profile

above the aortic valve will have some motion during the cardiac cycle, including bulk motion and changes in the vessel radius. In the case of the thoracic aorta, the aortic root and ascending aorta are very mobile throughout the cardiac cycle. They also change cross-sectional area.

The main novelties of the proposed method are three-fold:

- i. Calculation of a patient-specific velocity profile from flow MRI (phase-contrast MRI)
- ii. Use of a flexible B-spline framework for mapping the profile to the geometry of the model
- iii. Designing the mapping process in a way that the user can choose between maintaining flow rate and volume or velocity distribution between the flow imaging data and the aorta model

The proposed method has been developed as a plug-in to the CRIMSON software (<http://www.crimson.software/>) (Figueroa et al.).

3.4.2 Flow MRI

As part of their MRI acquisition, each subject underwent phase-contrast MRI (PC-MRI) images of the blood flow velocity field just above the aortic valve, at a plane orthogonal to the annulus of the aortic valve. This plane corresponded to the sinotubular Junction. This plane matched the inflow mesh of the aorta model. The data was acquired over 30 cardiac phases, with image size 256 x 256 pixels, and pixel size 1.48mm. The encoding velocity constant (V_{enc}) was set to 3m/s, and for subjects with aortic stenosis, it was set to 5m/s in order avoid aliasing. Flow MRI provides through-plane velocity.

3.4.3 Velocity and Flow Extraction

An in-house software written in *Matlab* (*The Mathworks Inc., Massachusetts, USA*) was used to generate the velocity profile from the Flow-MR. This software allows the user to extract the velocity profile and flow rate waveform from the PC-MRI images. The *Matlab* code processes velocity data by multiplying the image pixel intensity by the V_{enc} . This data is then ready for segmentation.

3.4.4 Lumen Segmentation

The in-house Matlab software featured a graphical interface that allows manual segmentation of the lumen boundaries of each of the 30 cardiac phases. This permits accurate data extraction despite the movements of the aorta during the cardiac cycle. The segmented boundaries were smoothed using cyclic B-splines to reduce inaccuracies due to the manual delineation of the lumen boundary. A segmentation mask was generated from the resulting segmentation, and the velocity profile was generated by applying the resulting mask to the flow-MR data.



Figure 3.10. Segmentation of the lumen boundaries from Flow MRI to create the velocity profile.

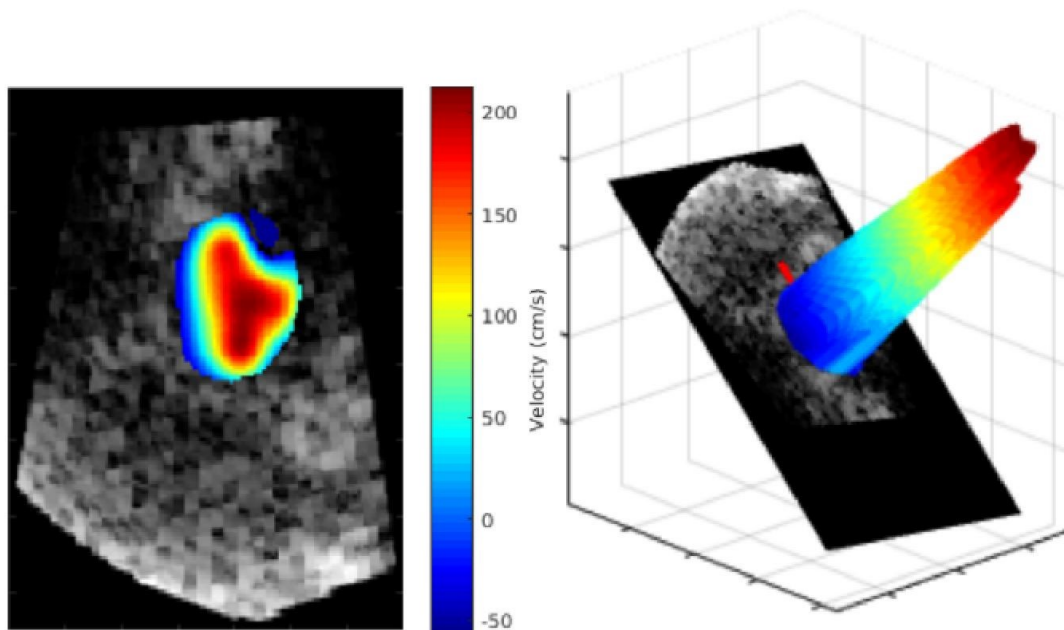


Figure 3.11. Velocity profile obtained from Flow MRI, before mapping to the aorta model geometry. On the left is shown the 2D velocity profile, and on the right is shown a 3D representation of the 2D velocity profile.

3.4.5 Mapping of Velocity Profile onto Inlet Mesh of Aorta Model

The inlet mesh from the aorta model derived from MRA data is fixed both temporally and spatially. In contrast, the inflow velocity profile derived from flow-MRI data has a lumen boundary which changes shape, size and position with each cardiac phase. Therefore, the inflow velocity profile needs to be mapped onto the fixed inlet mesh of the CFD aorta model. This mapping was carried out by finding a rigid alignment followed by a non-rigid adaption between the lumen boundary in the image and the fixed inlet boundary from the model. The mapping transforms points in the aorta model geometry to points in the velocity profile image geometry.

Firstly, the 3D contours are transformed into 2D. This is carried out by use of a matrix which characterises the coordinate transformations. There is a separate matrix for the velocity profile ($M_{Velocity Profile}$) and a matrix for the aorta model (M_{Model}). Thus, to form the 2D coordinates of each point (P_i^{2D}), the 3D coordinates of each point must be applied to the matrix:

$$P_i^{2D}_{Velocity Profile} = P_i^{3D}_{Velocity Profile} M_{Velocity Profile}^{-1}$$

And likewise

$$P_i^{2D}_{Model} = P_i^{3D}_{Model} M_{Model}^{-1}$$

Next, the offset and the rotation between the 2D contour from the velocity profile, and the 2D contour from the aorta model must be calculated. Thus, corresponding points between the two need to be established. The offset can be calculated by aligning the centroids of the 2D contours of the velocity profile and the aorta model. The rotation around the aligned centroids can then be calculated from a user-defined reference point. This point can be an anatomical landmark. In our studies, we always used the point on the lumen boundary of the aorta which lies most

anteriorly, i.e. closest to the anterior chest wall. This is because the anterior chest wall is visible in both the flow MRI image (for the velocity profile) and the MRA images (for the aorta model).

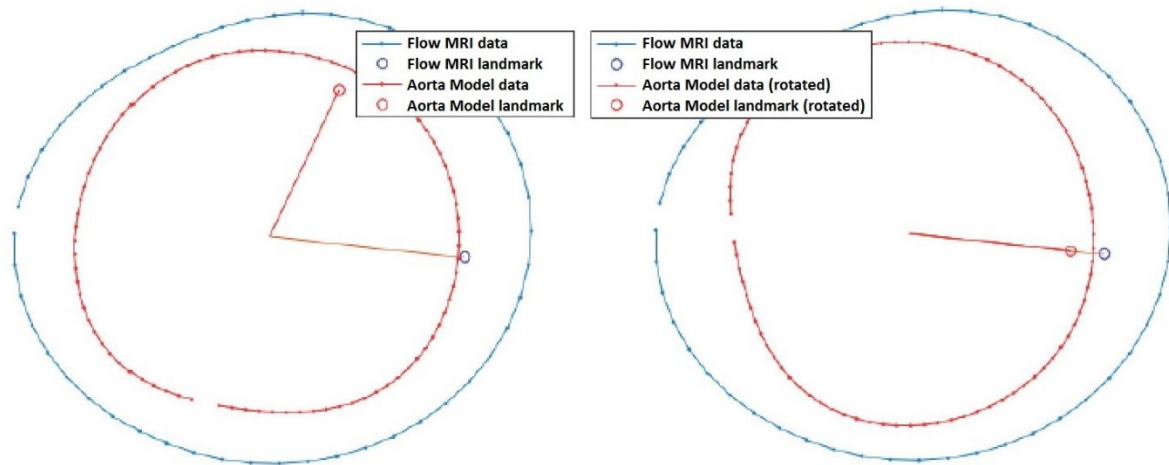


Figure 3.12. Rotation contour alignment. On the left is shown the Flow MRI data (in blue) and the aorta model data (in red) with their centroids aligned. On the right is shown the next step which is to carry out rotation alignment of the two datasets, so that their landmarks are lined up.

The next step is to apply a smooth deformation field to match the contours' shapes of the velocity profile and the aorta model. This forms the basis of a non-rigid alignment of the velocity profile contour to the aorta model contour. We used bicubic B-spline field to deform the aorta model contour to the velocity profile contour. In order to establish correspondences between the two rigidly aligned contours, we used K equally spaced points along the circumference of each contour. The corresponding points then determine K deformation vectors $\mathbf{v}(x_i, y_i), i = 1 \dots K$ along the contour (see Figure 3.12). In this figure, we used $K = 50$. The vectors between the corresponding points are interpolated using a smooth 2D B-spline

field. This obtains a dense deformation field to warp both the contours and the inlet surface, thus mapping velocities from flow MRI to the aorta model.

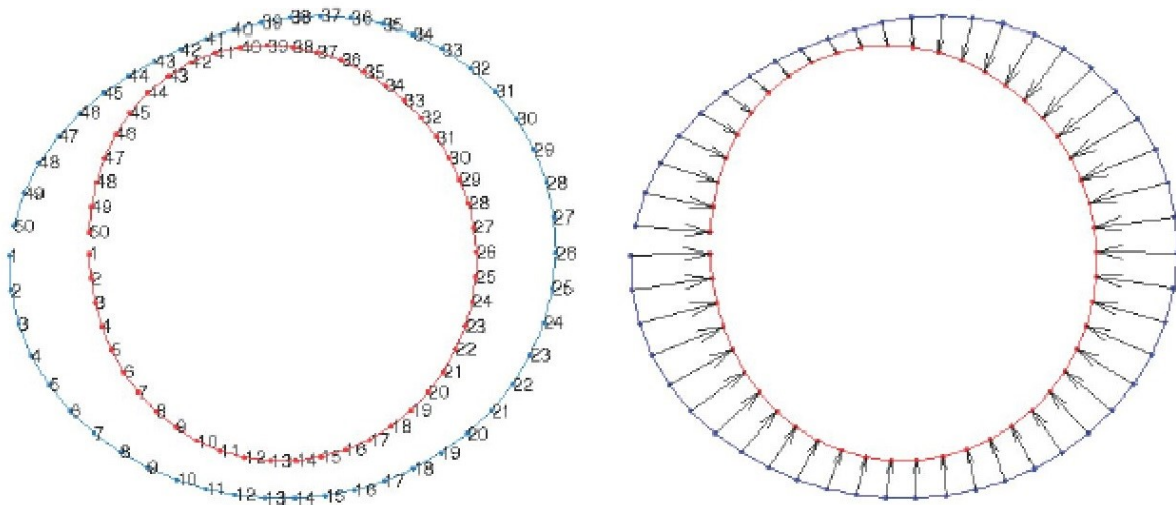


Figure 3.13. Non-rigid alignment between the Flow MRI derived contour and the aorta model contour at the inlet. The red line depicts the aorta model contour, and the blue line depicts the Flow MRI contour. On the left is shown the point by point correspondence between the two datasets. On the right is shown the deformation between contours.

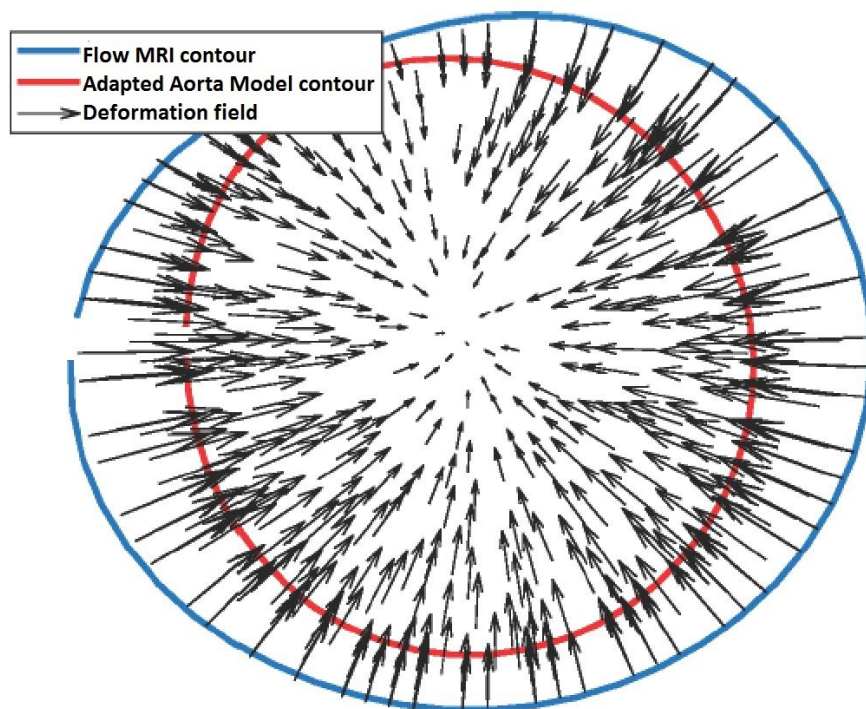


Figure 3.14. Dense deformation mapping from the aorta model to the Flow MRI imaging contour interpolated from vectors using bicubic B-splines.

The aorta model is typically a triangulated tetrahedral mesh, and at the inlet the velocities are defined as vectors at each mesh node. In order to calculate the corresponding velocity at each mesh node, the above transformations are carried out in reverse order:

- 1) Transform the mesh into 2D
- 2) Translate using the mesh centroid
- 3) Apply the deformation field from the aorta model to the velocity profile image
- 4) Apply the rotation between the aorta model to the velocity profile image
- 5) Translate using the centroid of the velocity profile derived contour
- 6) Transform the 2D points to the 3D space of the original image

This mapping process is carried out for each cardiac phase in the imaging data from flow MRI (typically 30 phases for each cardiac cycle). It is then temporally interpolated using cyclic B-splines to a continuous function. This can be sampled at the rate required by the CFD simulation's inflow boundary condition parameters.

Typically, the contour from the aorta model inlet and the contour from flow MRI have slightly different shape and surface area, partly due to variable motion and cross-sectional areas in flow MRI versus fixed cross-sectional area in MRA, differences between MRA imaging data and flow MRI imaging data, and segmentation errors. Since the surface area between the two may be different, the flow rate (which is dependent on velocity and area) may also be different. We therefore introduced a scalar trade-off factor λ . This factor is determined by the user and governs whether the velocity distribution is maintained ($\lambda=0$), the flow rate is maintained ($\lambda=1$) or the mapped profile trades between the two ($0 < \lambda < 1$). The final velocity is a function of the interpolated velocity v and surface areas of the aorta model and flow MRI (A_{Model} and $A_{Velocity Profile}$ respectively).

$$v_f = v \left((1 - \lambda) + \lambda \frac{A_{Model}}{A_{Velocity Profile}} \right)$$

The user must tune λ based on the target application. For the purposes of our studies, λ was set as 0 because our main focus of attention was investigating the effect of aortic valve morphology and resultant velocity profiles on haemodynamics of the aorta. Therefore, the spatiotemporal pattern of velocities exiting the aortic root were the most important factor to preserve in our patient-specific CFD simulations.

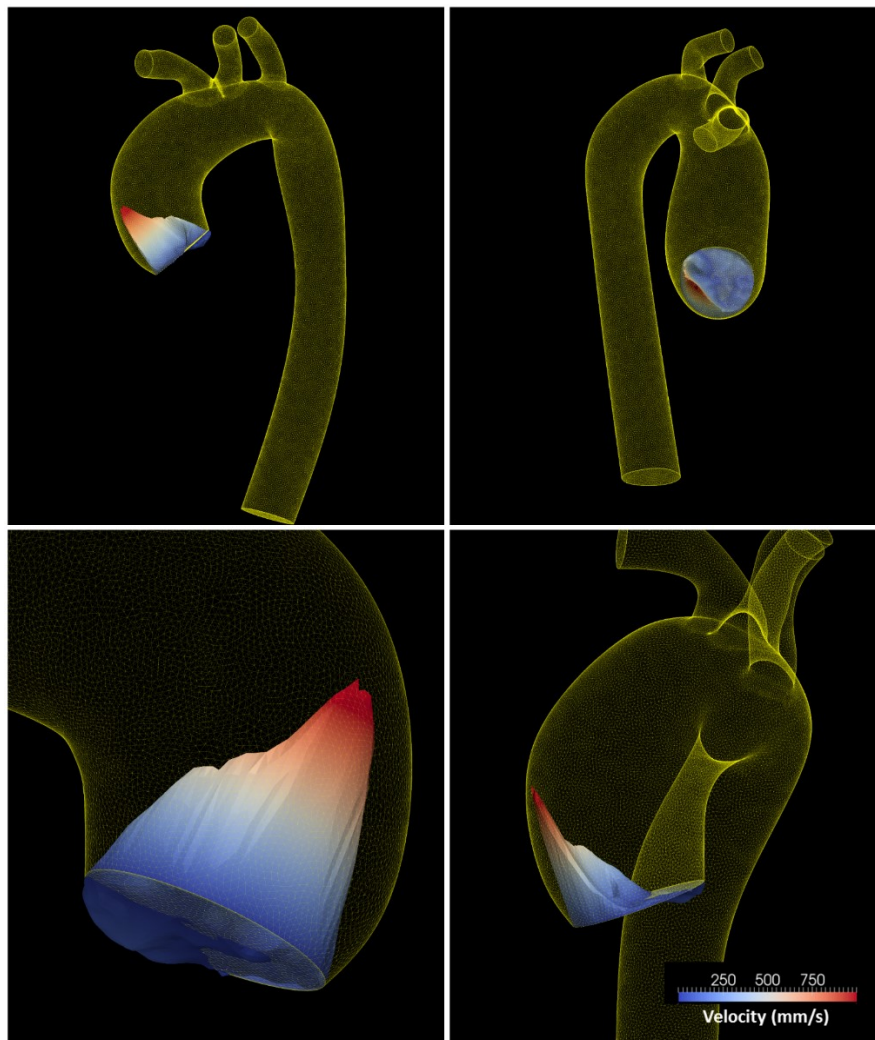


Figure 3.15. Inflow velocity profile mapped onto the inlet of the aorta mesh. The velocity magnitude is displayed with a colour scale, with red symbolising higher velocities and blue symbolising lower velocities (see velocity scale bottom right hand corner).

3.4.6 Validation of Mapping Process

To ensure correct spatiotemporal mapping of velocity data from flow MRI to the aorta model inlet, comparison was made between the flow MRI data and velocity maps taken just above the inlet of the aorta model following processing of the blood flow CFD simulations. The shape and orientation of the velocity encoded data from flow MRI was compared to the velocity maps from the CFD simulation in a spatiotemporal manner. Furthermore, velocity magnitudes such as peak velocity as well as flow rate were also compared between flow MRI data and CFD simulation data.

3.5 OUTFLOW BOUNDARY CONDITIONS

Patient-specific outflow boundary conditions were prescribed at each outlet in the innominate artery, left common carotid artery, left subclavian artery and descending aorta. Upper limb blood pressure was measured after each study using an automated sphygmomanometer cuff with participants in the supine position. A 3 element Windkessel RCR model (Figuroa et al. 2006, Vignon-Clementel IE 2006) was superimposed on each outlet. The Windkessel model represents the arterial tree (arteries, arterioles, capillaries, venules and veins) beyond the model outlet in an intuitive and physiological manner comprising of a proximal resistance (R_p), compliance (C), and a distal resistance (R_d) for each outlet.

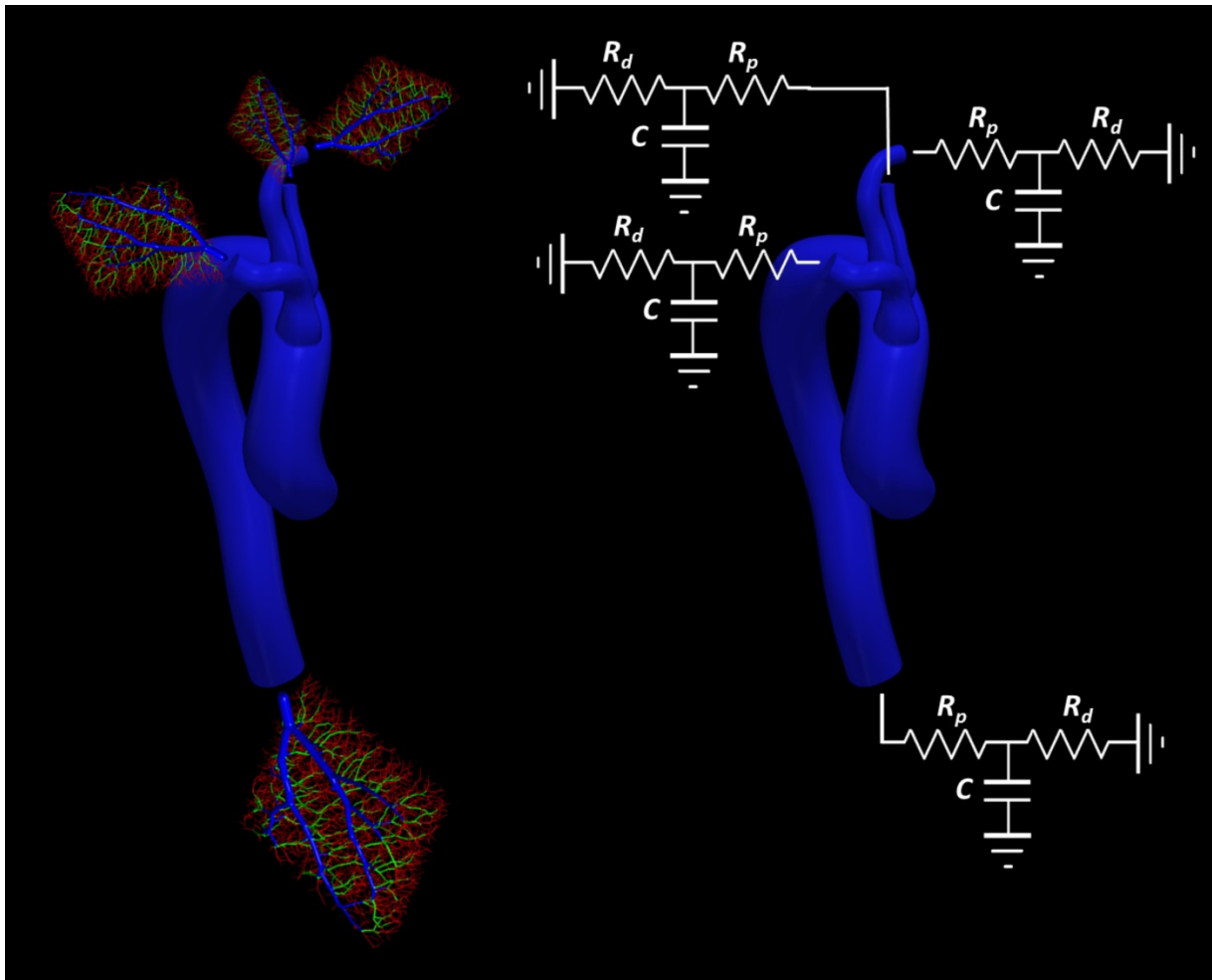


Figure 3.16. Four Windkessel outflow boundary conditions representing the distal vascular bed (arteries, arterioles, capillaries, venules and veins) of each of the outlets (innominate artery, left common carotid artery, left subclavian artery, descending aorta). R_p = proximal resistance, C = compliance, R_d = distal resistance.

R_T is the total resistance in the vascular system (systemic vascular resistance). These values were calculated in the following patient-specific manner:

$$R_{total} = \frac{P}{Q}$$

where P = patient's mean arterial pressure, Q = flow, or cardiac output, as derived from the PC-MRI inlet velocity profile.

$$R_{total} = \left(\sum_i \frac{1}{R_i} \right)^{-1}$$

and R_i is the total resistance for each individual outlet.

$$R_i = R_p + R_d$$

for each individual outlet, where R_p is proximal resistance, and R_d is the distal resistance. R_i is calculated using the following relationship:

$$\frac{R_{total}}{R_i} = \frac{A_i}{A_T}$$

where A_i is the cross-sectional area of the individual outlet, and A_T is the total cross-sectional area of all outlets in the model. We assumed the ratio of proximal to total resistance:

$$\frac{R_p}{(R_p + R_d)} = 0.056$$

(Laskey et al. 1990)

Similarly, C_T is the total compliance in the vascular system.

$$C_T = \sum_i C_i$$

and

$$\frac{C_i}{C_T} = \frac{A_i}{A_T}$$

Therefore the flow and compliance at each outlet is proportional to the outlet's area. The prescribed Windkessel parameters used for an example subject can be seen in the table below.

Table 3.1. Example values of the lumped parameter Windkessel boundary conditions for a subject. R_p = proximal resistance; R_d = distal resistance; C = compliance. The units of resistance are 10^3 dynes s / cm^5 . The units of compliance are 10^{-6} cm^5 / dynes.

Outlet	R_p	R_d	C
Descending Aorta	0.25	2.14	208
Brachiocephalic	1.36	9.23	48.3
Left Common Carotid	2.46	15.3	29.2
Left Subclavian	1.74	11.3	39.3

3.5.1 Validation of Outflow Boundary Conditions

Simulations were run for 3-8 cardiac cycles until achieving periodicity in the flow and pressure fields. Once periodicity was achieved, i.e. there was no cycle to cycle variation in blood pressure or flow splits, the blood pressure produced by the CFD simulation in the left subclavian artery was compared to the upper limb blood pressure recording of the patient after the MRI scan. The aim was for these to be the same, which would indicate that the CFD simulation had accurately replicated the patient's in-vivo haemodynamics. At this point the last cardiac cycle was used for the purposes of CFD analysis. If there were differences between the simulated and recorded blood pressures, the Windkessel parameters were adjusted accordingly and the simulation re-run until the simulated blood pressure equalled the recorded blood

pressure. If this was required, it involved very minimal adjustment of the Windkessel parameters.

3.6 QUANTIFICATION OF HAEMODYNAMIC INDICES

3.6.1 Flow Patterns

Different planes along the thoracic aorta were analysed for velocity maps (2D), velocity profiles (3D), and velocity vectors. Axial velocity was assessed by measuring the through-plane component of the velocity vectors in line with the long axis of the aorta at that plane. This was essentially a measure of forward flow. Radial velocity was assessed by measuring the component of the velocity vectors perpendicular to the long axis of the aorta. This measured non-axial helical flow. Particle streamlines offering three-dimensional visualisation of evolving aortic flow were calculated from temporally resolved velocity data for the entire thoracic aorta. Blood flow velocity maps (2D and 3D visualisation), axial and radial velocity and velocity streamlines were visualised using ParaView (Kitware, Inc., Clifton Park, NY).

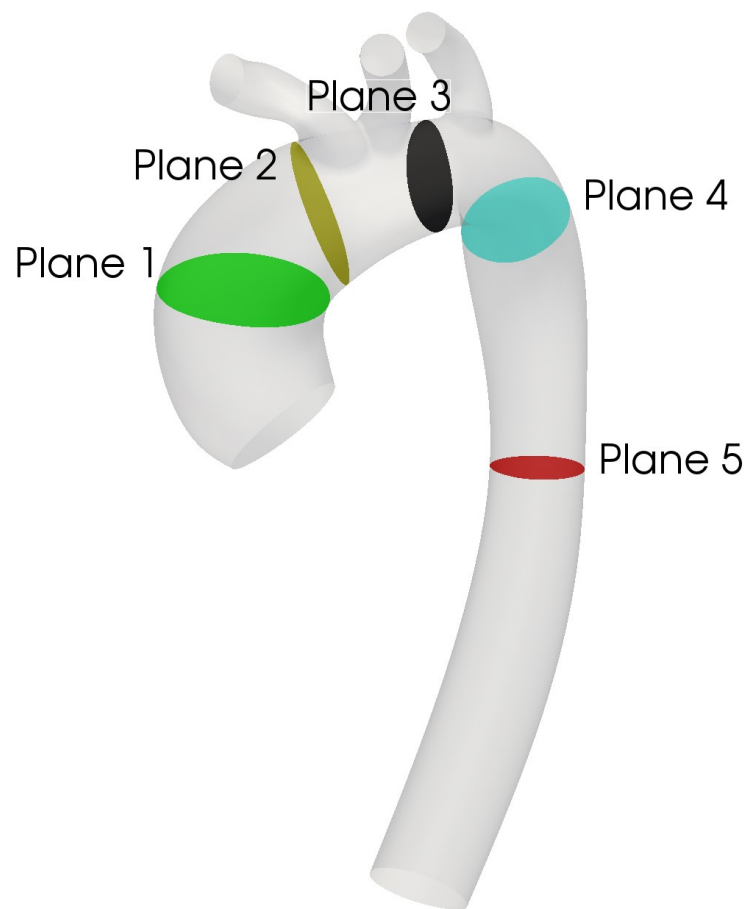


Figure 3.17. Five example planes along the thoracic aorta where in-depth analysis of velocity maps, velocity profiles, axial and radial velocity vectors were analysed.

3.6.2 Flow Asymmetry

Flow asymmetry ($\text{Flow}_{\text{asymmetry}}$) on each plane was obtained to assess whether flow was central or eccentric (Mahadevia et al. 2014). $\text{Flow}_{\text{asymmetry}}$ was obtained by calculating the centroid of the top 15% of peak systolic velocities ($V_{\text{max}}^{15\%}$) (point $\vec{x}_b = (x_b, y_b, z_b)$, Figure 3.18), and measuring its distance to the geometric centroid of each aortic plane (point $\vec{x}_a = (x_a, y_a, z_a)$).

The distance between centroids ($\|\vec{x}_b - \vec{x}_a\|$) is then divided by the equivalent radius of the plane (R_{eq}).

$$Flow_{asymmetry} = 100 \times \frac{\sqrt{(x_b - x_a)^2 + (y_b - y_a)^2 + (z_b - z_a)^2}}{R_{eq}}$$

A $Flow_{asymmetry}$ of 0% means that flow is central to the axis of the vessel, and a $Flow_{asymmetry}$ of 100% means that flow is completely eccentric and biased towards the periphery of the lumen.

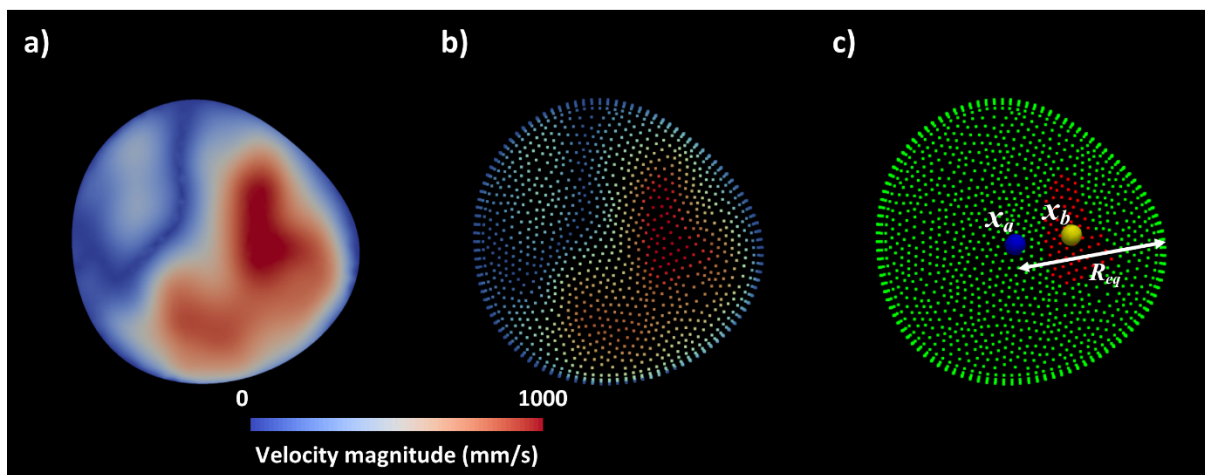


Figure 3.18. a) 2D representation of the velocity magnitude during peak systole; b) velocity magnitude represented by individual dots for each nodal point of the aortic inflow computational mesh; c) red dots represent the top 15% of velocities at peak systole ($V_{max}^{15\%}$), \vec{x}_a represents the centroid of the inflow face, \vec{x}_b represents the centroid of $V_{max}^{15\%}$, and R_{eq} represents the equivalent radius of the inflow face.

3.6.3 Flow Dispersion

This metric ($Flow_{dispersion}$) represents whether the flow at each plane is peaked or broad. $Flow_{dispersion}$ was calculated by dividing the area of the top 15% of peak systolic velocities ($V_{max}^{15\%}$) by the total area of the plane.

$$Flow_{dispersion} = 100 \times \frac{Area\ of\ Vmax^{15\%}}{Area\ of\ plane}$$

A high value of $Flow_{dispersion}$ means that the flow profile is broad and wide, whereas a low value indicates a pointed, sharp velocity profile.

3.6.4 Helicity

Helicity is a metric that represents the extent to which corkscrew-like motion occurs, and is governed by velocity and vorticity (Hardman et al. 2013). The kinetic helicity density per unit volume is defined as:

$$H_k = V \cdot (\nabla \times V)$$

where V is the blood velocity and $(\nabla \times V)$ the vorticity. A helical flow index (HFI) was calculated to quantitatively measure the degree of flow helicity. We released sets of immaterial particles at 50 equally spaced time instants throughout the cardiac cycle, created within a small spherical region in the root of the aorta. Particles were continuously released and tracked along the course of the thoracic aorta for 40 cycles using a time-step equal to $T/50$, where T was the cardiac period. Analyses were performed using only particles which had left the domain through the descending aortic outlet by the time the 40 cycles were completed. HFI_p is the helical flow index for each path-line, calculated over a particle trajectory j :

$$HFI_j = \frac{1}{N_j} \sum_i^{N_j} |\psi_i|$$

Here, ψ_i is the dimensionless normalised helicity, calculated as the cosine of the angle between velocity and vorticity vectors at each point of the pathline, computed at the i^{th} time-step after the particle entered the domain. N_j is the number of time-steps for which the j^{th} particle was

present in the domain. Steady Poiseuille flow gives a value of $\psi_i = 0$, whereas $|\psi_i| = 1$ occurs when flow is purely helical (Grigioni et al. 2005, Hardman et al. 2013, Morbiducci et al. 2009). $HFI_{systole}$ is the average HFI_j over all pathlines during the systolic phase, and $HFI_{diastole}$ is the average HFI_j over all pathlines during the diastolic phase. Specifically, the j^{th} particle is present for N_j time steps, which we index by the set $S_j := \{1, 2, \dots, N_j\}$. This set can be partitioned as two subsets, $S_{j, systole}$ and $S_{j, diastole}$, such that $S_{j, systole} \cup S_{j, diastole} = S_j$, and $S_{j, systole} \cap S_{j, diastole} = \emptyset$, where the step index is placed in $S_{j, systole}$ or $S_{j, diastole}$ according to whether that step occurred during the systolic or diastolic phase of the cardiac cycle. We then define

$$HFI_{j, systole} = \frac{1}{|S_{j, systole}|} \sum_{i \in S_{j, systole}} |\psi_i|$$

and

$$HFI_{j, diastole} = \frac{1}{|S_{j, diastole}|} \sum_{i \in S_{j, diastole}} |\psi_i|$$

Finally, with J defined to be the set of all particles which left the domain through the descending aortic outlet during the 40 cardiac cycles simulated, we compute

$$HFI_{systole} = \frac{1}{|J|} \sum_{j \in J} HFI_{j, systole}$$

and

$$HFI_{diastole} = \frac{1}{|J|} \sum_{j \in J} HFI_{j, diastole}$$

3.6.5 Wall Indices

The entire thoracic aorta was analysed for the wall indices of WSS and OSI. Given that the significant majority of aneurysms related to BAV are found in the ascending aorta, further in-depth sub-analysis of the ascending aorta was carried out. To do this, the section of aorta between the sinotubular junction and the brachiocephalic artery was analysed in isolation. In order to look for asymmetry and differences in wall indices on different sides of the aorta, further sub-analysis was performed by dividing the tubular ascending aorta into 8 anatomical sectors (see [Figure 3.19](#)). This divided the ascending aorta into anterior (A), right-anterior (RA), right (R), right-posterior (RP), posterior (P), left-posterior (LP), left (L), and left-anterior (LA) sectors.

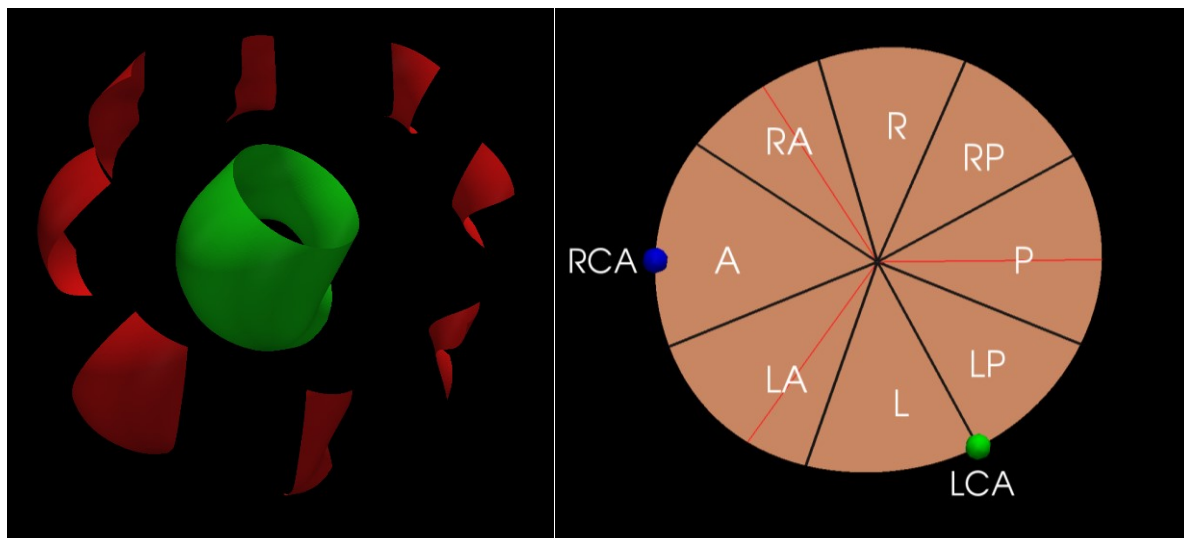
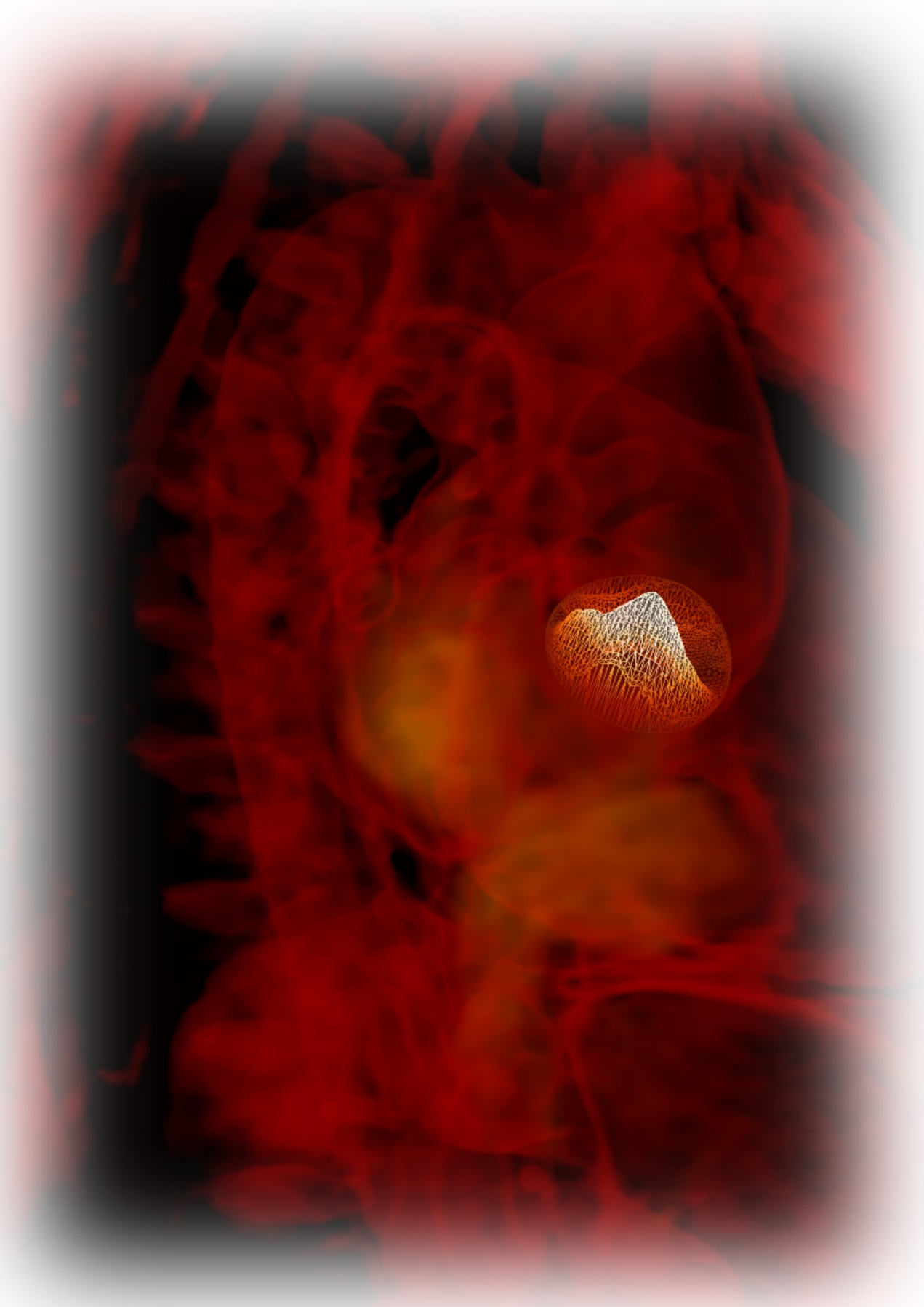


Figure 3.19. Division of the ascending aorta into 8 longitudinal sectors. A = anterior; RA = right-anterior; R = right; RP = right-posterior; P = posterior; LP = left-posterior; L = left; LA = left-anterior; RCA = right coronary artery; LCA = left coronary artery

WSS was measured throughout the cardiac cycle in the thoracic aorta, ascending aorta, and the 8 sectors of the ascending aorta. WSS_{max} was the highest value of WSS at peak systole. Mean wall shear stress (MWSS) was the WSS averaged over the cardiac cycle (time-averaged), and was similarly measured for the thoracic aorta, ascending aorta, and the 8 ascending aorta sectors. OSI was measured in an anatomically analogous fashion. The results were visualised using ParaView (Kitware, Inc., Clifton Park, NY).

When measuring WSS or MWSS for the 8 anatomical sectors, data from all data points (nodes) within that sector were integrated, and then divided by the area of that sector, to give the averaged WSS for that sector (at each time point of the cardiac cycle) and the averaged MWSS for that sector (across the entire cardiac cycle).

The methodology outlined in this chapter is general to the entire work. Further specific methodology relevant to each chapter will be described for the following 4 studies.



4

STUDY 1:

Impact of Patient-Specific Inflow Velocity Profile on Haemodynamics of the Thoracic Aorta

“A journey of a thousand miles begins with one step.”

Lao Tzu, 4th Century B.C.

Contents

4.1	Overview	121
4.2	Background	121
4.3	Methods	127
4.4	Study 1A Results: Flow Characteristics	132
4.5	Study 1B Results: Wall Mechanics	151
4.6	Summary	164

4.1 OVERVIEW

This first of four results chapters will compare patient-specific inflow velocity profiles (using the novel methodology proposed in this thesis) with idealised inflow velocity profiles (typically used in previous studies for the inflow boundary conditions). The effect of these different inflow boundary conditions on haemodynamics and mechanics of the thoracic aorta will be studied in detail.

Study 1A will look at the impact on flow characteristics, such as velocity patterns and waveforms, helicity, streamlines and pathlines, flow asymmetry, and flow dispersion. Study 1B will look in detail at aortic wall mechanics such as wall shear stress and oscillatory shear index.

4.2 BACKGROUND

Most CFD studies to date have used idealised velocity profiles for the inflow boundary conditions. Such studies have modelled inflow boundary conditions using simple profiles (such as parabolic or plug), measuring only a few in-vivo velocity parameters such as peak velocity, average velocity or flow rate (Campbell et al. 2012). Additionally, numerous studies have used inflow data acquired from another source altogether (typically literature), as the utilised imaging modality did not provide blood flow data (e.g., computed tomography). Some studies have even performed CFD with non-physiological inflow boundary conditions, such as non-pulsatile constant pressure (Nathan et al. 2011).

The need for accurate inflow boundary conditions is particularly important in the thoracic aorta. The natural anatomic inlet boundary of the thoracic aorta is the aortic valve, the gatekeeper between the heart and the systemic circulation. The complexity of this trileaflet valve, along

with its ring-like annulus, sinuses and feeding coronary arteries, may lead to highly intricate flow patterns entering the ascending aorta (Sigovan et al. 2015), far from the idealised profiles used traditionally. Therefore, it might be expected that use of idealised velocity profiles, which do not take into account different aortic valve morphologies, would be inappropriate for the study of thoracic aorta hemodynamics, and yield inaccurate CFD results.

A few studies have investigated the effect of using patient-specific inlet velocity profiles on CFD-simulated haemodynamics of the abdominal aorta (Chandra et al. 2013), carotid arteries (Campbell et al. 2012), cerebral arteries (Marzo et al. 2009), and coronary arteries (Myers et al. 2001). Recently, a study by Morbiducci et al. (Morbiducci et al. 2013) assessed the effect of inlet boundary conditions on the thoracic aorta of a healthy subject, and found that idealised boundary conditions can lead to misleading results.

The aim of this study is to assess the impact of MRI-based, patient-specific inflow velocity profiles as compared to idealised inflow velocity profiles (based on the patient's flow rate) in CFD simulations of thoracic aortic haemodynamics of both healthy and diseased states. The idealised velocity profiles correspond to parabolic and plug patterns, which are the most commonly used in the literature (Campbell et al. 2012, Mynard et al. 2013).

4.2.1 Idealised Velocity Profiles

In this study, we assigned idealised velocity profiles based on the subject's measured flow rate waveform (from Flow-MRI data above the aortic valve), and compared the haemodynamic results with patient-specific velocity profiles. We employed the commonly used *parabolic* and *plug* velocity profiles. To do this, we needed to satisfy the conservation of mass principle:

$$\dot{m} = \rho V_{avg} A_c = \int_{A_c} \rho u(r) dA_c$$

where \dot{m} = mass flow rate, ρ is the density, A_c is the cross-sectional area, $u(r)$ is the velocity profile. Then the average velocity for incompressible flow in a pipe of radius R can be expressed as:

$$V_{avg} = \frac{\int_{A_c} \rho u(r) dA_c}{\rho A_c} = \frac{\int_0^R \rho u(r) 2\pi r dr}{\rho \pi R^2} = \frac{2}{R^2} \int_0^R u(r)r dr$$

(Eq 4 – 1)

Therefore, by knowing the flow rate or the velocity profile, the average velocity can be determined (Munson et al. 2009).

Whether flow is truly laminar or turbulent depends on the Reynolds Number, a dimensionless ratio of inertial forces and viscous forces for internal flow in a pipe:

$$Re = \frac{\text{Inertial forces}}{\text{Viscous forces}} = \frac{V_{avg}D}{\nu} = \frac{\rho V_{avg}D}{\mu}$$

Where V_{avg} = average flow velocity, D = diameter of pipe, $\nu = \mu / \rho$ = kinematic viscosity of the fluid. The Reynolds Number at which flow becomes turbulent is called the Critical Reynolds Number, Re_{cr} , which is 2300 for a circular pipe (i.e. flow is laminar when $Re < 2300$, and turbulent when $Re > 2300$).

In fully developed laminar flow, each fluid particle moves along a streamline at a constant axial velocity. Flow is axisymmetric and free from swirl or helical components. The velocity profile $u(r)$ remains the same in the flow direction. The fluid velocity in a pipe changes from zero at the wall (because of the no-slip conditions), to a maximum velocity at the pipe centre (Munson et al. 2009).

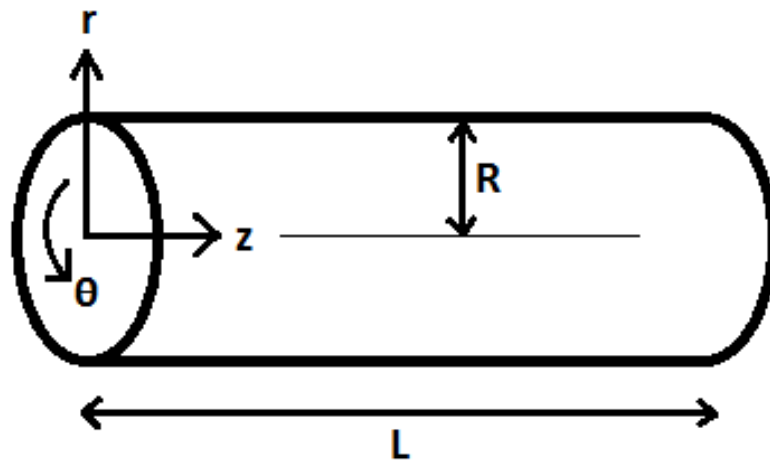


Figure 4.1. Poiseuille flow geometry in a pipe. The geometry of the coordinate system has its origin on the centre-line of the pipe entrance. r = radial coordinate, θ = angular coordinate, z = coordinate aligned with centre-line of the pipe, R = pipe radius, L = pipe length.

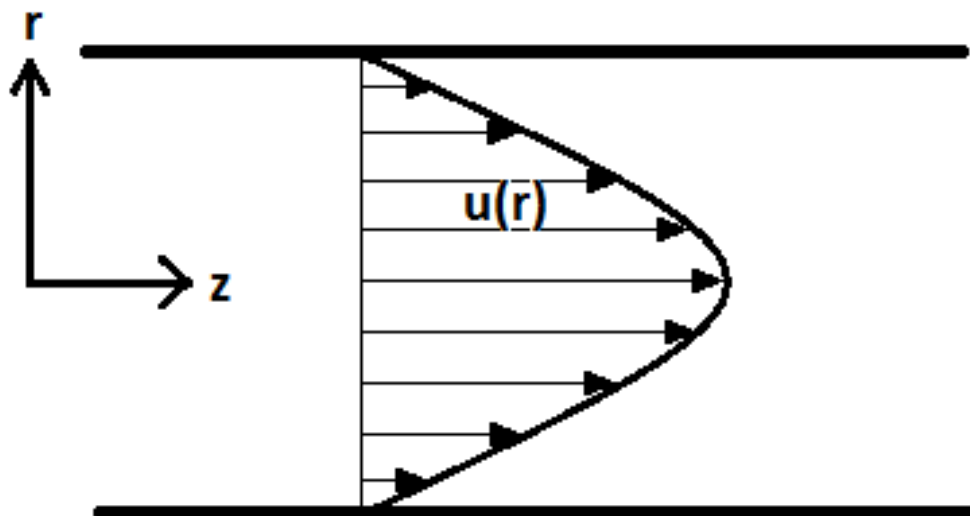


Figure 4.2. Parabolic velocity profile.

The velocity profile $u(r)$ is obtained by applying boundary conditions such as $du/dr = 0$ at $r = 0$ (because of axisymmetric flow), and $u = 0$ at $r = R$ (due to the no-slip conditions). Thus:

$$u(r) = -\frac{R^2}{4\mu} \left(\frac{dP}{dx} \right) \left(1 - \frac{r^2}{R^2} \right)$$

(Eq. 4 – 2)

Thus the velocity profile in fully developed laminar flow is *parabolic* in shape, with u_{max} at the centre of the pipe, and zero velocity at the wall. The average velocity is acquired by combining Equations 4-1 and 4-2 and integrating:

$$V_{avg} = \frac{2}{R^2} \int_0^R u(r)r \, dr = -\frac{2}{R^2} \int_0^R \frac{R^2}{4\mu} \left(\frac{dP}{dx} \right) \left(1 - \frac{r^2}{R^2} \right) r \, dr = -\frac{R^2}{8\mu} \left(\frac{dP}{dx} \right)$$

(Eq. 4 – 3)

Combining Equations 4-2 and 4-3, the velocity profile is modified to:

$$u(r) = 2V_{avg} \left(1 - \frac{r^2}{R^2} \right)$$

This means that V_{avg} and the *parabolic* velocity profile can easily be acquired from the flow rate waveform data from Flow-MRI (Munson et al. 2009).

As flow becomes more turbulent, the profile becomes less parabolic in shape, and more flat. The velocity of the fluid is more constant across the cross-section of the pipe, except for at the

wall where it drops sharply. If considering turbulent flow in detail along the wall, 4 regions can be characterised according to their distance from the wall. These are the viscous sublayer, buffer layer, overlap layer and turbulent layer (see Figure 4.3). There is high variability of flow characteristics in different areas of the pipe, and thus it is not as straightforward to define an analytical relationship for the velocity profile as there is for the laminar parabolic profile. Instead, a simple model of a *plug* profile is defined by the velocity of the fluid being assumed to be constant across any cross-section of the pipe perpendicular to the axis of the pipe, with a further assumption that there is no boundary layer adjacent to the inner wall of the pipe.

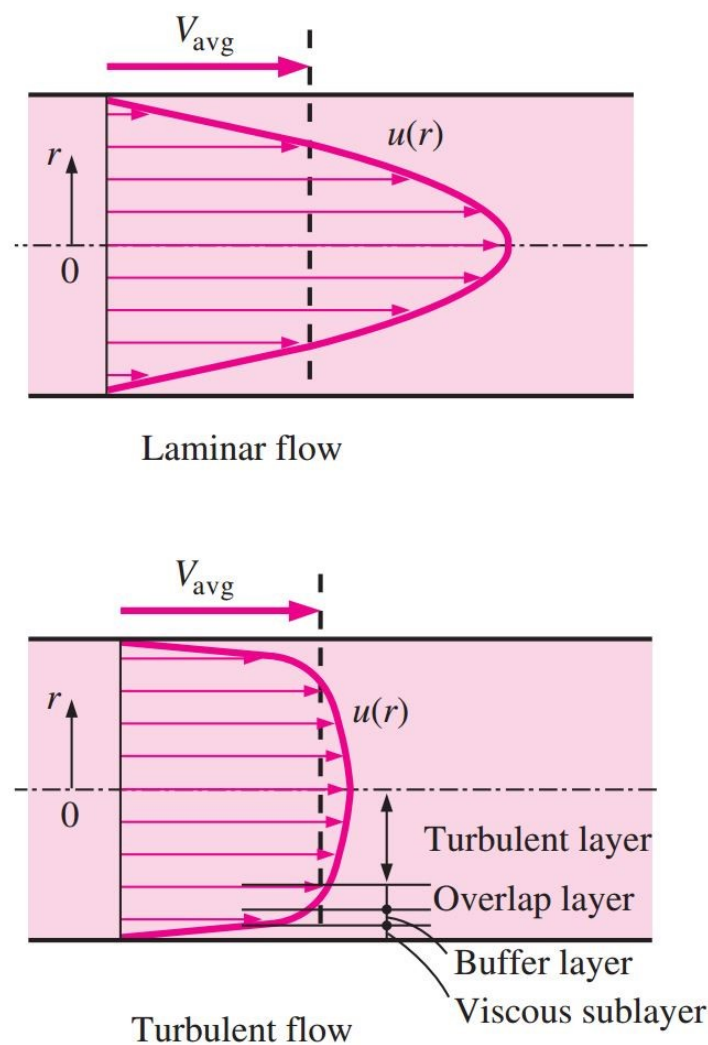


Figure 4.3. Parabolic velocity profile in a fully developed pipe flow (above); flatter velocity profile in turbulent flow (below). (Munson et al. 2009)

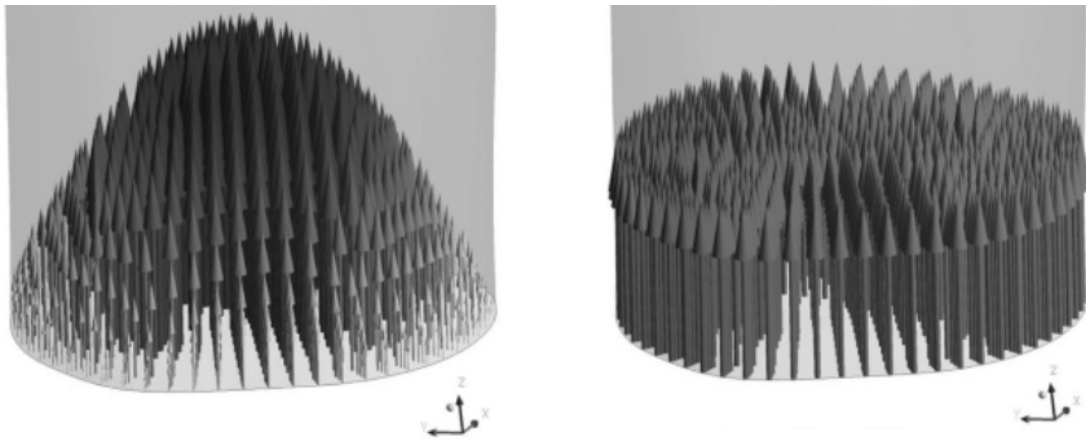


Figure 4.4. Velocity vectors (arrows pointing up) showing the parabolic (left) and plug (right) velocity profile shapes in 3-dimensions. (Campbell et al. 2012)

4.3 METHODS

Four subjects with different aortic valve morphologies were studied: a tricuspid aortic valve subject with normal valve morphology (*TAV*) was studied. Three BAV subjects with different aortic valve morphologies/pathologies were also studied. All had fusion of the right and left coronary cusps (the commonest BAV fusion pattern (Roberts 1970)), and are given the following abbreviations: *AS-BAV* – severe aortic stenosis; *AR-BAV* – severe aortic regurgitation; *N-BAV* – no stenosis or regurgitation. Diagnosis of severe aortic stenosis or regurgitation was based on trans-thoracic echocardiographic data, according to international guidelines (Vahanian et al. 2012).

This study was divided into 2 parts. Study 1A compared the effects of patient-specific versus idealised velocity profiles (parabolic and plug) on flow characteristics in the thoracic aorta. The indices investigated included velocity patterns and waveforms, helicity, streamlines and

pathlines, flow asymmetry, and flow dispersion. Two of the 4 subjects were assessed in Study 1A: *TAV* and *AS-BAV*. For both subjects, CFD was carried out using *patient-specific* inflow velocity profiles, idealised *parabolic* inflow velocity profiles, and idealised *plug* inflow velocity profiles. These 2 subjects were chosen for Study 1A as they represented two different aortic valves on opposite ends of the morphology spectrum, and would therefore be suitable for an in-depth exploration of the impact of patient-specific versus idealised inflow velocity profiles on flow characteristics.

Study 1B compared the effect of inflow velocity profiles on aortic wall mechanics, in particular WSS and OSI. All 4 subjects were studied: *TAV*, *AS-BAV*, *AR-BAV*, and *N-BAV*. For all 4 subjects, CFD was carried out using *patient-specific* inflow velocity profiles and idealised *parabolic* inflow velocity profiles.

Table 4.1. Demographics, aortic dimensions and Windkessel outlet boundary condition parameters. MAA = mid-ascending aorta; R_p = proximal resistance; R_d = distal resistance; C = capacitance. The units of resistance are 10^3 dynes s / cm^5 . The units of capacitance are 10^{-6} cm^5 / dynes.

	<i>AS-BAV</i>	<i>AR-BAV</i>	<i>N-BAV</i>	<i>TAV</i>
<i>Demographics</i>				
Sex	Male	Male	Male	Male
Age	52	62	28	32
Hypertension	Yes	Yes	No	No
Blood Pressure (mmHg)	120/85	130/75	135/85	120/80
B-blockers	No	Yes	Yes	No
ACEi/ARBs	Yes	Yes	No	No
<i>Aortic Dimensions</i>				
MAA diameter (mm)	44	45	58	24
Aortic Size Index (cm/m^2)	2.16	2.09	2.51	1.38
Svensson Index (cm^2/m)	8.9	8.2	14.8	2.7
<i>Windkessel Outlet Boundary Conditions</i>				
Brachiocephalic Artery				
R_p	0.79	0.25	0.33	1.36
R_d	18.2	4.61	3.53	9.23
C	28.2	69.7	74.0	48.3
Left Common Carotid Artery				
R_p	1.15	0.96	0.52	2.46
R_d	24.9	14.6	5.23	15.3
C	20.5	21.8	50.0	29.2
Left Subclavian Artery				
R_p	1.29	0.73	0.39	1.74
R_d	27.6	11.6	4.12	11.3
C	18.6	27.6	63.4	39.3
Descending Aorta				
R_p	0.17	0.07	0.08	0.25
R_d	4.69	1.54	1.15	2.14
C	109	207	227	208

4.3.1 Study Population

Subjects underwent CMR and MRA to image the entire thoracic aorta in accordance with Section 2.2.1. Slice thickness was 2.0 mm, with 60 sagittal slices per volume. Time-resolved, 2D through-plane flow-MRI was acquired orthogonally in the ascending aorta at the sino-tubular junction. Heart rates ranged between 60-85 bpm during which 30 images were reconstructed. The encoding velocity constant (V_{enc}) was set to 5000 mm/s in order to ensure no aliasing in subject *AS-BAV*, and 3000 mm/s in subjects *TAV*, *N-BAV* and *AR-BAV*. Imaging parameters were those described in Section 2.2.2.

Segmentation and meshing was carried out as defined in Sections 2.3.1 and 2.3.2. This resulted in a final anisotropic mesh consisting of approximately 2 – 5 million tetrahedral elements and 300,000 – 600,000 nodes for the different subjects.

Blood flow simulations were carried out using a stabilised finite element formulation using a global residual tolerance 0.001 and time-step size of 0.00025 s. Four to six cardiac cycles were produced until cycle-to-cycle periodicity in the flow and pressure fields was achieved. The last cardiac cycle was used for the purpose of data analysis for each subject.

The outflow boundary conditions were specified using a coupled-multi-domain method (Figuerola et al. 2006, Vignon-Clementel et al. 2006) in which 3-element Windkessel models were coupled to each outflow branch (e.g., innominate artery, left common carotid artery, left subclavian artery, and descending aorta) (Vignon-Clementel et al. 2010). Flow splits were estimated based on the relative cross-sectional area of each outlet. The mean outflow pressure for each outlet was assumed to be equal to that measured by the Dinamap device. The Windkessel parameters were estimated following the procedure described in Xiao et al. (Xiao et al. 2014). [Table 4.1](#) above gives the numerical values of these parameters for each branch.

4.3.2 Inflow Velocity Profile

We compared the results obtained using patient-specific (PS) velocity profiles with those obtained using idealised velocity profiles (parabolic and plug) mapped to the flow data of the subject. We refer to the three different inflow velocity profiles as: (i) V_{PS} ; (ii) V_{para} and (iii) V_{plug} . An in-house software written in *Matlab* (*The Mathworks Inc., Massachusetts, USA*) was used to extract velocity profiles from the flow-MRI images. This software allows the user to extract both the velocity profile V_{PS} and flow rate waveform from the PC-MRI images. The flow rate waveform was used to assign the 2 idealised velocity profiles (V_{para} and V_{plug}). The theoretical background for this process has already been described (Section 4.2.1). As for V_{PS} , the flow-MRI data was segmented and mapped onto the inlet mesh according to Sections 3.4.3 – 3.4.5.

4.3.3 Quantification of Flow Characteristics

2D and 3D visualisations of the velocity magnitude, and radial (in-plane) velocity vectors were extracted from the simulation data at three planes along the axis of the thoracic aorta. Plane 1 corresponds to the mid-ascending aorta, plane 2 to the transverse aortic arch, and plane 3 to mid-descending aorta. Radial velocity was assessed by measuring the component of the velocity vectors perpendicular to the long axis of the aorta at each plane. The radial velocities enable the estimation of non-axial helical flow. Particle streamlines offering three-dimensional visualisation of evolving aortic flow were calculated from temporally resolved velocity data for the entire thoracic aorta. Immaterial particle pathlines were calculated from temporally resolved velocity data for the entire thoracic aorta. Haemodynamic quantities were visualised using ParaView (Kitware, Inc., Clifton Park, NY). The following quantitative indices of flow

morphology were obtained: flow asymmetry ($\text{Flow}_{\text{asymmetry}}$), flow dispersion ($\text{Flow}_{\text{dispersion}}$) and helical flow index (HFI).

4.3.4 Quantification of Wall Mechanics

WSS and Oscillatory Shear Index (OSI) were measured for the entire thoracic aorta. Since the ascending aorta is the commonest site of aneurysm formation in BAV patients, further sub-analysis of the ascending aorta was undertaken. For each subject, the ascending aorta was divided into 8 sectors anatomically (anterior (A), right-anterior (RA), right (R), right-posterior (RP), posterior (P), left-posterior (LP), left (L), and left-anterior (LA) sectors).

Mean wall shear stress (MWSS) is the WSS averaged over the cardiac cycle (time-averaged). To compare differences in MWSS between V_{PS} and V_{para} velocity profiles, a point-by-point comparison of MWSS was carried out at each data node of the aortic models. At each node, % difference in MWSS was calculated between the patient-specific and parabolic simulations. To assess the differences more easily, the surface area of the aortic wall where the two respective BAV and TAV simulations had MWSS values within -25% and +25% of each other were visualised, and taken as a percentage of the total surface area (see [Figures 4.20 – 4.23](#)).

4.4 STUDY 1A RESULTS: FLOW CHARACTERISTICS

4.4.1 Velocity Patterns

[Figure 4.5](#) shows the inflow velocity profiles for subjects *TAV* and *AS-BAV* at peak systole. Despite having a slightly higher flow rate, *TAV* displays a profile ($V_{\text{PS}}^{\text{TAV}}$) with a lower velocity and broader pattern compared to subject B ($V_{\text{PS}}^{\text{AS-BAV}}$). There is some similarity in both

magnitude and 3D visualisation between V_{PS}^{TAV} and V_{para}^{TAV} , however V_{plug}^{TAV} is clearly different. Conversely, the high velocity and narrow eccentric profile of V_{PS}^{AS-BAV} bears no resemblance to that of V_{para}^{AS-BAV} or V_{plug}^{AS-BAV} .

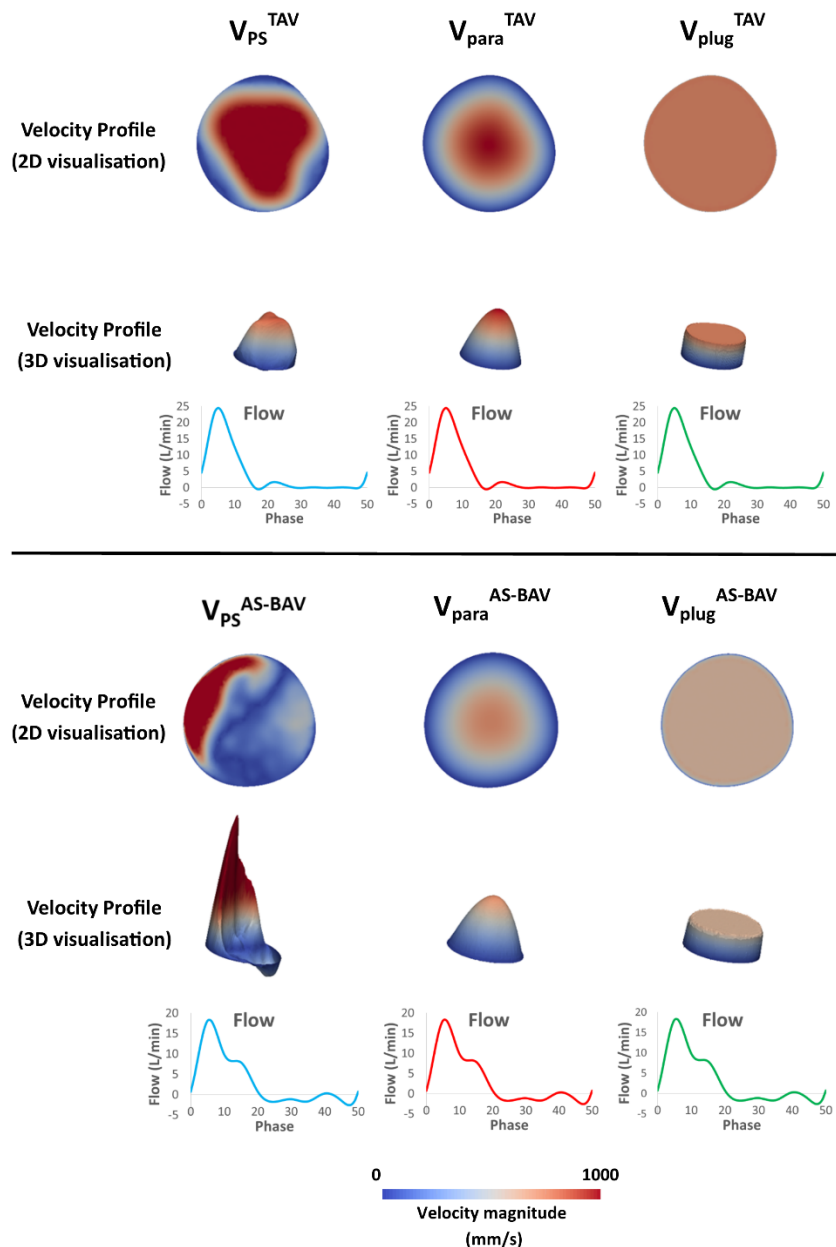


Figure 4.5. Inflow boundary conditions for subject *TAV* (above) and subject *AS-BAV* (below). 2D and 3D visualisations of the patient-specific (V_{PS}), parabolic (V_{para}), and plug (V_{plug}) velocity magnitude (first and second rows, respectively) at peak systole. The 3D visualisation of the velocity magnitude was obtained by warping the measured through-plane phase contrast data by a factor of 0.02.

Figures 4.6 – 4.11 depict 2D and 3D visualisations of the velocity magnitude, and radial velocity vectors at three different aortic locations (mid-ascending, transverse arch and mid-descending) at early, peak, and late systole for subjects *TAV* and *AS-BAV*, respectively.

In the mid-ascending aorta (plane 1) of *TAV*, the velocity maps and velocity profiles of V_{PS}^{TAV} and V_{para}^{TAV} are similar throughout the 3 phases of systole. The solution obtained with V_{plug}^{TAV} is however different for all time points except for early systole. In the transverse aortic arch (plane 2), V_{PS}^{TAV} , V_{para}^{TAV} and V_{plug}^{TAV} all show similar velocity maps and profiles for early and peak systole, but not for late systole. Lastly, in the mid-descending aorta (plane 3) V_{PS}^{TAV} , V_{para}^{TAV} and V_{plug}^{TAV} all show similar velocity maps throughout systole.

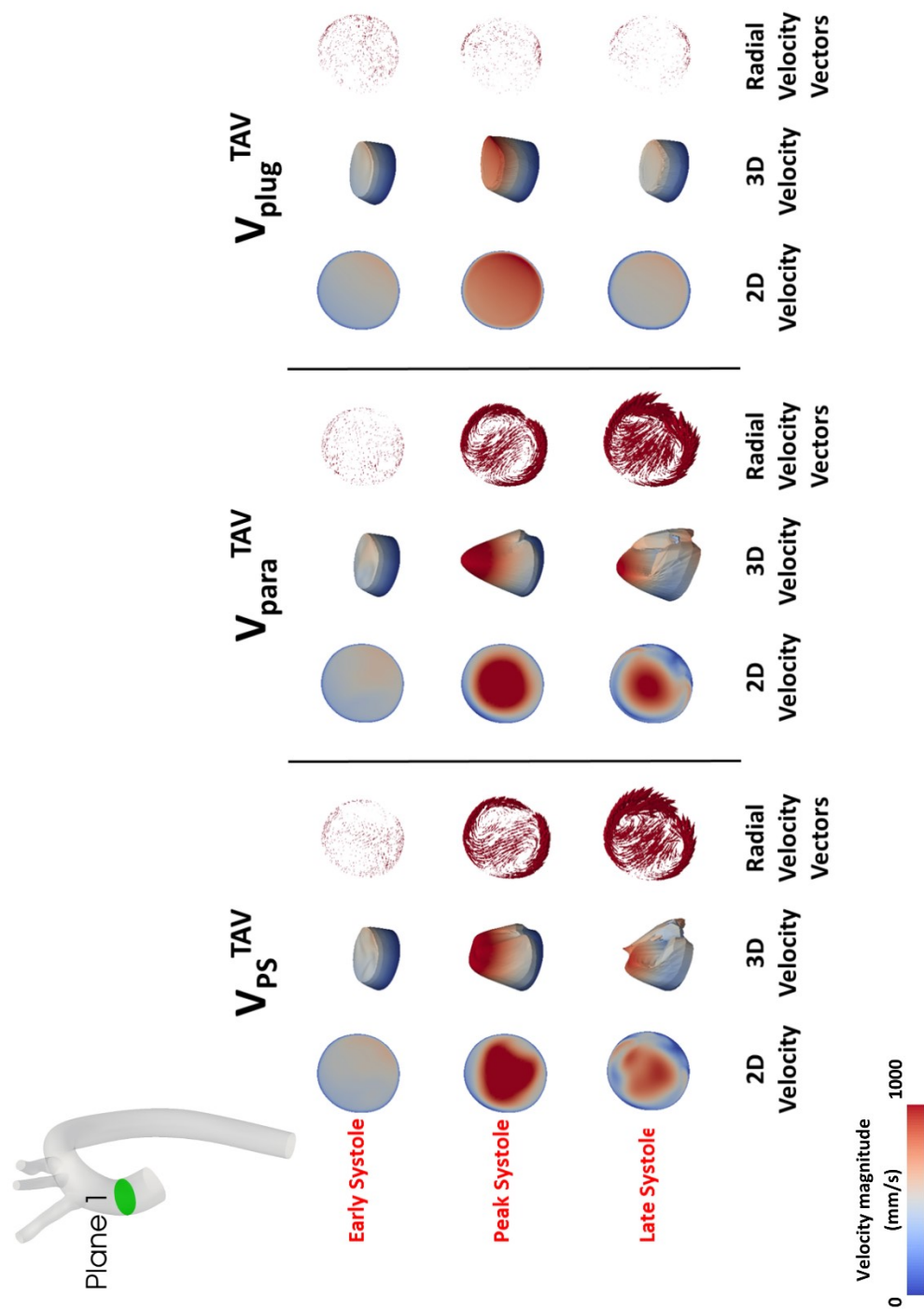


Figure 4.6. 2D and 3D representations of velocity magnitude, and radial (e.g. in-plane) velocity components at 3 planes of the thoracic aorta for subject TAV. Plane 1 corresponds to mid-ascending aorta.

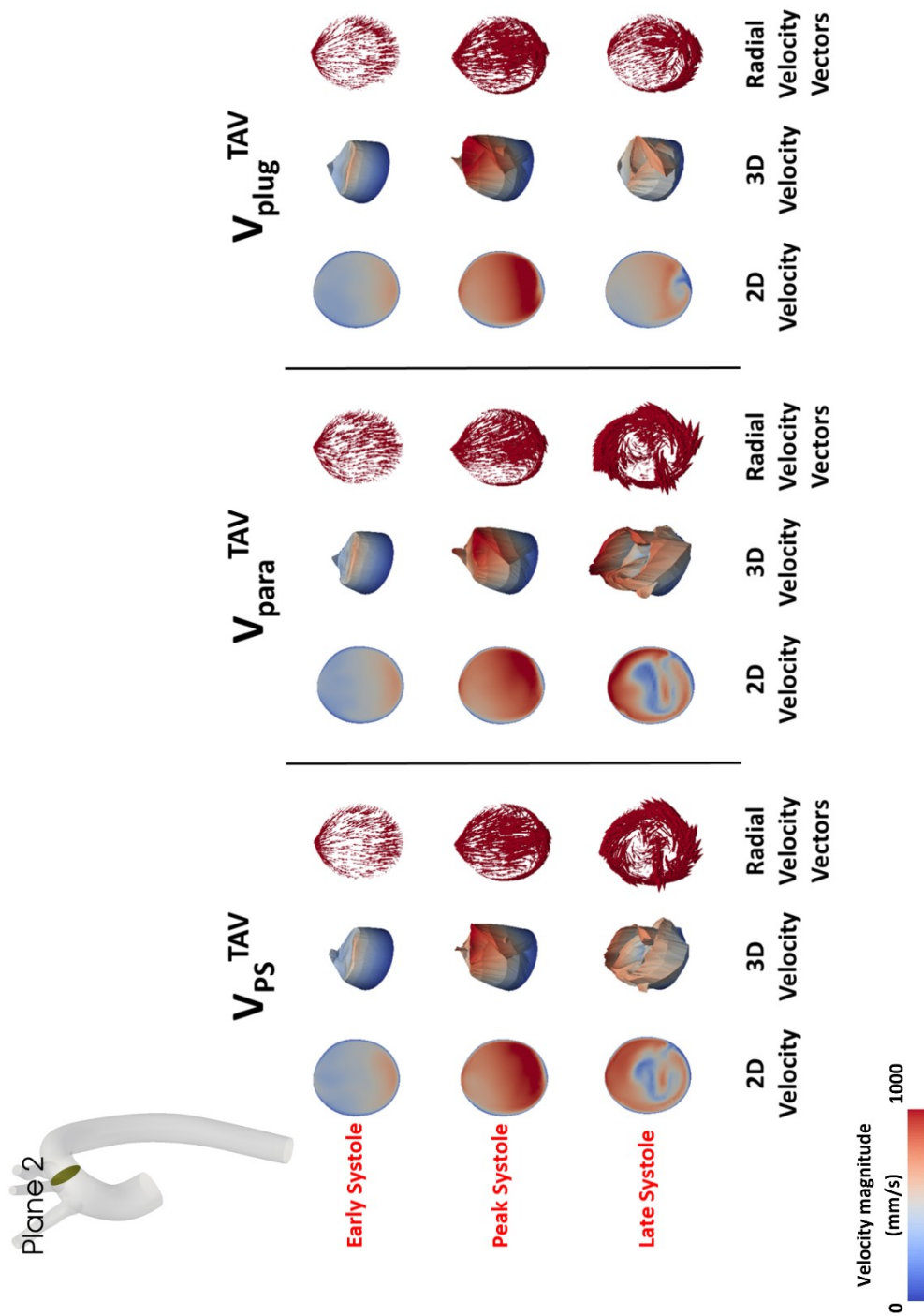


Figure 4.7. 2D and 3D representations of velocity magnitude, and radial (e.g. in-plane) velocity components at 3 planes of the thoracic aorta for subject *TAV*. Plane 2 corresponds to mid-arch.

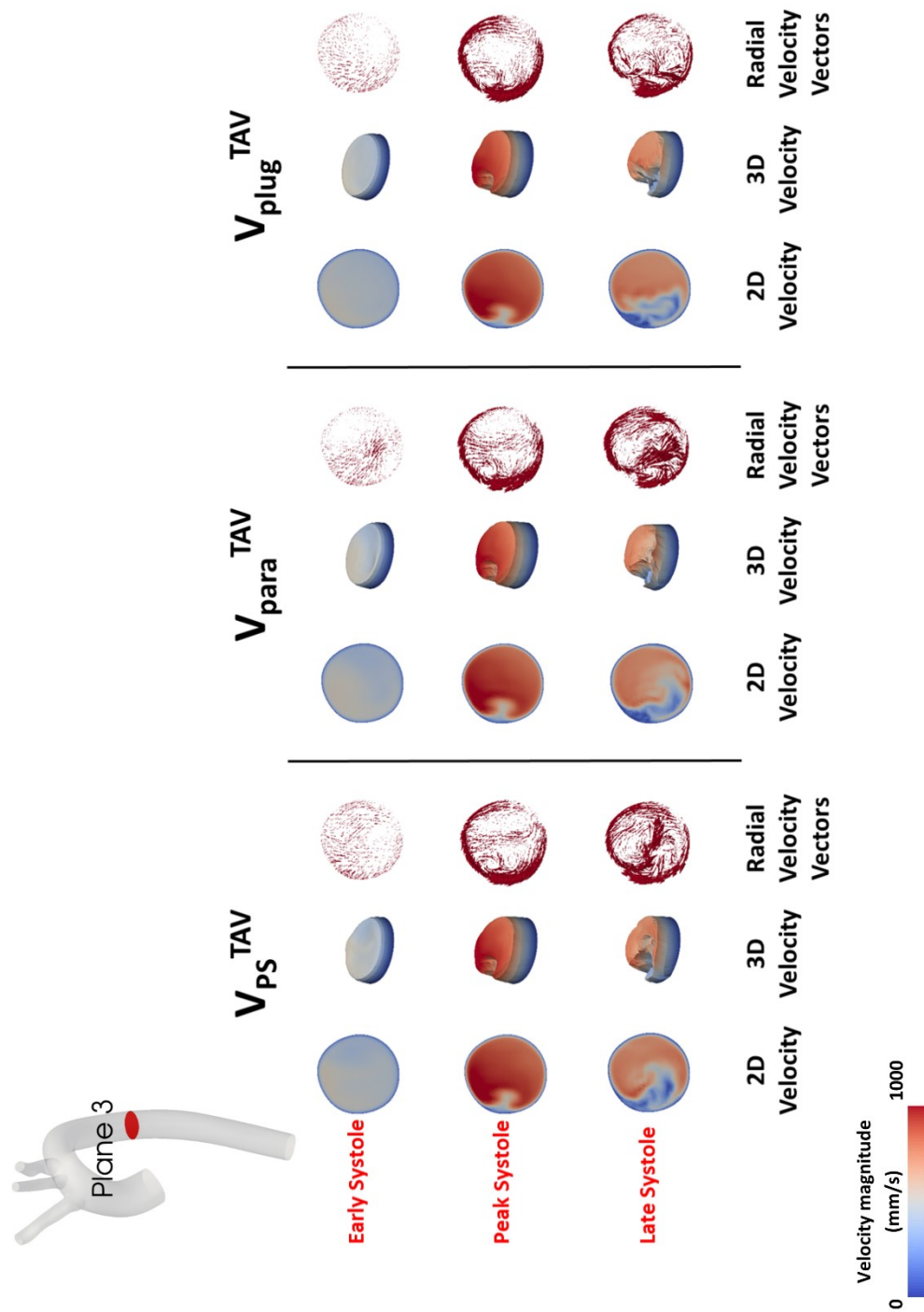


Figure 4.8. 2D and 3D representations of velocity magnitude, and radial (e.g. in-plane) velocity components at 3 planes of the thoracic aorta for subject TAV. Plane 3 corresponds to mid-descending aorta.

For *AS-BAV*, the differences introduced by the different inflow velocity profiles (V_{PS}^{AS-BAV} , V_{para}^{AS-BAV} , V_{plug}^{AS-BAV}) extend through most of the length of the thoracic aorta. **Figure 3.9** reveals high velocity profiles in the patient-specific profile simulation (V_{PS}^{AS-BAV}) in the ascending aorta (plane 1) at the lumen periphery (2D visualisation), and highly distorted and twisted flow (3D visualisation). On the other hand, V_{para}^{AS-BAV} and V_{plug}^{AS-BAV} show a relatively even distribution of velocities over the cross-section of the lumen. These differences are seen to continue along the transverse aortic arch (plane 2). As we go further to the descending aorta (plane 3), the velocity magnitude and profile becomes virtually identical throughout the 3 phases of systole between V_{PS}^{AS-BAV} , V_{para}^{AS-BAV} , and V_{plug}^{AS-BAV} .

Figures 4.6 – 4.11 also show the radial velocity vectors at the three aortic locations. Comparison of the vector direction and size is made for both subjects and for each inflow velocity profile. **Figures 4.6 – 4.8** show that V_{PS}^{TAV} and V_{para}^{TAV} show similar radial velocity vectors throughout all 3 planes of the thoracic aorta. V_{plug}^{TAV} shows very different profiles in peak and late systole in plane 1, however these differences become smaller during early and peak systole in plane 2. By plane 3, all 3 simulations shows similar radial velocity vectors throughout the cardiac cycle.

Figures 4.9 – 4.11 show that V_{PS}^{AS-BAV} has large radial vectors circulating around the lumen in a helical fashion. These vectors are different in direction and size to the radial vectors obtained with V_{para}^{AS-BAV} and V_{plug}^{AS-BAV} , and remain so for all aortic locations.

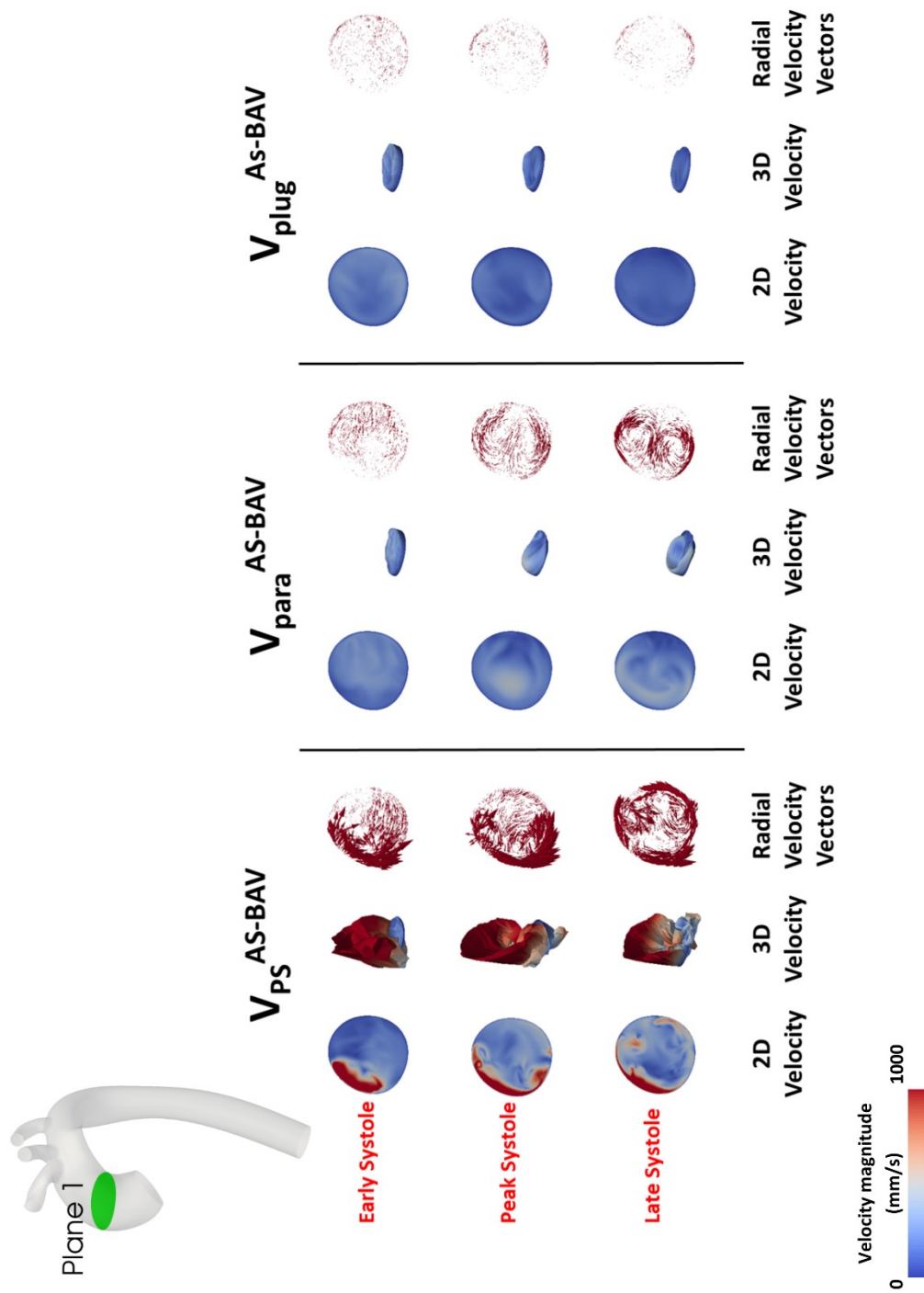


Figure 4.9. 2D and 3D representations of velocity magnitude, and radial (e.g. in-plane) velocity components at 3 planes of the thoracic aorta for subject *AS-BAV*. Plane 1 corresponds to mid-ascending aorta.

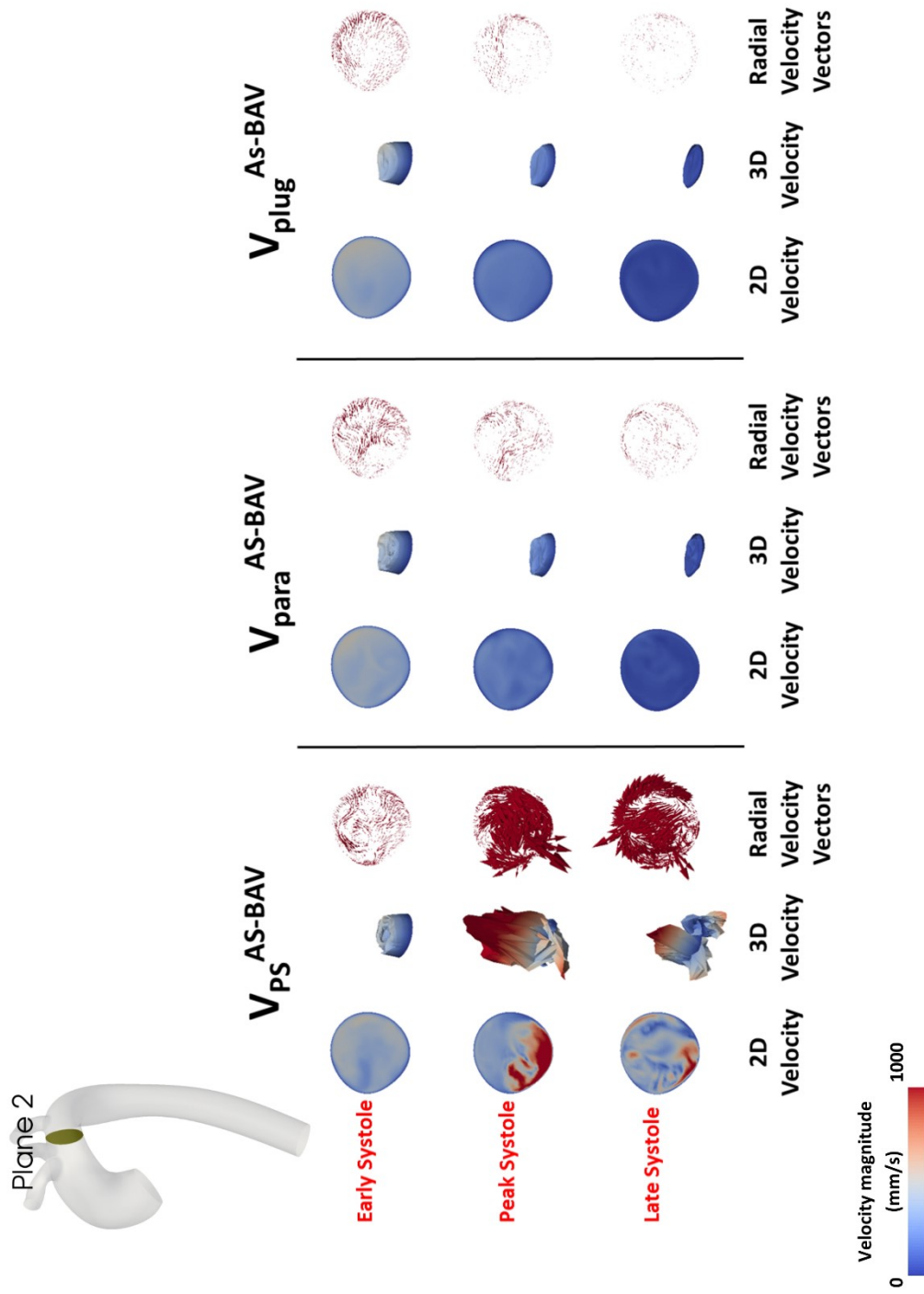


Figure 4.10. 2D and 3D representations of velocity magnitude, and radial (e.g. in-plane) velocity components at 3 planes of the thoracic aorta for subject *AS-BAV*. Plane 2 corresponds to mid-arch.

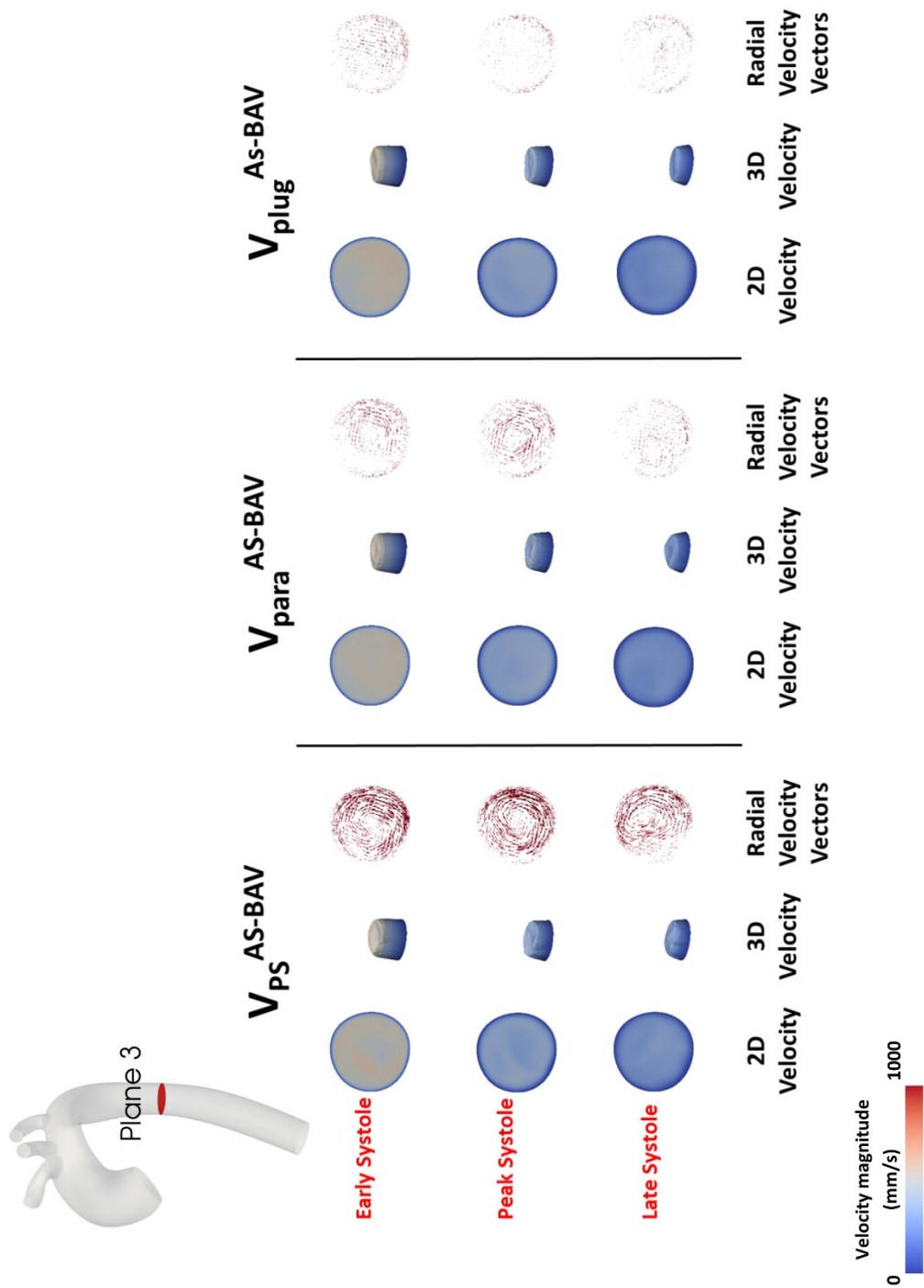


Figure 4.11. 2D and 3D representations of velocity magnitude, and radial (e.g. in-plane) velocity components at 3 planes of the thoracic aorta for subject *AS-BAV*. Plane 2 corresponds to mid-descending aorta.

4.4.2 Velocity Magnitude Waveforms

Figure 4.12 depicts waveforms for the maximum through-plane velocity (V_{\max}), maximum radial velocity and total flow for each of the 3 planes (mid-ascending, transverse aortic arch and mid-descending) for subjects *TAV* and *AS-BAV*.

For *TAV*, despite having identical flow rates for the 3 simulations, $V_{\text{plug}}^{\text{TAV}}$ clearly underestimates V_{\max} in the mid-ascending aorta and aortic arch compared to $V_{\text{PS}}^{\text{TAV}}$. Conversely, $V_{\text{para}}^{\text{TAV}}$ slightly overestimates V_{\max} in the ascending aorta and transverse aortic arch. The relative differences between radial velocities are much more apparent: $V_{\text{plug}}^{\text{TAV}}$ clearly underestimates this component compared to $V_{\text{PS}}^{\text{TAV}}$ and $V_{\text{para}}^{\text{TAV}}$, particularly in the ascending aorta. $V_{\text{para}}^{\text{TAV}}$ overestimates radial velocities in plane 1 relative to $V_{\text{PS}}^{\text{TAV}}$, and produces similar radial velocity profiles in planes 2 and 3.

As for *AS-BAV*, both $V_{\text{para}}^{\text{AS-BAV}}$ and $V_{\text{plug}}^{\text{AS-BAV}}$ grossly underestimate V_{\max} when compared to $V_{\text{PS}}^{\text{AS-BAV}}$ in planes 1 and 2. By plane 3, V_{\max} for $V_{\text{PS}}^{\text{AS-BAV}}$ declines and produces almost identical solutions as $V_{\text{para}}^{\text{AS-BAV}}$ and $V_{\text{plug}}^{\text{AS-BAV}}$. This correlates with the development of similar through-plane velocity patterns and profiles amongst all 3 simulations in plane 3 (Figure 4.11). As for the radial velocity profiles, $V_{\text{PS}}^{\text{AS-BAV}}$ shows significantly higher velocities compared to the idealised profiles throughout the aorta. This is consistent with the size of radial vectors seen in Figures 4.8 – 4.11. It is interesting to note that in plane 3, despite all three simulations having almost identical through-plane V_{\max} values, $V_{\text{PS}}^{\text{AS-BAV}}$ shows radial velocities twice as large compared to $V_{\text{para}}^{\text{AS-BAV}}$ and $V_{\text{plug}}^{\text{AS-BAV}}$.

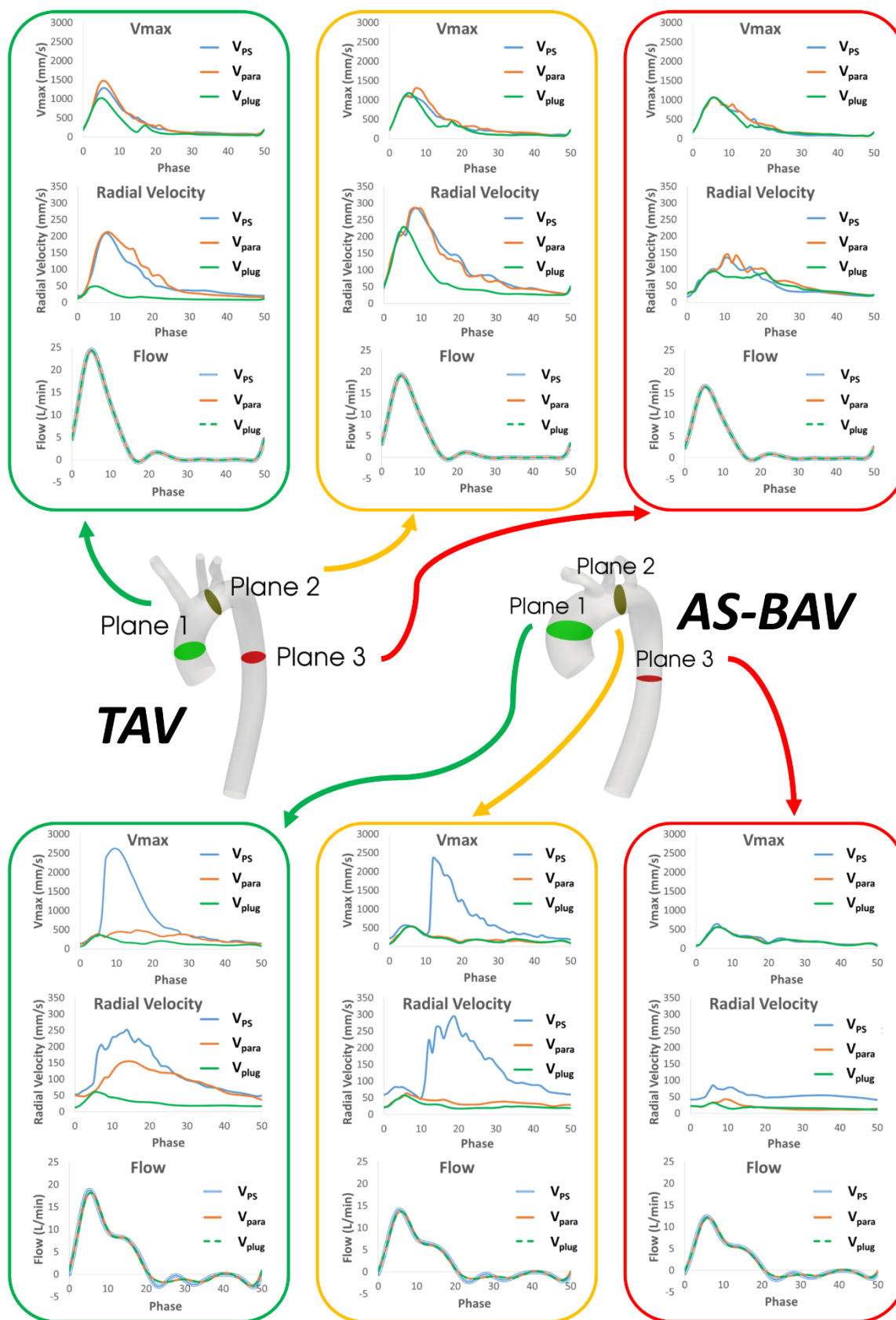


Figure 4.12. Maximal through-plane velocity (V_{max}), radial velocity and flow rate along the cardiac cycle at 3 planes for subjects *TAV* and *AS-BAV*.

4.4.3 Helicity

Table 4.2 shows the values for HFI during systole and diastole. For subject *TAV*, HFI was significantly underestimated by $V_{\text{plug}}^{\text{TAV}}$, but also (to a lesser degree) by $V_{\text{para}}^{\text{TAV}}$. For subject *AS-BAV*, HFI was similar for all 3 simulations.

Table 4.2. Helical Flow Index during systole, diastole, and the whole cardiac cycle for the thoracic aorta for particles which traversed the aorta and left the simulation domain through the descending aortic boundary.

	$V_{\text{PS}}^{\text{TAV}}$	$V_{\text{para}}^{\text{TAV}}$	$V_{\text{plug}}^{\text{TAV}}$	$V_{\text{PS}}^{\text{AS-BAV}}$	$V_{\text{para}}^{\text{AS-BAV}}$	$V_{\text{plug}}^{\text{AS-BAV}}$
HFI_{syst}	0.49	0.44	0.37	0.48	0.48	0.48
HFI_{diast}	0.49	0.44	0.37	0.50	0.51	0.51
HFI_{cycle}	0.49	0.44	0.37	0.49	0.49	0.50

4.4.4 Velocity Streamlines

Figure 4.13 depicts three-dimensional peak systolic velocity streamlines for both subjects. For subject *TAV*, $V_{\text{PS}}^{\text{TAV}}$ and $V_{\text{para}}^{\text{TAV}}$ show similar streamline patterns of vortical flow starting in the ascending aorta. By comparison, $V_{\text{plug}}^{\text{TAV}}$ shows parallel streamline. For subject *AS-BAV*, $V_{\text{PS}}^{\text{AS-BAV}}$ shows a corkscrew band of high velocity (seen in red) spiralling along the ascending aorta and transverse arch. This spiralling flow continues along the descending aorta. In contrast, $V_{\text{para}}^{\text{AS-BAV}}$ does not demonstrate the high velocity spiralling jet, and shows more parallel flow patterns with small vortical structures in the ascending aorta. $V_{\text{plug}}^{\text{AS-BAV}}$ displays parallel streamlines with almost negligible vortical patterns. These findings are in keeping with the results discussed above regarding radial velocity vectors.

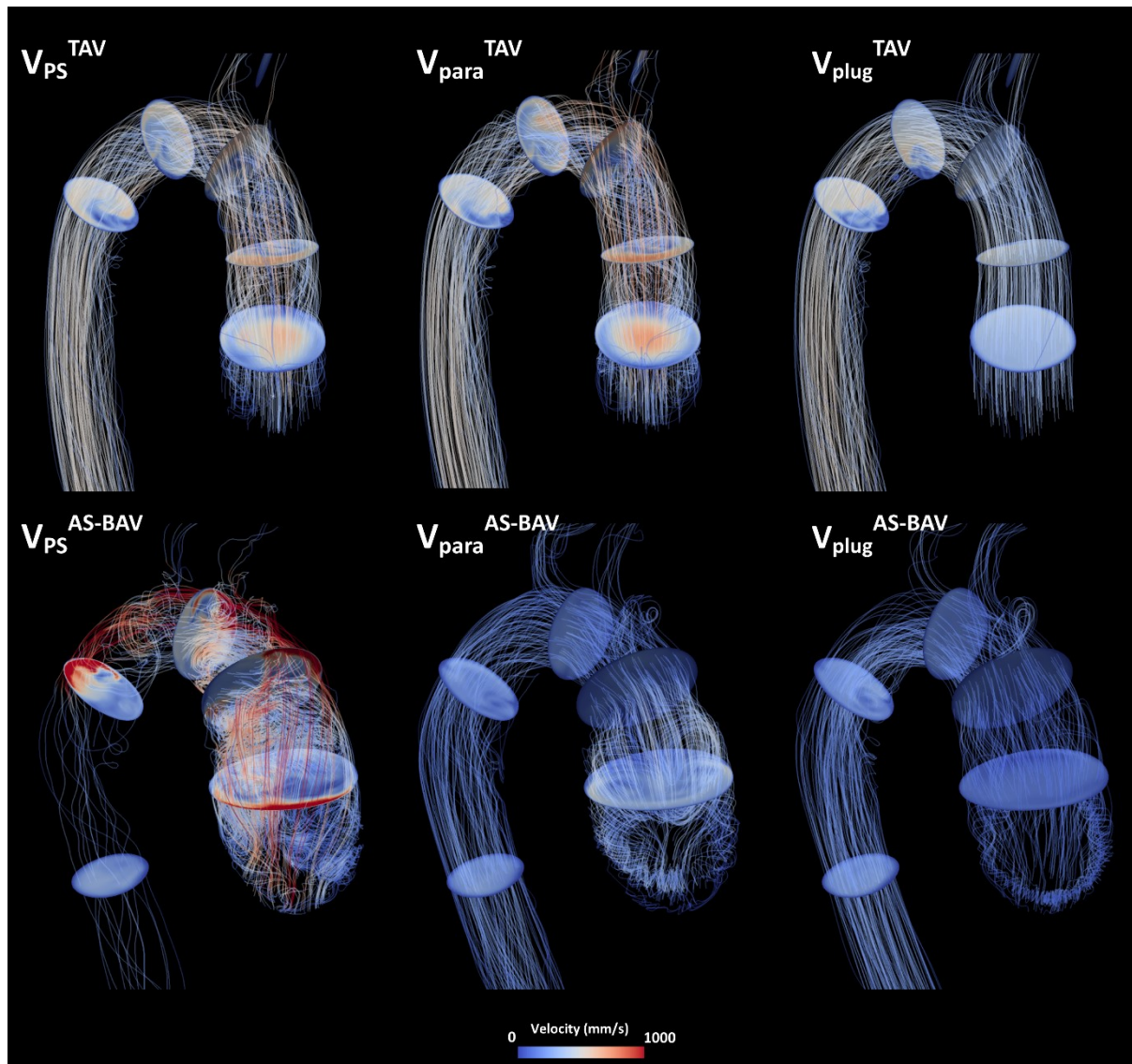


Figure 4.13. Velocity streamlines and 2D visualisation of velocity magnitude at 5 planes along the thoracic aorta during late systole.

4.4.5 Velocity Pathlines

Figure 4.14 depicts three-dimensional immaterial particle pathlines and mean absolute HFI calculated using the subject-specific inflow velocity profile for the two subjects over a single cardiac cycle. Even though the numerical values of HFI in the subject-specific profile case are not substantially different between the subject *TAV* and subject *AS-BAV*, (see Table 4.2), the difference in particle trajectories is significant. In *TAV*, the particles have moved in a uni-directional manner down the aorta and by the end of the first cycle they have almost left the domain. In contrast, particles injected in *AS-BAV* are still in the ascending aorta after 900 ms, having followed a very tortuous path. The particles shown for *AS-BAV* take almost twice as long as those shown for *TAV* to exit the simulation domain through the descending aortic boundary. Note that only eight particles are shown in this figure for the sake of clarity in the visualisation. The HFI indices presented in Table 4.2 were calculated using a much larger number of pathlines (approximately 700,000).



Figure 4.14. Pathlines and mean absolute HFI calculated using the subject-specific inflow velocity profile for subject *TAV* (top) and subject *AS-BAV* (bottom) at $t=100$, 200, 400, and 900 ms. Even though the numerical values of HFI are not substantially different between the healthy (*TAV*) and diseased (*AS-BAV*) cases (see Table 3.2), the difference in particle trajectories is remarkable. In *TAV*, the particles have moved in a uni-directional manner down the aorta and by the end of the first cycle they have almost left the domain. In contrast, particles injected in *AS-BAV* are still in the ascending aorta after 900 ms, having followed a very tortuous path. Note: only a small number of particles are tracked for the sake of clarity in the visualisation. The HFI indices were calculated using a much larger number of pathlines (approximately 700,000).

4.4.6 Flow Asymmetry and Dispersion

V_{PS}^{TAV} and V_{PS}^{AS-BAV} displayed very different $Flow_{asymmetry}$ trends throughout the aorta. V_{PS}^{TAV} showed symmetrical flow in plane 1, relatively asymmetrical flow in plane 2, and symmetrical flow in plane 3. Conversely, V_{PS}^{AS-BAV} showed highly asymmetrical flow for most of the thoracic aorta (planes 1 and 2), with $Flow_{asymmetry} > 80\%$ (see [Figure 4.15](#)). Interestingly, the idealised profiles V_{para} and V_{plug} for both subjects showed similar trends in plane 1, 2 and 3 ([Figure 4.15](#)).

[Figure 4.16](#) shows the flow dispersion results for subjects *TAV* and *AS-BAV*. $Flow_{dispersion}$ for V_{PS}^{TAV} was similar to the idealised profiles in planes 1 and 3. In the descending aorta (plane 3), flow became much broader for all 3 simulations. On the other hand V_{PS}^{AS-BAV} showed much smaller velocity dispersion compared to the 2 idealised profiles throughout the aorta.

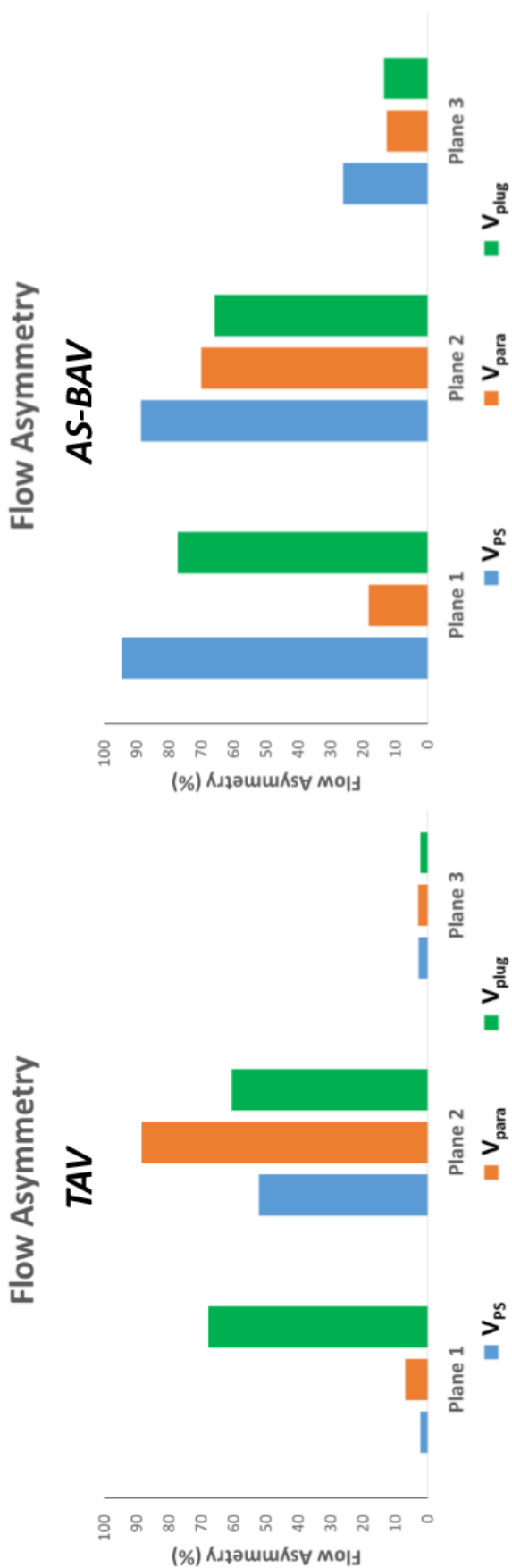


Figure 4.15. Flow_{asymmetry} along 3 planes of the thoracic aorta for subjects *TAV* and *AS-BAV*.

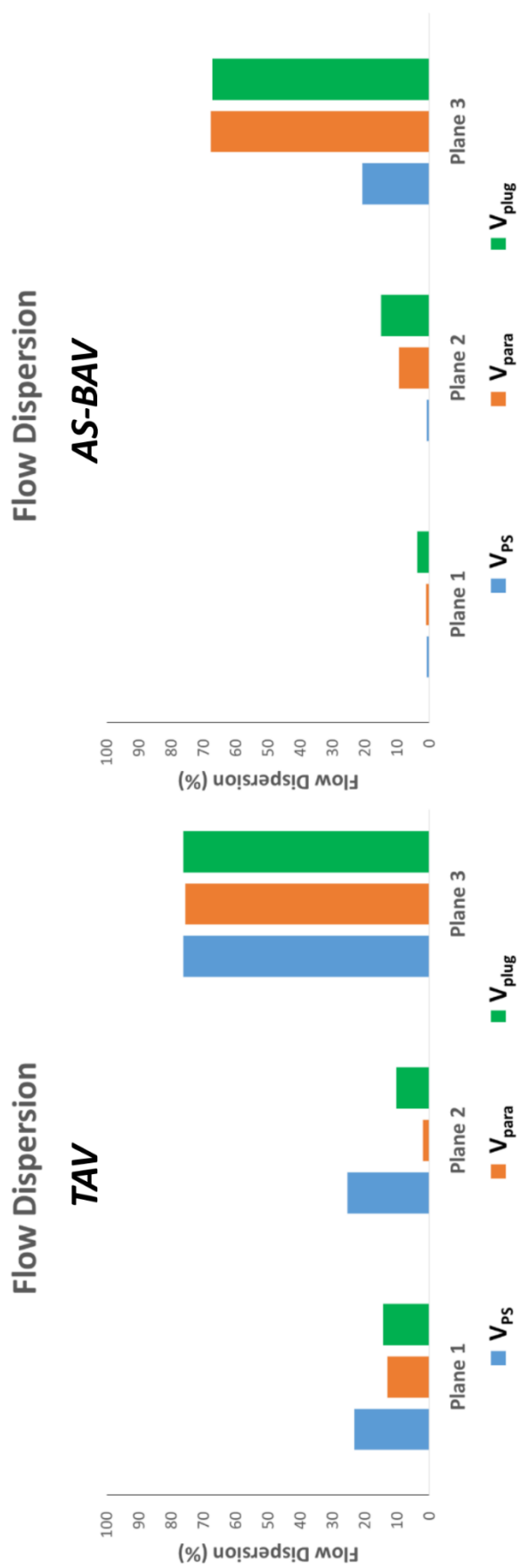


Figure 4.16. Flow dispersion along 3 planes of the thoracic aorta for subjects TAV and AS-BAV.

4.5 STUDY 1B RESULTS: WALL MECHANICS

4.5.1 Patient Demographics

The demographics and aortic dimensions for the subjects are displayed in [Table 4.1](#). In recognising the differences in aortic size relative to body size, two indices are also shown: the Aortic Size Index (Yale Index) (Davies et al. 2006), and the Svensson Index (SI) (Svensson et al. 2002). *N-BAV* had the largest indexed aortic size, followed by *AS-BAV*, then *AR-BAV* and *TAV*.

4.5.2 Velocity Profiles

[Figure 4.17](#) shows the 3-dimensional velocity profiles above the aortic valve for each of the 4 subjects at peak systole. The equivalent simulated parabolic velocity profile is also shown for each subject. It can be seen that BAV velocity profiles are asymmetrical, with the maximal velocity peak away from the centre of the lumen. *TAV* shows a velocity profile which is symmetrical, and comparable with its parabolic equivalent. The flow rate waveforms are shown for each subject underneath the velocity profiles.

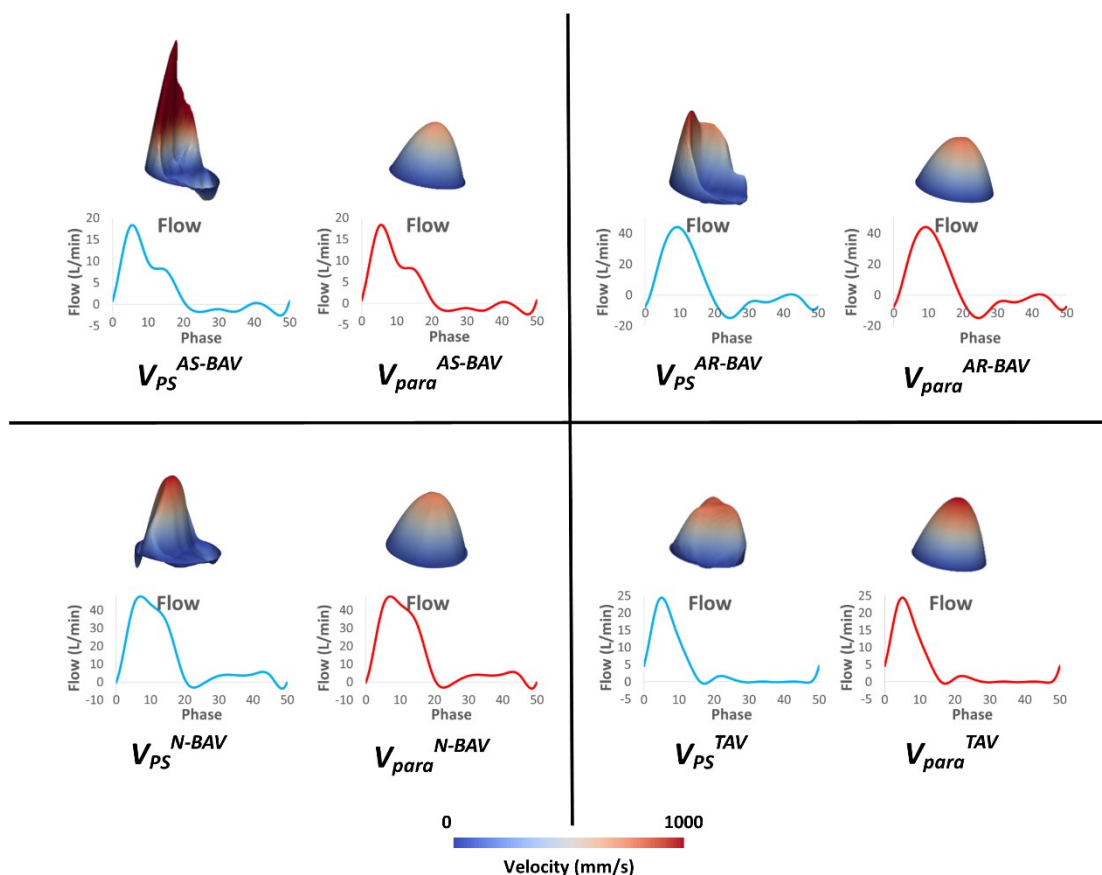


Figure 4.17. Patient-specific and parabolic velocity profiles for the 4 subjects, with corresponding flow rate waveforms.

4.5.3 Wall Shear Stress

Wall shear stress was measured in each of the 8 sectors of the ascending aorta throughout the cardiac cycle (Figure 4.18). WSS averaged for each sector at each time point was plotted against time over the cardiac cycle. WSS for V_{PS}^{TAV} and V_{para}^{TAV} is relatively similar amongst the 8 sectors, indicating that the parabolic inflow profile gives a reasonably comparable WSS result in the ascending aorta of a healthy tricuspid aortic valve.

AS-BAV and *N-BAV* show significantly higher WSS during systole as compared to their parabolic equivalents. The curves are splayed apart, particularly for *AS-BAV*, indicating an

asymmetrical distribution of WSS in the ascending aorta. *AR-BAV* shows lower WSS plots as compared to *AS-BAV* and *N-BAV*. However, it demonstrates 2 peaks of WSS in early and late systole. Its parabolic equivalent does not show the second peak of WSS.

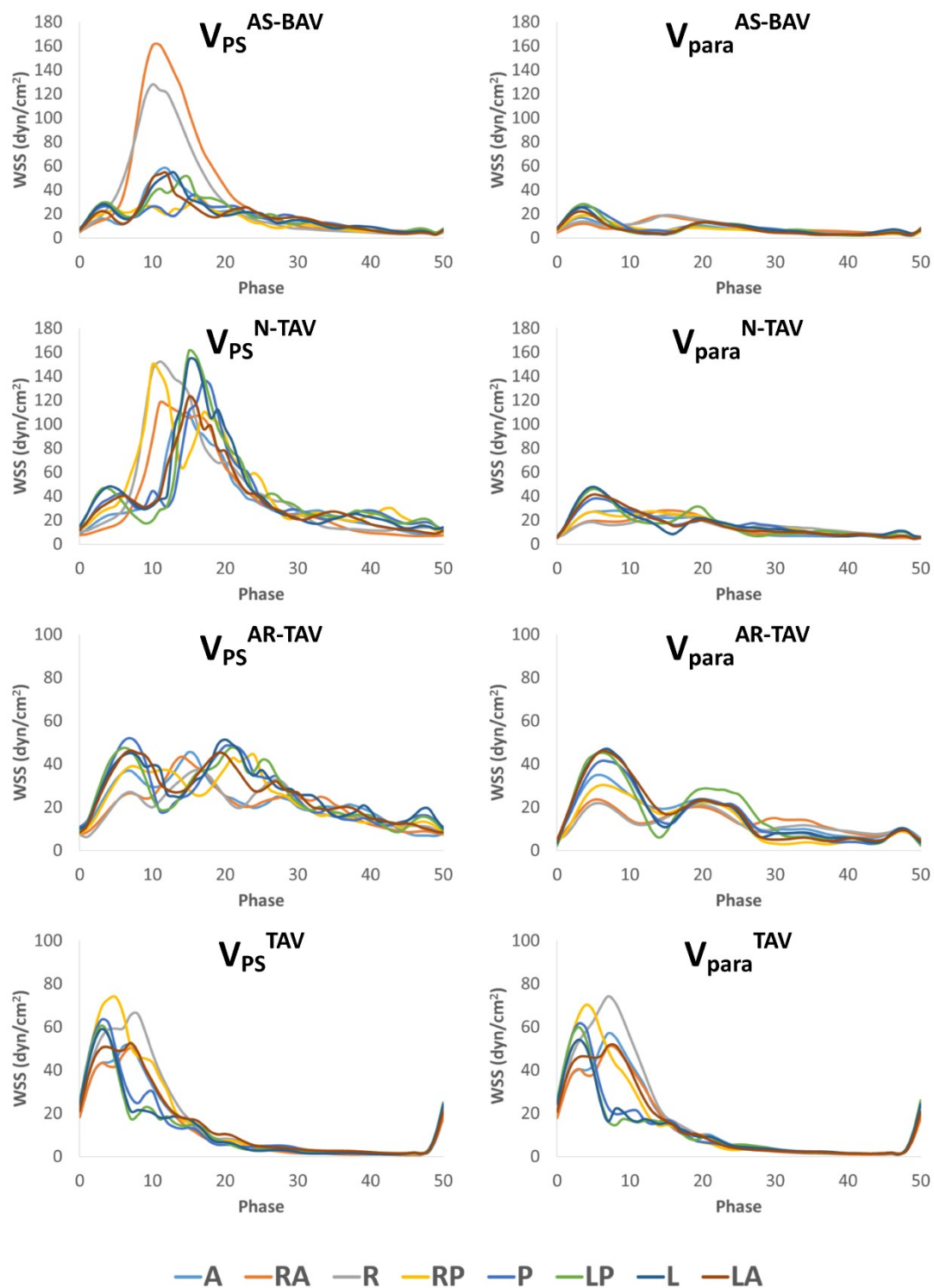


Figure 4.18. Wall shear stress (WSS) plots throughout the cardiac cycle. Each line represents one of the 8 anatomical sectors of the ascending aorta.

4.5.4 Mean WSS

Figure 4.19 shows the 3-dimensional radar plots of MWSS for the 8 sectors of the ascending aorta. V_{PS}^{TAV} and V_{para}^{TAV} show very similar and comparable MWSS values in the ascending aorta. Conversely, MWSS is higher for every sector in all 3 BAV subjects compared to their parabolic equivalents. *N-BAV* and *AS-BAV* show the biggest differences, with *AR-TAV* exhibiting smaller differences. For all 3 BAV subjects, the highest MWSS values are seen in the right-anterior (RA) sector of the ascending aorta, which corresponds to the greater curvature (convexity) of the ascending aorta.

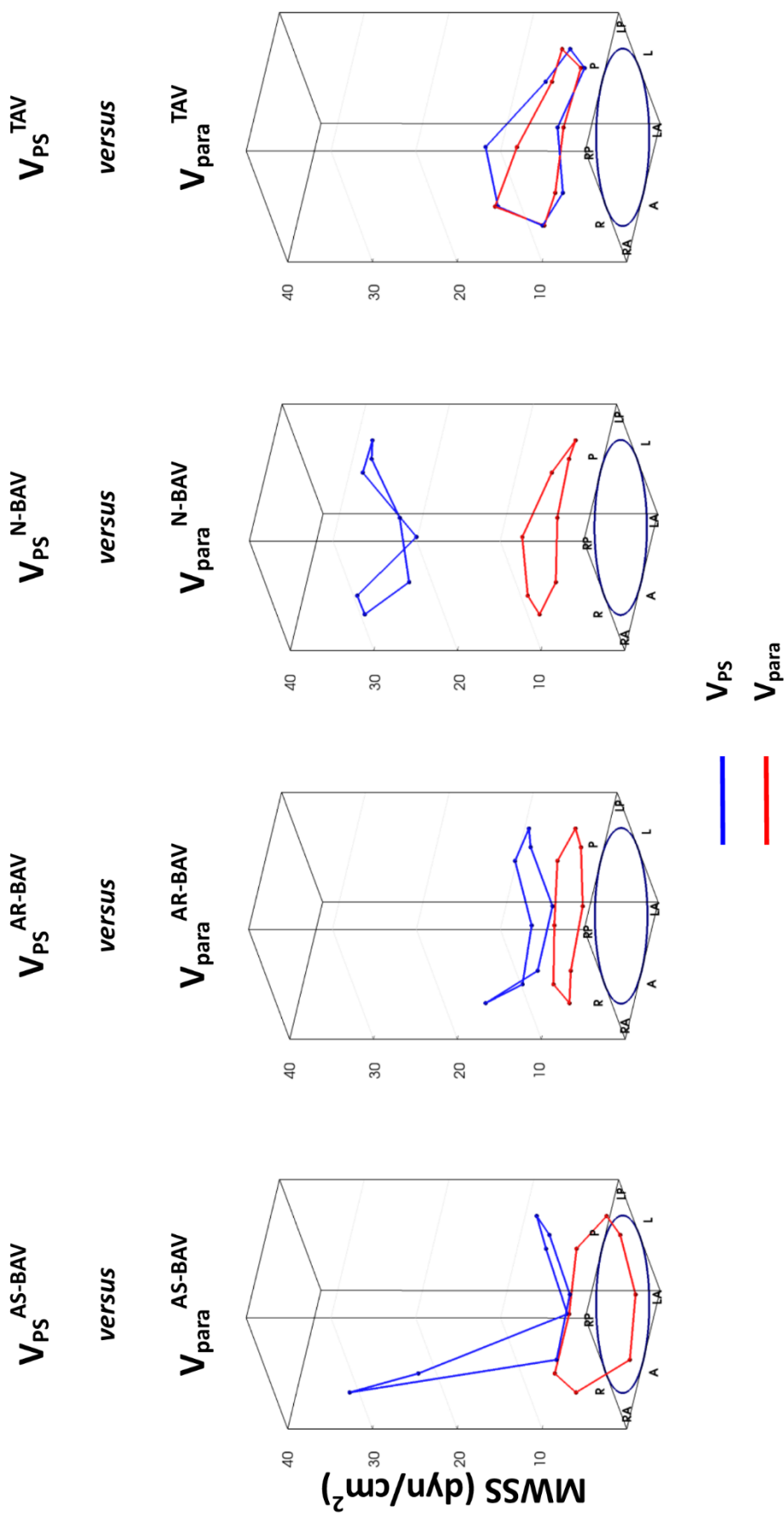


Figure 4.19. Plots of mean wall shear stress (MWSS) for each of the 8 sectors of the ascending aorta.

Figures 4.20 – 4.23 displays a point by point comparison of MWSS measurements between patient-specific simulations and their parabolic counterparts at each data node. The result is presented as % difference in MWSS between the two simulations. A negative percentage value indicates MWSS at that node is lower in the parabolic simulation as compared to patient-specific simulation. For further analysis, the percentage of the surface area where MWSS between the two simulations lies between -25% and +25% of each other is shown in the boxes.

AS-BAV shows the biggest difference when compared to its corresponding parabolic simulation. Only 4% of the ascending aorta, and 16% of the arch of V_{PS}^{AS-BAV} demonstrate MWSS values within -25% to +25% of V_{para}^{AS-BAV} . V_{PS}^{N-BAV} shows similar values in the ascending aorta (4%), but is more comparable with V_{para}^{N-BAV} in the arch (52%) and descending aorta (79%).

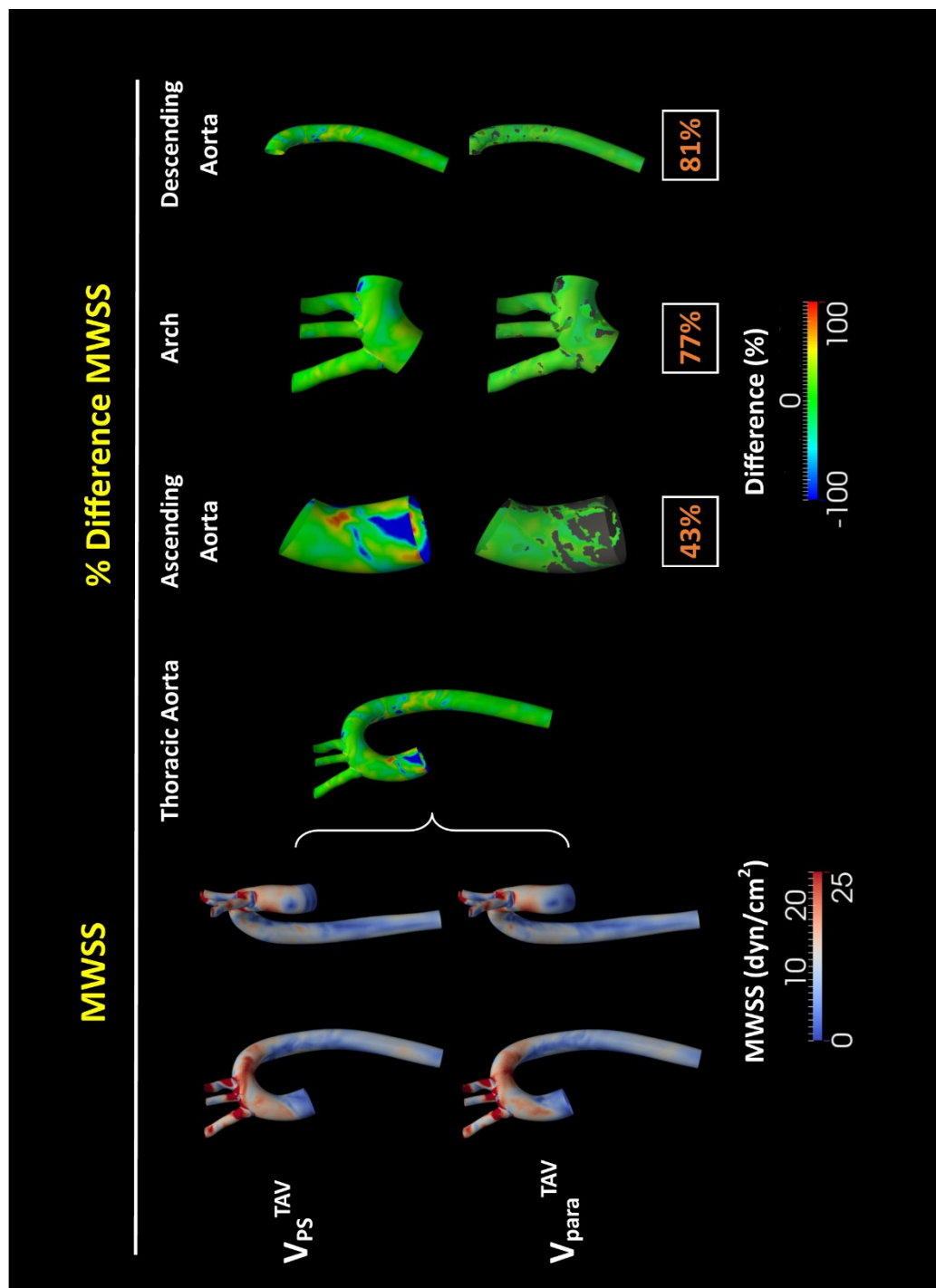


Figure 4.20. MWSS comparison for *TAV*. On the left, mean wall shear stress (MWSS) maps of the thoracic aorta. On the right, % Difference MWSS maps, with further sub-analysis of the ascending aorta, arch and descending aorta segments. Opaque green areas represent -25% to $+25\%$ difference in MWSS. Percentage values in the white boxes represent % area of aortic sector with MWSS values between -25% and $+25\%$

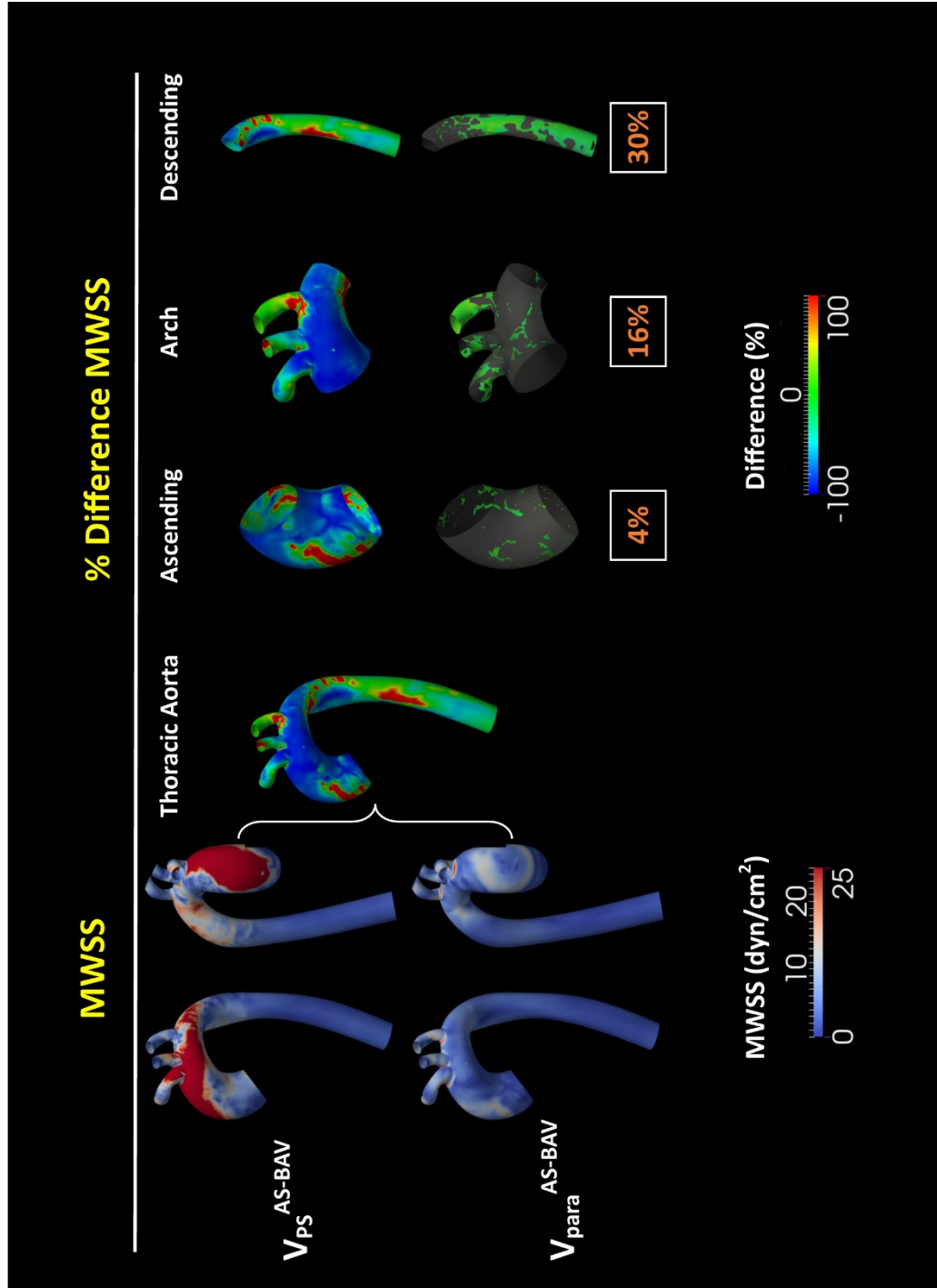


Figure 4.2.1. MWSS comparison for *AS-BAV*. On the left, mean wall shear stress (MWSS) maps of the thoracic aorta. On the right, % Difference MWSS maps, with further sub-analysis of the ascending aorta, arch and descending aorta segments. Opaque green areas represent -25% to $+25\%$ difference in MWSS. Percentage values in the white boxes represent % area of aortic sector with MWSS values between -25% and $+25\%$

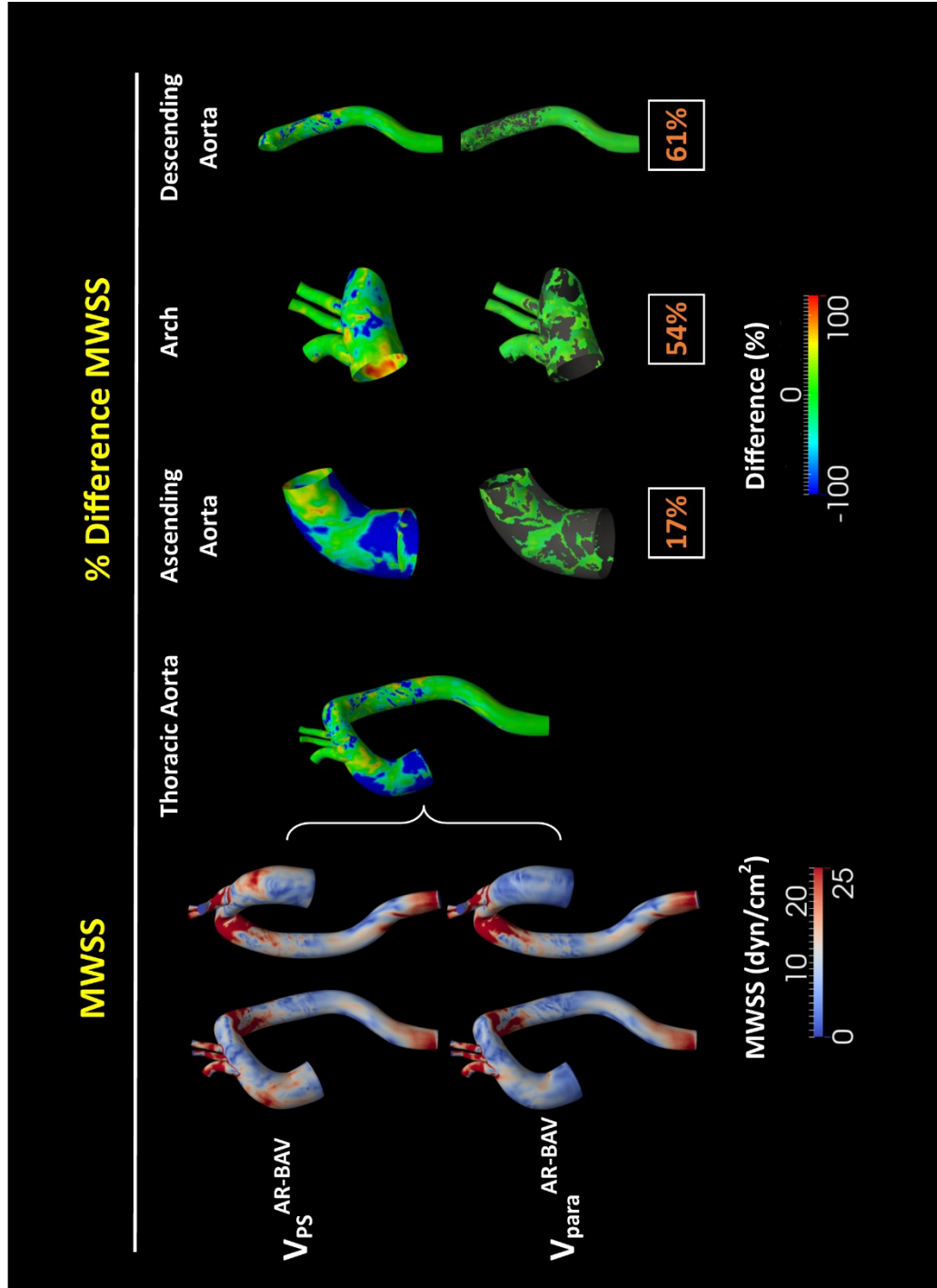


Figure 4.22. MWSS comparison for *AR-BAV*. On the left, mean wall shear stress (MWSS) maps of the thoracic aorta. On the right, % Difference MWSS maps, with further sub-analysis of the ascending aorta, arch and descending aorta segments. Opaque green areas represent -25% to $+25\%$ difference in MWSS. Percentage values in the white boxes represent % area of aortic sector with MWSS values between -25% and $+25\%$

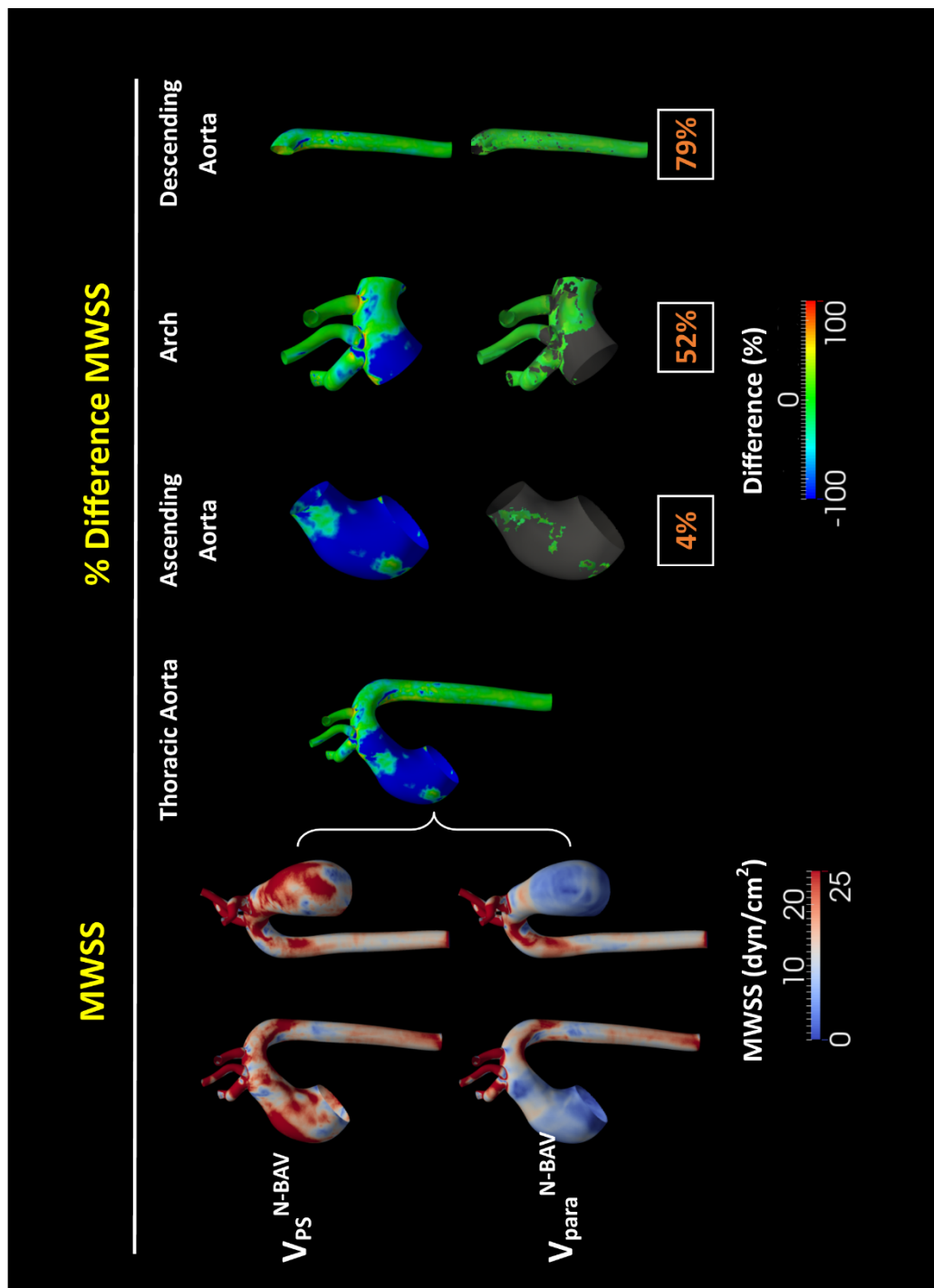


Figure 4.23. MWSS comparison for *N-BAV*. On the left, mean wall shear stress (MWSS) maps of the thoracic aorta. On the right, % Difference MWSS maps, with further sub-analysis of the ascending aorta, arch and descending aorta segments. Opaque green areas represent -25% to $+25\%$ difference in MWSS. Percentage values in the white boxes represent % area of aortic sector with MWSS values between -25% and $+25\%$

4.5.5 Oscillatory Shear Index

Ascending aorta OSI is similar for all 8 sectors when comparing V_{PS}^{TAV} and V_{para}^{TAV} . V_{PS}^{AR-BAV} and V_{para}^{AR-BAV} are also comparable, with only the right-anterior (RA) sector being lower in V_{para}^{AR-BAV} . V_{PS}^{AS-BAV} and V_{para}^{N-BAV} show significantly different OSI values when compared to their parabolic counterparts. All 3 BAV subjects show their lowest OSI levels in the right-anterior (RA) sector, corresponding to the greater curvature.

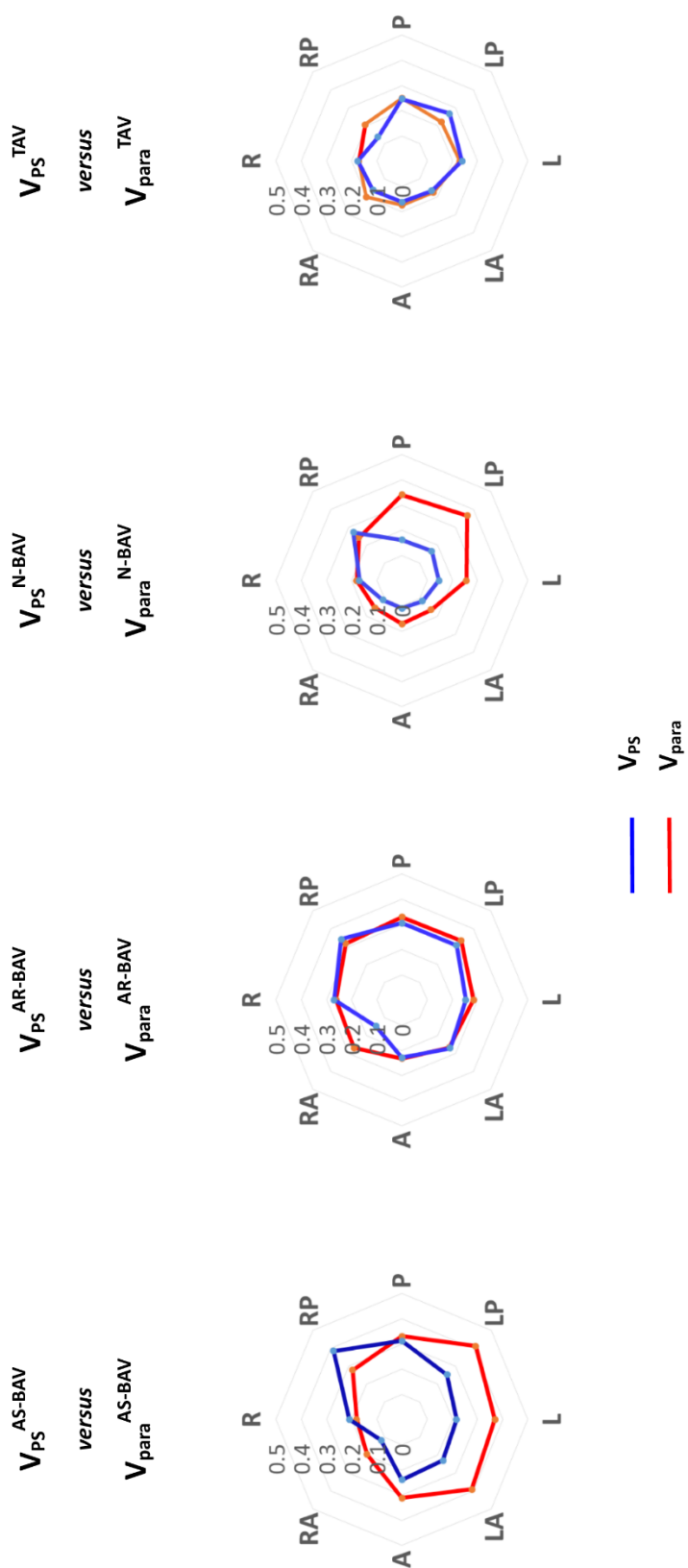
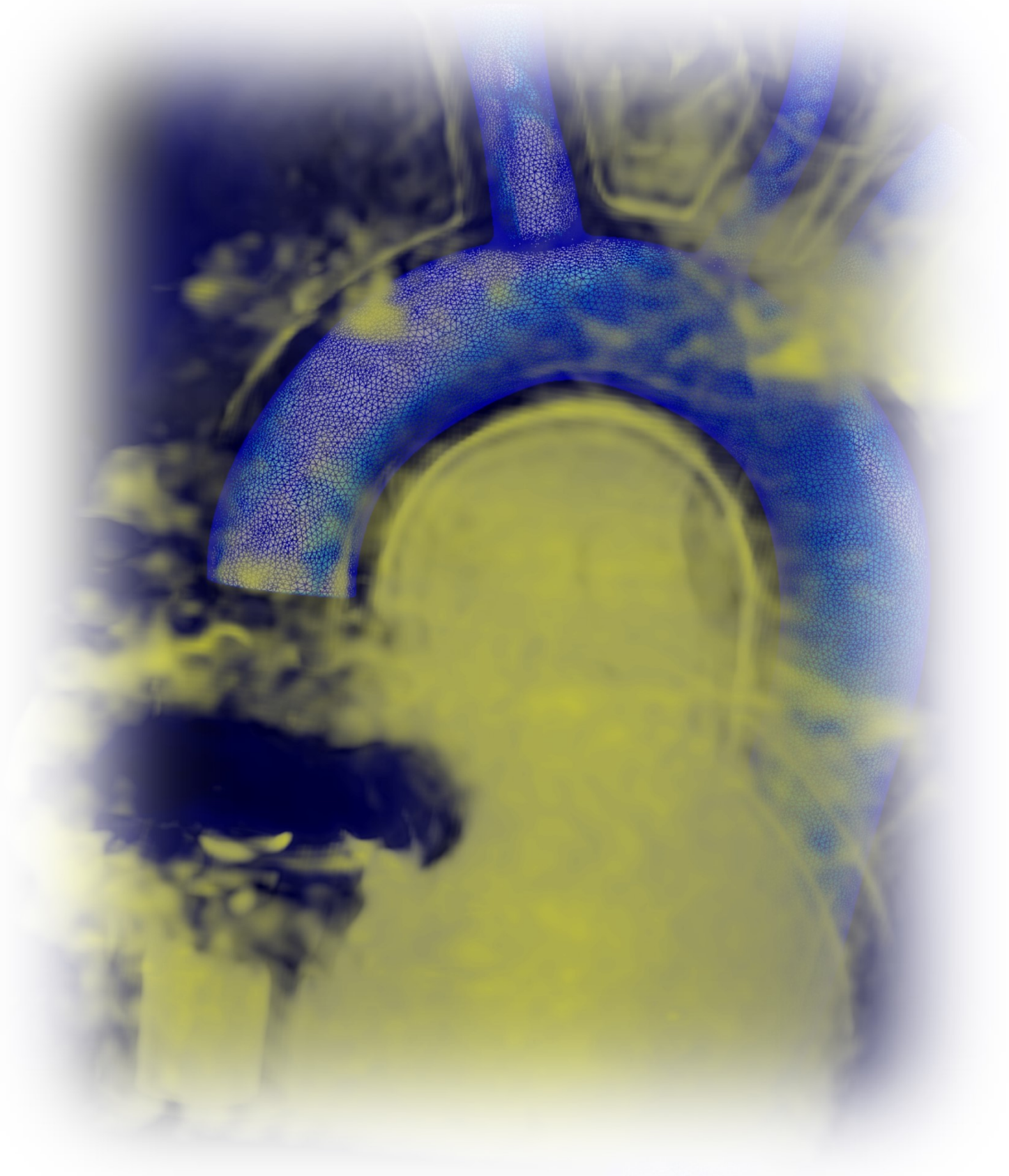


Figure 4.24. Radial graphs of oscillatory shear index (OSI) for each of the 8 sectors of the ascending aorta.

4.6 SUMMARY

This was a comparative study using patient-specific velocity inflow boundary conditions versus idealised velocity boundary conditions based on MRI measurements of velocity and flow in the ascending aorta. We have extracted patient-specific through-plane blood velocity data from flow-MRI and applied them as inflow boundary conditions to assess the effects of patient-specific inflow profiles versus idealised inflow profiles on haemodynamics in the thoracic aorta. Furthermore, we have also evaluated indices of flow disturbance such as helicity based on the computation of pathlines. Our analysis revealed that idealised inflow boundary conditions can significantly alter velocity patterns and underestimate velocity magnitudes, radial velocity components, helicity and complex flow in the thoracic aorta.

Wall indices such as WSS and OSI were significantly affected by using idealised inflow boundary conditions. WSS was grossly underestimated in the idealised parabolic velocity profile, and this was most pronounced in the ascending aorta. WSS in the descending thoracic aorta was more independent of the inflow velocity profile.



5

RESULTS - STUDY 2:

“In Vitro” Comparison of Aortic Haemodynamics in Bicuspid and Tricuspid Aortic Valves Using a Phantom Heart and Aorta Model

“Art has a double face, of expression and illusion, just like science has a double face: the reality of error and the phantom of truth.”

Publilius Syrus, 1st Century B.C.

Contents

5.1	Overview	167
5.2	Background	167
5.3	Methods	168
5.4	Results	174
5.5	Summary	184

5.1 OVERVIEW

This second results chapter will aim to compare aortic haemodynamics in BAV and TAV morphologies by using an in-vitro phantom heart and aorta (PHA) model. We used a piston-driven ventricle with programmable stroke profiles to pump fluid into a silicone thoracic aorta, with a trileaflet bioprosthetic porcine aortic valve at the interface between the phantom heart and the silicone aorta. The PHA was placed inside a MRI scanner and pulsatile flow driven through the aortic valve whilst MR angiography of the thoracic aorta model was taken as well as phase-contrast flow MRI sequences above the aortic valve. The trileaflet valve was then “bicuspidised” and the process repeated with the new bicuspid valve in the right-left fusion position, and then again in the right-non fusion position. In this way, aortic shape and size, cardiac output, flow rate waveform, heart rate, systemic vascular resistance and blood pressure were matched between the 3 simulations. By using computational fluid dynamics, we measured haemodynamic parameters such as flow patterns and streamlines, wall shear stress and oscillatory shear index.

5.2 BACKGROUND

One of the difficulties facing studies comparing BAV with tricuspid aortic valve (TAV) haemodynamics is that adequate matching of patient characteristics is difficult. Due to the present experimental nature of these imaging studies, most of the preliminary haemodynamic observations are in small samples of patients.

As well as aortic valve morphology, a number of factors may be involved in bringing about different haemodynamic results – age, sex, aortic size, aortic stiffness, hypertension, diabetes mellitus, medication including B-blockers and angiotensin receptor blockers. Furthermore,

even if these factors are matched adequately, there are many individual haemodynamic influences which have an effect on different measured indices such as WSS. For example, blood pressure (BP) will affect the systemic vascular resistance which in turn affects the resistance and capacitance of the vascular beds distal to the major aortic branches (Vignon-Clementel et al. 2006). Cardiac output and the flow rate waveform exiting the aortic valve affect the velocity and shear rates in the ascending aorta. Furthermore, whereas patients with similar size measurements at specific locations in the aorta (for example, mid-ascending aorta) may appear matched, the individual shape and morphology of each patient's aorta will have a significant effect on indices such as WSS (Campbell et al. 2012). As a result, accurate matching and meaningful comparison of BAV and TAV aortic haemodynamics is challenging.

Mechanical models of the heart and aorta allow for a “physical” tool to study different factors affecting aortic haemodynamics in an “in vitro” environment. They can be used to validate numerical simulations previous to translation into clinical practice. Furthermore, they allow for strict control over certain haemodynamic parameters whilst assessing the effects of others. One such study used a simplified full-scale silicone arterial tree model to assess pressure wave reflection (Segers et al. 2000). Others have used mechanical models to verify computational simulations (Alastruey et al. 2011).

5.3 METHODS

5.3.1 Phantom Heart and Aorta Model

A phantom heart and aorta (PHA) model was created by using a piston/cylinder ventricle to pump blood into a silicone thoracic aorta (comprising of the ascending aorta, arch and descending aorta). The silicone aorta model had 3 head and neck branches (innominate artery,

left common carotid artery and left subclavian artery). The piston/cylinder ventricle was driven by a computer controlled (LabVIEW, National Instruments, Austin, TX, USA) stepper motor (SMH60, Parker, Cleveland, OH, USA) (Gaddum et al. 2017). This setup provided controllable flow profiles into the silicone thoracic aorta. Fluid entered the ventricle through a low vibration swing mitral valve (Gaddum et al. 2012, Gaddum et al. 2014), and exited through a trileaflet porcine aortic valve. Fluid was pumped through the aortic valve and along the silicone aorta model, exiting through 4 outlets: the 3 head and neck vessels and the descending aorta. Each outlet had a clamp resistor at its end to provide a consistent resistance in all blood simulations. Fluid exiting the aorta model would enter a large reservoir which acted as the venous return and the atrium. This reservoir was large enough to house the whole PHA model, and therefore any fluid exiting the aorta model would return via the reservoir, back through the mitral valve and into the ventricle again. This also allowed for the aorta model to be immersed in fluid, thereby giving clear definition to the MRI images (Figure 5.1). Beat frequency was 1 Hz (60 bpm), with a stroke volume of 70ml / beat.

The working fluid was water, with the addition of gadolinium (gadodiamide, Omniscan®, GE Healthcare, Waukesha, WI). In order to recreate T1 longitudinal relaxation properties of the working fluid to be similar to blood (a T1 of 1600ms (Lu et al. 2004)), gadolinium was added to the working fluid based on a series of dilution tests. T1 values of serial gadolinium concentrations in 50ml water were assessed using an inversion-recovery T1 weighted gradient echo sequence (Varma et al. 2014).

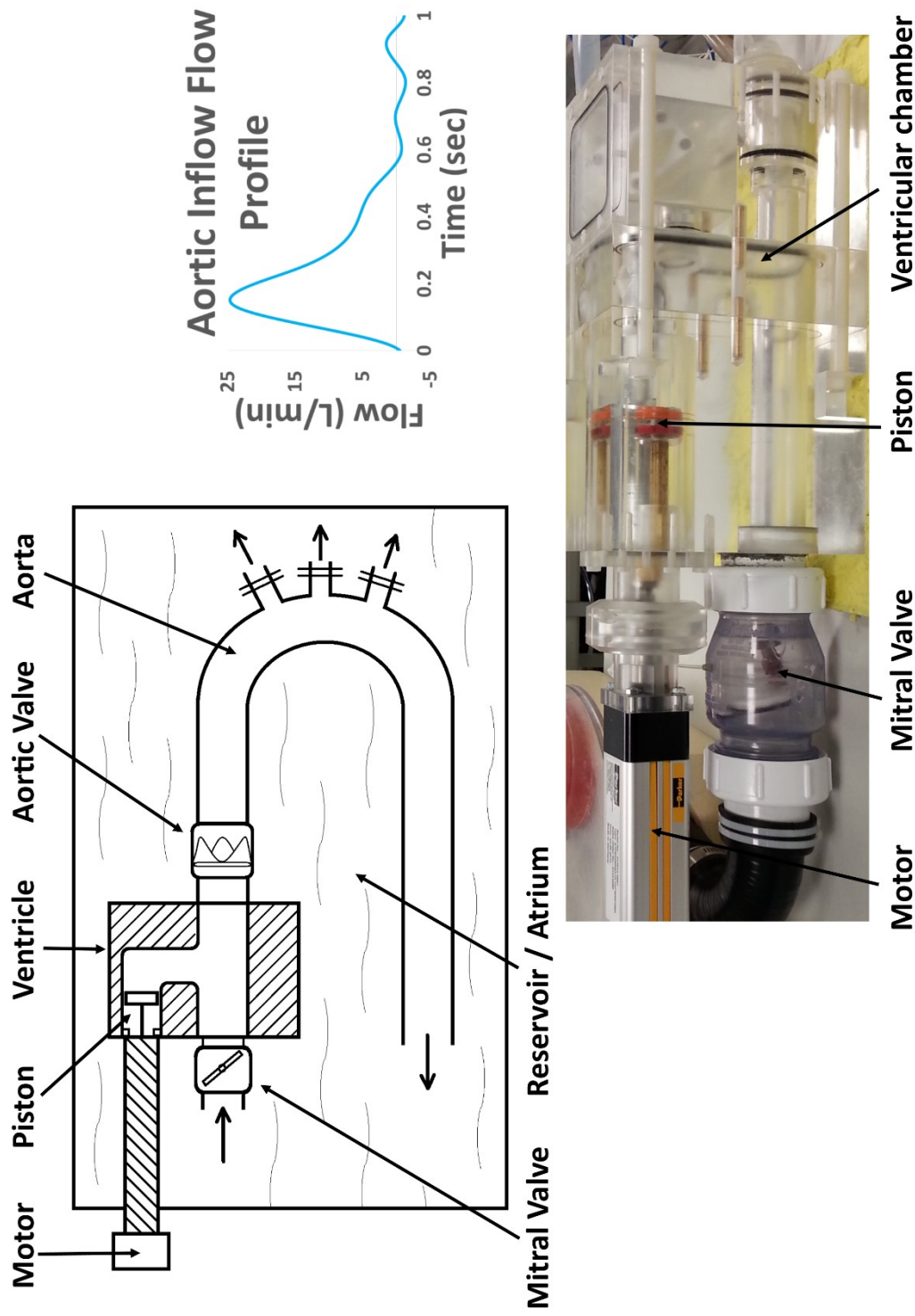


Figure 5.1. Schematic diagram (top-left) showing the components of the PHA model, including the motor and piston head, ventricle, mitral and aortic valves, thoracic aorta, and atrium / reservoir. Picture of phantom heart (bottom-right). Graph (top-right) of aortic inflow flow profile as measured just above the aortic valve.

5.3.2 Aortic Valve

A tricuspid porcine bioprosthesis aortic valve (29mm Carpentier-Edwards Perimount valve, Edwards Lifesciences, Irvine, CA, USA) was placed at the interface between the piston/cylinder ventricle and the silicone thoracic aorta model. After running the blood flow simulations with this tricuspid valve, the valve was removed and two of its leaflets were sutured together using 6/0 polypropylene suture (Figure 5.2). This resulted in a bicuspid aortic valve with a raphe (the commonest type of bicuspid aortic (Schaefer et al. 2008)). The valve was then placed back in the PHA model, with the valve orientated to mimic a right-left fusion BAV (BAV-RL), and subsequently rotated to mimic a right-non fusion BAV (BAV-RN).

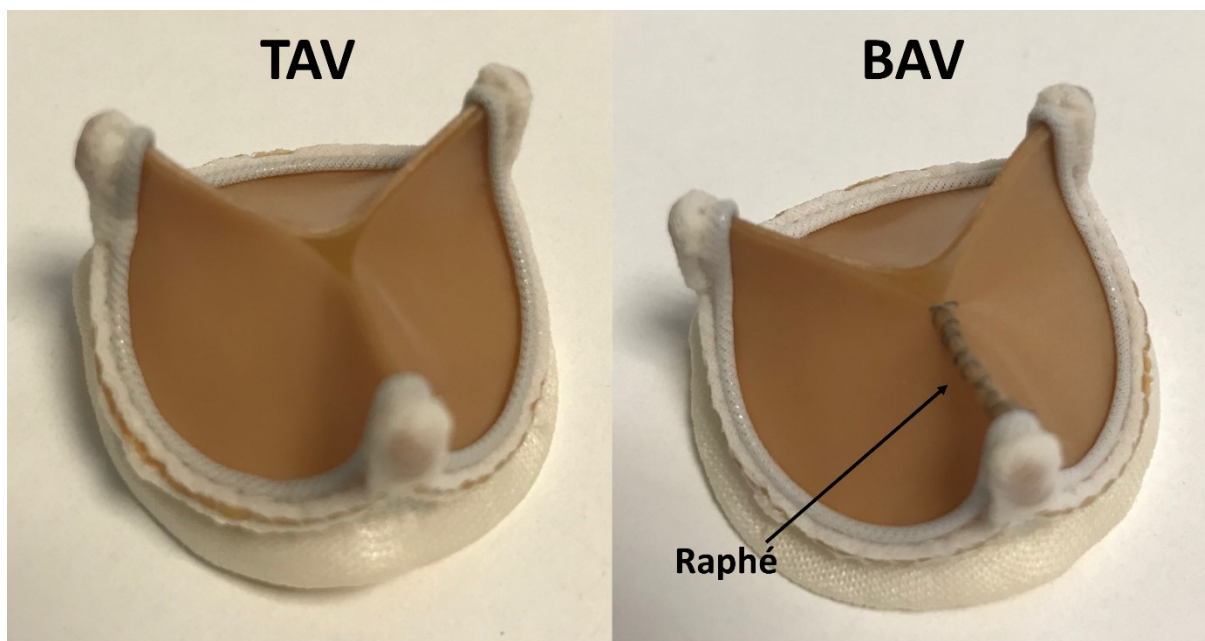


Figure 5.2. Trileaflet bioprosthesis valve (left) and “bicuspidised” bioprosthesis valve (right) with 2 leaflets sutured together to create a raphe.

5.3.3 Imaging & CFD

Cardiac Magnetic Resonance imaging (CMR) and Magnetic Resonance Angiography (MRA) was carried out with the PHA model working at 60bpm, using a Philips Achieva 3T scanner (Philips Medical Systems, Eindhoven, Netherlands). The inflow profile above the aortic valve was acquired using a time-resolved, velocity encoded 2D anatomic and through-plane PC-MRI (flow MRI) positioned orthogonally in the ascending aorta just above the aortic valve. Thirty images were reconstructed during one cardiac cycle. In order to avoid aliasing, velocity sensitivity was set at 300 cm/s.

Segmentation and meshing was carried out as defined in Sections 3.3.1 and 3.3.2. A tetrahedral anisotropic mesh (approximately 2.4 million elements and 420,000 nodes) was created by discretising the geometric model.

Blood flow simulations were carried out using a stabilized finite element formulation using a global residual tolerance 0.001 and time-step size of 0.00025 s. Four to six cardiac cycles were produced until cycle-to-cycle periodicity in the flow and pressure fields was achieved. The last cardiac cycle was used for the purpose of data analysis for each subject.

The outflow boundary conditions were specified using a coupled-multi-domain method (Figuroa et al. 2006, Vignon-Clementel et al. 2006) in which 3-element Windkessel models were coupled to each outflow branch (e.g. innominate artery, left common carotid artery, left subclavian artery, and descending aorta) (Vignon-Clementel et al. 2010). Flow splits were estimated based on the relative cross-sectional area of each outlet. The Windkessel parameters were estimated following the procedure described in Xiao et al. (Xiao et al. 2014). [Table 5.1](#) gives the numerical values of these parameters for each branch.

Table 5.1. Values of the lumped parameter Windkessel boundary conditions for each outlet. R_p = proximal resistance; R_d = distal resistance; C = capacitance. The units of resistance are 10^3 dynes s / cm^5 . The units of capacitance are 10^{-6} cm^5 / dynes.

Outlet	Windkessel Parameters		
	R_p	R_d	C
Brachiocephalic Artery	0.05	0.60	7.49
Left Common Carotid Artery	0.20	2.14	2.09
Left Subclavian Artery	0.14	1.55	2.88
Descending Aorta	0.01	0.21	21.3

5.3.4 Haemodynamic Parameters

Flow data from PC-MRI image acquisition was used to create 3-dimensional velocity profiles above the aortic valve. Velocity streamlines for the entire thoracic aorta were calculated from temporally resolved velocity data.

MWSS and OSI were measured at 7 planes along the thoracic aorta: plane 1 – proximal ascending aorta; plane 2 – mid-ascending aorta; plane 3 – distal ascending aorta; plane 4 – mid arch; plane 5 – distal arch; plane 6 – mid-descending aorta; plane 7 – distal descending aorta. The results were visualised using ParaView (Kitware, Inc., Clifton Park, NY).

For each subject, the ascending aorta was divided into 8 sectors anatomically from proximal ascending aorta to the distal ascending aorta. The 8 sectors were labelled anterior (A), right-anterior (RA), right (R), right-posterior (RP), posterior (P), left-posterior (LP), left (L), and left-anterior (LA).

5.4 RESULTS

5.4.1 Velocity Profiles

Figure 5.3 shows the velocity profiles measured by PC-MRI (flow MRI) above the 3 different aortic valves used. For TAV, the velocity profile is broad and symmetrical, with the highest velocities seen in the centre of the lumen. For BAV-RL and BAV-RN, the velocity profile is asymmetrical and slanted towards the non-fused cusp. Here, the highest velocities are seen near the periphery of the lumen. Furthermore, peak velocities are slightly higher in the BAV profiles compared to TAV (1.9m/s for BAV-RL, 1.9m/s for BAV-RN, and 1.6m/s for TAV).

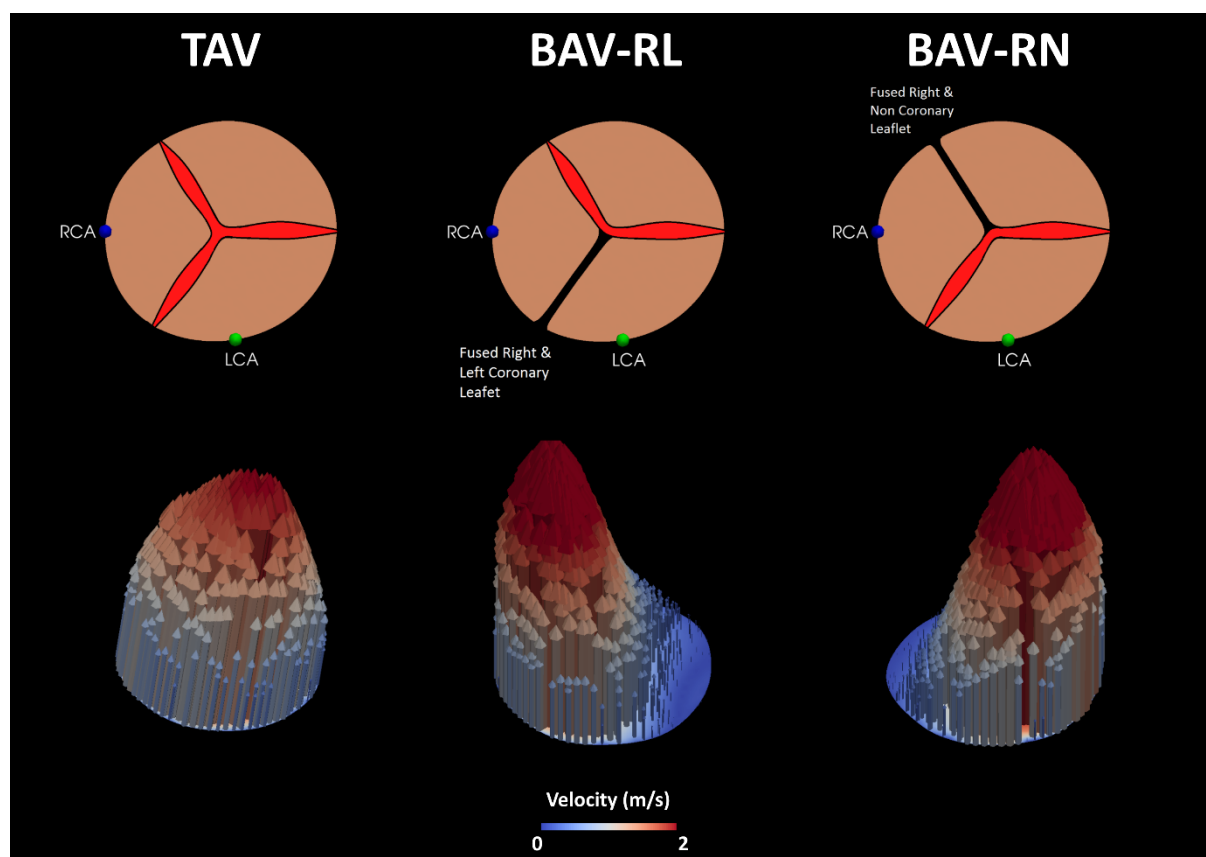


Figure 5.3. Velocity profiles above the aortic valve for the 3 simulations. Arrows show velocity vectors with velocity magnitude represented by arrow length and colour.

5.4.2 Flow Patterns

Figures 5.4 and 5.5 show velocity streamlines at peak systole for the 3 simulations. TAV shows a central stream of higher velocity (shown in red) with relatively parallel laminar streamlines seen in the arch and descending aorta. BAV-RL and BAV-RN show a high velocity jet entering the ascending aorta at the periphery of the lumen (albeit on opposite sides of the aorta), and continuing to travel along the ascending aorta and arch close to the vessel wall. Velocity streamlines in the arch and descending aorta are less laminar in BAV-RL and BAV-RN as compared to TAV, especially in BAV-RN where the streamlines are disorganised.

The velocity maps at each of the 7 planes in Figures 5.4 and 5.5 show that in BAV-RL and BAV-RN the systolic jet maintains its higher velocity at the periphery of the lumen throughout the whole of the ascending aorta and into the arch, whereas in TAV the jet disperses by the distal ascending aorta. The jet in BAV-RL travels around the ascending aorta and arch in a clock-wise direction, whereas in BAV-RN the jet spirals in an anti-clockwise direction. This is best seen in the 7 plane velocity maps in Figure 5.5.

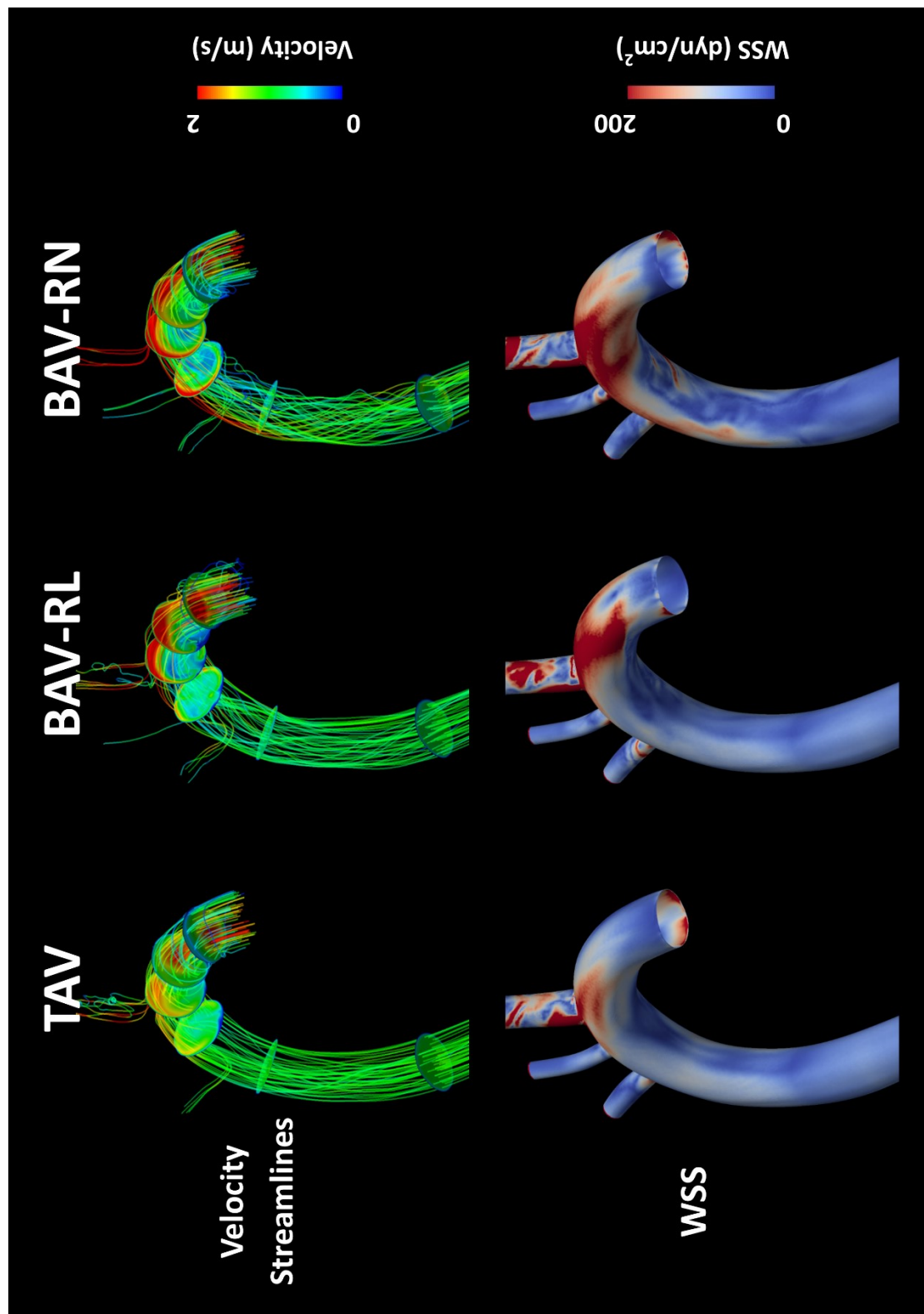


Figure 5.4. Velocity streamlines and velocity maps at the 7 aortic planes (top) at peak systole for the 3 simulations. Wall shear stress maps (bottom) at peak systole.

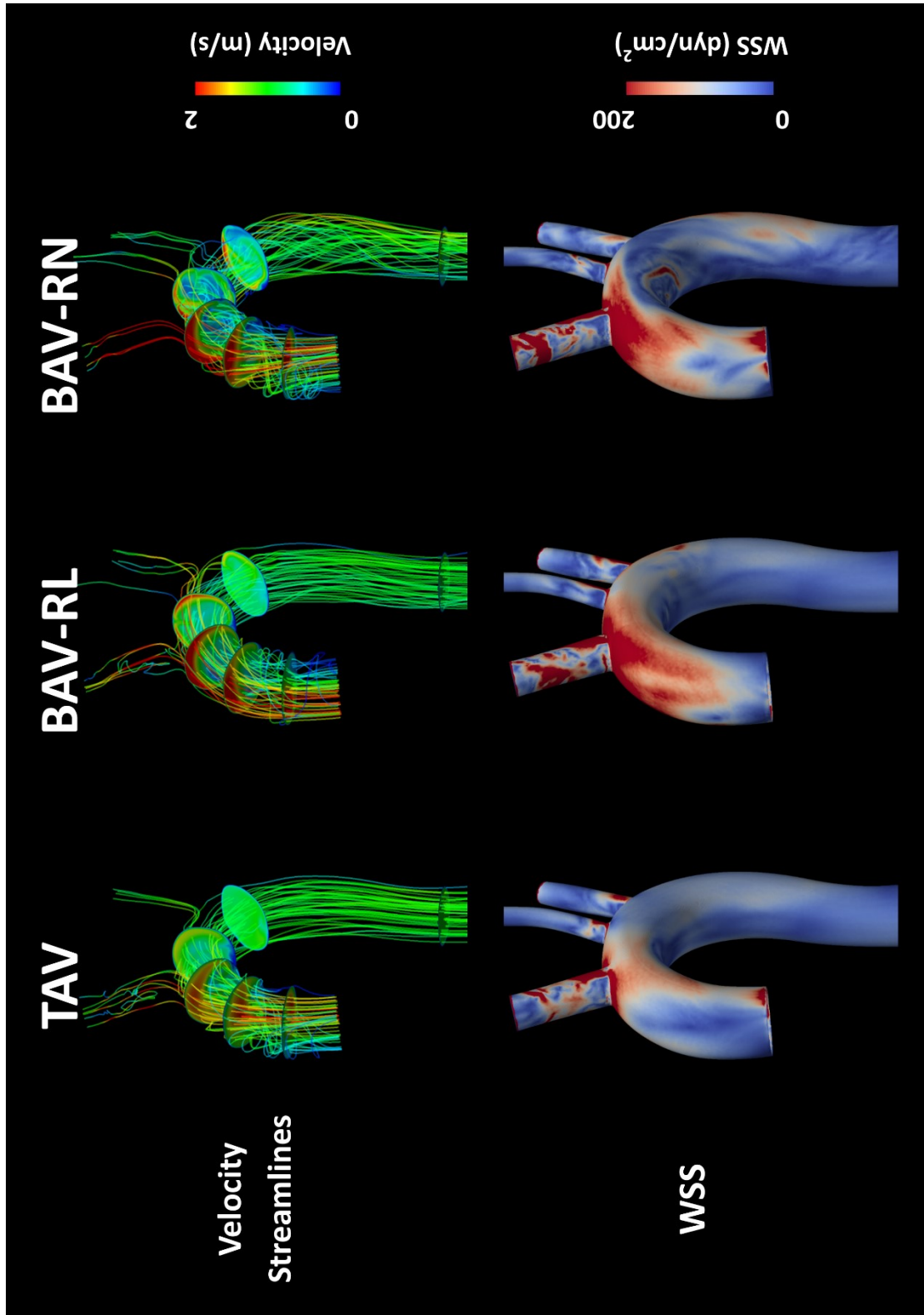


Figure 5.5. Velocity streamlines and velocity maps at the 7 aortic planes (top) at peak systole for the 3 simulations. Wall shear stress maps (bottom) at peak systole.

5.4.3 Wall Shear Stress

Figures 5.4 and 5.5 show WSS at peak systole. In the TAV simulation, the aorta has a relatively even distribution of low WSS (blue colour) throughout, with a small area of slightly elevated WSS in the distal ascending aorta and arch. In contrast, BAV-RL and BAV-RN both show significantly higher WSS (red colour) in the mid to distal ascending aorta and arch. In BAV-RN, the high WSS extends further into the arch than in BAV-RL. When comparing to the velocity streamlines, it can be seen that the areas of high WSS seen in BAV-RL and BAV-RN correspond to the location of high velocity jets.

MWSS (cycle-averaged) was measured at each of the 7 planes along the aorta. Figure 5.6 visually shows MWSS rings (corresponding to MWSS levels at the vessel wall along each of the 7 planes). Yellow colour depicts higher MWSS levels. TAV shows relatively even levels of low MWSS throughout (blue and purple colour). BAV-RL and BAV-RN show more yellow rings indicating higher MWSS levels, particularly in the ascending aorta.

Figure 5.7 is a graph of MWSS averaged across each of the 7 planes for the 3 simulations. MWSS was significantly higher for BAV-RL and BAV-RN as compared to TAV for the proximal, mid and distal ascending aorta (planes 1-3), as well as the mid-arch (plane 4). BAV-RN also showed higher MWSS in the distal arch (plane 6). The highest MWSS levels occurred in the distal ascending aorta (plane 3) for all 3 simulations (44.1 dyn/cm² for BAV-RN, 35.6 dyn/cm² for BAV-RL, and 21.5 dyn/cm² for TAV).

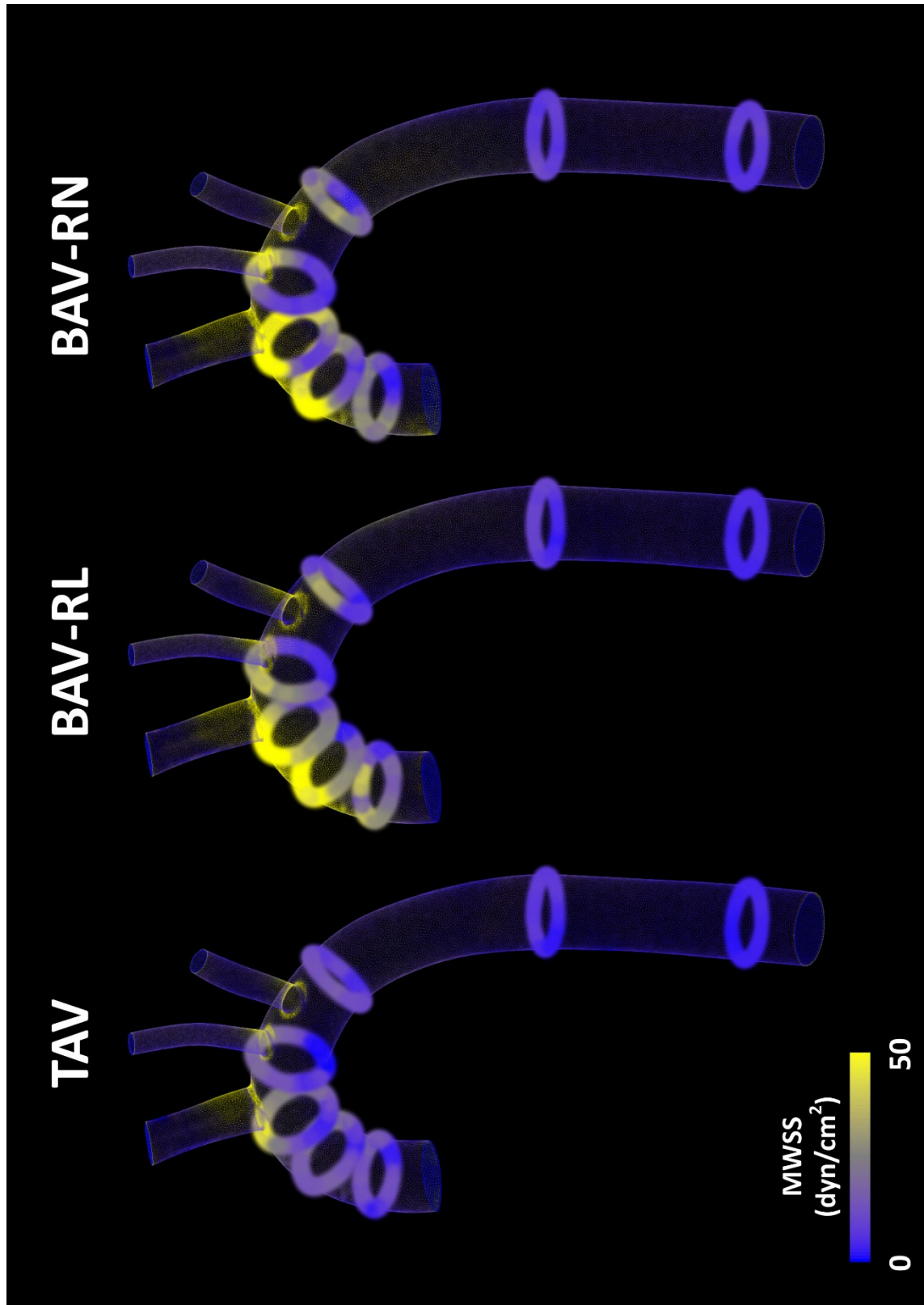


Figure 5.6. MWSS maps at the 7 planes along the thoracic aorta. Yellow colour represents higher MWSS levels.

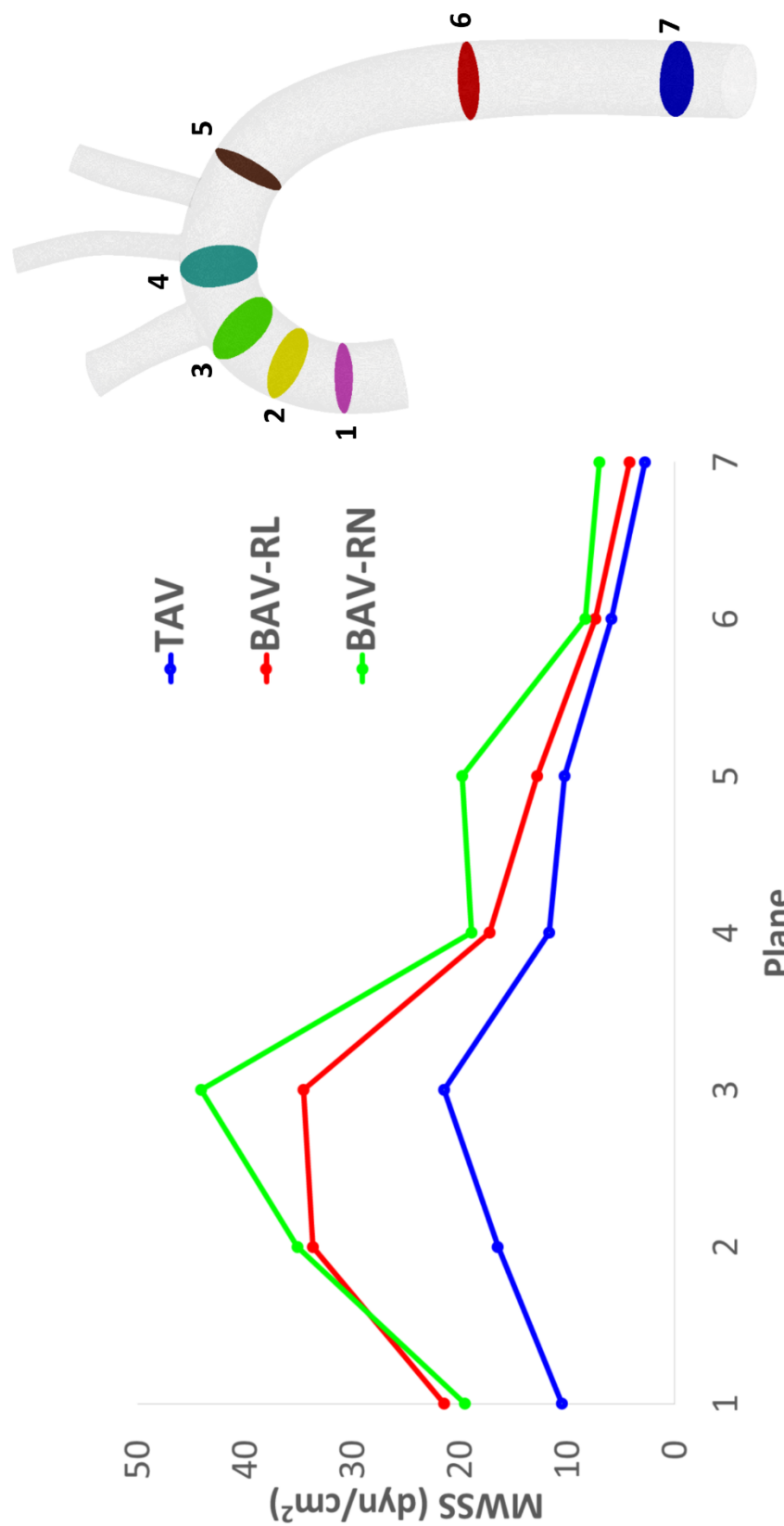


Figure 5.7. Graph showing averaged MWSS at each of the 7 aortic planes; plane 1 – proximal ascending aorta; plane 2 – mid-ascending aorta; plane 3 – distal ascending aorta; plane 4 – mid-arch; plane 5 – distal arch; plane 6 – mid-descending aorta; plane 7 – distal descending aorta.

The ascending aorta was divided into 8 sectors, and MWSS and OSI were averaged across the cross-sectional area of each sector. [Figure 5.8](#) shows 3-dimensional radar plots of MWSS for each of the 8 sectors. TAV shows a relatively horizontal flat ring which indicates an even distribution of MWSS across the 8 sectors. In contrast, BAV-RL and BAV-RN both show very uneven distribution of MWSS across the circumference of the ascending aorta. Both show significantly higher levels of MWSS (when compared to TAV) in the anterior (A), right-anterior (RA) and right (R) sectors of the ascending aorta. For example, MWSS in the right-anterior (RA) sector measured at 13.1 dyn/cm² for TAV, 41.8 dyn/cm² for BAV-RL, and 37.8 dyn/cm² for BAV-RN.

5.4.4 Oscillatory Shear Index

[Figure 5.9](#) shows radar plots of OSI for each of the 8 sectors of the ascending aorta. TAV shows similar OSI values (~0.15) in all sectors except for the anterior (A), left-anterior (LA) and left (L) sectors, which show higher OSI values (0.2 – 0.3). BAV-RN shows globally lower OSI values, with the lowest levels (< 0.1) in the anterior (A), right-anterior (RA), right (R) and right-posterior (RP) sectors of the ascending aorta. BAV-RL has its lowest OSI values (< 0.1) in the left-anterior (LA), anterior (A), right-anterior (RA) and right (R) sectors.

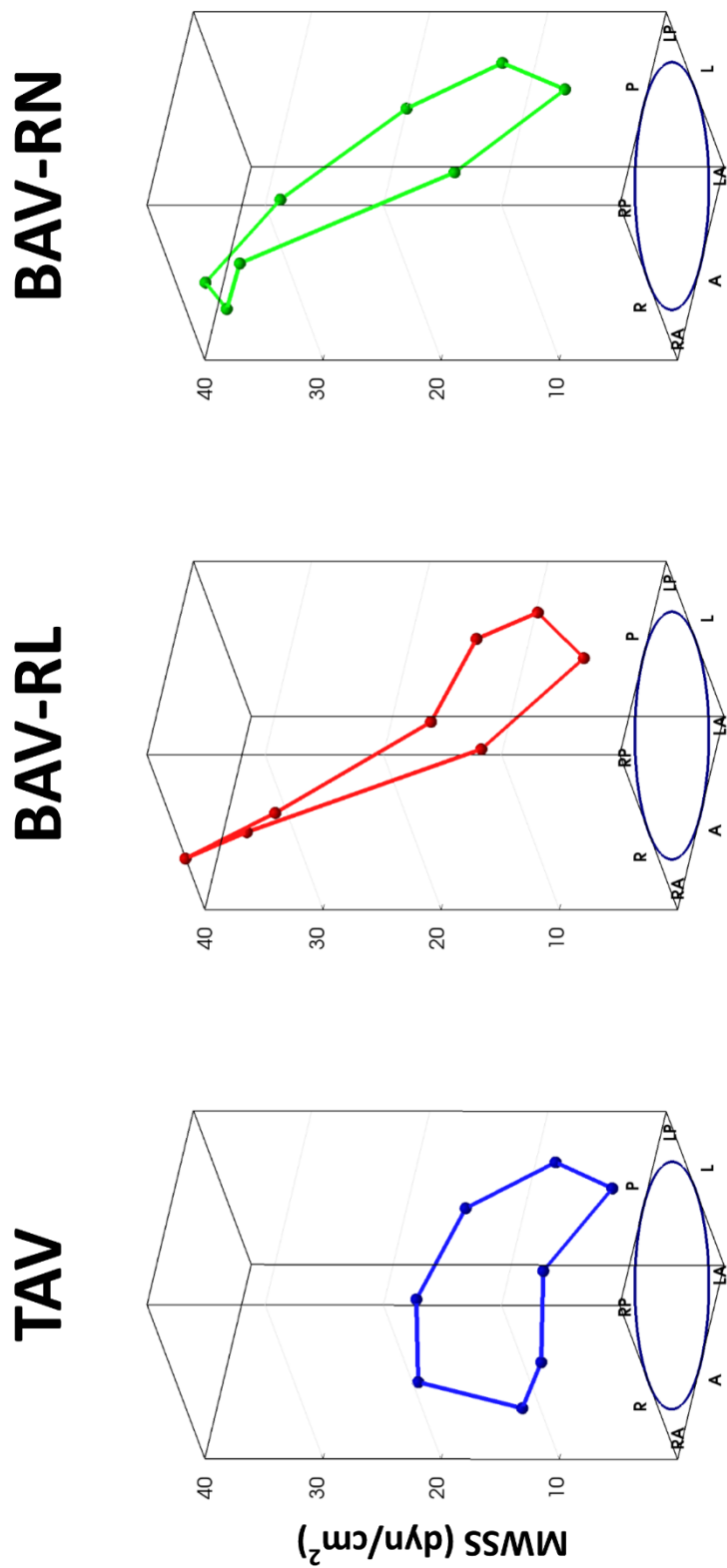


Figure 5.8. Three-dimensional radar plots of MWSS for each of the 8 sectors of the ascending aorta.

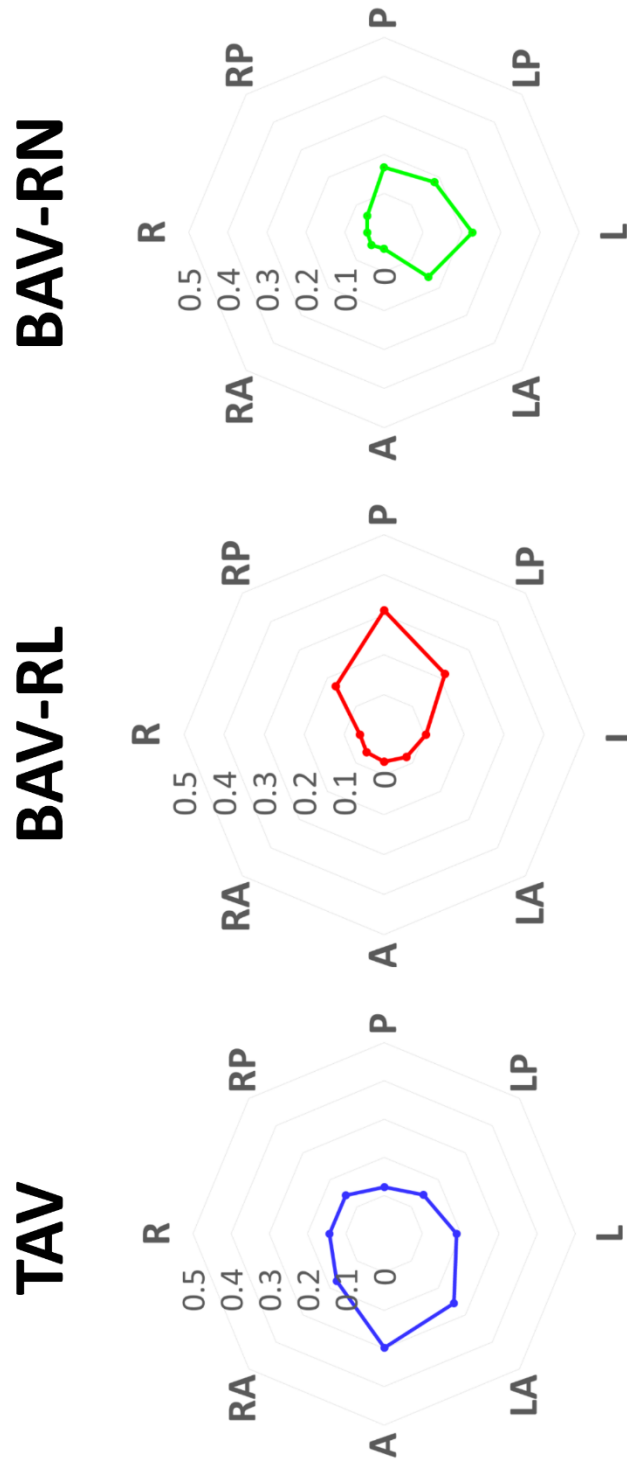
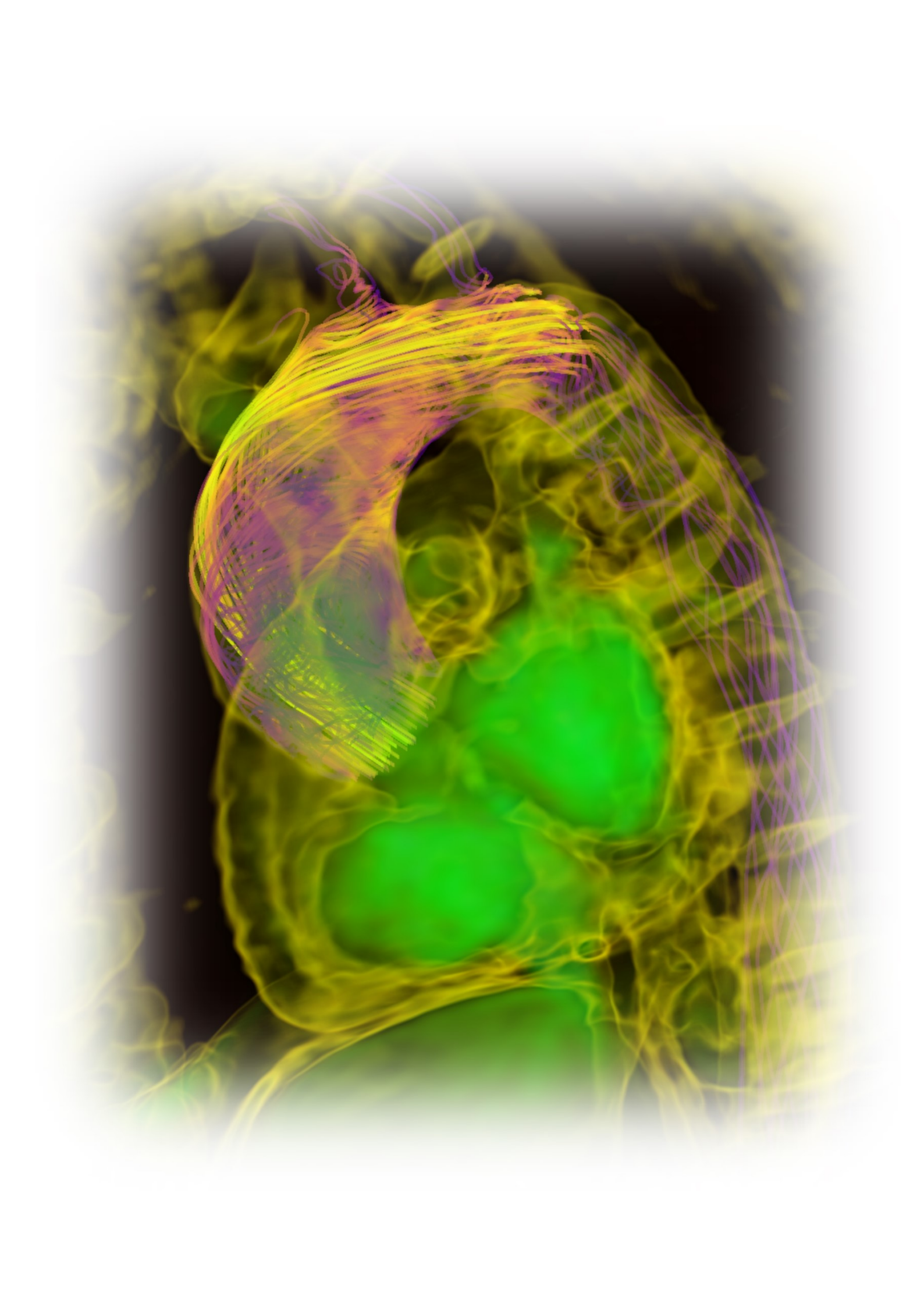


Figure 5.9. Radar plots of OSI for each of the 8 sectors of the ascending aorta.

5.5 SUMMARY

This phantom study represents a novel method of comparing BAV and TAV haemodynamics in a controlled in-vitro environment where factors such as aortic shape and size, cardiac output, flow rate waveform, heart rate, systemic vascular resistance and blood pressure can be matched. By using a porcine bioprosthetic valve and then “bicuspidising” it, we showed that BAV velocity profiles exhibit higher velocity jets at the periphery of the aortic lumen. These jets continue along the ascending aorta and arch before dispersing. Wall shear stress was higher in the ascending aorta (and arch in the case of right-non fusion BAV), with the highest levels in the corresponding greater curvature. Oscillatory shear index was lowest in these same sectors.



6

RESULTS - STUDY 3:

Assessment of Aortic Hemodynamics in a Spectrum of Aortic Valve Pathologies

“There is no disease more conducive to clinical humility than aneurysm of the aorta.”

William Osler, 1849 - 1919

Contents

6.1	Overview	187
6.2	Background	187
6.3	Methods	188
6.4	Results	191
6.5	Summary	202

6.1 OVERVIEW

This third results chapter will look at the effect of different aortic valve morphologies on haemodynamics of the thoracic aorta. Patient-specific CFD was used to assess velocity profiles, flow patterns, WSS and OSI in a spectrum of different valve morphologies and pathologies. A total of 45 subjects were studied, divided into 5 groups consisting of healthy and functionally normal tricuspid aortic valves, tricuspid aortic stenosis, tricuspid aortic regurgitation, bicuspid aortic stenosis with right-left cusp fusion, and bicuspid aortic stenosis with right-non cusp fusion. Haemodynamic recordings were used alongside MRI data to run patient-specific CFD.

6.2 BACKGROUND

For many years, treatment guidelines and intervention criteria have concentrated on traditional echocardiographic measurements for the aortic valve (AV) (Nishimura et al. 2014, Vahanian et al. 2012). Furthermore, size remains the principal decision-making index for treatment of the thoracic aorta (Erbel et al. 2014, Svensson et al. 2013). However, there is growing evidence that haemodynamics play an important role in aneurysm formation, with effects on endothelial homeostasis, smooth muscle response, and fibroblast function (Gnasso et al. 2001, Gnasso et al. 1996, Gnasso et al. 1997, Malek et al. 1999, Wootton et al. 1999).

Flow characteristics are highly variable in the thoracic aorta, where the inflow velocity profile is largely dependent on the morphology of the AV. The AV may be stenotic or regurgitant, tricuspid or bicuspid in nature. These different morphologies can lead to alteration of both the velocity and symmetry of blood flowing into the ascending aorta (Mahadevia et al. 2014).

Guidelines for the treatment of aortic disease concentrate on maximal aortic diameter and risk factors for dissection (Erbel et al. 2014, Svensson et al. 2013). Current European Society of

Cardiology guidelines (Vahanian et al. 2012) and American Heart Association guidelines (Nishimura et al. 2014) for intervention on the AV focus on markers of severity of aortic stenosis (AS) and aortic regurgitation (AR). Echocardiographic indices such as maximum aortic velocity (V_{max}), mean pressure gradient, and AV area are used to guide surgical treatment of AS. Jet width, vena contracta, regurgitant volume and fraction, flow reversal, and left ventricular dilatation are indices used to guide intervention for AR. Some of these haemodynamic indices assess the functional effect of aortic valve pathology on the left ventricle. They do not functionally assess its effect on the aorta.

6.3 METHODS

6.3.1 Study Population

45 subjects were studied. They were divided into the following 5 groups: *N-TAV* – subjects with structurally normal tricuspid aortic valves (n=5); *AR-TAV* – aortic regurgitation tricuspid aortic valves (n=10); *AS-TAV* – aortic stenosis tricuspid aortic valves (n=10); *AS-BAV(RL)* – aortic stenosis bicuspid aortic valves with fusion of right and left coronary cusps (n=10); *AS-BAV(RN)* – aortic stenosis bicuspid aortic valves with fusion of right and non-coronary cusps (n=10). Diagnosis of AS or AR was based on trans-thoracic echocardiographic data. AS was defined as aortic $V_{max} > 4$ m/s, mean pressure gradient > 40 mmHg, AV area < 1.0 cm², or AV area index < 0.6 cm²/m². AR was defined as jet width $> 65\%$ of left ventricular outflow tract, vena contracta ≥ 0.6 cm, regurgitant volume > 60 ml/beat, or effective regurgitant orifice ≥ 0.3 cm² (Nishimura et al. 2014). Patients with coarctation were excluded. Full demographics can be found in [Table 6.1](#).

Table 6.1. Demographics, aortic dimensions and hemodynamic indices in the 5 study groups. All continuous data are given as mean \pm standard deviation. *AR-TAV* = aortic regurgitation tricuspid aortic valve; *AS-TAV* = aortic stenosis tricuspid aortic valve; *AS-BAV(RL)* = aortic stenosis bicuspid aortic valve with right left cusp fusion; *AS-BAV(RN)* = aortic stenosis bicuspid aortic valve right non cusp fusion; STJ = sinotubular junction; SOV = sinuses of Valsalva; MAA = mid-ascending aorta; MWSS = mean wall shear stress; OSI = oscillatory shear index; ACEi = angiotensin converting enzyme inhibitor; ARBs = angiotensin II receptor blockers. * denotes significant difference after ANOVA and independent-sample t-test ($p < 0.01$) between the marked group and *N-TAV*. † denotes significant difference between the marked group and *N-TAV*, *AS-TAV* and *AR-TAV*.

	TAV	AR-TAV	AS-TAV	AS-BAV(RL)	AS-BAV(RN)
Demographics					
n	5	10	10	10	10
Male, n (%)	5 (100)	4 (40)	2 (20)	3 (30)	8 (80)
Age	31.3 \pm 3.1	54.0 \pm 10.8	78.0 \pm 1.4*	63.5 \pm 7.5*	64.0 \pm 8.6
Hypertension	1 (20)	3 (30)	5 (50)	4 (40)	4 (40)
B-Blockers	1 (20)	2 (20)	4 (40)	3 (30)	3 (30)
ACEi / ARBs	1 (20)	2 (20)	5 (50)	3 (30)	4 (40)
Aortic Dimensions (mm)					
SOV diameter	28.8 \pm 1.3	33.9 \pm 1.9	34.4 \pm 2.8	32.2 \pm 2.4	35.6 \pm 5.1
STJ diameter	22.8 \pm 0.9	29.7 \pm 1.6	26.3 \pm 2.2	29.9 \pm 2.7	31.8 \pm 2.0
MAA diameter	23.5 \pm 1.0	32.4 \pm 2.4	32.0 \pm 4.3	37.2 \pm 4.4*	39.9 \pm 2.4*

Subjects underwent CMR and MRA to image the entire thoracic aorta in accordance with Section 3.2.1. Slice thickness was 2.0 mm, with 60 sagittal slices per volume. Time-resolved, 2D through-plane flow-MRI was acquired orthogonally in the ascending aorta at the sinotubular junction. Heart rates ranged between 50-95 bpm during which 30 images were reconstructed. The encoding velocity constant (V_{enc}) was set between 1500 and 5000 mm/s depending on the degree of AS, in order to ensure no aliasing. Imaging parameters were those described in Section 3.2.2.

Segmentation and meshing was carried out as defined in Sections 3.3.1 and 3.3.2. This resulted in a final anisotropic mesh consisting of approximately 2 – 6 million tetrahedral elements and 300,000 – 650,000 nodes for the different subjects.

Blood flow simulations were carried out using a stabilised finite element formulation using a global residual tolerance 0.001 and time-step size of 0.00025 s. Four to six cardiac cycles were produced until cycle-to-cycle periodicity in the flow and pressure fields was achieved. The last cardiac cycle was used for the purpose of data analysis for each subject.

6.3.2 Statistical Analysis

Data is presented as mean \pm standard deviation. For each group, data was tested for Gaussian distribution using the Shapiro-Wilk test. One-way analysis of variance (ANOVA) was used to test for difference in results between groups. If this revealed $p < 0.05$, multiple comparisons were carried out between all groups using independent-sample t tests. A p value < 0.01 was considered significant following Bonferroni correction to adjust for multiple comparisons. All statistical analysis was carried out using SPSS (version 21, IBM).

6.4 RESULTS

6.4.1 Velocity Profiles

Figure 6.1 depicts 2D and 3D visualisations of velocity profiles above the AV for a representative subject from each of the 5 groups. When AS is present, the velocity profiles are very peaked and narrow, compared to the broader velocity profiles of *N-TAV* and *AR-TAV*. BAV patients show high velocity in the periphery of the lumen, whereas TAV patients display more central velocity jets.

When assessing for $\text{Flow}_{\text{asymmetry}}$, flow became more asymmetrical in a step-wise fashion from *N-TAV* \rightarrow *AR-TAV* \rightarrow *AS-TAV* \rightarrow *AS-BAV(RL)* \rightarrow *AS-BAV(RN)* (Figure 5.2). BAV patients had $\text{Flow}_{\text{asymmetry}}$ almost twice the magnitude of the TAV patients, indicating blood flow was much more eccentric and asymmetrical (Table 5.2).

Table 6.2. Hemodynamic indices in the 5 study groups. All continuous data are given as mean \pm standard deviation. *AR-TAV* = aortic regurgitation tricuspid aortic valve; *AS-TAV* = aortic stenosis tricuspid aortic valve; *AS-BAV(RL)* = aortic stenosis bicuspid aortic valve with right left cusp fusion; *AS-BAV(RN)* = aortic stenosis bicuspid aortic valve right non cusp fusion; MWSS = mean wall shear stress; OSI = oscillatory shear index. * denotes significant difference after ANOVA and independent-sample t-test ($p < 0.01$) between the marked group and *N-TAV*. † denotes significant difference between the marked group and *N-TAV*, *AS-TAV* and *AR-TAV*.

	TAV	AR-TAV	AS-TAV	AS-BAV(RL)	AS-BAV(RN)
$\text{Flow}_{\text{asymmetry}}$ (%)	4.7 \pm 2.1	23.2 \pm 5.3	41.1 \pm 9.8	72.6 \pm 17.2	78.9 \pm 6.5†
MWSS ^{Asc Aorta} (dyn/cm ²)	9.8 \pm 5.4	17.4 \pm 8.8	35.0 \pm 20.1	27.3 \pm 10.0	37.1 \pm 4.0*
OSI ^{Asc Aorta}	0.18 \pm 0.04	0.21 \pm 0.04	0.19 \pm 0.02	0.18 \pm 0.03	0.13 \pm 0.02

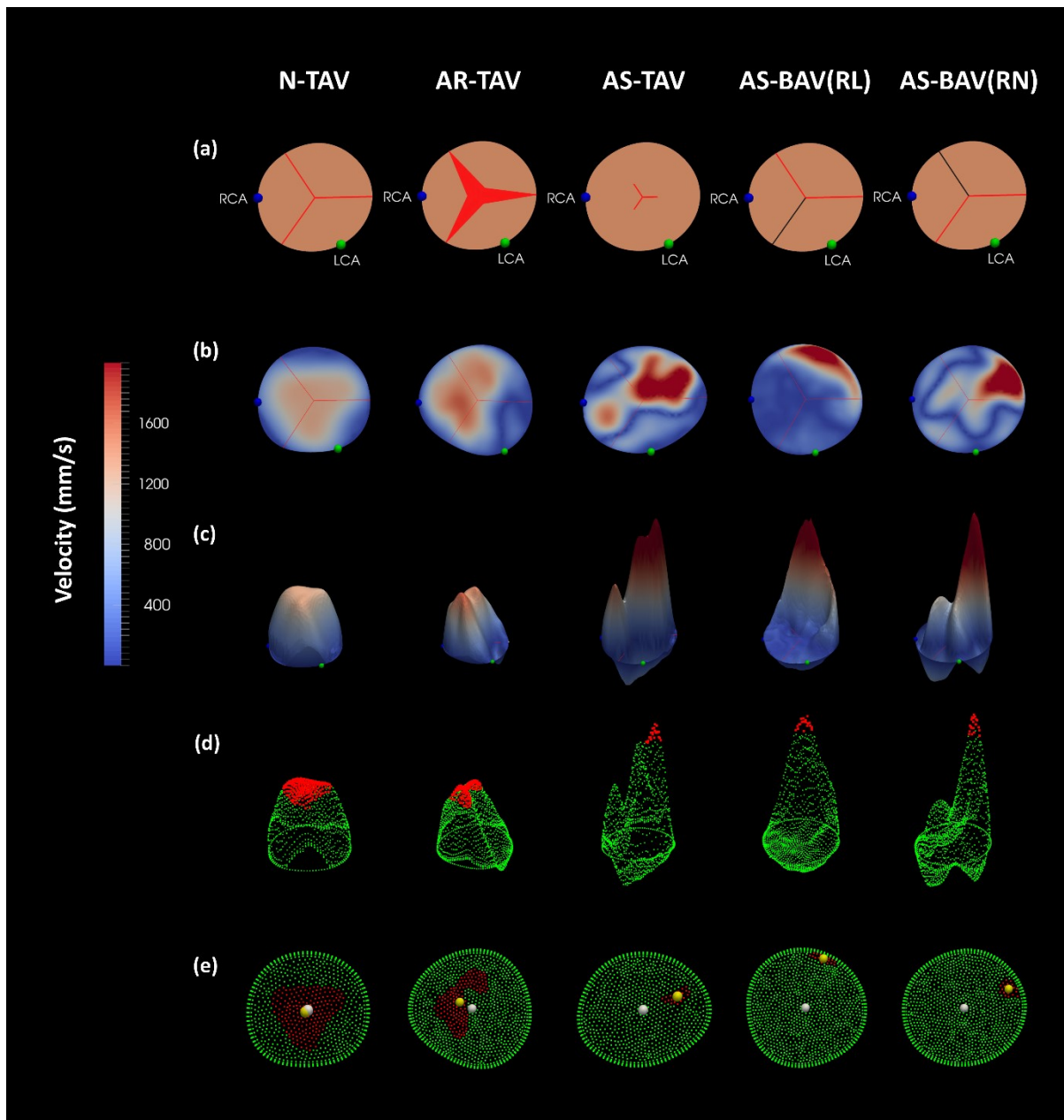


Figure 6.1. **(a)** schematic diagram of AV morphology in the 5 study groups; **(b)** 2D visualisation of the velocity profile above the AV at peak systole; **(c)** 3D visualisation of the velocity profile above the AV at peak systole; **(d)** 3D schematic of the location of the top 15% of velocity at peak systole ($V_{max}^{15\%}$), as shown in red; **(e)** 2D map of the location of $V_{max}^{15\%}$ (white circle = centroid of inflow, yellow circle = centroid of $V_{max}^{15\%}$). RCA = right coronary artery, LCA = left coronary artery.

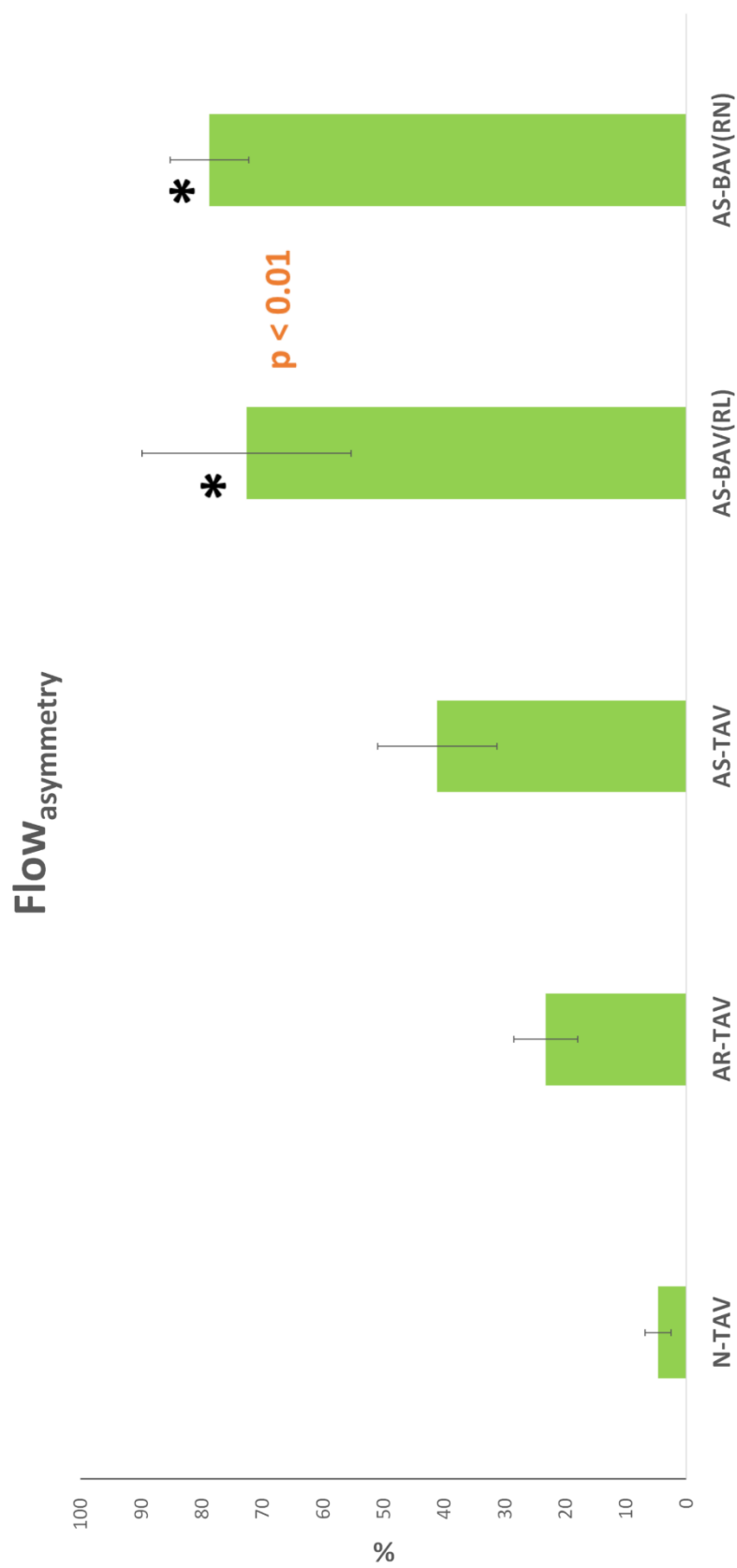


Figure 6.2. Graph showing Flow_{asymmetry} (mean ± standard deviation) for the 5 study groups. * denotes significant difference after ANOVA and independent-sample t-test ($p < 0.01$) between the marked group and *N-TAV*.

6.4.2 Flow Patterns

The *N-TAV* group show laminar flow patterns with relatively uniform parallel 3D velocity streamlines indicating undisrupted flow (Figure 6.3). *AS-TAV* and *AR-TAV* show a slightly higher degree of disrupted flow compared to the *N-TAV* group. BAV patients display the most degree of cork-screw like flow with high velocity jets travelling in a spiral manner around the ascending aorta and arch.

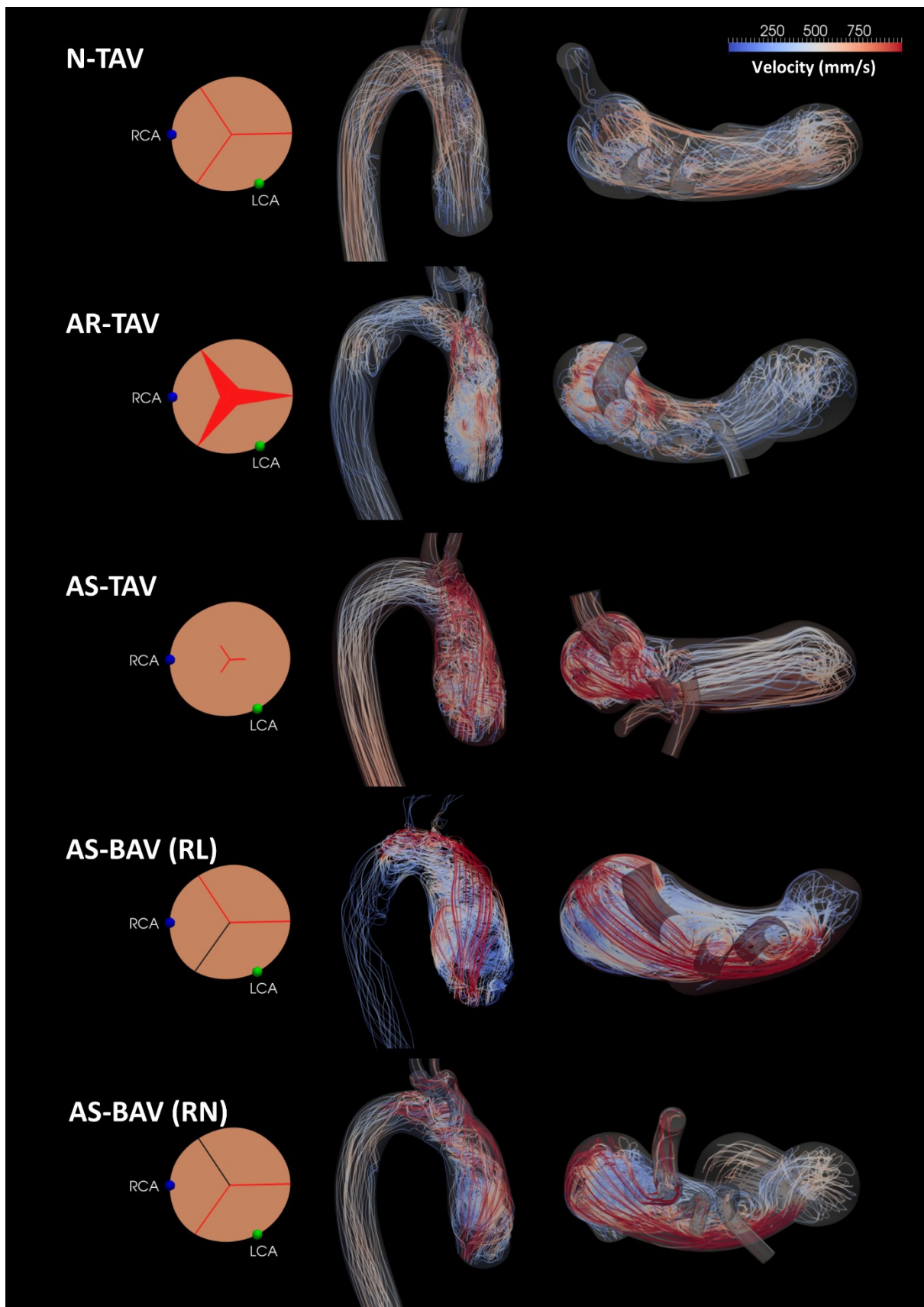


Figure 6.3. 3D velocity streamlines showing trajectory of velocity during peak systole for example patients from the 5 study groups. Higher velocity jets are represented by red colour.

6.4.3 Wall Shear Stress

Figure 6.4 shows cycle-averaged, or mean WSS (MWSS) maps throughout the thoracic aorta for each of the 5 groups. The 3 groups with AS show high levels of MWSS in the ascending aorta, predominantly affecting the greater curvature. *N-TAV* and *AR-TAV* show lower levels of MWSS. Table 6.2 shows the values of MWSS averaged over the ascending aorta ($MWSS^{Asc\ Aorta}$). $MWSS^{Asc\ Aorta}$ was similar in *N-TAV* and *AR-TAV*. *AS-BAV(RN)* showed the highest $MWSS^{Asc\ Aorta}$ at 37.1 ± 4.0 dyn/cm².

For each subject, the ascending aorta was divided into 8 sectors circumferentially. WSS averaged for each sector at each time point was plotted against time over the cardiac cycle (Figure 6.5). For *N-TAV* and *AR-TAV*, WSS plots are low in magnitude and the curves remain close together throughout the cardiac cycle, indicating relatively symmetrical and uniform WSS distribution around the ascending aorta. In contrast, the 3 AS groups (*AS-BAV(RL)*, *AS-BAV(RN)* and *AS-TAV*), show higher WSS plots in the first one-third of the cardiac cycle (corresponding to systole). The sectors displaying high WSS are the right-anterior (RA) and right (R) sectors for the BAV patients, and the anterior (A), right-anterior (RA), and right (R) sectors for the TAV aortic stenosis patients. This indicates significantly asymmetrical WSS distribution.

The 3-dimensional radar plots shown in Figure 6.6 reveal an asymmetrical distribution of MWSS around the circumference of the ascending aorta in the 3 AS groups. When comparing between groups, MWSS in the anterior (A), right-anterior (RA) and right (R) sectors for *AS-BAV(RN)* is statistically higher when compared to *N-TAV* and *AR-TAV* ($p < 0.01$). MWSS in the right-anterior (RA) sector for *AS-BAV(RL)* is higher when compared to *N-TAV* (but only achieving $p < 0.05$).

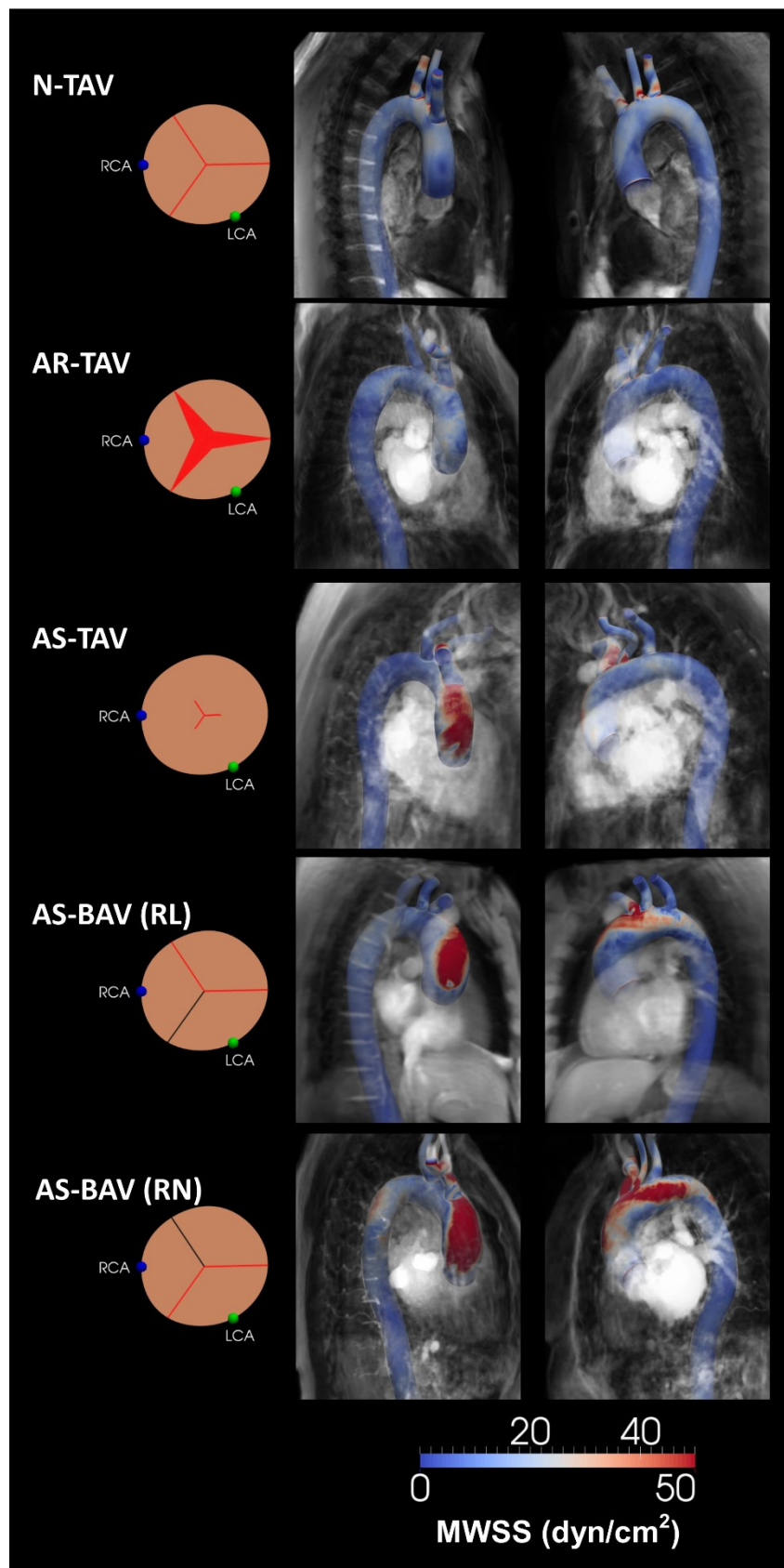


Figure 6.4. Mean wall shear stress (MWSS) maps for example patients from the 5 study groups. The MWSS maps look at the thoracic aorta from 2 different views. Red colour represents areas of high WSS.

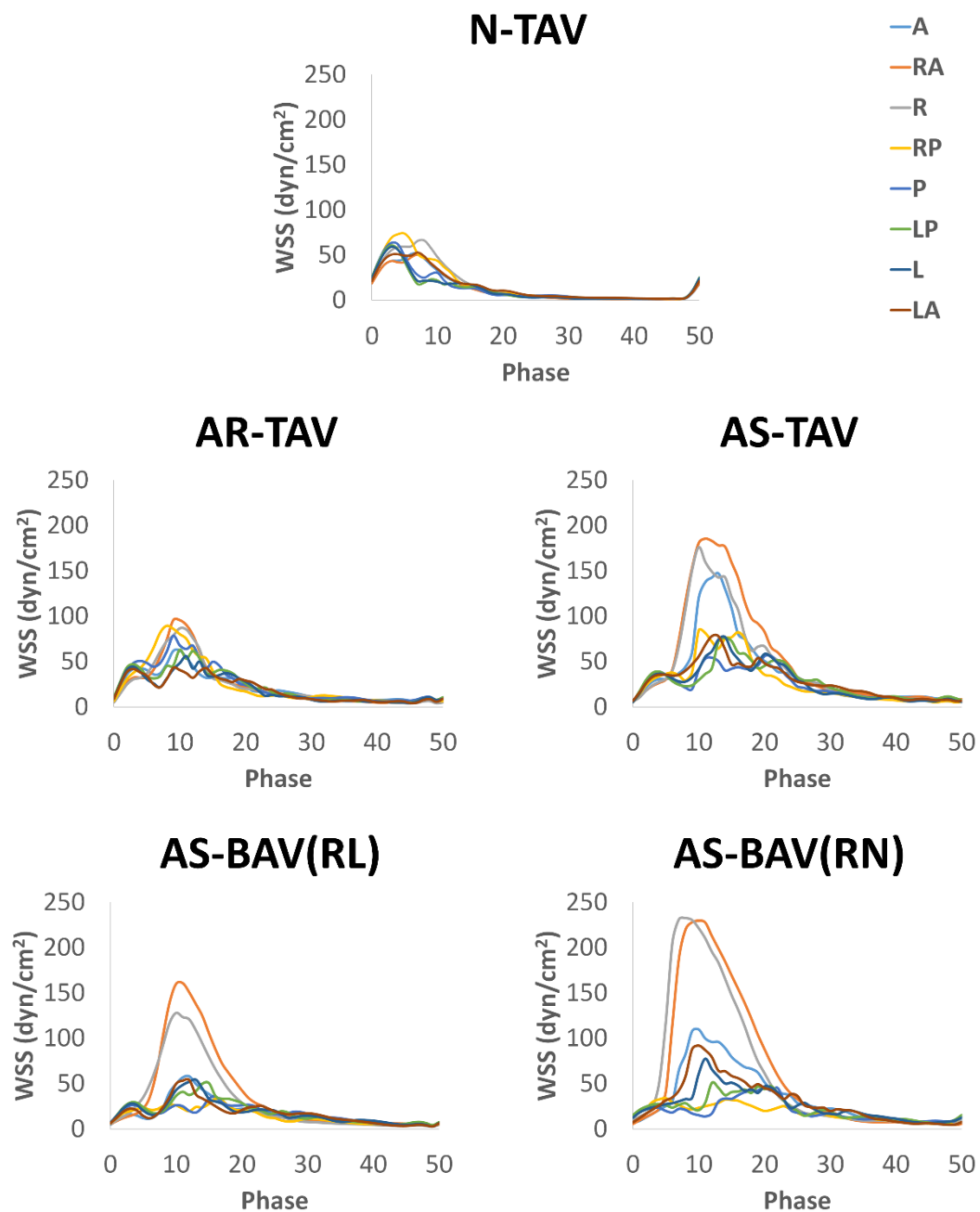


Figure 6.5. Wall shear stress (WSS) plots throughout the cardiac cycle for example patients from each of the 5 groups. Each line represents one of the 8 anatomical sectors of the ascending aorta. A = anterior; RA = right-anterior; R = right; RP = right-posterior; P = posterior; LP = left-posterior; L = left; LA = left-anterior. RCA = right coronary artery; LCA = left coronary artery.

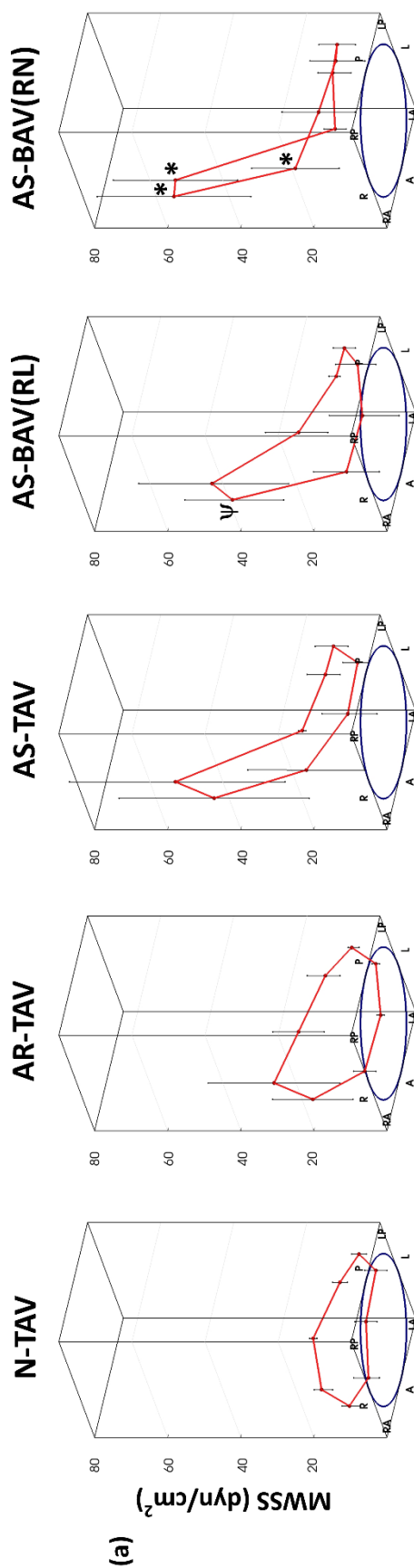


Figure 6.6. Plots of mean wall shear stress (MWSS) for each of the 8 sectors of the ascending aorta. Error bars represent standard deviations of MWSS. * indicates statistically significant differences for *AS-BAV(RN)* cohorts in comparison with *N-TAV* and *AR-TAV* ($p < 0.01$). ψ represents differences for *AS-BAV(RL)* cohorts in comparison with *AR-TAV* ($p < 0.05$). A = anterior; RA = right-anterior; R = right; RP = right-posterior; P = posterior; LP = left-posterior; L = left; LA = left-anterior. RCA = right coronary artery; LCA = left coronary artery.

6.4.4 Oscillatory Shear Index

Table 6.2 shows that ascending aorta oscillatory shear index ($OSI^{Asc\ Aorta}$) is lower in *AS-BAV(RN)* ($OSI^{Asc\ Aorta} = 0.13 \pm 0.02$, compared to 0.18 ± 0.03 for *AS-BAV(RL)*, 0.19 ± 0.02 for *AS-TAV*, 0.21 ± 0.04 for *AR-TAV*, and 0.18 ± 0.04 for *N-TAV*). Only *N-TAV* showed symmetrical OSI values in the ascending aorta (**Figure 6.6**). Both bicuspid groups showed relatively lower OSI levels in the right-anterior (RA) sectors. For *AS-BAV(RN)*, this was statistically significant for the anterior (A), right-anterior (RA) and right (R) sectors when compared to *N-TAV* ($p < 0.01$). The tricuspid subjects (*AS-TAV* and *AR-TAV*) have higher OSI levels on the left side of the aorta, with a significantly higher OSI in the left-anterior (LA) sector for *AS-TAV* when compared to *AS-BAV(RN)* ($p < 0.01$) (see **Figure 6.7**).

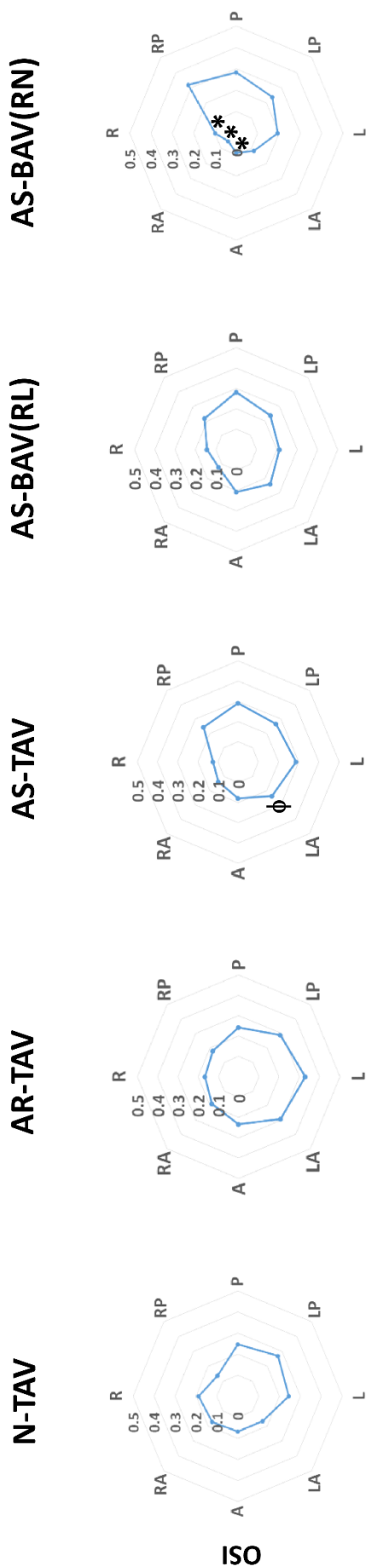
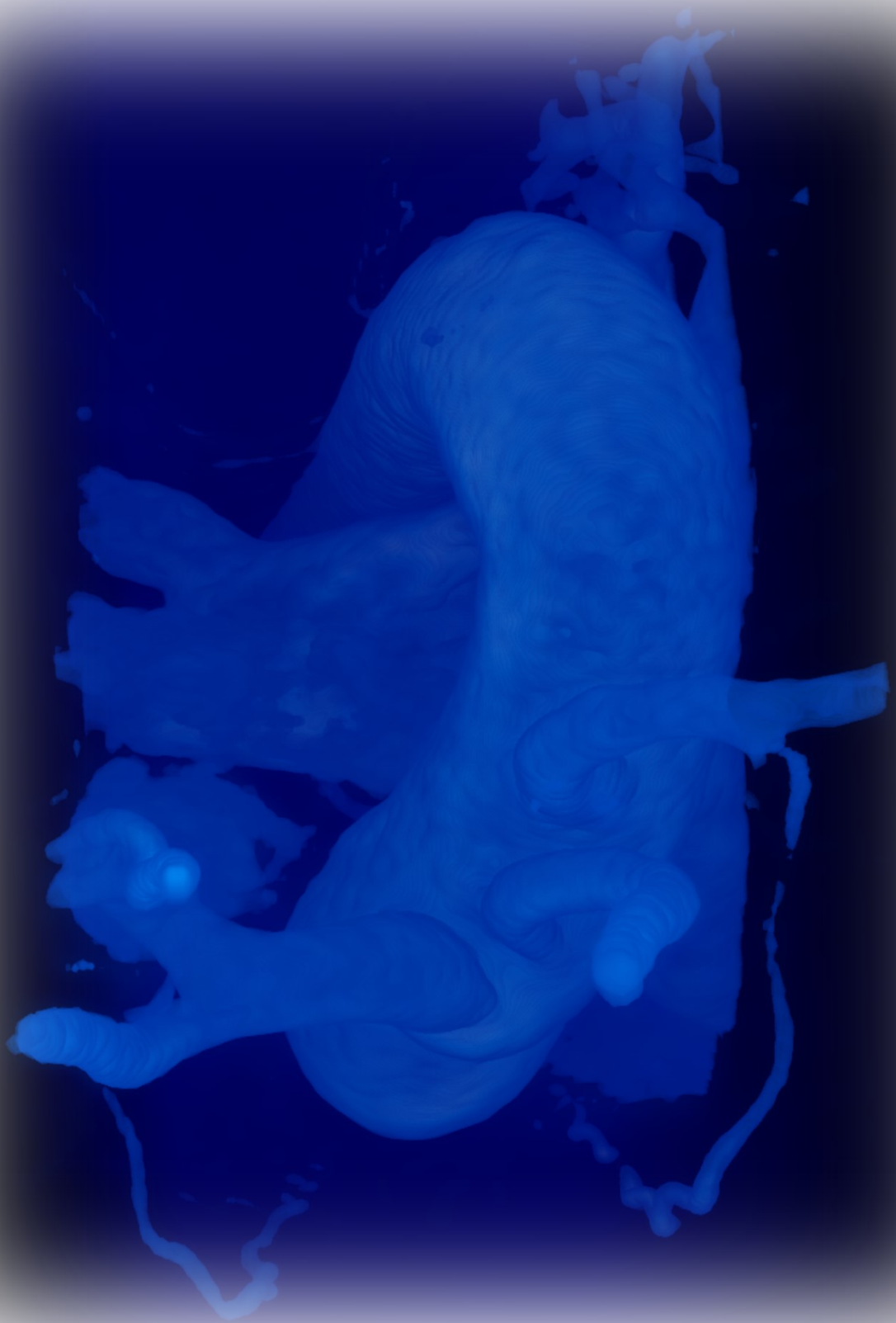


Figure 6.7. Radial graphs of oscillatory shear index (OSI) for each of the 8 sectors of the ascending aorta. * indicates statistically significant differences for *AS-BAV(RN)* cohorts in comparison with *N-TAV* and *AR-TAV* ($p < 0.01$). ϕ represents statistically significant differences for *AS-TAV* cohorts in comparison with *AS-BAV(RN)* ($p < 0.01$). A = anterior; RA = right-anterior; R = right; RP = right-posterior; P = posterior; LP = left-posterior; L = left; LA = left-anterior. RCA = right coronary artery; LCA = left coronary artery.

6.5 SUMMARY

The results from this study show that there are increased velocity jets found at the periphery of the aorta in BAV patients. Velocity streamlines show that these narrow jets impact on the greater curvature of the ascending aorta, and subsequently spiral around the ascending aorta and arch. They cause increased wall shear stress and reduced oscillatory shear index at the greater curvature, corresponding to larger mid-ascending aorta diameters. The outcomes in aortic haemodynamics from this study may relate to a potential explanation for the increased incidence of aortopathy in BAV patients, and indeed to some degree of post-stenotic dilatation seen in some TAV aortic stenosis patients.



7

RESULTS - STUDY 4:

Effect of Valve-Sparing Aortic Root Replacement on Haemodynamics of the Thoracic Aorta

“A thing is right when it tends to preserve the integrity, stability, and beauty of the biotic community. It is wrong when it tends otherwise.”

Aldo Leopold, 1887 - 1948

Contents

7.1	Overview	205
7.2	Background	205
7.3	Methods	207
7.4	Results	211
7.5	Summary	226

7.1 OVERVIEW

This fourth results chapter will analyse aortic haemodynamics before and after valve-sparing aortic root replacement, using the remodelling technique described by Professor Sir Magdi Yacoub. MR imaging and patient-specific CFD were used to compare flow aortic root geometry, flow patterns, axial and radial velocity along the aorta, and wall WSS in different sectors of the thoracic aorta. Further attention was given to sub-analysing the aortic root, by measuring WSS in the individual aortic sinuses of Valsalva, as well as the preserved portion of the native aortic root (interleaflet triangles and commissures).

7.2 BACKGROUND

Surgical management of the aneurysmal aortic root has been the subject of much controversy over the past 3 decades. A composite valved-graft (Bentall) procedure replaces the aortic root and valve (Bentall et al. 1968), but necessitates life-long anticoagulation when mechanical valves are used. To avoid the long-term disadvantages of anticoagulation, thromboembolism, and endocarditis, as well as valve degeneration when bioprosthetic valves are used, valve-sparing root replacement (VSRR) procedures were first introduced in the early 1990s. Yacoub described the remodelling technique which involves replacing the diseased sinuses of Valsalva by 3 tongue-shaped extensions of the tube graft (Sarsam et al. 1993), thus maintaining the sinus shape of the root. David described the reimplantation technique where the aortic valve is sutured inside a cylindrical tube graft (David et al. 1992). In both procedures, the aortic valve leaflets, their hinges, interleaflet triangles and commissures of the native aortic root are preserved. These are more challenging operations compared to the Bentall procedure, requiring the surgeon to craft an aortic root in which the suspensory support of the aortic valve has to be

reconstructed without causing any deformity or asymmetry, any small degree of which would cause valvular regurgitation.

The aortic root is a dynamic structure comprising of the valve leaflets and hinges, commissures, interleaflet triangles, sinuses of Valsalva, annulus, and coronary ostia. Leonardo de Vinci first illustrated the vortical flow patterns of the aortic root in the 16th century (Vinci 1513). Bellhouse described how retrograde vortices in the sinuses of Valsalva allow for smooth closure of the leaflets and promote coronary flow (Bellhouse et al. 1968a, Bellhouse et al. 1968b). More recently, their role in valve opening and closure as well as leaflet stresses has been demonstrated (Katayama et al. 2008, Pisani et al. 2013). These reasons, along with those of eliminating the disadvantages of prosthetic valve replacement, are why more surgeons are embarking on this technically challenging operation of VSRR.

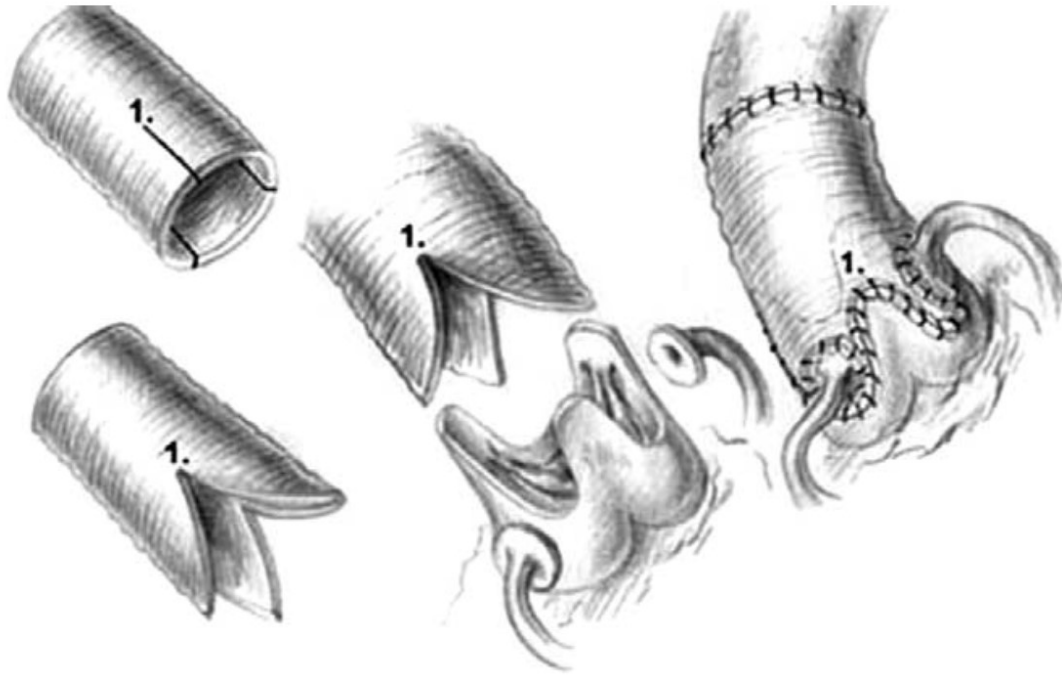


Figure 7.1. The sinuses of Valsalva have been excised from the aortic root, leaving the native valve leaflets and hinges, interleaflet triangles and commissures. A tube graft is tailored to create 3 neo-sinuses of Valsalva. (Hopkins 2003)

7.3 METHODS

7.3.1 Study Population

A total of 10 subjects with dilatation of the aortic root undergoing VSRR using the remodelling technique were studied. All 10 subjects had standard of care imaging pre-op and post-op for comparison of aortic measurements before and after surgery. Three subjects underwent CFD analysis both pre and post-op following VSRR. A further 7 subjects had CFD analysis post-op only. Post-op imaging was carried out between 12 – 24 months following the operation. All 10

subjects had a diagnosis of aneurysm of the aortic root \pm ascending aorta, with a normally functioning trileaflet aortic valve (no significant aortic stenosis or regurgitation).

Subjects underwent CMR and MRA to image the entire thoracic aorta in accordance with Section 3.2.1. Slice thickness was 1.0 - 2.0 mm, with 60 – 80 sagittal slices per volume. Time-resolved, 2D through-plane flow-MRI was acquired orthogonally in the ascending aorta at the level of the aortic valve. Heart rates ranged between 60-85 bpm during which 30 images were reconstructed. The encoding velocity constant (V_{enc}) was set between 3000 mm/s in order to ensure no aliasing. Imaging parameters were those described in Section 3.2.2.

Segmentation and meshing was carried out as defined in Sections 3.3.1 and 3.3.2. This resulted in a final anisotropic mesh consisting of approximately 5 – 7 million tetrahedral elements for the different subjects.

Blood flow simulations were carried out using a stabilised finite element formulation using a global residual tolerance 0.001 and time-step size of 0.00025 s. Four to six cardiac cycles were produced until cycle-to-cycle periodicity in the flow and pressure fields was achieved. The last cardiac cycle was used for the purpose of data analysis for each subject.

7.3.2 Haemodynamic Parameters

As well as the aortic root diameter, the surface area of each sinus of Valsalva was calculated pre-op and post-op to assess for root geometry and symmetry. This was done using the 3D aortic models reconstructed from the imaging data. Root symmetry was calculated by dividing the surface area of the smallest sinus by that of the largest sinus in each patient, and multiplying by 100.

Aortic 3D velocity streamlines were calculated from temporally resolved velocity data for the entire thoracic aorta, with blood velocity magnitude coded by colour. Velocity vectors were visualised at different planes along the aorta, to show the direction and pattern of flow at each location. Further sub-analysis at each plane separated the axial (parallel to the aortic wall) and radial (perpendicular to the aortic wall) components of velocity, which were plotted against time throughout the cardiac cycle. This demonstrated at each plane what proportion was forward flow (axial) and what proportion was helical (radial).

WSS was obtained for the entire thoracic aorta throughout the cardiac cycle. The aorta was divided into root, ascending, arch and descending. At the aortic root, further in-depth sub-analysis was carried out by measuring peak WSS in each of the sinuses of Valsalva separately, in order to look for asymmetry in WSS distribution. Furthermore, the areas of the root corresponding to the interleaflet triangles and commissures were analysed separately to assess for peak WSS. This area of the root is preserved and not replaced by synthetic graft in VSRR, and is the only part of the native root wall which remains post-op. It therefore represents “preserved” aortic tissue which continues to be susceptible to haemodynamic stresses (Figure 7.2).

The remaining thoracic area was also analysed for peak WSS: greater curvature of the ascending aorta; lesser curvature of the ascending aorta; arch; descending aorta.

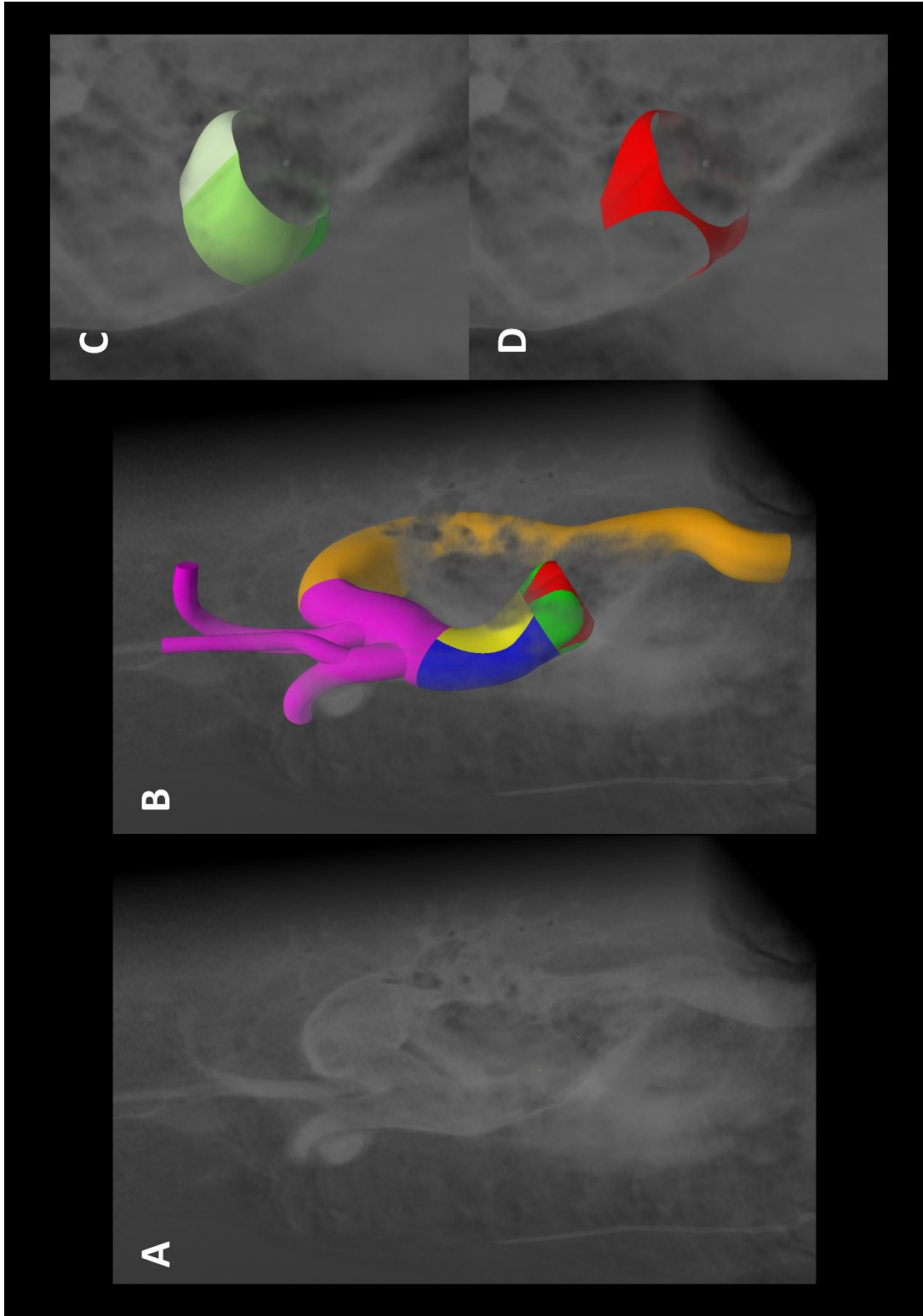


Figure 7.2. (A) MRA aorta; (B) 3D model of the aorta showing different segments (green = sinuses of Valsalva; red = interleaflet triangles and commissures; blue = greater curvature of ascending aorta; yellow = lesser curvature of ascending aorta; pink = arch; orange = descending aorta); (C) sinuses of Valsalva; (D) preserved part of the aortic root (interleaflet triangles and commissures).

7.3.3 Statistical Analysis

Data is presented as mean \pm standard deviation. For measurements of aortic diameter (Table 7.1), data was tested for Gaussian distribution using the Shapiro-Wilk test, and a paired t-test used to determine differences before and after surgery. Other haemodynamic parameters did not undergo statistical analysis, as only 3 patients had both pre and post-op haemodynamic data, with a further 7 patients with only post-op haemodynamic data. These parameters are presented as mean \pm standard deviation for 3 patients in the pre-op group, and mean \pm standard deviation for 10 patients in the post-op group.

7.4 RESULTS

7.4.1 Patient Demographics

A total of 10 patients who underwent VSRR using the remodelling technique were studied. The demographics and aortic dimensions are shown in Table 7.1. Mean age was 50 ± 14 years, with 80% of patients being male. The predominant diagnosis was Marfan Syndrome (90%).

Proximal aortic dimensions were significantly lower post-op compared to pre-op as expected. Root diameter at mid-sinus level decreased from 47.5 ± 3.3 mm to 35.7 ± 2.1 mm ($p < 0.05$). Size reduction was also seen at the sinotubular junction (38.9 ± 6.5 mm pre-op versus 29.6 ± 2.4 mm post-op, $p < 0.05$) and at mid-ascending aorta (37.4 ± 7.0 mm pre-op versus 29.6 ± 4.3 mm post-op, $p < 0.05$). There were no differences at the arch or descending aorta as would be expected.

Post-VSRR dimensions show a constant diameter of ~ 29 mm for the sinotubular junction, mid-ascending aorta and arch, and a larger 35.7mm for the root, demonstrating that the 3 tongue-

shaped extensions of the tube graft do create a sinus-shaped aortic root in the remodelling technique. This was confirmed visually by the 3D aorta models (Figures 7.2).

Table 7.1. Demographics and aortic dimensions. All continuous data are given as mean \pm standard deviation. NS = non-significant.

	Pre-op	Post-op	
Patients (n)	10		
Mean Age (yrs)	50 \pm 14		
Male	8 (80%)		
Marfan Syndrome	9 (90%)		
Annuloaortic ectasia	1 (10%)		
<i>Aortic dimensions (mm)</i>			
Sinuses of Valsalva	47.5 (\pm 3.3)	35.7 (\pm 2.1)	p<0.05
Sinotubular junction	38.9 (\pm 6.5)	29.6 (\pm 2.4)	p<0.05
Mid-ascending aorta	37.4 (\pm 7.0)	29.6 (\pm 4.3)	p<0.05
Arch	28.9 (\pm 6.9)	28.6 (\pm 6.2)	NS
Descending	25.0 (\pm 2.7)	25.3 (\pm 3.8)	NS
<i>Root Geometry</i>			
<i>Sinus of Valsalva Surface Area (cm²)</i>			
Right coronary sinus	16.4 (\pm 3.2)	9.4 (\pm 2.1)	
Left coronary sinus	13.9 (\pm 3.6)	9.4 (\pm 1.6)	
Non coronary sinus	13.9 (\pm 3.3)	8.3 (\pm 1.8)	
Root Symmetry	84%	89%	

7.4.2 Root Geometry

Figure 7.3 shows the pre and post-op 3D shape of the aortic root for 3 patients. The 3 sinuses of Valsalva are shown in different colours. Here, post-op models show 3 individual sinuses are created using the remodelling technique. The surface areas for the 3 sinuses of Valsalva are shown in Table 7.1. Before surgery, the right coronary sinus was the largest ($16.4 \pm 3.2 \text{ cm}^2$, compared to $13.9 \pm 3.6 \text{ cm}^2$ for the left coronary sinus, and $13.9 \pm 3.3 \text{ cm}^2$ for the non-coronary sinus). There was a significant reduction in sinus surface area post-op (post-op surface area $\sim 9 \text{ cm}^2$ for all sinuses). Root symmetry (a measure of similarity in surface area of each sinus of Valsalva) was calculated by:

$$\text{Root Symmetry (\%)} = \frac{\text{Smallest Sinus Surface Area}}{\text{Largest Sinus Surface Area}} \times 100$$

Root symmetry was increased from 84% pre-op to 89% post-op.

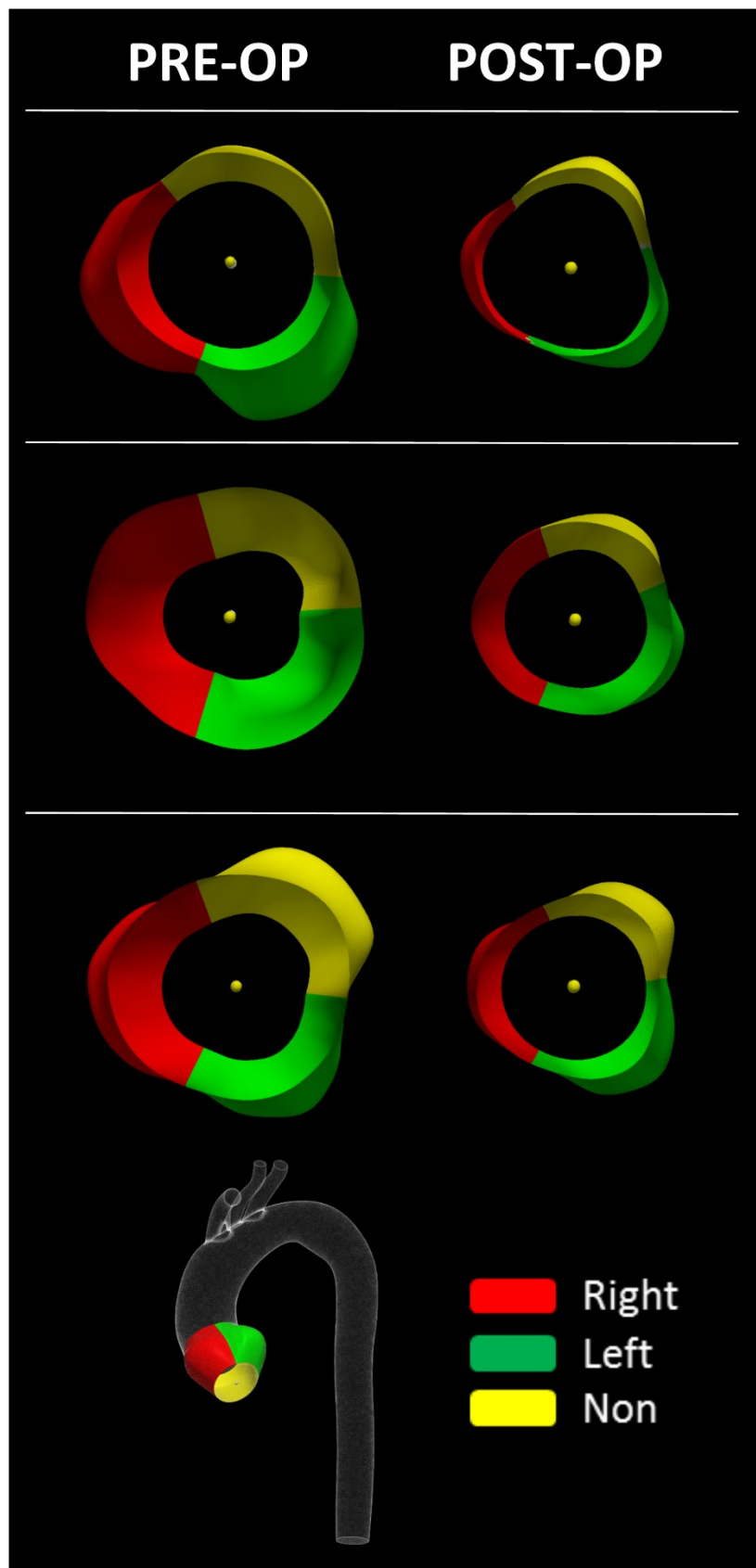


Figure 7.3. Pre and post-op 3-dimensional shape of the aortic root for 3 subjects. The individual sinuses of Valsalva are displayed in different colours.

7.4.3 Velocity Streamlines and Flow Patterns

Figure 7.4 shows velocity streamlines for a patient pre and post-op during early and late systole. Velocity magnitude is colour coded. During early systole, pre-op streamlines show a disrupted flow pattern in the root and proximal aorta, with no obvious organised vortex formation in the root. Post-op velocity streamlines appear much more laminar (parallel), with little disruption along the ascending aorta, arch and descending aorta during early systole. Two distinct and symmetrical vortices can be seen in the sinuses.

In late systole, pre-op streamlines show the high velocity jet (seen in red) impacting on the greater curvature of the ascending aorta, and flow dispersal around the impaction. There is disturbed flow in the ascending aorta and arch, with loss of laminar flow. Following VSRR, the high velocity jet travels further along the ascending aorta in line and parallel with the ascending aorta, to finally turn when it reaches the proximal arch. Flow in the ascending aorta, arch and descending aorta appears more laminar when compared to pre-op.

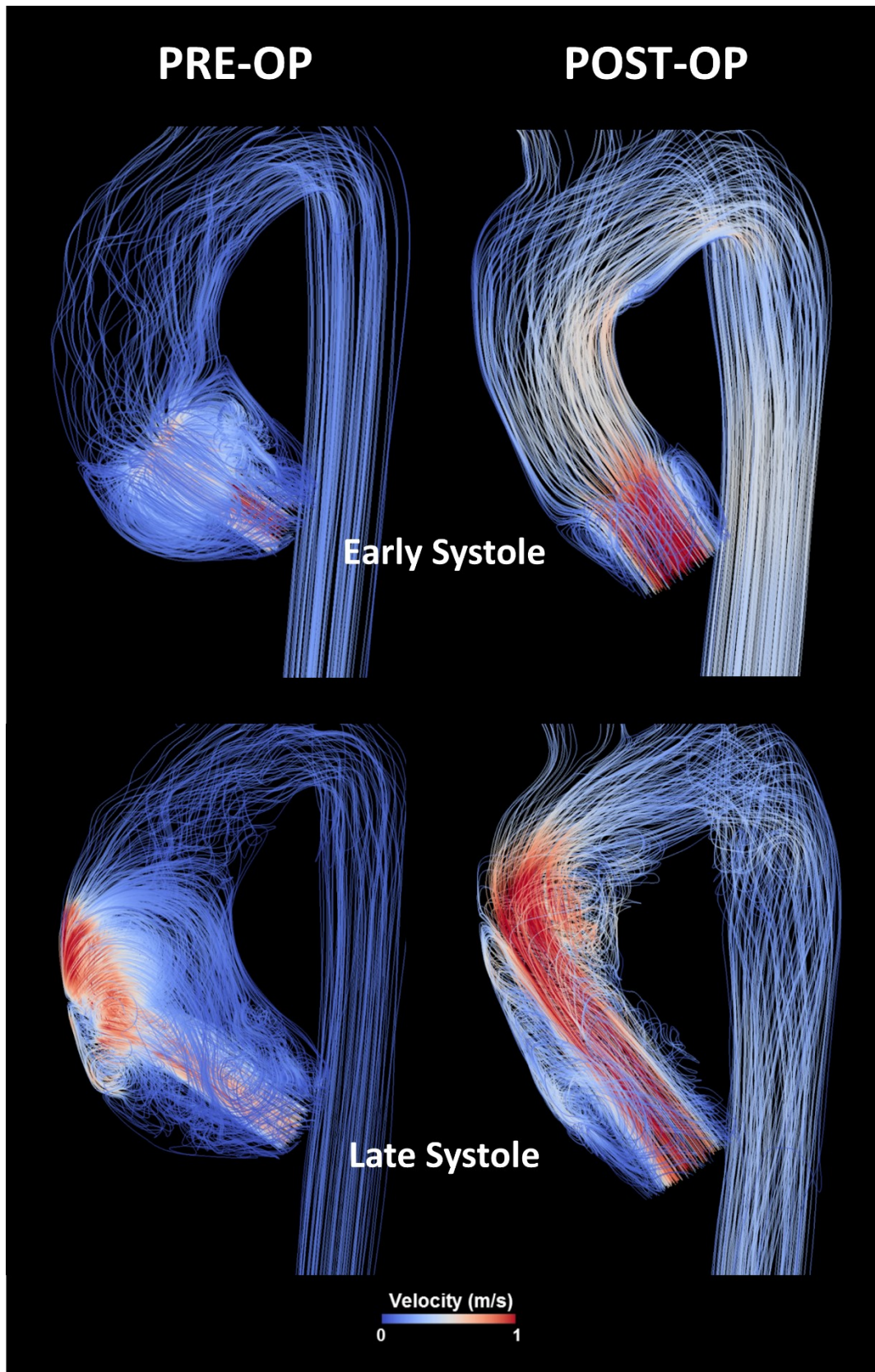


Figure 7.4. Velocity Streamlines for a subject pre and post-op during early systole (top) and late systole (bottom).

7.4.4 Axial and Radial Velocity

Velocity vectors were assessed at different planes along the aorta (mid-sinus, sinotubular junction, mid-ascending aorta, mid-arch, descending aorta). These planes were perpendicular to the aortic wall at each location. [Figure 7.5](#) (top) shows how before surgery, the mid-sinus and sinotubular junction planes show central velocity vectors during systole. But at the mid-ascending aorta plane, higher magnitude velocity vectors are seen at the periphery of the plane, indicating eccentric flow at the aortic wall. In comparison, post-op velocity vectors are relatively central in the mid-sinus, sinotubular junction and mid-ascending aorta during systole.

[Figure 7.5](#) (bottom) shows velocity vectors in the mid-sinus plane divided into axial (parallel to the direction of the aorta) and radial (perpendicular to the direction of the aorta) components. When comparing pre and post-op vectors, post-op axial vector profile appears slightly more symmetrical. Furthermore, pre-op radial velocity vectors look haphazard, with scattered eddies (swirls) of radial velocity unevenly distributed around the sinuses of Valsalva. In contrast, post-op radial vectors show 3 distinct eddies in each sinus of Valsalva.

Averaged axial velocity and radial velocity were plotted against time throughout the cardiac cycle for 3 aortic planes (mid-sinus of Valsalva, mid-ascending aorta, and mid-arch). [Figure 7.6](#) shows these plots for an example patient. At the level of the sinuses of Valsalva, axial velocity was significantly higher than radial velocity, as would be expected. Following VSRR, axial velocity was increased, with a reduction in radial velocity during systole. This pattern was repeated at the level of the mid-ascending aorta, where axial velocity was higher and radial velocity was lower post-VSRR. At the level of mid-arch, axial velocity was only marginally higher post-op, and radial velocity was lower than before surgery.

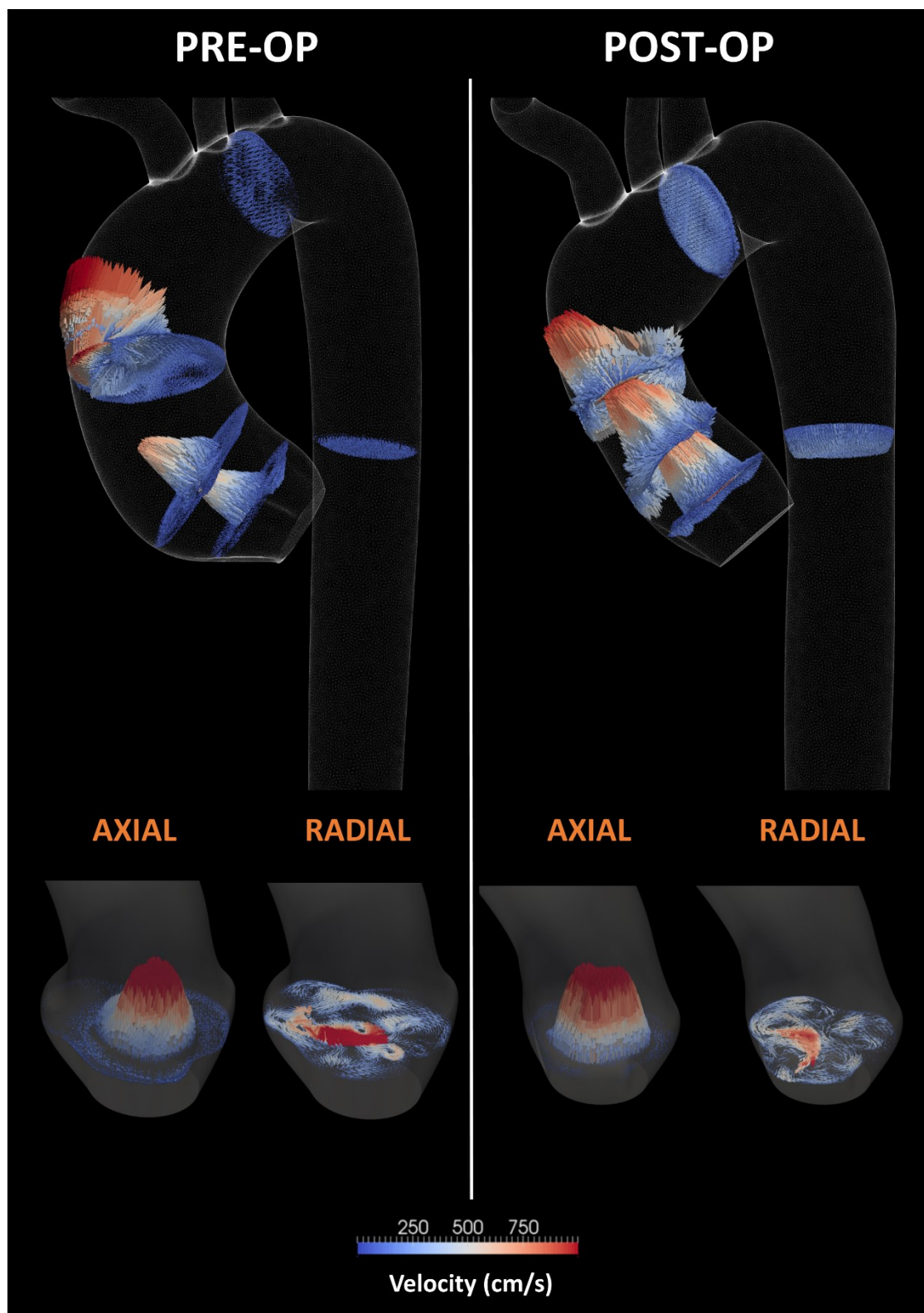


Figure 7.5. (Top) Velocity vectors during systole at mid-sinus, sinotubular junction, mid-ascending aorta, mid-arch, and mid-descending aorta before and after surgery for a patient. (Bottom) Velocity vectors during systole separated into axial and radial vectors at the mid-sinus level.

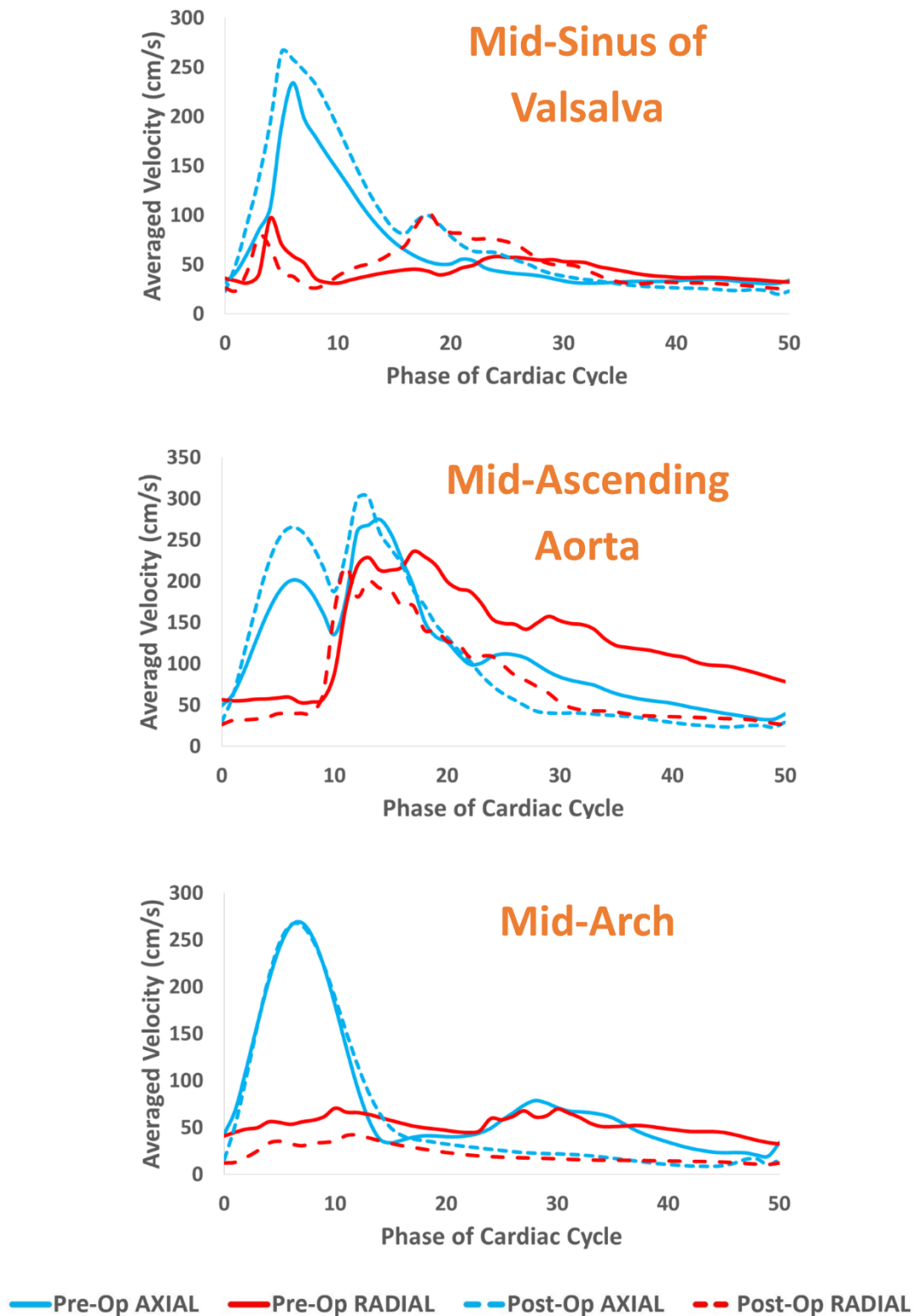


Figure 7.6. Averaged velocity throughout the cardiac cycle before and after surgery at the mid-sinus, mid-ascending aorta, and mid-arch planes for an example patient. Velocity is separated into axial and radial velocity.

7.4.5 Wall Shear Stress – Aortic Root

WSS was measured for the thoracic aorta throughout the cardiac cycle. Further sub-analysis of the aortic root allowed for measurement of peak WSS in each of the individual sinuses of Valsalva. [Figure 7.7](#) shows wall shear stress maps during peak systole in each sinus. The radar plot shows that prior to VSRR, peak WSS was highest in the left and right coronary sinuses (105.9 ± 15.6 dyn/cm² and 106.1 ± 21.1 dyn/cm² respectively), and lowest in the non-coronary sinus (53.9 ± 7.6 dyn/cm²). Post-op, there is a much more even distribution of peak WSS, with a general trend towards reduction (90.2 ± 14.8 dyn/cm², 94.2 ± 14.8 dyn/cm², and 91.7 ± 14.8 dyn/cm² for the left, right and non-coronary sinuses respectively).

The “preserved” aortic root (the interleaflet triangles and commissures) showed lower peak WSS post-op compared to pre-op. Peak WSS in the “preserved” root measured 105.8 ± 30.7 dyn/cm² pre-op compared to 92.7 ± 17.0 dyn/cm² post-op. When sub-analysing the “preserved” aortic root, pre-op peak WSS was highest in the right-left (RL) commissure (103.7 ± 14.3 dyn/cm²), and lower in the right-non (RN) and left-non (LN) commissures (58.3 ± 12.5 dyn/cm² and 62.1 ± 30.7 dyn/cm² respectively) (see [Figure 7.8](#)). Post-op, there was again a more even distribution of peak WSS (peak WSS 62.2 ± 8.6 dyn/cm², 81.4 ± 28.7 dyn/cm² and 84.9 ± 24.9 dyn/cm² in the RL, RN and LN commissures respectively).

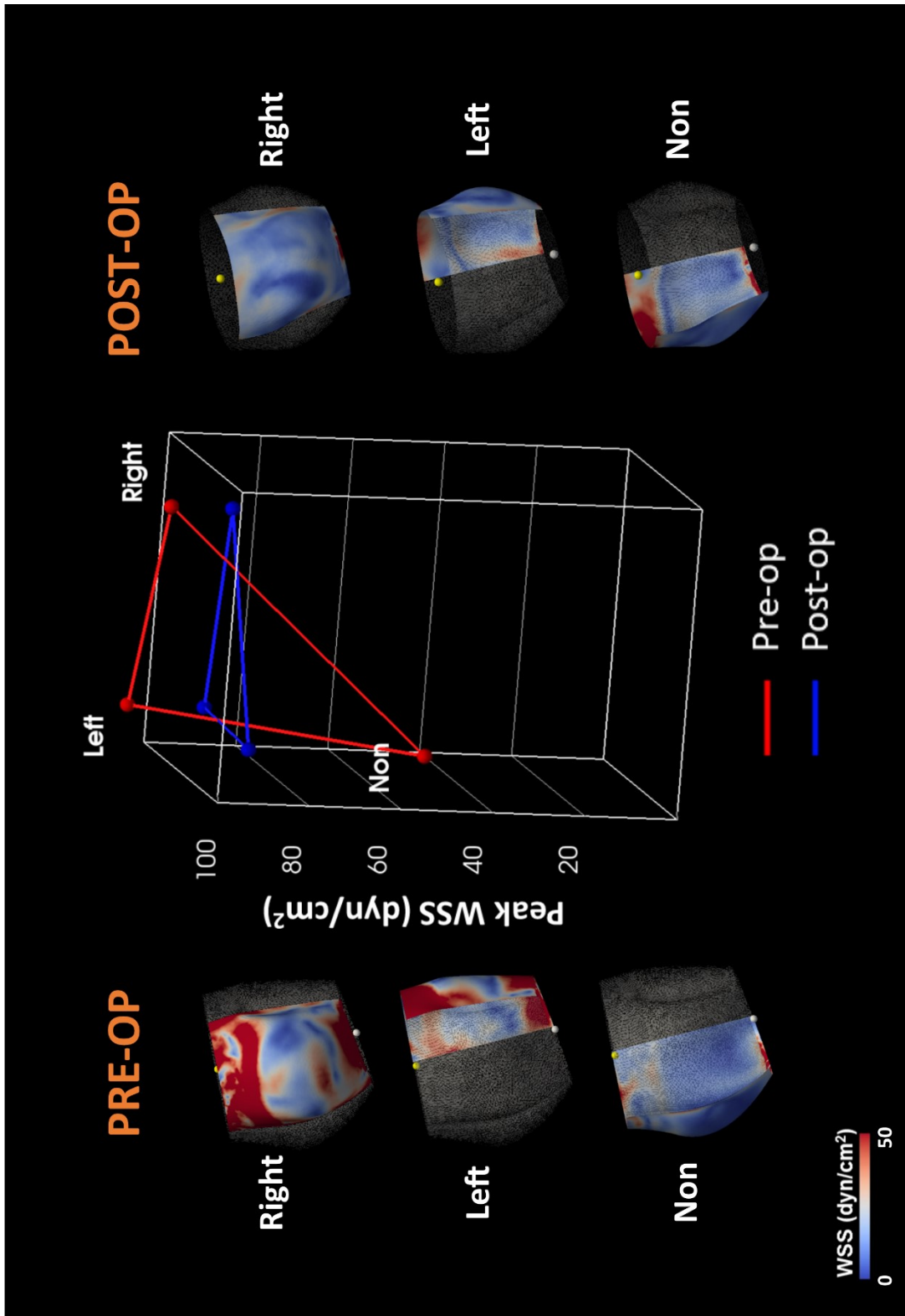


Figure 7.7. WSS maps during peak systole in each of the individual sinuses of Valsalva before and after surgery. Radar plot showing pre-op (red) and post-op (blue) peak WSS in each sinus.

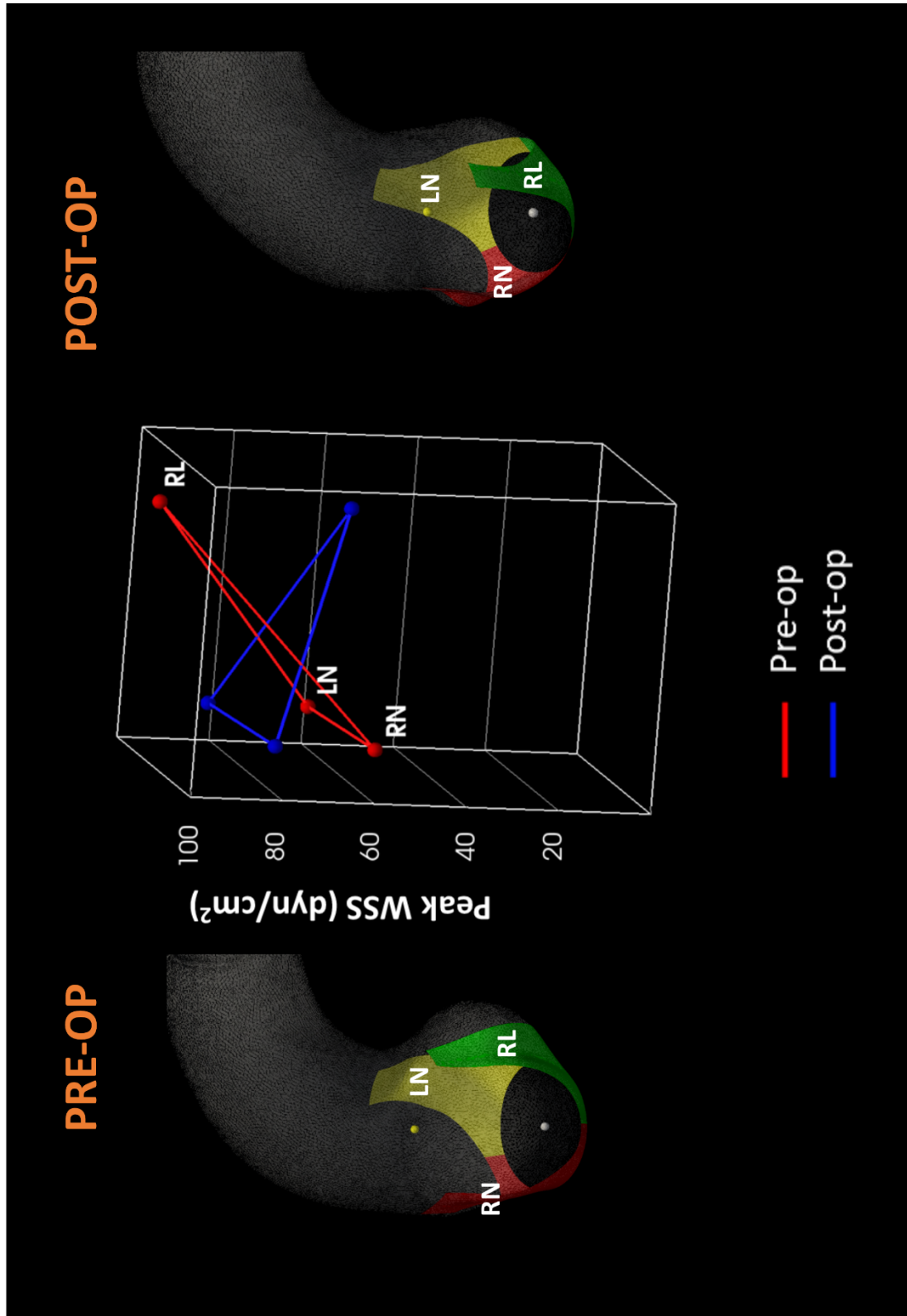


Figure 7.8. The preserved native interleaflet triangles and commissures before and after surgery. Radar plot showing pre-op (red) and post-op (blue) peak WSS in each interleaflet triangle and commissure. RL = right-left; RN = right-non; LN = left-non.

7.4.6 Wall Shear Stress – Remaining Aorta

The remainder of the thoracic aorta was sub-analysed for WSS (Figure 7.9). Peak WSS reduced from 359.1 ± 90.1 dyn/cm² pre-op to 199.3 ± 83.7 dyn/cm² post-op in the greater curvature of the ascending aorta (Figure 7.10). There was no significant change in the lesser curvature (174.0 ± 24.9 dyn/cm² pre-op compared to 171.3 ± 34.6 dyn/cm² post-op). However, in the aortic arch, there was a slight increase in peak WSS (75.0 ± 24.3 dyn/cm² pre-op and 192.1 ± 109.5 dyn/cm² post-op). The same trend was seen in the descending aorta (27.9 ± 8.5 dyn/cm² pre-op and 105.8 ± 56.9 dyn/cm² post-op).

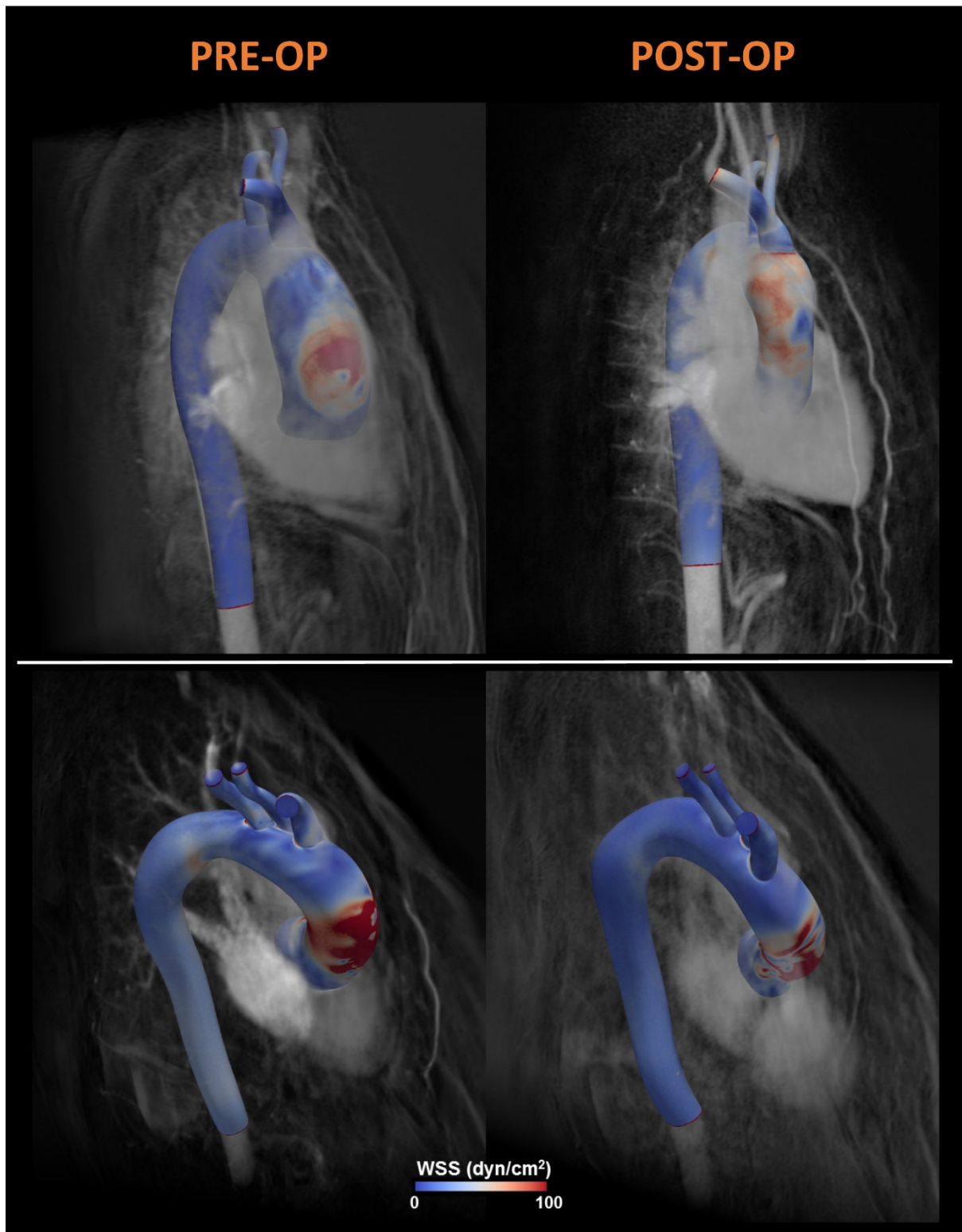


Figure 7.9. WSS maps during systole for two patients before and after VSRR.

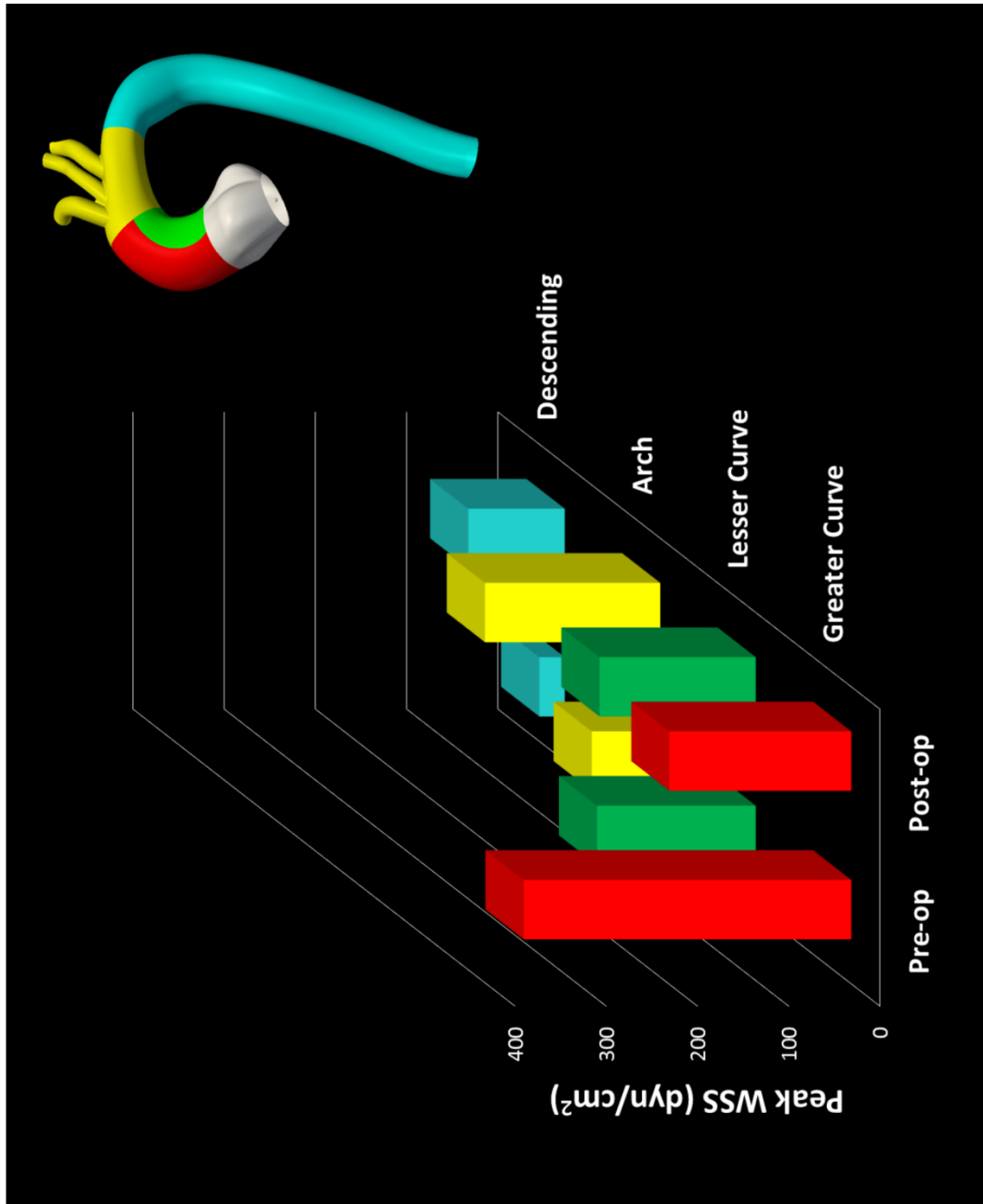


Figure 7.10. Peak WSS before and after surgery for each sector of the remaining thoracic aorta.

7.5 SUMMARY

This study shows that valve-sparing aortic root replacement, using the remodelling technique, leads to reduced sinus size and improved symmetry. WSS is reduced post-op in the native preserved aortic root (interleaflet triangles and commissures) and greater curvature of the ascending aorta. There is increased axial velocity, and reduced radial velocity, indicating enhanced forward flow. The small increase in WSS in the arch and descending aorta indicates the need for continued surveillance and follow-up of the thoracic aorta.

8

DISCUSSION:

“The aim of argument, or of discussion, should not be victory, but progress.”

Joseph Joubert, 1754 - 1824

Contents

8.1	Overview	228
8.2	Study 1: Impact of Patient-Specific Inflow Profile	228
8.3	Study 2: “In Vitro” Comparison Using Phantom	233
8.4	Study 3: Aortic Valve Pathologies	235
8.5	Study 4: Valve-Sparing Aortic Root Replacement	237
8.6	Limitations	240

8.1 OVERVIEW

In this chapter, a full discussion and interpretation of the results of the previous four chapters will be presented. The chapter is divided into four sections, each corresponding to the individual studies. The limitations of each of the four studies will also be discussed.

8.2 STUDY 1: IMPACT OF PATIENT-SPECIFIC INFLOW VELOCITY PROFILE ON HAEMODYNAMICS OF THE THORACIC AORTA

In this study, we presented a methodology for extracting velocity and flow data just distal to the aortic valve, segmenting, and mapping this data onto the inflow mesh of the CFD model. This approach, in combination with non-invasive pressure data and 3-element Windkessel models for outflow boundary conditions, produced a patient-specific workflow for simulating thoracic aortic blood flow. Using this methodology, we have demonstrated the differences in aortic haemodynamics between simulations run with patient-specific inflow velocity profiles versus idealised inflow velocity profiles (e.g. parabolic and plug) on subjects, with different aortic valve morphologies.

Our study demonstrated important differences between healthy and diseased aortic haemodynamics, and also stark differences for each subject between simulations run with patient-specific vs idealised inflow velocity profiles.

In Study 1A, we assessed flow characteristics. In the case of the healthy aortic valve TAV , the idealised parabolic profile V_{para}^{TAV} produced velocity maps and profiles similar to those obtained with the patient-specific profile V_{PS}^{TAV} . Furthermore, other parameters such as V_{max} and radial velocity were also comparable between V_{PS}^{TAV} and V_{para}^{TAV} . This indicates that a parabolic profile is potentially a reasonable choice if an idealised inflow profile has to be used

due to the lack of patient-specific velocity data for simulations involving disease-free aortic valves. However, it must be noted that despite the similarities mentioned above, other haemodynamic parameters showed significant differences between simulations run with idealised and patient-specific velocity profiles. For example $\text{Flow}_{\text{asymmetry}}$ in the transverse aortic arch was almost double in $V_{\text{para}}^{\text{TAV}}$ compared to $V_{\text{PS}}^{\text{TAV}}$. Helicity was also significantly underestimated during systole and diastole using the idealised velocity profiles. Furthermore, solutions obtained with the idealised plug profile $V_{\text{plug}}^{\text{TAV}}$ differed quite substantially from the patient-specific profile $V_{\text{PS}}^{\text{TAV}}$ in the ascending aorta.

In the case of the BAV subject with aortic valvular stenosis *AS-BAV*, simulations run with the patient-specific velocity profile $V_{\text{PS}}^{\text{AS-BAV}}$ revealed how the eccentric asymmetrical inflow profile led to highly complex velocity maps and velocity profiles along most of the length of the thoracic aorta. These complex velocity patterns were not replicated by the two idealised velocity profiles. Despite having identical flow rates to $V_{\text{PS}}^{\text{AS-BAV}}$, the idealised inflow profiles produced different peak velocities (V_{max}) and velocity patterns. Results obtained with idealised inflow profiles $V_{\text{para}}^{\text{AS-BAV}}$ and $V_{\text{plug}}^{\text{AS-BAV}}$ did not demonstrate the high degree of radial velocity obtained with $V_{\text{PS}}^{\text{AS-BAV}}$, neither in direction nor in magnitude.

The results acquired for HFI showed relatively similar values for the patient-specific simulations of both the healthy *TAV* and diseased subjects *AS-BAV*. However, based on the particle pathlines which were used to calculate helicity, the trajectories for these 2 subjects are significantly different. This may question the lack of suitability of HFI as a haemodynamic parameter in capturing relevant numerical differences between healthy and diseased patient-specific velocity profiles.

In Study 1B, we assessed for wall mechanics. For *TAV*, $V_{\text{PS}}^{\text{TAV}}$ and $V_{\text{para}}^{\text{TAV}}$ gave relatively similar low WSS results amongst the 8 sectors of the ascending aorta when looking at both

WSS trends during the cardiac cycle as well as MWSS. This indicates that the parabolic inflow profile gives a reasonably comparable WSS result in the ascending aorta of a healthy tricuspid aortic valve. In comparison, *AS-BAV* and *N-BAV* showed significantly higher WSS during systole as compared to their parabolic equivalents. So in the case of BAV, the idealised parabolic velocity profile did not produce an accurate representation of WSS levels.

When carrying out a point-by-point node-by-node comparison of MWSS measurements between patient-specific simulations and their parabolic counterparts at each data node, BAV subjects exhibited significant differences when compared to their parabolic equivalents. For *AS-BAV*, only 4% of the ascending aorta, and 16% of the arch of the patient-specific simulation demonstrated MWSS values within -25% to +25% of its parabolic equivalent. A similar trend was seen for *N-BAV*, with values of 4% in the ascending aorta, 52% in the arch and 79% in the descending aorta, and for *AR-BAV*, with values of 17% in the ascending aorta, 54% in the arch and 61% in the descending aorta. *TAV* showed more comparable values, with 43% in the ascending aorta, 77% in the arch, and 81% in the descending aorta.

Most differences observed between patient-specific and idealised simulations spanned the entire ascending aorta and to a lesser degree the aortic arch. They started to dissipate in the descending aorta. In the descending aorta, velocity maps and profiles, radial vectors, V_{max} , and $Flow_{asymmetry}$ became equal and formed similar patterns and magnitudes. Comparison of MWSS measurements showed much higher values (% of nodes with MWSS values within -25% to +25% of the parabolic simulation) in the descending aorta, indicating that patient-specific simulations and idealised parabolic simulations yielded similar MWSS results in the descending aorta. The descending thoracic aorta is the first relatively straight location of the thoracic aorta. If free of disease, its cross-section remains relatively constant. These properties allow the flow to reattach and become fully developed.

Our results provide insight into the factors governing haemodynamics in different parts of the thoracic aorta. The most striking differences in haemodynamic parameters between the patient-specific and idealised simulations were seen in the ascending aorta. This shows that ascending aorta haemodynamics is largely dependent on the inflow, which is itself dependent on aortic valve morphology. Similarly, descending aorta haemodynamics is largely independent of aortic valve morphology.

MWSS was higher in all 8 sectors of the ascending aorta for all 3 BAV subjects compared to the parabolic equivalent. There was an asymmetrical distribution of MWSS in the ascending aorta, with the highest MWSS affecting the right-anterior (RA) sector, which corresponds to the greater curvature of the ascending aorta.

A number of studies have been carried out on other parts of the vascular system, including the carotid arteries (Steinman et al. 2002) and abdominal aorta (Figueroa et al. 2006, Waller et al. 1994a), to examine the effects of different inflow boundary conditions on CFD simulations. The abdominal aorta has been investigated by Hardman et al. (Hardman et al. 2013) who compared patient-specific inflow profiles to idealised Womersley profiles generated from the patient's flow-MRI centre-line velocity data. They found that the idealised Womersley profile produced simplified flow patterns with an absence of helical flow. The Helical Flow Index was lower in the Womersley simulation. They also found the maximum velocity of the idealised inlet simulation to be half the magnitude of the patient-specific simulations. The Womersley simulation also displayed smaller radial velocity vectors. These trends were similar to our findings in the thoracic aorta.

Morbiducci et al. investigated the effects of patient-specific inflow profiles versus idealised plug profiles in the thoracic aorta of a healthy subject, and found significant differences in haemodynamic results (Morbiducci et al. 2013), in keeping with our study's results. They also

compared the use of 3-component versus single-component (through-plane) prescribed patient-specific inflow profiles, and found that single-component (through-plane) inflow profiles captured sufficient accuracy in haemodynamic results without the need for the use of 3-component inflow profiles. This was also seen in the abdominal aorta by Chandra et al. (Chandra et al. 2013), who compared 3-component with single-component (through-plane) patient-specific inflow profiles in diseased abdominal aneurysms. In our study, we used single-component (through-plane) patient-specific inflow profiles, and assessed haemodynamics in both a healthy and a diseased subject. We further assessed other parameters such as $Flow_{asymmetry}$ and $Flow_{dispersion}$.

Previous methods of mapping inflow velocity data to the model inlet have included the Schwarz-Christoffel (SC) method (Boutsianis et al. 2008, Chandra et al. 2013). This method requires that the inlet is defined by a closed polygon, which normally is the case with polygonal meshes, however there may be a restriction in other types of models. Particularly, relieving this polygonal constraint is useful when image data is segmented, as smooth closed curves are normally used for inlet delineation. In this study, our mapping scheme allows mapping of the segmented image to any smooth rigid or non-rigid contour. It uses a flexible B-spline framework to map the inflow velocity data to the model inlet, and addresses changes in shape and size between the imaging data and the model inlet.

This study demonstrates that use of idealised inflow velocity profiles produce haemodynamic solutions which are significantly different to patient-specific velocity profiles in subjects with valve pathology. Idealised velocity profiles show little difference in aortic haemodynamics between diseased and healthy subjects, which is in stark contrast to haemodynamic results obtained from using patient-specific velocity profiles. For these reasons, idealised velocity profiles are highly unsuitable for disease research.

8.3 STUDY 2: “IN VITRO” COMPARISON OF AORTIC HAEMODYNAMICS IN BICUSPID AND TRICUSPID AORTIC VALVES USING A PHANTOM HEART AND AORTA MODEL

This is the first study to carry out an “in-vitro” comparison of thoracic aorta haemodynamics between BAV and TAV morphologies by using a phantom heart and aorta model. By matching for aortic size and morphology, haemodynamics such as cardiac output, flow rate waveform, systemic vascular resistance and blood pressure, we were able to make a direct comparison between two simulations where aortic valve morphology was the only differing factor.

Results from this study showed that BAV morphology produced altered flow patterns in the thoracic aorta. Whereas systolic flow jets were relatively central within the lumen of the aorta in the TAV simulation, they were located more peripherally towards the aortic wall in the BAV simulations. Furthermore, the presence of BAV led to a degree of flow acceleration, leading to slightly higher velocities exiting the aortic valve during peak systole for both BAV simulations. These jets travelled around the ascending aorta and arch in a clock-wise direction (right-hand helical) in BAV-RL, whereas in BAV-RN the jets travelled in an anti-clockwise direction (left-hand helical). This is in keeping with 4D flow MRI studies by Barker et al. (Barker et al. 2012).

WSS was elevated in both BAV simulations, compared to a relatively even distribution of lower WSS throughout the thoracic aorta of the TAV simulation. The mid and distal ascending aorta were the sites of the highest levels of WSS in both BAV-RL and BAV-RN. WSS continued to be higher in the mid and distal arch of BAV, although to a lower level. BAV-RN had slightly higher WSS compared to BAV-RL.

Since the commonest location of aneurysm formation in BAV is the ascending aorta, further sub-analysis of this region was undertaken. Our results showed that in TAV, WSS was evenly distributed around the circumference of the ascending aorta. In contrast, both BAV simulations

demonstrated raised WSS in the anterior (A), right anterior (RA) and right (R) sectors of the ascending aorta. These correspond anatomically to the greater curvature of the ascending aorta.

Our results are in keeping with earlier CFD studies, which have shown increased WSS in the ascending aorta of BAV patients (Rinaudo et al. 2014, Viscardi et al. 2010, Wendell et al. 2013). 4D flow MRI studies by Mahadevia et al. also found WSS to be higher in the greater curvature of the ascending aorta of BAV patients (Mahadevia et al. 2014). The greater curvature is the site of typical dilatation in BAV, with evidence of increased medial degeneration (Della Corte et al. 2006), reduction of type I and III collagen, and an increase in smooth muscle apoptosis (Della Corte et al. 2008). Guzzardi et al. correlated regions of increased WSS in BAV patients with extracellular matrix dysregulation and elastic fibre degeneration (Guzzardi et al. 2015), both involved in aneurysm formation.

Oscillatory shear index throughout the ascending aorta was generally lower in the BAV simulations. When comparing the 8 sectors, lower OSI was seen predominantly in the greater curvature. Elevated OSI has been associated with increased vessel wall thickness (Campbell et al. 2012), and it may be proposed that lower OSI may be related to thinning of the wall. The greater curvature of the ascending aorta is typically the site of wall thinning (Della Corte et al. 2006). Raised WSS and lowered OSI may interact together to activate mechanisms involved in wall thinning and aneurysm formation.

8.4 STUDY 3: ASSESSMENT OF AORTIC HAEMODYNAMICS IN A SPECTRUM OF AORTIC VALVE PATHOLOGIES

The results from this study show that the presence of BAV was associated with eccentric blood flow patterns and high helicity. AS, whether bicuspid or tricuspid, led to higher WSS levels in the ascending aorta, with the WSS distribution being asymmetrical and highest in AS-BAV(RN). OSI was also asymmetrically distributed, with the lowest levels found in patients with AS-BAV(RN). These findings corresponded with larger mid-ascending aorta diameters in BAV patients.

The results of this study question whether a patient-specific functional assessment of the thoracic aorta should be undertaken instead of size measurements alone. Guidelines of intervention on the aorta consist of maximal aortic diameter as the principal management criteria, with treatment recommended at smaller diameters in the presence of risk factors such as connective tissue disorders or family history of dissection (Erbel et al. 2014). However, despite these guidelines, there is still an incidence of rupture or dissection when the aorta is below these size criteria.

The findings from this study provide new insights into the adequacy of traditional long-standing indices of valve assessment. Maximum aortic velocity, pressure gradients, valve area, regurgitant volumes and vena contracta are some of the established echocardiographic indices used to assess AV function (Vahanian et al. 2012). Whilst some of these haemodynamic indices relate to symptoms and signs of aortic valve pathology, and assess its effect on the left ventricle, they do not help in the assessment of aortic valve-related aortopathy. There is as of yet no robust functional assessment of the effect of the AV on the aorta, both in terms of flow changes and mechanical stresses.

Evidence shows a strong association between BAV and aneurysm of the ascending aorta, with a risk of subsequent dissection or rupture (Della Corte et al. 2007). Yet the decision of when to intervene surgically on this group of patients can be difficult. The degree of aortic dilatation can be highly variable, and management guidelines are supported by limited evidence. It is not uncommon to be presented with a BAV patient who has an intermediate severity of valve dysfunction and a moderate degree of aortic dilatation. This patient may not fulfil current criteria for surgical intervention on the AV or the aorta, however assessment of some of the functional indices outlined in this study may help decision making.

Wall shear stress was higher in the presence of AS, whether BAV or TAV. MWSS was highest in the right-non fusion BAV patients. The WSS distribution was highly asymmetrical, with the right-anterior (RA) and right (R) sectors experiencing the highest levels of WSS. These sectors correlate with the greater curvature of the ascending aorta. It is interesting to note that both BAV groups had significantly larger mid-ascending aorta diameters compared to *N-TAV*. These trends are in keeping with earlier CFD studies (Rinaudo et al. 2014, Viscardi et al. 2010), although our results are based on larger patient numbers, less hemodynamic assumptions, and more patient-specific parameters. 4D flow MRI studies by Mahadevia et al. also found WSS to be higher in sectors corresponding to the greater curvature of the ascending aorta in patients with BAV (Mahadevia et al. 2014). Meierhofer et al. also used 4D flow MRI and measured WSS to be up to 7.5 dyn/cm^2 (0.75 N/m^2) in the ascending aorta of healthy tricuspid valve patients (Meierhofer et al. 2013), corresponding to $9.8 \pm 5.4 \text{ dyn/cm}^2$ measured in our study. WSS measurements for BAV patients in their study were higher than TAV patients, but were not as high as the levels seen in our study. This may be due to lack of aortic stenosis or insufficiency in their BAV patients.

This study's results also correlate well with the findings of Della Corte et al. who found that medial degeneration was more severe in the greater curvature of BAV aortas (Della Corte et

al. 2006). Type I and III collagen were reduced in this area. Smooth muscle cell apoptosis was seen to be increased in the greater curvature of BAV aortas even before significant dilatation had occurred (Della Corte et al. 2008).

Oscillatory shear index throughout the ascending aorta was lower in the right-non BAV group. When comparing the 8 sectors, lower OSI was seen in the A, RA and R sectors. These findings correlated well with those seen in Study 2. The 3 sectors which demonstrated lower OSI were those corresponding to the greater curvature of the ascending aorta, typically the site of wall thinning (Della Corte et al. 2006).

8.5 STUDY 4: EFFECT OF VALVE-SPARING AORTIC ROOT REPLACEMENT ON HAEMODYNAMICS OF THE THORACIC AORTA

In this study, we have compared aortic haemodynamics in subjects with aneurysms of the aortic root before and after valve-sparing aortic root replacement using the remodelling technique. We have shown that not only is the surface area of the new sinuses of Valsalva smaller as would be expected, but there is also an improvement in the symmetry of the sinuses following surgery. Velocity streamlines show more laminar flow patterns in the aorta, with more symmetrical vortex formation in the root. There was an increase in axial velocity and reduction in radial velocity following surgery indicating an improvement in forward flow. Wall shear stress was reduced following surgery in the native preserved aortic root and neo-ascending aorta, but slightly increased in the arch and descending aorta.

In recent years, the operation of valve-sparing aortic root replacement has gained much attention, not least of which has been in comparing the remodelling technique (Sarsam et al. 1993) with the reimplantation technique (David et al. 1992). Support for the remodelling

technique has focused on its capacity to create 3 neo-sinuses of Valsalva, with the proposed benefits of mimicking the retrograde vortices which allow for leaflet opening and closure, as well as coronary flow. Our results show that the reduction in size as well as improvement in symmetry of the sinuses of Valsalva following surgery were associated with more distinct symmetrical vortices in the sinuses of Valsalva. This correlated well with the eddy currents seen when isolating radial velocity vectors in the mid-sinus plane. Pre-op radial velocity vectors in the mid-sinus plane showed haphazard eddies, whereas following surgery, 3 distinct and symmetrical eddies were seen in the 3 neo-sinuses of Valsalva. This supports the numerical study by Ranga et al. who created a finite element model of the aortic root and found that preservation of sinus geometry in the remodelling technique was an important factor in end-systolic vortex formation (Ranga et al. 2006). Newer versions of the reimplantation technique have tried to re-create the sinus shape of the root by using pre-fabricated bulb-shaped conduits, instead of the straight cylinder conduit. A 4D Flow MRI study of haemodynamics following VSRR (reimplantation technique) by Oechtering et al. found that using an anatomically sinus shaped prosthesis recreated intermediate and large vortices in the root, which was comparable to age-matched volunteers (Oechtering et al. 2016).

We have shown that following VSRR, there is an increase in axial (forward) velocity and reduction in radial (helical) velocity. This indicates an improvement in forward flow, and is supported by velocity streamlines. Pre-op streamlines show a high velocity jet impacting on the greater curvature of the ascending aorta, with surrounding flow dispersion. Post-op streamlines show more laminar flow patterns, with the systolic jet reaching further along the ascending aorta before turning at the arch. Indeed, this is likely to explain why WSS was reduced in the greater curvature of the ascending aorta following surgery. Increased WSS has been identified in the ascending aorta of patients with BAV (Mahadevia et al. 2014), and predominantly affects the greater curvature. Furthermore, areas of high WSS in the greater

curvature have been associated with elastin degradation (Guzzardi et al. 2015). It may explain why this is the typical site of aneurysm formation in BAV. Accordingly, a reduction in WSS following VSRR indicates a haemodynamic change which may prevent future dilatation.

Our results showed a reduction in WSS following VSRR in the aortic root and greater curvature of the ascending aorta. Given that the neo-sinuses of Valsalva and most of the ascending aorta are made up of synthetic graft material, this finding does not necessarily relate to practical benefit. However, given that often the synthetic tube graft does not reach the arch, and ends short of the distal ascending aorta, there may be some benefit in a reduction of WSS in the native distal ascending aorta in preventing future dilatation.

The areas of the native aortic root which are preserved during VSRR are the interleaflet triangles and commissures. Our results show that there was also a reduction in WSS in this native preserved section of the aortic root. When sub-analysing each commissure, there was a trend towards a more even distribution of WSS across all 3 commissures. This may potentially help to prevent future dilatation. Indeed, the main criticism of the remodelling technique is that of the potential for the annulus to dilate and produce aortic regurgitation (Hanke et al. 2009). This has led to some modification of the technique to include an annular stabilising ring (Lansac et al. 2010). Future studies which look at longitudinal follow-up may help decipher whether WSS in the native preserved aortic root relates to post-op dilatation.

We found that following surgery, WSS was slightly elevated in the aortic arch and descending aorta. This may be explained by adjustment of the systolic velocity jet to travel further along the ascending aorta and into the arch before it contacts the aortic wall. It appears that the burden of absorbing the systolic jet has transferred from the ascending aorta pre-operatively to the arch and descending aorta post-operatively. The levels of WSS experienced by the arch and descending aorta post-operatively are not as high as those experienced by the ascending aorta

pre-operatively, which is likely due to loss of velocity as the jet has to travel further before it reaches the arch. Regardless, this is an interesting finding, and indicates the need for follow-up surveillance imaging of the remainder of the thoracic aorta following VSRR.

8.6 LIMITATIONS

Computations were performed under the assumption of rigid walls. Our results may have overestimated WSS, given that increasing compliance and elasticity causes a small reduction in WSS (Xiong et al. 2011). To address this issue, fluid-structure interaction (FSI) analysis which takes into account aortic wall elasticity is needed. A FSI simulation that can accommodate the large displacements and deformations of the ascending thoracic aorta can be accomplished with an Arbitrary Lagrangian-Eulerian formulation (Taylor et al. 2009), although this approach will significantly increase the computational cost. As to how much a full FSI model would alter the results seen in this study remains to be investigated. However, Brown et al. compared a full FSI model with that of a rigid model in a healthy aorta, and found similar results in flow fields, including very similar HFI results (Brown et al. 2012). Future work to assess the impact of FSI models in simulations of diseased aortas would be important.

In our model, we assumed the vessels to behave in a rigid manner. However, the flow-MRI information was dynamically acquired on a fixed Eulerian plane, containing different material sections of the ascending aorta due to its complex motion and deformation. Indeed, the aortic root moves up and down following the contraction and relaxation of the heart, and also deforms radially due to the pulsatile pressure. Our method mapped the history of velocities enclosed within the dynamic segmentations of the aortic root on the fixed Eulerian plane onto the fixed inlet face of the rigid aortic model reconstructed from single-phase MRA data. To address this

issue, a flow-MRI sequence that measures velocity on a Lagrangian plane moving together with the aorta is needed.

Another limitation of the present work is the lack of information on flow splits between the different outflow branches of the aorta. Due to this lack of data, we distributed the measured aortic inflow according to the cross sectional area of the different branches. Additional flow-MRI measurements in the upper branch vessels and descending aorta would remedy this problem.

In our study, we used single-component (through-plane) patient-specific inflow profiles. It is possible to use 3-component (x, y, z planes) inflow profiles, acquired using 4D flow-MRI. The through-plane component is the largest and most important of the velocity components (easily an order of magnitude larger or more than the in-plane components). We believe that this approach is adequate for our purposes. Measurement and imposition of 3-component phase contrast data would necessarily require filtering the MRI data to make sure that a divergence-free velocity field is used as inflow boundary condition for the CFD simulations. A divergence-free velocity condition, a hallmark of incompressible flows, needs to be rigorously satisfied, and this condition will not be met in general in 3-component MRI velocity data. Single-component (through-plane) data does not suffer from this drawback and can therefore be directly used for our purposes. Morbiducci et al. compared the use of 3-component versus single-component prescribed patient-specific inflow profiles, and found that single-component (through-plane) inflow profiles captured sufficient accuracy in haemodynamic results without the need for the use of 3-component inflow profiles. This was also seen in the abdominal aorta by Chandra et al. who compared 3-component with single-component (through-plane) patient-specific inflow profiles in diseased abdominal aneurysms (Chandra et al. 2013).

CFD simulations assume that blood is a Newtonian fluid – i.e. that the velocity gradient is a linear function of the applied stress. Water and many other liquids exhibit such behaviour and are for that reason called Newtonian or ideal fluids. On the other hand, whole blood which is essentially a suspension of erythrocytes, leukocytes and platelets in blood plasma, can be considered as a Newtonian fluid under certain circumstances. Blood has been shown to behave as a Newtonian fluid in large arteries such as the aorta (Grigioni et al. 2005).

In Study 2 (Phantom Study), the bioprosthetic aortic valve was placed inside a straight cylinder, whereas in human anatomy the aortic root is sinus-shaped and contains the origins of the coronary arteries. The shape of the human aortic root creates eddy currents and vortices, which would not have been replicated in our PHA model. Despite this, flow patterns, streamlines and WSS distributions in our PHA model correlated well with clinical studies on human subjects (Mahadevia et al. 2014). Future studies can incorporate the sinus-shaped root into the PHA model.

In Study 3 (Aortic Valve Pathologies), results have not been adjusted for patient characteristics such as age. Future studies should contain different AV morphology groups such as aortic regurgitation BAV, and even mixed AV disease groups (mixed AS and AR). Furthermore, a comparison of BAV morphologies with different degrees of stenosis or regurgitation should be made to assess haemodynamic parameters in bicuspid patients with less than severe AS or AR.

In Study 4 (VSRR), the number of subjects with both pre and post-operative imaging to carry out CFD analysis is small, therefore statistical analysis of haemodynamic indices cannot be performed. Future studies with more subjects would show if the differences in haemodynamic results seen in this study before and after surgery are statistically significant. Our aorta model did not include the coronary arteries, and would therefore have underestimated some of the complexities of flow patterns in the aortic root.

9

CONCLUSIONS:

“Every leaf of the tree becomes a page of the book, once the heart is opened and it has learnt to read.”

Saadi, 1208 - 1291

Contents

9.1	Study 1: Impact of Patient-Specific Inflow Profile	244
9.2	Study 2: “In Vitro” Comparison Using Phantom	245
9.3	Study 3: Aortic Valve Pathologies	245
9.4	Study 4: Valve-Sparing Aortic Root Replacement	246

9.1 STUDY 1: IMPACT OF PATIENT-SPECIFIC INFLOW VELOCITY PROFILE ON HAEMODYNAMICS OF THE THORACIC AORTA

In this study, we have demonstrated differences in aortic hemodynamics between simulations run with patient-specific inflow velocity profiles versus idealised inflow velocity profiles (e.g., parabolic and plug) on subjects with different aortic valve morphologies. Our analysis revealed that idealised inflow boundary conditions can significantly alter velocity patterns and underestimate velocity magnitudes, radial velocity components, helicity and complex flow in the thoracic aorta. Wall indices such as WSS and OSI were significantly affected by using idealised inflow boundary conditions. WSS was grossly underestimated in the idealised parabolic velocity profile, and this was most pronounced in the ascending aorta. WSS in the descending thoracic aorta was more independent of the inflow velocity profile. There were important differences between healthy and diseased aortic hemodynamics.

The use of idealised inflow velocity profiles produces hemodynamic solutions in which differences between diseased and healthy subjects are minimised, therefore making them highly unsuitable for disease research. The aortic valve and its highly complex structure and predisposition to pathological change means that the inflow velocities into the thoracic aorta can be highly variable. This study demonstrated the importance of utilising patient-specific boundary conditions to produce meaningful results not only in healthy but also diseased aortic hemodynamics.

9.2 STUDY 2: “IN VITRO” COMPARISON OF AORTIC HAEMODYNAMICS IN BICUSPID AND TRICUSPID AORTIC VALVES USING A PHANTOM HEART AND AORTA MODEL

This phantom study represents the first study of its kind to compare BAV and TAV haemodynamics in a controlled in-vitro environment. By using a porcine bioprosthetic valve and then “bicuspidising” it, we showed that BAV velocity profiles exhibit higher velocity jets at the periphery of the aortic lumen. These jets continue along the ascending aorta and arch before dispersing. Wall shear stress was higher in the ascending aorta (and arch in the case of right-non fusion BAV), with the highest levels in the corresponding greater curvature. Oscillatory shear index was lowest in these same sectors.

These findings provide an in-vitro validation of MRI and CFD studies on human subjects, and lend further support to a mechanistic link between aortic valve morphology and aortopathy.

9.3 STUDY 3: ASSESSMENT OF AORTIC HEMODYNAMICS IN A SPECTRUM OF AORTIC VALVE PATHOLOGIES

The outcomes in aortic hemodynamics from this study may relate to a potential explanation for the increased incidence of aortopathy in BAV patients, and indeed to some degree of post-stenotic dilatation seen in some TAV aortic stenosis patients. Our results show that there are increased velocity jets found at the periphery of the aorta in BAV patients. Velocity streamlines show that these narrow jets impact on the greater curvature of the ascending aorta, and subsequently spiral around the ascending aorta and arch. They cause increased wall shear stress and reduced oscillatory shear index at the greater curvature, corresponding to larger mid-ascending aorta diameters. These findings provide a possible mechanistic link between aortic valve morphology and aortopathy. CFD is a non-invasive functional assessment of the thoracic

aorta, and may enable development of an improved personalized approach to the diagnosis and management of aortic disease beyond traditional guidelines.

9.4 STUDY 4: EFFECT OF VALVE-SPARING AORTIC ROOT REPLACEMENT ON HAEMODYNAMICS OF THE THORACIC AORTA

Valve-sparing aortic root replacement, using the remodelling technique, leads to reduced sinus size and improved symmetry of the aortic root. There is a reduction in WSS in the native preserved aortic root (interleaflet triangles and commissures) and greater curvature of the ascending aorta following surgery. There is increased axial velocity and reduced radial velocity post-op, indicating enhanced forward flow. The aortic arch and descending aorta exhibit small increases in WSS, thus indicating the need for continued surveillance and follow-up of the thoracic aorta.

10

FUTURE WORK:

“For time and the world do not stand still. Change is the law of life. And those who look only to the past or the present are certain to miss the future.”

John F. Kennedy, 1917 - 1963

Contents

10.1 Addressing Limitations	248
10.2 Future Projects	249
10.3 Final Words	252

10.1 ADDRESSING LIMITATIONS

Our models were formulated under the assumption of rigid walls. Fluid-structure interaction (FSI) analysis would address this limitation by taking into account displacements, deformations and elasticity of the aorta. This would come at a higher computational cost (time taken to run a simulation). In this work, with the assumption of rigid walls, average aortic mesh size was between 5 – 7 million elements, with a time step size of 0.00025 seconds for the CFD simulations. Computational time to run 3 cardiac cycles averaged between 18 – 36 hours. FSI analysis would certainly make this computational time longer. However it would be important to investigate how much the results seen in this study would be altered, especially with different aortic valve morphologies, and with different size and shape of the aorta.

Further information regarding flow splits of the head and neck vessels and descending aorta would help further improve the accuracy of outflow boundary conditions. This would require flow-MRI measurements at each branch taken perpendicular to the vessel axis. These flow measurements could then be used to calculate the proximal resistance, capacitance and distal resistance of the Windkessel outflow boundary condition model.

In order to utilise 3-component (x, y, z planes) inflow profiles for the inflow boundary conditions, 4D flow-MRI acquisition would be required as well as modification of the in-house software written in *Matlab* (*The Mathworks Inc., Massachusetts, USA*) in order to be able to extract 3 components of velocity, segment and map onto the inflow mesh. This would require extraction of the whole “volume” of velocity data for the entire thoracic aorta, followed by sampling of that data on a single plane which is at the location of the inflow mesh. Measurement and imposition of 3-component phase contrast data would necessarily require filtering the MRI data to make sure that a divergence-free velocity field is used as inflow boundary condition for the CFD simulations. Achieving this would allow comparison of 3-component and single-

component (through-plane) inflow profiles to see if there are significant differences in haemodynamic indices such as WSS.

10.2 FUTURE PROJECTS

10.2.1 Longitudinal Studies

CFD provides a sophisticated non-invasive method of acquiring haemodynamic data in the thoracic aorta. To fully acquire clinical relevance, longitudinal studies will be required to look at the long-term effects of these haemodynamic parameters on clinical outcomes. Patients who undergo functional imaging with measurement of these haemodynamic indices can subsequently be monitored by routine clinical assessment and imaging. These can include serial measurements of aortic size, rate of growth, as well as the development of acute aortic events.

There are two clinical groups of patients in whom it would be both appropriate and imperative to carry out these longitudinal studies. The first is patients with BAV who either have a normally functioning aortic valve (no stenosis or regurgitation), mild stenosis/regurgitation or moderate stenosis/regurgitation without any other indications for surgery (for e.g. aortic size above treatment criteria). These patients would normally undergo surveillance monitoring of both the aortic valve and the aorta. It would be important to measure haemodynamic indices such as WSS in these patients at the initial point of diagnosis (or as early as possible), and to follow up the aortic size and rate of growth over time. This would allow for direct assessment of the link between such haemodynamic parameters and aortic dilatation.

The second group of patients would be those with connective tissue disorders such as Marfan Syndrome. These patients have an inherent genetic and histopathological reason for aortic dilatation. However, not all patients with the same gene mutations have aortic dilatation or

aortic events at the same rate. It is still unclear why some dilate or dissect earlier than others. It would be interesting to see if haemodynamic indices play a role in accelerating the disease process to promote early rather than late dilatation.

These studies would likely be the most important in implementing functional assessment of the aorta into routine clinical practice.

10.2.2 Histopathological / Proteomic Comparison Studies

In order to further investigate the effects of haemodynamic indices such as WSS on pathological change in the aortic wall, a study which carries out analysis on surgical biopsy specimens of the aorta at designated areas would be necessary. In patients who require surgery (either in the form of aortic valve replacement, aortic root replacement, or aortic valve and ascending aorta replacement), full-thickness biopsy specimens of the aorta could be taken. In the case of aortic valve replacement, this could be achieved in the greater curvature and lesser curvature (by sampling the aorta at the two ends of the oblique aortotomy incision). In the case of aortic root replacement and aortic valve and ascending aorta replacement, further sampling can be taken in other areas of the proximal aorta. These locations can then be correlated to the patient-specific CFD model for that subject, and haemodynamic indices such as WSS or OSI can be measured at those locations.

Laboratory analysis of the aortic samples could involve both histopathological analysis as well as more advanced proteomics. Measurement of the thickness of the tunica media would show whether areas of high WSS are linked with medial thinning. Further analysis of elastin and fibrillin may corroborate the findings of Guzzardi et al. in showing elastic fibre degradation in areas of high WSS (Guzzardi et al. 2015). Proteomics analysis would further investigate

upregulation or downregulation of proteins involved in cell signalling pathways implicated in aneurysm formation.

10.2.3 Post Intervention Studies

Study 4 investigated differences in haemodynamics before and after valve-sparing root surgery. Further studies to assess the effect of the Bentall root replacement procedure (valve-conduit graft) would be interesting, particularly looking at the consequences of absent sinuses of Valsalva. Further to this, comparison of the remodelling technique VSRR of Yacoub (Sarsam et al. 1993) with that of the reimplantation technique VSRR of David (David et al. 1992) would be appealing.

Currently, a number of different bioprosthetic and mechanical aortic valves exist which offer different geometries and materials. As newer prosthetic valves enter the market, valve companies strive to improve long-term durability as well as reducing valve-related complications such as thrombosis, haemolysis and patient-prosthetic mismatch. Comparison of haemodynamics before and after valve replacement could be carried out, as well as comparison of different valve types. This would be particularly important in the case of BAV, in which some studies show no further dilatation of the aorta after isolated aortic valve replacement (Abdulkareem et al. 2013), and other studies show continued dilatation post-op (Naito et al. 2017).

Another area of interest would be in comparing aortic haemodynamics following surgical aortic valve replacement (AVR) and trans-catheter aortic valve implantation (TAVI). TAVI is now an established treatment for management of aortic stenosis for patients who are deemed high risk for standard surgical aortic valve replacement (Cribier et al. 2002) (Leon et al. 2010) (Smith et al. 2011). There is as yet little knowledge of aortic haemodynamics following TAVI.

The only study to date comparing TAVI and surgical AVR has used 4D flow MRI to show more vortices and helices with AVR, eccentric flow with more AVR and TAVI, and raised WSS in the ascending aorta in both AVR and TAVI compared to controls (Trauzeddel et al. 2016). As indications for TAVI use are starting to push into the realms of younger less risky surgical candidates, it is imperative to have a good understanding of the resulting aortic haemodynamics post-TAVI.

10.3 FINAL WORDS

The spectrum of aortic disease is varied and complex. Aortic size alone does not distinguish between different pathological processes which vary in their risk of acute complications. Traditional guidelines for the aorta, which focus on maximal aortic diameter, have remained largely unchanged for many years. Data from epidemiological studies and registries indicate acute aortic dissection or rupture can occur when the aortic size is below intervention criteria. Aortic valve morphology, particularly in the case of BAV, is deeply related to aortopathy. Evidence is now growing for the haemodynamic link between the valve and aortic dilatation. This has highlighted the need to develop a functional assessment of the thoracic aorta in order to understand the haemodynamic causes for aortopathy, as well as a means of better predicting complications. CFD provides a potential method of acquiring this functional assessment, and with development and validation may prove to be the game-changer in the management of aortopathy. The future of tackling this disease process must surely be more patient-specific than it is today.

BIBLIOGRAPHY

Abdulkareem N, Soppa G, Jones S, Valencia O, Smelt J, Jahangiri M. Dilatation of the remaining aorta after aortic valve or aortic root replacement in patients with bicuspid aortic valve: a 5-year follow-up. *Ann Thorac Surg.* 2013;96:43-9.

Alastruey J, Khir AW, Matthys KS, Segers P, Sherwin SJ, Verdonck PR, Parker KH, Peiro J. Pulse wave propagation in a model human arterial network: Assessment of 1-D visco-elastic simulations against in vitro measurements. *J Biomech.* 2011;44:2250-8.

Anderson RH. Clinical anatomy of the aortic root. *Heart.* 2000;84:670-3.

Anderson RH, Webb S, Brown NA, Lamers W, Moorman A. Development of the heart: (2) Septation of the atriums and ventricles. *Heart.* 2003a;89:949-58.

Anderson RH, Webb S, Brown NA, Lamers W, Moorman A. Development of the heart: (3) formation of the ventricular outflow tracts, arterial valves, and intrapericardial arterial trunks. *Heart.* 2003b;89:1110-8.

Baciewicz FA, D. G. Penney, W. A. Marinelli, and, Marinelli. R. Torsional ventricular motion and rotary blood flow. What is the clinical significance. *Cardiac Chronicle.* 1991;5:1-8.

Barker AJ, Markl M, Burk J, Lorenz R, Bock J, Bauer S, Schulz-Menger J, von Knobelsdorff-Brenkenhoff F. Bicuspid aortic valve is associated with altered wall shear stress in the ascending aorta. *Circ Cardiovasc Imaging.* 2012;5:457-66.

Bauer M, Gliuch V, Siniawski H, Hetzer R. Configuration of the ascending aorta in patients with bicuspid and tricuspid aortic valve disease undergoing aortic valve replacement with or without reduction aortoplasty. *J Heart Valve Dis.* 2006;15:594-600.

Bellhouse BJ, Bellhouse FH. Mechanism of closure of the aortic valve. *Nature*. 1968a;217:86-7.

Bellhouse BJ, Bellhouse FH, Reid KG. Fluid mechanics of the aortic root with application to coronary flow. *Nature*. 1968b;219:1059-61.

Bellhouse BJ, Reid KG. Fluid mechanics of the aortic valve. *Br Heart J*. 1969;31:391.

Bentall H, De Bono A. A technique for complete replacement of the ascending aorta. *Thorax*. 1968;23:338-9.

Beroukhim RS, Kruzick TL, Taylor AL, Gao D, Yetman AT. Progression of aortic dilation in children with a functionally normal bicuspid aortic valve. *Am J Cardiol*. 2006;98:828-30.

Bissell MM, Hess AT, Biasioli L, Glaze SJ, Loudon M, Pitcher A, Davis A, Prendergast B, Markl M, Barker AJ, Neubauer S, Myerson SG. Aortic dilation in bicuspid aortic valve disease: flow pattern is a major contributor and differs with valve fusion type. *Circ Cardiovasc Imaging*. 2013;6:499-507.

Boutsianis E, Gupta S, Boomsma K, Poulidakos D. Boundary conditions by Schwarz-Christoffel mapping in anatomically accurate hemodynamics. *Ann Biomed Eng*. 2008;36:2068-84.

Brown AG, Shi Y, Marzo A, Staicu C, Valverde I, Beerbaum P, Lawford PV, Hose DR. Accuracy vs. computational time: translating aortic simulations to the clinic. *J Biomech*. 2012;45:516-23.

Campbell IC, Ries J, Dhawan SS, Quyyumi AA, Taylor WR, Oshinski JN. Effect of inlet velocity profiles on patient-specific computational fluid dynamics simulations of the carotid bifurcation. *J Biomech Eng.* 2012;134:051001.

Cebral JR, Vazquez M, Sforza DM, Houzeaux G, Tateshima S, Scrivano E, Bleise C. Analysis of hemodynamics and wall mechanics at sites of cerebral aneurysm rupture. *J Neurointerv Surg.* 2015;7:530-6.

Cebral JR, Yim PJ, Lohner R, Soto O, Choyke PL. Blood flow modeling in carotid arteries with computational fluid dynamics and MR imaging. *Acad Radiol.* 2002;9:1286-99.

Chandra S, Raut SS, Jana A, Biederman RW, Doyle M, Muluk SC, Finol EA. Fluid-structure interaction modeling of abdominal aortic aneurysms: the impact of patient-specific inflow conditions and fluid/solid coupling. *J Biomech Eng.* 2013;135:81001.

Chandran KB. Flow dynamics in the human aorta. *J Biomech Eng.* 1993;115:611-6.

Chandran KB, Yearwood TL, Wieting DW. An experimental study of pulsatile flow in a curved tube. *J Biomech.* 1979;12:793-805.

Charitos EI, Sievers H-H. Anatomy of the aortic root: implications for valve-sparing surgery. *Annals of Cardiothoracic Surgery.* 2013;2:53-6.

Chien S, Li S, Shyy YJ. Effects of mechanical forces on signal transduction and gene expression in endothelial cells. *Hypertension.* 1998;31:162-9.

Clayton M. Medicine: Leonardo's anatomy years. *Nature.* 2012;484:314-6.

Cohn L. Cardiac Surgery in the Adult. 2008:825-40.

Cotrufo M, Della Corte A. The association of bicuspid aortic valve disease with asymmetric dilatation of the tubular ascending aorta: identification of a definite syndrome. *J Cardiovasc Med (Hagerstown)*. 2009;10:291-7.

Cotrufo M, Della Corte A, De Santo LS, Quarto C, De Feo M, Romano G, Amarelli C, Scardone M, Di Meglio F, Guerra G, Scarano M, Vitale S, Castaldo C, Montagnani S. Different patterns of extracellular matrix protein expression in the convexity and the concavity of the dilated aorta with bicuspid aortic valve: preliminary results. *J Thorac Cardiovasc Surg*. 2005;130:504-11.

Criado FJ, Abul-Khoudoud OR, Domer GS, McKendrick C, Zuzga M, Clark NS, Monaghan K, Barnatan MF. Endovascular repair of the thoracic aorta: lessons learned. *Ann Thorac Surg*. 2005;80:857-63; discussion 63.

Cribier A, Eltchaninoff H, Bash A, Borenstein N, Tron C, Bauer F, Derumeaux G, Anselme F, Laborde F, Leon MB. Percutaneous transcatheter implantation of an aortic valve prosthesis for calcific aortic stenosis: first human case description. *Circulation*. 2002;106:3006-8.

David TE, Feindel CM. An aortic valve-sparing operation for patients with aortic incompetence and aneurysm of the ascending aorta. *J Thorac Cardiovasc Surg*. 1992;103:617-21; discussion 22.

Davies PF. Flow-mediated endothelial mechanotransduction. *Physiol Rev*. 1995;75:519-60.

Davies RR, Gallo A, Coady MA, Tellides G, Botta DM, Burke B, Coe MP, Kopf GS, Elefteriades JA. Novel measurement of relative aortic size predicts rupture of thoracic aortic aneurysms. *Ann Thorac Surg*. 2006;81:169-77.

de Kerchove L, El Khoury G. Anatomy and pathophysiology of the ventriculo-aortic junction: implication in aortic valve repair surgery. *Ann Cardiothorac Surg*. 2013a;2:57-64.

de Kerchove L, El Khoury G. Anatomy and pathophysiology of the ventriculo-aortic junction: implication in aortic valve repair surgery. *Annals of Cardiothoracic Surgery*. 2013b;2:57-64.

de Sa M, Moshkovitz Y, Butany J, David TE. Histologic abnormalities of the ascending aorta and pulmonary trunk in patients with bicuspid aortic valve disease: clinical relevance to the Ross procedure. *J Thorac Cardiovasc Surg*. 1999;118:588-94.

Della Corte A, Bancone C, Quarto C, Dialetto G, Covino FE, Scardone M, Caianiello G, Cotrufo M. Predictors of ascending aortic dilatation with bicuspid aortic valve: a wide spectrum of disease expression. *Eur J Cardiothorac Surg*. 2007;31:397-404; discussion -5.

Della Corte A, De Santo LS, Montagnani S, Quarto C, Romano G, Amarelli C, Scardone M, De Feo M, Cotrufo M, Caianiello G. Spatial patterns of matrix protein expression in dilated ascending aorta with aortic regurgitation: congenital bicuspid valve versus Marfan's syndrome. *J Heart Valve Dis*. 2006;15:20-7; discussion 7.

Della Corte A, Quarto C, Bancone C, Castaldo C, Di Meglio F, Nurzynska D, De Santo LS, De Feo M, Scardone M, Montagnani S, Cotrufo M. Spatiotemporal patterns of smooth muscle cell changes in ascending aortic dilatation with bicuspid and tricuspid aortic valve stenosis: focus on cell-matrix signaling. *J Thorac Cardiovasc Surg*. 2008;135:8-18, .e1-2.

Dingemans KP, Teeling P, Lagendijk JH, Becker AE. Extracellular matrix of the human aortic media: an ultrastructural histochemical and immunohistochemical study of the adult aortic media. *Anat Rec*. 2000;258:1-14.

Efstathopoulos EP, Patatoukas G, Pantos I, Benekos O, Katritsis D, Kelekis NL. Wall shear stress calculation in ascending aorta using phase contrast magnetic resonance imaging. Investigating effective ways to calculate it in clinical practice. *Phys Med*. 2008;24:175-81.

Elefteriades JA, Farkas EA. Thoracic aortic aneurysm clinically pertinent controversies and uncertainties. *J Am Coll Cardiol*. 2010;55:841-57.

Erbel R, Aboyans V, Boileau C, Bossone E, Bartolomeo RD, Eggebrecht H, Evangelista A, Falk V, Frank H, Gaemperli O, Grabenwoger M, Haverich A, Iung B, Manolis AJ, Meijboom F, Nienaber CA, Roffi M, Rousseau H, Sechtem U, Sirnes PA, Allmen RS, Vrints CJ. 2014 ESC Guidelines on the diagnosis and treatment of aortic diseases: Document covering acute and chronic aortic diseases of the thoracic and abdominal aorta of the adult. The Task Force for the Diagnosis and Treatment of Aortic Diseases of the European Society of Cardiology (ESC). *Eur Heart J*. 2014;35:2873-926.

Farin GE. *Nurb Curves and Surfaces: From Projective Geometry to Practical Use*: A.K. Peters; 1995.

Farthing S, Peronneau P. Flow in the thoracic aorta. *Cardiovasc Res*. 1979;13:607-20.

Figueroa C, Khlebnikov R, Lau KD, Arthurs CJ, Dillon-Murphy D, Alastruey-Arison J, Aguirre M. www.crimson.software.

Figueroa CA, Taylor CA, Yeh V, Chiou AJ, Zarins CK. Effect of curvature on displacement forces acting on aortic endografts: a 3-dimensional computational analysis. *J Endovasc Ther*. 2009;16:284-94.

Figueroa CA, Vignon-Clementel IE, Jansen KC, Hughes TJ, Taylor CA. A coupled momentum method for modeling blood flow in three-dimensional deformable arteries. *Comput Methods Appl Mech Eng*. 2006;195:5685-706.

Fillinger MF, Marra SP, Raghavan ML, Kennedy FE. Prediction of rupture risk in abdominal aortic aneurysm during observation: wall stress versus diameter. *J Vasc Surg*. 2003;37:724-32.

Fillinger MF, Raghavan ML, Marra SP, Cronenwett JL, Kennedy FE. In vivo analysis of mechanical wall stress and abdominal aortic aneurysm rupture risk. *J Vasc Surg.* 2002;36:589-97.

Frazin LJ, Lanza G, Vonesh M, Khasho F, Spitzzeri C, McGee S, Mehlman D, Chandran KB, Talano J, McPherson D. Functional chiral asymmetry in descending thoracic aorta. *Circulation.* 1990;82:1985-94.

Frazin LJ, Vonesh MJ, Chandran KB, Shipkowitz T, Yaacoub AS, McPherson DD. Confirmation and initial documentation of thoracic and abdominal aortic helical flow. An ultrasound study. *ASAIO J.* 1996;42:951-6.

Friedman MH, Hutchins GM, Bargeron CB, Deters OJ, Mark FF. Correlation between intimal thickness and fluid shear in human arteries. *Atherosclerosis.* 1981;39:425-36.

Gaddum NR, Alastruey J, Chowienczyk P, Rutten MCM, Segers P, Schaeffter T. Relative Contributions from the Ventricle and Arterial Tree to Arterial Pressure and its Amplification: An Experimental Study. *Am J Physiol Heart Circ Physiol.* 2017:ajpheart.00844.2016.

Gaddum NR, Fraser JF, Timms DL. Increasing the transmitted flow pulse in a rotary left ventricular assist device. *Artif Organs.* 2012;36:859-67.

Gaddum NR, Stevens M, Lim E, Fraser J, Lovell N, Mason D, Timms D, Salamonsen R. Starling-like flow control of a left ventricular assist device: in vitro validation. *Artif Organs.* 2014;38:E46-56.

Gambillara V, Montorzi G, Haziza-Pigeon C, Stergiopoulos N, Silacci P. Arterial wall response to ex vivo exposure to oscillatory shear stress. *J Vasc Res.* 2005;42:535-44.

Garg V, Muth AN, Ransom JF, Schluterman MK, Barnes R, King IN, Grossfeld PD, Srivastava D. Mutations in NOTCH1 cause aortic valve disease. *Nature*. 2005;437:270-4.

Gibbons GH, Dzau VJ. The emerging concept of vascular remodeling. *N Engl J Med*. 1994;330:1431-8.

Gnasso A, Carallo C, Irace C, De Franceschi MS, Mattioli PL, Motti C, Cortese C. Association between wall shear stress and flow-mediated vasodilation in healthy men. *Atherosclerosis*. 2001;156:171-6.

Gnasso A, Carallo C, Irace C, Spagnuolo V, De Novara G, Mattioli PL, Pujia A. Association between intima-media thickness and wall shear stress in common carotid arteries in healthy male subjects. *Circulation*. 1996;94:3257-62.

Gnasso A, Irace C, Carallo C, De Franceschi MS, Motti C, Mattioli PL, Pujia A. In vivo association between low wall shear stress and plaque in subjects with asymmetrical carotid atherosclerosis. *Stroke*. 1997;28:993-8.

Grigioni M, Daniele C, Morbiducci U, Del Gaudio C, D'Avenio G, Balducci A, Barbaro V. A mathematical description of blood spiral flow in vessels: application to a numerical study of flow in arterial bending. *J Biomech*. 2005;38:1375-86.

Guzzardi DG, Barker AJ, van Ooij P, Malaisrie SC, Puthumana JJ, Belke DD, Mewhort HE, Svystonyuk DA, Kang S, Verma S, Collins J, Carr J, Bonow RO, Markl M, Thomas JD, McCarthy PM, Fedak PW. Valve-Related Hemodynamics Mediate Human Bicuspid Aortopathy: Insights From Wall Shear Stress Mapping. *J Am Coll Cardiol*. 2015;66:892-900.

Hahn RT, Roman MJ, Mogtader AH, Devereux RB. Association of aortic dilation with regurgitant, stenotic and functionally normal bicuspid aortic valves. *J Am Coll Cardiol*. 1992;19:283-8.

Hanke T, Charitos EI, Stierle U, Robinson D, Gorski A, Sievers HH, Misfeld M. Factors associated with the development of aortic valve regurgitation over time after two different techniques of valve-sparing aortic root surgery. *J Thorac Cardiovasc Surg.* 2009;137:314-9.

Hardman D, Semple SI, Richards JM, Hoskins PR. Comparison of patient-specific inlet boundary conditions in the numerical modelling of blood flow in abdominal aortic aneurysm disease. *Int J Numer Method Biomed Eng.* 2013;29:165-78.

Hiratzka LF, Creager MA, Isselbacher EM, Svensson LG, Nishimura RA, Bonow RO, Guyton RA, Sundt TM, III. Surgery for aortic dilatation in patients with bicuspid aortic valves. *The Journal of Thoracic and Cardiovascular Surgery.* 2016;151:959-66.

Hopkins RA. Aortic valve leaflet sparing and salvage surgery: evolution of techniques for aortic root reconstruction. *Eur J Cardiothorac Surg.* 2003;24:886-97.

Humphrey JD. Mechanisms of arterial remodeling in hypertension: coupled roles of wall shear and intramural stress. *Hypertension.* 2008;52:195-200.

Humphrey JD, Taylor CA. Intracranial and abdominal aortic aneurysms: similarities, differences, and need for a new class of computational models. *Annu Rev Biomed Eng.* 2008;10:221-46.

Huntington K, Hunter AG, Chan KL. A prospective study to assess the frequency of familial clustering of congenital bicuspid aortic valve. *J Am Coll Cardiol.* 1997;30:1809-12.

Ikonomidis JS, Ruddy JM, Benton SM, Jr., Arroyo J, Brinsa TA, Stroud RE, Zeeshan A, Bavaria JE, Gorman JH, 3rd, Gorman RC, Spinale FG, Jones JA. Aortic dilatation with bicuspid aortic valves: cusp fusion correlates to matrix metalloproteinases and inhibitors. *Ann Thorac Surg.* 2012;93:457-63.

Isselbacher EM. Thoracic and abdominal aortic aneurysms. *Circulation*. 2005;111:816-28.

Katayama S, Umetani N, Sugiura S, Hisada T. The sinus of Valsalva relieves abnormal stress on aortic valve leaflets by facilitating smooth closure. *J Thorac Cardiovasc Surg*. 2008;136:1528-35, 35.e1.

Kilner PJ, Yang GZ, Mohiaddin RH, Firmin DN, Longmore DB. Helical and retrograde secondary flow patterns in the aortic arch studied by three-directional magnetic resonance velocity mapping. *Circulation*. 1993;88:2235-47.

Kim HJ, Vignon-Clementel IE, Figueroa CA, LaDisa JF, Jansen KE, Feinstein JA, Taylor CA. On coupling a lumped parameter heart model and a three-dimensional finite element aorta model. *Ann Biomed Eng*. 2009;37:2153-69.

LaDisa JF, Jr., Dholakia RJ, Figueroa CA, Vignon-Clementel IE, Chan FP, Samyn MM, Cava JR, Taylor CA, Feinstein JA. Computational simulations demonstrate altered wall shear stress in aortic coarctation patients treated by resection with end-to-end anastomosis. *Congenit Heart Dis*. 2011;6:432-43.

Langille BL. Arterial remodeling: relation to hemodynamics. *Can J Physiol Pharmacol*. 1996;74:834-41.

Lansac E, Di Cerna I, Sleilaty G, Bouchot O, Arnaud Crozat E, Blin D, Acar C, Debauchez M. An aortic ring to standardise aortic valve repair: preliminary results of a prospective multicentric cohort of 144 patients. *Eur J Cardiothorac Surg*. 2010;38:147-54.

Laplace PS. *Traite de Mecanique Celeste*. 1805;vol 4.

Laskey WK, Parker HG, Ferrari VA, Kussmaul WG, Noordergraaf A. Estimation of total systemic arterial compliance in humans. *J Appl Physiol* (1985). 1990;69:112-9.

Layton K, Kallmes D, Cloft H, Lindell E, Cox V. Bovine Aortic Arch Variant in Humans: Clarification of a Common Misnomer. *Am J Neuroradiol.* 2006;27:1541-2.

Lee KW, Wood NB, Xu XY. Ultrasound image-based computer model of a common carotid artery with a plaque. *Med Eng Phys.* 2004;26:823-40.

Lee SW, Steinman DA. On the relative importance of rheology for image-based CFD models of the carotid bifurcation. *J Biomech Eng.* 2007;129:273-8.

LeMaire SA, Wang X, Wilks JA, Carter SA, Wen S, Won T, Leonardelli D, Anand G, Conklin LD, Wang XL, Thompson RW, Coselli JS. Matrix metalloproteinases in ascending aortic aneurysms: bicuspid versus trileaflet aortic valves. *J Surg Res.* 2005;123:40-8.

Leon MB, Smith CR, Mack M, Miller DC, Moses JW, Svensson LG, Tuzcu EM, Webb JG, Fontana GP, Makkar RR, Brown DL, Block PC, Guyton RA, Pichard AD, Bavaria JE, Herrmann HC, Douglas PS, Petersen JL, Akin JJ, Anderson WN, Wang D, Pocock S. Transcatheter aortic-valve implantation for aortic stenosis in patients who cannot undergo surgery. *N Engl J Med.* 2010;363:1597-607.

Les AS, Shadden SC, Figueroa CA, Park JM, Tedesco MM, Herfkens RJ, Dalman RL, Taylor CA. Quantification of hemodynamics in abdominal aortic aneurysms during rest and exercise using magnetic resonance imaging and computational fluid dynamics. *Ann Biomed Eng.* 2010;38:1288-313.

Li L, Terry CM, Shiu YT, Cheung AK. Neointimal hyperplasia associated with synthetic hemodialysis grafts. *Kidney Int.* 2008;74:1247-61.

Li Z, Kleinstreuer C. Blood flow and structure interactions in a stented abdominal aortic aneurysm model. *Med Eng Phys.* 2005;27:369-82.

Lu H, Clingman C, Golay X, van Zijl PC. Determining the longitudinal relaxation time (T1) of blood at 3.0 Tesla. *Magn Reson Med*. 2004;52:679-82.

Mahadevia R, Barker AJ, Schnell S, Entezari P, Kansal P, Fedak PW, Malaisrie SC, McCarthy P, Collins J, Carr J, Markl M. Bicuspid aortic cusp fusion morphology alters aortic three-dimensional outflow patterns, wall shear stress, and expression of aortopathy. *Circulation*. 2014;129:673-82.

Malek AM, Alper SL, Izumo S. Hemodynamic shear stress and its role in atherosclerosis. *JAMA*. 1999;282:2035-42.

Markl M, Draney MT, Hope MD, Levin JM, Chan FP, Alley MT, Pelc NJ, Herfkens RJ. Time-resolved 3-dimensional velocity mapping in the thoracic aorta: visualization of 3-directional blood flow patterns in healthy volunteers and patients. *J Comput Assist Tomogr*. 2004;28:459-68.

Markl M, Frydrychowicz A, Kozerke S, Hope M, Wieben O. 4D flow MRI. *J Magn Reson Imaging*. 2012;36:1015-36.

Markl M, Schnell S, Wu C, Bollache E, Jarvis K, Barker AJ, Robinson JD, Rigsby CK. Advanced flow MRI: emerging techniques and applications. *Clin Radiol*. 2016.

Marzo A, Singh P, Reymond P, Stergiopoulos N, Patel U, Hose R. Influence of inlet boundary conditions on the local haemodynamics of intracranial aneurysms. *Comput Methods Biomech Biomed Engin*. 2009;12:431-44.

McKusick VA. Association of congenital bicuspid aortic valve and Erdheim's cystic medial necrosis. *Lancet*. 1972;1:1026-7.

Meierhofer C, Schneider EP, Lyko C, Hutter A, Martinoff S, Markl M, Hager A, Hess J, Stern H, Fratz S. Wall shear stress and flow patterns in the ascending aorta in patients with bicuspid aortic valves differ significantly from tricuspid aortic valves: a prospective study. *Eur Heart J Cardiovasc Imaging*. 2013;14:797-804.

Metaxa E, Tremmel M, Natarajan SK, Xiang J, Paluch RA, Mandelbaum M, Siddiqui AH, Kolega J, Mocco J, Meng H. Characterization of critical hemodynamics contributing to aneurysmal remodeling at the basilar terminus in a rabbit model. *Stroke*. 2010;41:1774-82.

Migliavacca F, Balossino R, Pennati G, Dubini G, Hsia TY, de Leval MR, Bove EL. Multiscale modelling in biofluidynamics: application to reconstructive paediatric cardiac surgery. *J Biomech*. 2006;39:1010-20.

Milner JS, Moore JA, Rutt BK, Steinman DA. Hemodynamics of human carotid artery bifurcations: computational studies with models reconstructed from magnetic resonance imaging of normal subjects. *J Vasc Surg*. 1998;28:143-56.

Morbiducci U, Ponzini R, Gallo D, Bignardi C, Rizzo G. Inflow boundary conditions for image-based computational hemodynamics: impact of idealized versus measured velocity profiles in the human aorta. *J Biomech*. 2013;46:102-9.

Morbiducci U, Ponzini R, Rizzo G, Cadioli M, Esposito A, De Cobelli F, Del Maschio A, Montecvecchi FM, Redaelli A. In vivo quantification of helical blood flow in human aorta by time-resolved three-dimensional cine phase contrast magnetic resonance imaging. *Ann Biomed Eng*. 2009;37:516-31.

Morgan-Hughes GJ, Roobottom CA, Owens PE, Marshall AJ. Dilatation of the aorta in pure, severe, bicuspid aortic valve stenosis. *Am Heart J*. 2004;147:736-40.

Moyle KR, Antiga L, Steinman DA. Inlet conditions for image-based CFD models of the carotid bifurcation: is it reasonable to assume fully developed flow? *J Biomech Eng.* 2006;128:371-9.

Muller J, Sahni O, Li X, Jansen KE, Shephard MS, Taylor CA. Anisotropic adaptive finite element method for modelling blood flow. *Comput Methods Biomech Biomed Engin.* 2005;8:295-305.

Munson BR, Young DF, Okiishi TH, Huebsch WW. *Fundamentals of Fluid Mechanics.* 2009;6th Edition.

Myers JG, Moore JA, Ojha M, Johnston KW, Ethier CR. Factors influencing blood flow patterns in the human right coronary artery. *Ann Biomed Eng.* 2001;29:109-20.

Mynard JP, Wasserman BA, Steinman DA. Errors in the estimation of wall shear stress by maximum Doppler velocity. *Atherosclerosis.* 2013;227:259-66.

Naito S, Gross T, Disha K, von Kodolitsch Y, Reichenspurner H, Girდაuskas E. Late post-AVR progression of bicuspid aortopathy: link to hemodynamics. *Gen Thorac Cardiovasc Surg.* 2017;65:252-8.

Nakamura M, Wada S, Yamaguchi T. Computational analysis of blood flow in an integrated model of the left ventricle and the aorta. *J Biomech Eng.* 2006;128:837-43.

Nataatmadja M, West M, West J, Summers K, Walker P, Nagata M, Watanabe T. Abnormal extracellular matrix protein transport associated with increased apoptosis of vascular smooth muscle cells in marfan syndrome and bicuspid aortic valve thoracic aortic aneurysm. *Circulation.* 2003;108 Suppl 1:II329-34.

Nathan DP, Xu C, Plappert T, Desjardins B, Gorman JH, 3rd, Bavaria JE, Gorman RC, Chandran KB, Jackson BM. Increased ascending aortic wall stress in patients with bicuspid aortic valves. *Ann Thorac Surg.* 2011;92:1384-9.

Nishimura RA, Otto CM, Bonow RO, Carabello BA, Erwin JP, 3rd, Guyton RA, O'Gara PT, Ruiz CE, Skubas NJ, Sorajja P, Sundt TM, 3rd, Thomas JD, American College of Cardiology/American Heart Association Task Force on Practice G. 2014 AHA/ACC guideline for the management of patients with valvular heart disease: a report of the American College of Cardiology/American Heart Association Task Force on Practice Guidelines. *J Am Coll Cardiol.* 2014;63:e57-185.

Nistri S, Sorbo MD, Marin M, Palisi M, Scognamiglio R, Thiene G. Aortic root dilatation in young men with normally functioning bicuspid aortic valves. *Heart.* 1999;82:19-22.

Oechtering TH, Hons CF, Sieren M, Hunold P, Hennemuth A, Huellebrand M, Drexel J, Scharfschwerdt M, Richardt D, Sievers HH, Barkhausen J, Frydrychowicz A. Time-resolved 3-dimensional magnetic resonance phase contrast imaging (4D Flow MRI) analysis of hemodynamics in valve-sparing aortic root repair with an anatomically shaped sinus prosthesis. *J Thorac Cardiovasc Surg.* 2016;152:418-27.e1.

Pape LA, Tsai TT, Isselbacher EM, Oh JK, O'Gara P T, Evangelista A, Fattori R, Meinhardt G, Trimarchi S, Bossone E, Suzuki T, Cooper JV, Froehlich JB, Nienaber CA, Eagle KA. Aortic diameter ≥ 5.5 cm is not a good predictor of type A aortic dissection: observations from the International Registry of Acute Aortic Dissection (IRAD). *Circulation.* 2007;116:1120-7.

Piazza N, de Jaegere P, Schultz C, Becker AE, Serruys PW, Anderson RH. Anatomy of the aortic valvar complex and its implications for transcatheter implantation of the aortic valve. *Circ Cardiovasc Interv.* 2008;1:74-81.

Pisani G, Scaffa R, Ieropoli O, Dell'Amico EM, Maselli D, Morbiducci U, De Paulis R. Role of the sinuses of Valsalva on the opening of the aortic valve. *J Thorac Cardiovasc Surg.* 2013;145:999-1003.

Prasad A, Xiao N, Gong XY, Zarins CK, Figueroa CA. A computational framework for investigating the positional stability of aortic endografts. *Biomech Model Mechanobiol.* 2013;12:869-87.

Presbitero P, Demarie D, Villani M, Perinetti EA, Riva G, Orzan F, Bobbio M, Morea M, Brusca A. Long term results (15-30 years) of surgical repair of aortic coarctation. *Br Heart J.* 1987;57:462-7.

Pritchard WF, Davies PF, Derafshi Z, Polacek DC, Tsao R, Dull RO, Jones SA, Giddens DP. Effects of wall shear stress and fluid recirculation on the localization of circulating monocytes in a three-dimensional flow model. *J Biomech.* 1995;28:1459-69.

Ranga A, Bouchot O, Mongrain R, Ugolini P, Cartier R. Computational simulations of the aortic valve validated by imaging data: evaluation of valve-sparing techniques. *Interact Cardiovasc Thorac Surg.* 2006;5:373-8.

Rinaudo A, Pasta S. Regional variation of wall shear stress in ascending thoracic aortic aneurysms. *Proc Inst Mech Eng H.* 2014;228:627-38.

Roberts WC. The congenitally bicuspid aortic valve. A study of 85 autopsy cases. *Am J Cardiol.* 1970;26:72-83.

Sarsam MA, Yacoub M. Remodeling of the aortic valve anulus. *J Thorac Cardiovasc Surg.* 1993;105:435-8.

Schaefer BM, Lewin MB, Stout KK, Gill E, Prueitt A, Byers PH, Otto CM. The bicuspid aortic valve: an integrated phenotypic classification of leaflet morphology and aortic root shape. *Heart*. 2008;94:1634-8.

Segers P, Verdonck P. Role of tapering in aortic wave reflection: hydraulic and mathematical model study. *J Biomech*. 2000;33:299-306.

Sigovan M, Dyverfeldt P, Wrenn J, Tseng EE, Saloner D, Hope MD. Extended 3D approach for quantification of abnormal ascending aortic flow. *Magn Reson Imaging*. 2015.

Smith CR, Leon MB, Mack MJ, Miller DC, Moses JW, Svensson LG, Tuzcu EM, Webb JG, Fontana GP, Makkar RR, Williams M, Dewey T, Kapadia S, Babaliaros V, Thourani VH, Corso P, Pichard AD, Bavaria JE, Herrmann HC, Akin JJ, Anderson WN, Wang D, Pocock SJ. Transcatheter versus surgical aortic-valve replacement in high-risk patients. *N Engl J Med*. 2011;364:2187-98.

Soerensen DD, Pekkan K, de Zelicourt D, Sharma S, Kanter K, Fogel M, Yoganathan AP. Introduction of a new optimized total cavopulmonary connection. *Ann Thorac Surg*. 2007;83:2182-90.

Steinman DA. Image-based computational fluid dynamics modeling in realistic arterial geometries. *Ann Biomed Eng*. 2002;30:483-97.

Steinman DA, Thomas JB, Ladak HM, Milner JS, Rutt BK, Spence JD. Reconstruction of carotid bifurcation hemodynamics and wall thickness using computational fluid dynamics and MRI. *Magn Reson Med*. 2002;47:149-59.

Stewart AB, Ahmed R, Travill CM, Newman CG. Coarctation of the aorta life and health 20-44 years after surgical repair. *Br Heart J*. 1993;69:65-70.

Stuhne GR, Steinman DA. Finite-element modeling of the hemodynamics of stented aneurysms. *J Biomech Eng.* 2004;126:382-7.

Svensson LG, Adams DH, Bonow RO, Kouchoukos NT, Miller DC, O'Gara PT, Shahian DM, Schaff HV, Akins CW, Bavaria JE, Blackstone EH, David TE, Desai ND, Dewey TM, D'Agostino RS, Gleason TG, Harrington KB, Kodali S, Kapadia S, Leon MB, Lima B, Lytle BW, Mack MJ, Reardon M, Reece TB, Reiss GR, Roselli EE, Smith CR, Thourani VH, Tuzcu EM, Webb J, Williams MR. Aortic valve and ascending aorta guidelines for management and quality measures. *Ann Thorac Surg.* 2013;95:S1-66.

Svensson LG, Khitin L. Aortic cross-sectional area/height ratio timing of aortic surgery in asymptomatic patients with Marfan syndrome. *J Thorac Cardiovasc Surg.* 2002;123:360-1.

Taylor CA, Draney MT, Ku JP, Parker D, Steele BN, Wang K, Zarins CK. Predictive medicine: computational techniques in therapeutic decision-making. *Comput Aided Surg.* 1999;4:231-47.

Taylor CA, Figueroa CA. Patient-specific modeling of cardiovascular mechanics. *Annu Rev Biomed Eng.* 2009;11:109-34.

Thubrikar MJ. *The aortic valve*: CRC press; 1989.

Tilea I, Suci H, Tilea B, Tatar CM, Ispas M, Serban RC. Anatomy and Function of Normal Aortic Valvular Complex. In: Aikawa E, editor. *Calcific Aortic Valve Disease*. Rijeka: InTech; 2013. p. Ch. 02.

Torii R, Xu XY, El-Hamamsy I, Mohiaddin R, Yacoub MH. Computational biomechanics of the aortic root. *Aswan Heart Centre Science & Practice Series.* 2011;2011:16.

Trauzeddel RF, Lobe U, Barker AJ, Gelsinger C, Butter C, Markl M, Schulz-Menger J, von Knobelsdorff-Brenkenhoff F. Blood flow characteristics in the ascending aorta after TAVI compared to surgical aortic valve replacement. *Int J Cardiovasc Imaging*. 2016;32:461-7.

Tutar E, Ekici F, Atalay S, Nacar N. The prevalence of bicuspid aortic valve in newborns by echocardiographic screening. *Am Heart J*. 2005;150:513-5.

Vahanian A, Alfieri O, Andreotti F, Antunes MJ, Baron-Esquivias G, Baumgartner H, Borger MA, Carrel TP, De Bonis M, Evangelista A, Falk V, Lung B, Lancellotti P, Pierard L, Price S, Schafers HJ, Schuler G, Stepinska J, Swedberg K, Takkenberg J, Von Oppell UO, Windecker S, Zamorano JL, Zembala M, Guidelines ESCCfP, Joint Task Force on the Management of Valvular Heart Disease of the European Society of C, European Association for Cardio-Thoracic S. Guidelines on the management of valvular heart disease (version 2012): the Joint Task Force on the Management of Valvular Heart Disease of the European Society of Cardiology (ESC) and the European Association for Cardio-Thoracic Surgery (EACTS). *Eur J Cardiothorac Surg*. 2012;42:S1-44.

Vallabhajosyula P, Bavaria JE, Szeto WY. Hybrid Approaches to Complex Aortic Arch Aneurysms. *Operative Techniques in Thoracic and Cardiovascular Surgery*. 2012;17:15-26.

Varma N, Hinojar R, D'Cruz D, Arroyo Ucar E, Indermuehle A, Peel S, Greil G, Gaddum N, Chowienczyk P, Nagel E, Botnar RM, Puntmann VO. Coronary vessel wall contrast enhancement imaging as a potential direct marker of coronary involvement: integration of findings from CAD and SLE patients. *JACC Cardiovasc Imaging*. 2014;7:762-70.

Verma S, Siu SC. Aortic dilatation in patients with bicuspid aortic valve. *N Engl J Med*. 2014;370:1920-9.

Vesalius A. *De Humani Corporis Fabrica*. 1544.

Vignon-Clementel IE, Alberto Figueroa C, Jansen KE, Taylor CA. Outflow boundary conditions for three-dimensional finite element modeling of blood flow and pressure in arteries. *Computer Methods in Applied Mechanics and Engineering*. 2006;195:3776-96.

Vignon-Clementel IE FC, Jansen KE, Taylor CA. Outflow boundary conditions for three-dimensional finite element modeling of blood flow and pressure in arteries. *Comput Methods Appl Mech Eng*. 2006;195:3776-96.

Vignon-Clementel IE, Figueroa CA, Jansen KE, Taylor CA. Outflow boundary conditions for 3D simulations of non-periodic blood flow and pressure fields in deformable arteries. *Comput Methods Biomech Biomed Engin*. 2010;13:625-40.

Vinci Ld. The aortic valve. Royal Collection at Her Majesty Queen Elizabeth II. 1513.

Viscardi F, Vergara C, Antiga L, Merelli S, Veneziani A, Puppini G, Faggian G, Mazzucco A, Luciani GB. Comparative finite element model analysis of ascending aortic flow in bicuspid and tricuspid aortic valve. *Artif Organs*. 2010;34:1114-20.

Wake AK, Oshinski JN, Tannenbaum AR, Giddens DP. Choice of in vivo versus idealized velocity boundary conditions influences physiologically relevant flow patterns in a subject-specific simulation of flow in the human carotid bifurcation. *J Biomech Eng*. 2009;131:021013.

Waller B, Howard J, Fess S. Pathology of aortic valve stenosis and pure aortic regurgitation. A clinical morphologic assessment--Part I. *Clin Cardiol*. 1994a;17:85-92.

Waller BF, Howard J, Fess S. Pathology of aortic valve stenosis and pure aortic regurgitation: a clinical morphologic assessment--Part II. *Clin Cardiol*. 1994b;17:150-6.

Wang KC, Dutton RW, Taylor CA. Improving geometric model construction for blood flow modeling. *IEEE Eng Med Biol Mag*. 1999;18:33-9.

Ward C. Clinical significance of the bicuspid aortic valve. *Heart*. 2000;83:81-5.

Wendell DC, Samyn MM, Cava JR, Ellwein LM, Krolikowski MM, Gandy KL, Pelech AN, Shadden SC, LaDisa JF, Jr. Including aortic valve morphology in computational fluid dynamics simulations: initial findings and application to aortic coarctation. *Med Eng Phys*. 2013;35:723-35.

Wootton DM, Ku DN. Fluid mechanics of vascular systems, diseases, and thrombosis. *Annu Rev Biomed Eng*. 1999;1:299-329.

Xiao N, Alastruey J, Figueroa CA. A systematic comparison between 1-D and 3-D hemodynamics in compliant arterial models. *Int J Numer Method Biomed Eng*. 2014;30:204-31.

Xiao N, Humphrey JD, Figueroa CA. Multi-Scale Computational Model of Three-Dimensional Hemodynamics within a Deformable Full-Body Arterial Network. *J Comput Phys*. 2013;244:22-40.

Xiong G, Figueroa CA, Xiao N, Taylor CA. Simulation of blood flow in deformable vessels using subject-specific geometry and spatially varying wall properties. *Int J Numer Method Biomed Eng*. 2011;27:1000-16.

Yearwood TL, Chandran KB. Experimental investigation of steady flow through a model of the human aortic arch. *J Biomech*. 1980;13:1075-88.

Yearwood TL, Chandran KB. Physiological pulsatile flow experiments in a model of the human aortic arch. *J Biomech*. 1982;15:683-704.

Yeung JJ, Kim HJ, Abbruzzese TA, Vignon-Clementel IE, Draney-Blomme MT, Yeung KK, Perakash I, Herfkens RJ, Taylor CA, Dalman RL. Aortoiliac hemodynamic and morphologic adaptation to chronic spinal cord injury. *J Vasc Surg.* 2006;44:1254-65.

Zarins CK, Giddens DP, Bharadvaj BK, Sottiurai VS, Mabon RF, Glagov S. Carotid bifurcation atherosclerosis. Quantitative correlation of plaque localization with flow velocity profiles and wall shear stress. *Circ Res.* 1983;53:502-14.

Last night
I begged the Wise One to tell me
the secret of the world.
Gently, gently he whispered,
“Be quiet,
the secret cannot be spoken,
it is wrapped in silence.”

Rumi, 1207 - 1273